Multigrid Analysis and Embedded Boundary Conditions for Discontinuous Galerkin Discretization

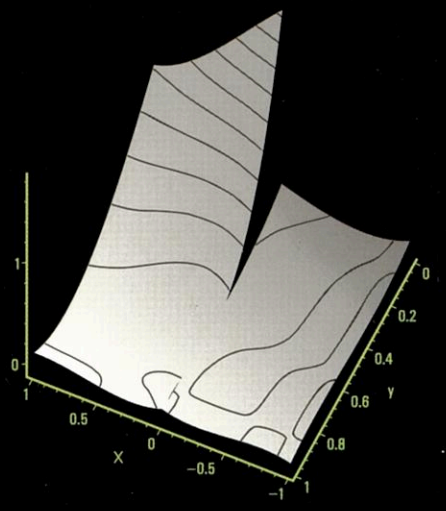

Marc H. van Raalte

Stellingen behorende bij het proefschrift

Multigrid Analysis and Embedded Boundary Conditions for Discontinuous Galerkin Discretization

door

Marc H. van Raalte

I. Multiroosteriteratie met een puntsgewijze blokrelaxatie-algoritme als smoother is een zeer efficiënte manier om het stelsel van vergelijkingen afkomstig van puur elliptische discontinue Galerkin (DG) discretisaties op te lossen.
[*Hoofdstuk 2 tot en met 4 van dit proefschrift*]

II. De twee-niveaus analyse wordt aanzienlijk vereenvoudigd wanneer de blok-Toeplitz operatoren in puntsgewijze notatie worden weergegeven.
[*Hoofdstuk 2 tot en met 5 van dit proefschrift*]

III. Eenvoudige multiroosteriteratie, voor het oplossen van de convectie-diffusievergelijking, gediscretiseerd met een DG-methode, is robuust mits de 'interior penalty' term wordt gebruikt in de DG-discretisatie.
[*Hoofdstuk 5 van dit proefschrift*]

IV. Het is voor de betrouwbaarheid van de Fourier analyse van belang dat de inverse van de blok-Toeplitz operator begrensd is.
[*Hoofdstuk 5 van dit proefschrift*]

V. De inwendige-rand-techniek voor problemen met een gekromde rand kan tot een eenvoudige en nauwkeurige DG-discretisatie leiden en is direct toepasbaar in een multiroosteralgoritme.
[*Hoofdstuk 6 & 7 van dit proefschrift*]

VI. Om te bewerkstelligen dat bij een eindige elementen-discretisatie van een elliptische vergelijking de convectieterm aan het 'upwind' principe voldoet, is het van belang om de oplossing in een discontinue functieruimte te benaderen.

VII. Het begrip 'zo vrij als een vogeltje' krijgt bij het huidige natuurbeheer een wat sinistere betekenis.

VIII. Nu roken maatschappelijk onaanvaardbaar is geworden, biedt de mobiele telefoon een nieuw verslavend houvast.

IX. Het handhaven van een numerus fixus bij de studie medicijnen staat haaks op het streven van de overheid naar een vrije marktwerking in de zorgsector.

X. Het kan iemand beter halverwind gaan, daar bij deze koers de boot sneller en stabieler is.

XI. Het opbouwen van een netwerk is niet altijd net werk.

XII. Net zoals bij het schaken leidt een goede stelling niet altijd tot succes.

Multigrid Analysis and Embedded Boundary Conditions for Discontinuous Galerkin Discretization

Multigrid Analysis and Embedded Boundary Conditions for Discontinuous Galerkin Discretization

ACADEMISCH PROEFSCHRIFT

ter verkrijging van de graad van doctor
aan de Universiteit van Amsterdam
op gezag van de Rector Magnificus
prof. mr. P.F. van der Heijden
ten overstaan van een door
het college voor promoties ingestelde commissie,
in het openbaar te verdedigen in de Aula der Universiteit
op maandag 6 december 2004, te 13:00 uur

door

Marc Hartog van Raalte

geboren te Velsen

Promotiecommissie:

Promotor:	prof. dr. P. W. Hemker
Copromotor:	dr. W. Hoffmann
Overige leden:	prof. dr. A. Doelman
	prof. dr. ir. B. Koren
	prof. dr. ir. J. J. W. van der Vegt
	prof. dr. J. G. Verwer
	prof. dr. ir. P. Wesseling

Faculteit der Natuurwetenschappen, Wiskunde en Informatica

Voor mijn grootouders

'Doe wel en val niet om'.

Preface

Writing the last two pages of this thesis, I realize that this is the close of a pleasant and interesting period of four years of research. I conducted this research at the Centre of Mathematics and Computer Science (CWI) in Amsterdam between 2000 and 2004 and it has been financially supported by the Kortedeweg-de Vries (KdV) institute of the University of Amsterdam. I am fully aware that I could not have completed this thesis without the support and advice of a number of people, to whom I am very grateful.

First, I would like to thank my promoter Piet Hemker for the fantastic cooperation in the course of the project. Not only his expert knowledge in numerical analysis has proved invaluable, but also his ability to explain complicated mathematical problems in a clear and simple way. The hours of sparring left a deep impression on me and they form the basis for the contents of this thesis.

I was also very fortunate to be able to cooperate with my supervisor Walter Hoffmann. His inexhaustible enthusiasm for this research and his superior advice, especially in the field of the linear algebra, have contributed significantly to the realization of this thesis. Moreover, I want to extend my gratitude to him for his great support both in the research project and in the difficulties of daily life.

I further thankfully acknowledge Barry Koren. If he did not introduce me at the CWI, I would not have worked on this thesis. Moreover, he always showed a keen interest in the progress of the research.

The inspiring working atmosphere and the many friendly colleagues made my stay at the CWI a pleasant and fruitful one. In particular I enjoyed the in depth discussions with my roommate Anton Kuut, which kept us both sharp in our research project. Moreover I enjoyed the pleasant company of Domenico La-

haye and David Echeverria, while the 'philosophical' conversations with Michel Mandjes will be hard to forget.

During my research period I had to take care of a part of the Introduction in Numerical Analysis course at the KdV institute, supervised by Pia Pfluger. In view of her experience and knowledge in this field, she provided valuable help in giving this course and she made it a pleasant distraction from my investigations.

Finally, I could never have worked on this research with such inspiration and freedom without the understanding and support of my parents, my sister and most of all my Maaike.

Amsterdam, October 2004.

Contents

Chapter 1

Introduction

1.1 Motivation for the present research

Many physical aspects in daily life are modeled by partial differential equations. Examples are the flow of fluids, which are described by the Navier-Stokes equations, the radiation of electromagnetic waves, modeled by the Maxwell equations or the heat equations, describing the heat conduction in materials.

Although the fundamental processes which these equations describe differ considerably, partial differential equations in general share a nasty property. They are too complex to be solved analytically. As a consequence, the emphasis in solving these equations shifts from finding a solution in closed form toward the numerical approximation of the solution.

The increasing availability of powerful computers makes the application of numerical methods, such as finite volume, finite difference and finite element methods feasible for the accurate approximation of the solutions and, therefore, their numerical analysis is a most relevant subject.

This thesis concerns aspects of the numerical solution of elliptic partial differential equations, where the efficiency of the solution method and the accuracy of the numerical approximation play a central role.

Let us discuss the efficiency of the solution method in some detail. The application of a numerical method for the computation of an approximate solution generally requires the solution of a large system of algebraic equations, formally denoted by

$$L_h u_h = f_h. \tag{1.1}$$

Here, the subscript h denotes a parameter that influences the accuracy and also the size of the system. Because, solving this system can be quite demanding with respect to computer resources, efficiency both in data storage and in computational time are essential aspects in the numerical treatment of partial differential equations. To keep control of the data storage, it is of importance that the number of unknowns in the equations, the degrees of freedom (dofs) that determine the approximation, should more or less be proportional to the complexity of the solution of the partial differential equation. If, the solution locally has a complex structure, such as in the case of boundary layers, shear layers or shock waves, the amount of degrees of freedom in the approximation should be sufficiently large to ensure that the approximation captures these particularities of the solution. However, at locations in the domain where the solution is smooth, the density of the degrees of freedom in the approximation may be reduced in order to reduce the number of equations and unknowns in (1.1) and hence to reduce the data storage and computation time. Moreover, to make efficient use of computer time, we should rely on a solution method, in which the amount of work scales proportional to the number of unknowns in the system of algebraic equations.

Considering the aspect of the accuracy of the approximation, not only the degrees of freedom is an essential aspect, but also the numerical treatment of the domain on which the partial differential equation is approximated. To guarantee an accurate approximation of the boundary value problem, the boundary of the domain should be approximated with the same order of accuracy as required for the approximate solution.

In this context, the selection of a special class of finite element methods in an automatic mesh refinement (h-refinement) and polynomial-order adaptation (p-refinement) algorithm can be crucial for an accurate treatment of elliptic partial differential equations and its application can be an efficient means to keep control of the number of degrees of freedom. Because of their efficiency for very large algebraic systems, a multigrid method should be the method of choice for the solution of these equations. Hence, finally aiming at an hp-self-adaptive multigrid method, in this thesis we study the convergence of multigrid (MG) iteration for the solution of a linear second order elliptic equation, discretized by discontinuous Galerkin (DG) methods. Aiming at high-order of accuracy of the approximate solution, we introduce a novel DG-discretization technique for the treatment of elliptic equations defined on curved domains. This technique shows its use in cases where regular rectangular grids are preferred and it therefore fits well within the structure of the self-adaptive MG algorithm.

1.2 Aspects studied in the thesis

In this section we give a short overview of the main aspects studied in this work.

First, we discuss some properties of the DG discretization methods for the elliptic boundary value problem, that are of interest in view of our research. For an excellent overview and analysis of the various DG methods, however, we refer to [3].

Next we give a flavor of an important aspect of multigrid iteration for the solution of the system of equations arising from DG discretizations: the choice of the smoother. For a complete treatment of multigrid iteration we refer to standard works as [7, 45, 49].

Further, we introduce the basic idea behind the novel high-order DG discretization technique studied in the Chapters 6 and 7, for treating elliptic equations defined on curved domains, discretized on a regular rectangular mesh.

DG methods

DG methods are a special class of finite element methods. They approximate the *continuous* solution of an elliptic boundary value problem by a *discontinuous* function. As an example, we show in Figure 1.1 the solution obtained by a fourth-order DG approximation of an elliptic equation discretized on the unit square.

In this figure we see a coarse DG discretization on only four regular rectangular cells and a finer DG discretization on sixteen cells. On each cell, the solution of the boundary value problem is locally approximated by a fourth-order polynomial. In the left figure, the DG discretization is still too coarse to accurately approximate the solution of the elliptic equation. As a consequence, we see large discontinuities across the cell interfaces in the DG discretization. Halving the gridsize in each of the two coordinate directions, the DG method approximates the solution more accurately. The visible discontinuities in the approximation have vanished.

Hence, in contrast to the classical finite element method, DG methods approximate the solution of the boundary value problem in a space of discontinuous finite-dimensional polynomial functions. The inter-element continuity requirements for the approximation at the cell boundaries are not incorporated in the approximation space, but arise as additional terms in the discrete equations.

Although this discretization approach seems not to be natural, it is because of this discontinuity in the approximating function, that DG methods owe their flexibility in mesh refinement (h-refinement) and polynomial-order adaptation

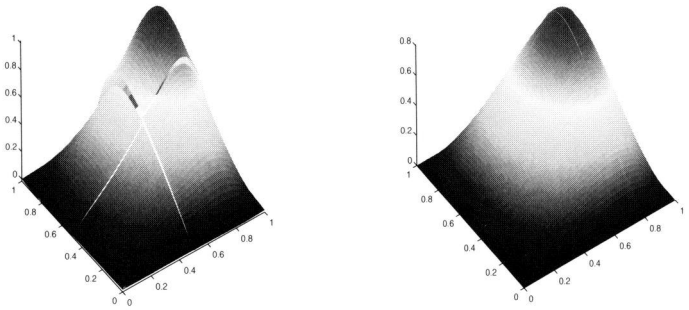

coarse discretization fine discretization

Figure 1.1: A fourth-order DG discretization (the Baumann-Oden DG-method) of the elliptic problem $\Delta u = f$ defined on the unit square. In the left figure, we see the DG discretization on four regular rectangular cells. The discretization is still too coarse in order to capture the solution by means of the cubic polynomials. Notice the typical discontinuities over the interior cell interfaces. On halving the gridsize in each of the two coordinate directions, the visible discontinuities have vanished.

(p-refinement). Since no inter-element continuity in the approximation space is required, we do not have to take care of this continuity restriction when we locally refine the mesh or we locally adapt the order of the polynomials. As a consequence, mesh refinement and order adaptation in a DG method is much more convenient than in the classical finite element discretization. Therefore, we prefer DG methods for hp-self-adaptive solution methods.

Because of the discontinuities, the DG approximation is two-valued at the interior cell boundaries (see Figure 1.1) and the DG method produces more degrees of freedom for a given order of accuracy than the classical finite element method. Therefore, for a regular mesh and a fixed order of accuracy, we solve a larger system of discrete equations, compared with the classical finite element method. This leads to some inefficiency when simple smooth functions are approximated.

Multigrid iteration

To efficiently solve the system of discrete equations (1.1), obtained from a DG method, we rely on iterative methods of defect-correction type

$$u_h^{(k+1)} = u_h^{(k)} - G_h(L_h u_h^{(k)} - f_h). \tag{1.2}$$

Here, G_h is an approximate inverse of a discrete DG operator L_h as in (1.1). Starting with an initial guess of the approximation, $u_h^{(0)}$, we hope that for a properly constructed approximate inverse G_h, the iterative process (1.2), converges rapidly to the discrete solution $u_h = L_h^{-1} f_h$ of the DG method. Hence, the error $u_h - u_h^{(k)}$, should decrease rapidly within a small number of iteration sweeps.

However, usual iterative methods of the type (1.2), have the property, that the rate of convergence strongly depends on the number of equations and unknowns in the system (1.1). Whereas for coarse DG discretizations, (1.2) shows good convergence, the rate of convergence drops significantly, if the solution of DG discretizations on finer meshes is required. Therefore, to speed up the convergence of (1.2), we rely on multigrid (MG) iteration.

The multigrid approach is to consider a coarse mesh and a sequence of finer meshes. The MG algorithm obtains its efficiency, from the fact that, during the iteration process, highly varying modes in the error can be efficiently damped on fine meshes, whereas slowly varying modes in the error can be dealt with on coarse meshes. Then, if the iterative procedure (1.2) damps within a small number of iteration sweeps the high frequencies in the error, the slowly varying modes can be represented on the coarser meshes and damped by means of the coarse grid correction (CGC), i.e., by cheaply solving a relative small set of additional correction equations. Hence, within a few iteration sweeps of (1.2) and a small amount of additional work on the coarser grids, we find the solution of the system (1.1).

However, to guarantee the success of MG iteration, the relaxation method (1.2) must sufficiently damp the high frequency modes in the error, i.e, the method must show good smoothing behavior. We quantify this 'good smoothing' behavior by considering Figure 1.2.

In this figure, we see the error $u_h - u_h^{(3)}$ after a small number of iteration sweeps ($k = 3$) for the two different types of iterative methods that are studied in this thesis: the *cellwise* and the *pointwise* block-relaxation method. Although for both methods the error $u_h - u_h^{(3)}$ is not sufficiently small, we see in the left figure that the function is highly non-smooth and discontinuous, whereas in the

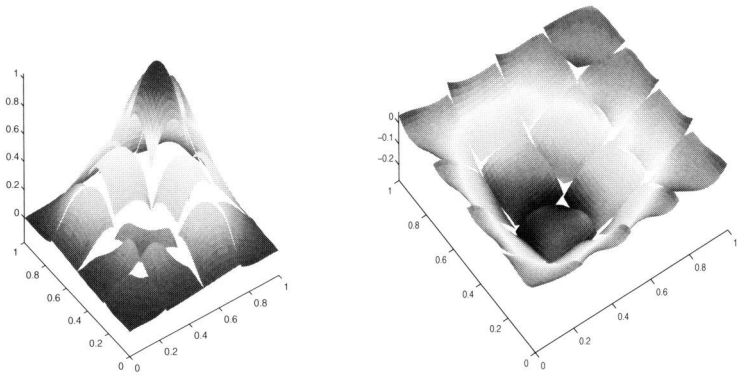

poor smoothing good smoothing

Figure 1.2: The error $u_h - u_h^{(3)}$, shown on a regular rectangular mesh, after three iterations with the relaxation method of the type (1.2), that may serve as smoother in the MG algorithm for DG approximations. In the left figure, we see poor smoothing of the relaxation (cellwise Gauss-Seidel). The error is highly irregular and discontinuous and cannot be damped by means of a coarse grid correction. In the right figure, we see good smoothing of the relaxation (pointwise Gauss-Seidel). The error is sufficiently smooth in order to be damped in the MG coarse grid correction.

right figure we see a sufficiently smooth function. In the multigrid process, a sufficiently smooth error can be represented on coarser meshes and can therefore be damped by the coarse grid correction. This accelerates the convergence of (1.2) essentially.

This thesis presents a detailed convergence analysis of multigrid iteration with the possible *cellwise* and *pointwise* block-relaxation methods as smoothers for the solution of the discrete equations arising from DG discretizations.

Embedded boundaries

In view of our multigrid algorithm, it is convenient to discretize the boundary value problem on regular rectangular meshes. Then a difficulty arises if the equation is defined on a curved domain. The boundary of the domain cannot follow the grid lines of the orthogonal mesh. For that purpose, we introduce a technique for high-order DG discretizations for solving elliptic equations, which are defined on a curved domain, while we maintain the basic orthogonal mesh.

Of coarse, the classical finite element approach can be used to locally adapt the shape of the cells to the curved boundary. However, the mesh generation technique, in particular for three-dimensional problems, is generally a complicated task, while the regularity of the mesh is not ensured. Moreover, the way to handle the generation of coarser meshes is paved with difficulties. Therefore, we study the possibility to 'embed' the curved boundary in the regular rectangular cell.

We show the main idea by the example in Figure 1.3. In this figure, we see the solution of a two-dimensional DG discretization, discretized on a domain, with a part of the boundary embedded. In the left top figure we see the domain Ω on which the equation is defined with a curved circular boundary segment.

To partition this domain Ω in regular rectangular cells, we slightly extend the domain by introducing a small fictitious part $\widetilde{\Omega}$, as shown in the right top figure, and we consider the equation on the larger domain, i.e., the domain of interest Ω and the fictitious part $\widetilde{\Omega}$. Next, we partition the total domain in regular rectangular cells, as shown, and we straightforwardly discretize the problem with a DG method on this partitioning. As a consequence, the circular boundary cannot follow the grid lines and hence is embedded. According to the principles, that underly DG methods, we impose the embedded Dirichlet boundary condition in the DG variational form. In the left bottom figure, we see a fourth order DG discretization with cubic polynomials on each cell. At cells where the boundary is embedded, the approximation satisfies the Dirichlet boundary condition. In the right bottom figure, we see the same DG approximation on the total domain, the union the of domain of interest and the fictitious part of the domain. Notice, the polynomial continuation in the fictitious part of the domain.

An anlysis of this discretization technique is presented in the Chapters 6 and 7 of the thesis.

1.3 Outline of the thesis

We organize the contents of the thesis as follows. The first four chapters are devoted to the multigrid (MG) convergence analysis for DG methods. In the last two chapters, we study the discretization technique of the embedded boundary. This yields the following outline.

In the next chapter we study the convergence of multigrid iteration for the solution of the discrete system arising from DG discretizations of the Poisson equation, viz. the Baumann-Oden DG, the symmetric DG and the symmet-

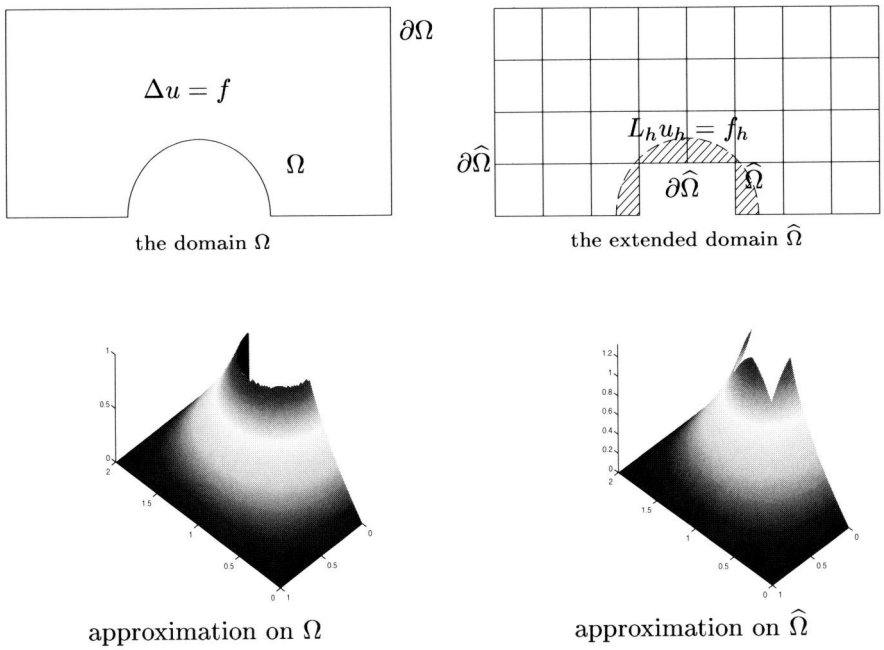

Figure 1.3: An elliptic problem defined on a curved domain, discretized by a DG method on a regular rectangular mesh. The circular part of the domain boundary cannot follow the grid lines of the mesh and is for that purpose 'embedded'. On the circular boundary, the solution has to satisfy the Dirichlet boundary condition $u = 1$. In the left bottom figure, we see a fourth-order DG discretization on the domain of interest. In the right bottom figure, we see the same DG discretization, shown on the total domain, the domain of interest and the extended 'fictitious' part of the domain.

ric interior penalty DG method. In this initial study, we restrict ourselves to the discretization of the Poisson equation in one space dimension. We describe the DG discretizations and we introduce the MG algorithm. Then, we distinguish between the concept of cellwise and pointwise relaxation methods that may serve as smoothers in the MG algorithm and we show how the different relaxation procedures are related to the discrete DG operator. To study the convergence of MG iteration, we introduce the Fourier analysis tools as needed for the smoothing and two-level analysis. By Fourier two-level analysis we compute smoothing factors and spectral norms. We conclude that an efficient MG algorithm can be constructed, based on pointwise smoothing. By numerical experiments we illustrate the analyzed MG convergence.

In Chapter 3, we study MG iteration for DG discretizations of the Poisson equation with linear elements, since this case may be used to accelerate the higher-order solution in the p-hierarchical structure of the hp-adaptive approximation case. This case is special, because an interior penalty term is compulsory for stability.

Having studied MG convergence for DG discretizations of the one-dimensional Poisson equation, in Chapter 4 we analyze MG iteration for two-dimensional DG discretizations. Starting with the DG variational form we introduce the discretization stencils and we extend the Fourier analysis tools for the two-dimensional smoothing and two-level analysis. We show that again the pointwise smoothing strategy leads to efficient MG iteration.

In Chapter 5 we study the convergence of MG iteration for the convection-diffusion equation and the convection dominated equation, discretized by DG methods. Restricting to DG discretizations in one space dimension, by Fourier smoothing and two-level analysis we determine smoothing factors and spectral norms. The analysis shows that a small number of classical MG cycles is sufficient to solve the convection diffusion equation efficiently.

In Chapter 6 we introduce the embedded boundary value problem for high-order DG discretizations on regular rectangular meshes. We give an exposure of weak forms, that can be used for the discretization of boundary value problems defined on a curved domain. We first restrict ourselves to simple experiments in one and two dimensions, in order to identify the various properties of the methods. Then in the last chapter we extend the embedded boundary technique for DG disctretizations to complete regular rectangular grids. We study the convergence and the regularity of the discrete operator. The presented technique fits with the discontinuous Galerkin discretization and can directly be applied in combination with a full MG algorithm.

The research in this thesis will be published or has been published before.

This thesis presents a re-edited version.

Chapter 2 has been published as:
P.W. Hemker, W. Hoffmann and M.H. van Raalte. Two-level Fourier analysis of a multigrid approach for discontinuous Galerkin discretization. *SIAM Journal on Scientific Computing*, 25:1018-1041, 2004.

Chapter 3 has been published as:
P.W. Hemker, W. Hoffmann and M.H. van Raalte. Fourier two-level analysis for discontinuous Galerkin discretization with linear elements. *Numerical Linear Algebra with Applications*, 11:473-491, 2004.

Chapter 4 has been published as:
P.W. Hemker and M.H. van Raalte. Fourier two-level analysis for higher dimensional discontinuous Galerkin discretization. *Computing and Visualization in Science*, 7:159-172, 2004.

Chapter 5 has been submitted to *Numerical Linear Algebra with Applications* as: P.W. Hemker and M.H. van Raalte Two-level multigrid analysis for the convection-diffusion equation discretized by a discontinuous Galerkin method.

Chapter 6 has been published as:
P.W. Hemker, W. Hoffmann and M.H. van Raalte. Discontinuous Galerkin discretization with embedded boundary conditions. *Computational Methods in Applied Mathematics*, 3:135-158, 2003.

Chapter 7 has been published as:
M.H. van Raalte. A feasibility study for DG discretization with embedded Dirichlet boundary condition. *Applied Numerical Mathematics*, 51:361-383, 2004.

Chapter 2

Two-level analysis for DG discretization with cubic elements

Summary

In this chapter we study a multigrid (MG) method for the solution of a linear second order elliptic equation, discretized by discontinuous Galerkin (DG) methods, and we give a detailed analysis of the convergence for different block-relaxation strategies.

We find that pointwise block-partitioning gives much better results than the classical cellwise partitioning. Both for the Baumann–Oden method and for the symmetric DG method, with and without interior penalty (IP), the block-relaxation methods (Jacobi, Gauss–Seidel, and symmetric Gauss–Seidel) give excellent smoothing procedures in a classical MG setting. Independent of the mesh size, simple MG cycles give convergence factors of 0.075–0.4 per iteration sweep for the different discretization methods studied.

2.1 Introduction

Although discontinuous Galerkin (DG) methods are traditionally used for the solution of hyperbolic equations [9, 30, 41], recently there has been renewed

interest in their application to elliptic problems. Early methods for elliptic problems [13, 36] were considered unattractive because they resulted in discrete systems that showed saddle-point problem behavior. The nondefinite spectrum makes time-stepping procedures unstable and makes many iterative methods inadequate for the computation of steady solutions. This is fixed by introducing an interior penalty (IP) to penalize the discontinuity in the discrete solution [2, 43, 50], which is effective but leaves the user with the quite arbitrary choice of an $\mathcal{O}(h^{-1})$ penalty parameter.

In 1998 Oden, Babuška, and Baumann [37] (see also [5, 6]) published another stable method of DG type without such a free parameter. This interesting method, however, results in an asymmetric discrete operator, even for the discretization of a symmetric continuous problem. In this chapter we consider the asymmetric (Baumann) and the symmetric discretization methods, both with and without IP. For an excellent survey and a unified analysis of the different DG methods for elliptic problems we refer to [3].

The motivation for our present research lies in our interest in the *hp*-self-adaptive solution of more general and three-dimensional problems on dyadic grids. Here DG methods are particularly attractive because of their ability to conveniently handle difficulties related to order- and grid-adaptation [29, 44]. For the solution of the resulting discrete systems we want to rely on multigrid (MG) methods because of their expected optimal efficiency. The framework of the combined adaptive discretization and the MG solution process is found, e.g., in [8, 19].

We emphasize that our approach is quite different from the analysis of MG as a preconditioner, analyzed for DG methods in [15]. Considering MG as an independent solution process gives us the opportunity not only to solve a linear system but also to simultaneously create the adaptive grid together with solving the discrete (linear) system. This use of MG allows us to drop the Krylov-space iteration (as, e.g., conjugate gradient or GMRES), preserving the optimal $\mathcal{O}(N)$ property [16]. Moreover, the local mode analysis allows us to study not only the symmetric positive definite case but also the asymmetric and nonpenalized methods.

In this chapter we study the convergence of the MG method by smoothing analysis and by analyzing the two-level convergence behavior, restricting ourselves to the discretized Poisson equation in one space dimension. Without considerably extra complexity a similar analysis can be made for two or three space dimensions. In Chapter 4 (see also [25]) we show that, using the same techniques as used in this chapter, but with proper modifications for more dimensions, again an efficient MG method can be constructed.

In this chapter we show that the discrete operator can be partitioned in block-tridiagonal form in two essentially different ways: *cellwise* and *pointwise*. For each of these partitionings, block-relaxation methods (block-Jacobi, block-Gauss–Seidel) can be used as smoothing procedures in the MG algorithm. It appears that the type of block-partitioning makes an essential difference: the pointwise block-partitioning shows a much better convergence than the usual cellwise block-partitioning. It appears that pointwise block-partitioning even leads to good smoothing for the symmetric DG method of saddle-point type.

The outline of this chapter is as follows. In Section 2.2 we describe the DG discretizations used. We select a particular basis in the space of piecewise polynomial functions for the test and trial spaces in order to introduce the distinction between cellwise and pointwise block-partitionings. We introduce the MG algorithm and describe in detail the grid-transition operators used.

In Section 2.3 we develop the Fourier analysis tools needed to make the local mode analysis for the block-Toeplitz matrices: the discretization operator, the prolongation, and the restriction operator. Then, in Section 2.4 we apply the smoothing analysis to the cellwise and pointwise partitioned discretizations. We determine the smoothing factors and compute optimal damping parameters. The results motivate us to continue with the two-level analysis for the pointwise partitioning exclusively. Therefore, in Section 2.5 we take the MG coarse-grid correction into account. We compute the spectral radii for the error reduction operators. It appears that an error reduction factor of 0.075 (for symmetric Gauss–Seidel (SGS)) to 0.4 (for damped Jacobi) per MG-sweep is predicted for the nonpenalized discretizations. For the penalized method the convergence is somewhat slower, but still faster than 0.6 per MG-sweep. In order to see what can be the worst possible behavior in a single as well as a couple of iteration sweeps, we also compute the corresponding spectral norms. We conclude that, for pointwise smoothers, MG converges rapidly in all cases.

In Section 2.6 we show by Fourier analysis the consistency and the convergence of the discretization stencils obtained by the DG methods. This gives some additional insight into the accuracy of the different methods and the lack of adjoint consistency of Baumann's method as indicated in [3]. In the final section we show some numerical results that illustrate the analyzed behavior and show the fast convergence of the MG method.

2.2 The DG discretization

2.2.1 DG methods

In order to describe the discretization method studied in this chapter, we first give the special weak form of the equation as used for these DG discretization methods. On an open cube Ω, with boundary $\partial\Omega = \Gamma_D \cup \Gamma_N$, we consider the Poisson equation, partly with Neumann and partly with Dirichlet boundary conditions:

$$-\nabla \cdot \nabla u = f \text{ on } \Omega; \quad u = u_0 \text{ on } \Gamma_{\mathrm{D}} \cap \partial\Omega, \quad u_n = g \text{ on } \Gamma_N \cap \partial\Omega. \tag{2.1}$$

On Ω we introduce a uniform partitioning Ω_h, i.e., a set of disjoint rectangular, open cells Ω_e in Ω, all of identical shape:

$$\Omega_h = \left\{ \Omega_e \;\middle|\; \cup_e \overline{\Omega}_e = \overline{\Omega},\ \Omega_i \cap \Omega_j = \emptyset,\ i \neq j \right\}. \tag{2.2}$$

We define on Ω_h the *broken Sobolev space* [5, 6, 37] for nonnegative integer k,

$$H^k(\Omega_h) = \left\{ u \in L_2(\Omega) \,\middle|\, u|_{\Omega_e} \in H^k(\Omega_e) \quad \forall \Omega_e \in \Omega_h \right\}.$$

Then, the weak form of the equation, associated with the DG methods, reads as follows [6, 37]: Find $u \in H^1(\Omega_h)$ such that

$$B(u, v) = L(v) \quad \forall v \in H^1(\Omega_h), \tag{2.3}$$

where

$$\begin{aligned} B(u,v) = &\sum_{\Omega_e \in \Omega_h} \int_{\Omega_e} \nabla u \cdot \nabla v dx - \int_{\Gamma_{\mathrm{int}} \cup \Gamma_{\mathrm{D}}} \langle \nabla u \rangle \cdot [v]\, ds \\ &+ \sigma \int_{\Gamma_{\mathrm{int}} \cup \Gamma_{\mathrm{D}}} \langle \nabla v \rangle \cdot [u]\, ds + \mu \int_{\Gamma_{\mathrm{int}} \cup \Gamma_{\mathrm{D}}} [u] \cdot [v]\, ds \end{aligned} \tag{2.4}$$

and

$$\begin{aligned} L(v) = &\sum_{\Omega_e \in \Omega_h} \int_{\Omega_e} fv\, dx + \sigma \int_{\Gamma_{\mathrm{D}}} \langle \nabla v \rangle \cdot [u_0]\, ds \\ &+ \mu \int_{\Gamma_{\mathrm{D}}} [u_0] \cdot [v]\, ds + \int_{\Gamma_N} gv\, ds. \end{aligned}$$

Here Γ_{int} is the union of all interior cell faces, and $\sigma \neq 0$ and $\mu \geq 0$ are parameters identifying the different DG methods. ($\sigma = 1$ for Baumann's method;

$\sigma = -1$ for symmetric DG; $\mu > 0$ is the IP parameter.) The jump operator $[\cdot]$ and the average operator $\langle\cdot\rangle$ are defined at the common interface $\Gamma_{i,j}$ between two adjacent[1] cells Ω_i and Ω_j by

$$\begin{aligned} [w(x)] &= w(x)|_{\partial\Omega_i}\mathbf{n}_i + w(x)|_{\partial\Omega_j}\mathbf{n}_j, \\ \langle w(x)\rangle &= \frac{1}{2}\left(w(x)|_{\partial\Omega_i} + w(x)|_{\partial\Omega_j}\right), \end{aligned} \tag{2.5}$$

for $x \in \Gamma_{i,j} \subset \Gamma_{\text{int}}$. Here $\mathbf{n}_i$ is the unit outward pointing normal for cell Ω_i. In the case of a vector valued function, τ, we define

$$\begin{aligned} [\tau(x)] &= \tau(x)|_{\partial\Omega_i} \cdot \mathbf{n}_i + \tau(x)|_{\partial\Omega_j} \cdot \mathbf{n}_j, \\ \langle \tau(x)\rangle &= \frac{1}{2}\left(\tau(x)|_{\partial\Omega_i} + \tau(x)|_{\partial\Omega_j}\right). \end{aligned} \tag{2.6}$$

The DG discretization is obtained by specifying the finite-dimensional trial and test space $S_h \subset H^1(\Omega_h)$ as the space of piecewise polynomials of degree less than $2p$ on the partitioning Ω_h:

$$S_h = \left\{\phi_{i,e} \in P^{2p-1}(\Omega_e), \quad \Omega_e \in \Omega_h\right\}.$$

Notice that we restrict ourselves to odd degree $k = 2p - 1$. The discrete equations now read as follows: Find $u_h \in S_h$ such that

$$B(u_h, v_h) = L(v_h) \qquad \forall v_h \in S_h. \tag{2.7}$$

2.2.2 Choice of a basis

To completely describe the discrete matrix obtained, we should provide S_h with a basis. Therefore we introduce the following basis polynomials on the one-dimensional unit interval:

$$\phi_{2n+k}(t) = t^{n+k}(1-t)^{n+1-k}, \quad n = 0, 1, \ldots, p-1, \quad k = 0, 1. \tag{2.8}$$

On the unit cube, $\hat{\Omega} \subset \mathbb{R}^d$, we use a basis of tensor-product polynomials based on (2.8). A basis for $P^{2p-1}(\Omega_e)$ is obtained by the usual affine mapping $\hat{\Omega} \to \Omega_e$.

The basis thus obtained has two advantages. First, it is hierarchical. This means that we can (locally) increase the accuracy of the approximation just by extending the basis with higher order polynomials. Second, the coefficients of

[1] At a Dirichlet boundary the interface with a virtual (flat, exterior) adjacent cell, containing only the Dirichlet data, is used.

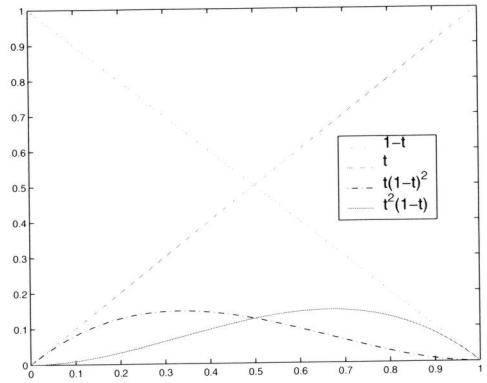

Figure 2.1: $\phi_{n,k}(t) = t^{n+k}(1-t)^{n+1-k}$, $n = \{0,1\}$, $k = \{0,1\}$.

the first degree polynomials represent function values at the cell-corners, while the coefficients of the polynomials of degree 3 can be associated with corrections for the derivatives at the cell-corners. All higher order polynomials, $\phi_{n,k}$, $n \geq 2$, are genuine bubble functions and correspond to interior cell corrections only.

A slightly better alternative basis satisfying our purposes is, defined on $[-1,+1]$, the basis $(x-1)^p(x+1)^q$ for $(p,q) = (1,0)$, $(0,1)$, $(2,1)$, $(1,2)$, and $(x-1)^2(x+1)^2 P_n^{(4,4)}(x)$ with $n = 0,1,\ldots$, and $P_n^{(4,4)}$ the Jacobi polynomials [1, p. 774]. The first four polynomials in this basis are essential for our purpose because they represent function values and first derivatives at the cell boundaries. These are the same as in (2.8) for $p \leq 2$. The new, higher order polynomials satisfy the useful L_2-orthogonality property. This basis also relieves the restriction to odd degree k for $k > 3$.

If we are interested in fast convergence of the solution procedure for the discrete system, the coefficients for the bubble functions are of less importance because they can be eliminated by static condensation or dealt with by defect correction. Therefore, in our analysis in the following sections we restrict ourselves to the case $p = 2$, in which the above two alternatives coincide. Furthermore, we restrict ourselves to the one-dimensional equation because this is the building block for the higher-dimensional case, where we essentially use tensor-product polynomials.

Using the basis $\{\phi_i\}_{i=0}^3$, the approximate solution reads

$$u_h = \sum_{e=1}^{N}\sum_{i=0}^{3} c_{i,e}\phi_i((x-x_e)/h) \equiv \sum_{e=1}^{N}\sum_{i=0}^{3} c_{i,e}\phi_{i,e}(x),$$

and we obtain the explicit form of the discrete system, $L_h u_h = f_h$,

$$\begin{aligned}\sum_{e=1}^{N}\sum_{i=0}^{3} c_{i,e} \Big(&\int_{\Omega_e} \phi'_{i,e}(x)\phi'_{j,e}(x)dx - \langle \phi'_{i,e}(x)\rangle \cdot [\phi_{j,e}(x)]\,|_{\Gamma_{\mathrm{Dint}}} \\ &+ \sigma\,[\phi_{i,e}(x)]\cdot\langle \phi'_{j,e}(x)\rangle\,|_{\Gamma_{\mathrm{Dint}}} + \mu\,[\phi_{i,e}(x)]\cdot[\phi_{j,e}(x)]\,|_{\Gamma_{\mathrm{Dint}}}\Big) \\ = \sum_{e=1}^{N}\sum_{i=0}^{3} \int_{\Omega_e} &f\phi_{j,e}(x)dx + \sigma\,[u_0]\cdot\langle \phi'_{j,e}(x)\rangle\,|_{\Gamma_{\mathrm{D}}} \\ &+ \mu\,[u_0]\cdot[\phi_{j,e}(x)]\,|_{\Gamma_{\mathrm{D}}} + g\phi_{j,e}(x)|_{\Gamma_N},\end{aligned} \tag{2.9}$$

for $4N$ test functions $\phi_{j,e}$. As usual, the resulting one-dimensional discrete operator has a block-tridiagonal structure. We want to emphasize that for solving this discrete system by block-relaxation we can follow two distinct approaches. The usual approach is to order the basis functions *cellwise*. Then the choice of a particular basis for the polynomial space is of less importance and the variables in each block are associated with the coefficients of the polynomial approximation in the corresponding cell. The other approach is by ordering the coefficients *pointwise* and to associate with each point the left- and right-sided values of the function and its derivative. (In fact, this motivates the particular choice of our basis (2.8).)

Ordering the equations (the weighting functions $\phi_{e,j}$) and coefficients *cellwise* as $[c_{e,0}, c_{e,2}, c_{e,3}, c_{e,1}]$ yields the following discretization stencil:

$$\left[\begin{array}{cccc|ccc|ccc} -\frac{1}{2} & 0 & -\frac{1}{2} & \frac{1-\sigma}{2}-h\mu & \frac{1+\sigma}{2}+h\mu & \frac{1}{2} & 0 & \frac{-1-\sigma}{2} & \frac{1}{2}\sigma & 0 & 0 & 0 \\ 0 & 0 & 0 & \frac{1}{2}\sigma & -\frac{1}{2}\sigma & \frac{2}{15} & \frac{1}{30} & 0 & 0 & 0 & 0 & 0 \\ 0 & 0 & 0 & 0 & 0 & \frac{1}{30} & \frac{2}{15} & -\frac{1}{2}\sigma & \frac{1}{2}\sigma & 0 & 0 & 0 \\ 0 & 0 & 0 & \frac{1}{2}\sigma & \frac{-1-\sigma}{2} & 0 & \frac{1}{2} & \frac{1+\sigma}{2}+h\mu & \frac{1-\sigma}{2}-h\mu & -\frac{1}{2} & 0 & -\frac{1}{2} \end{array}\right]. \tag{2.10}$$

If we order the equations and coefficients *pointwise*, according to function values and corrections on derivatives at the cell-interfaces, $[c_{e-1,3}, c_{e-1,1}, c_{e,0}, c_{e,2}]$, we get the stencil

(2.11)

$$\left[\begin{array}{cccc|cccc|cccc}
0 & 0 & 0 & \frac{1}{30} & \frac{2}{15} & -\frac{1}{2}\sigma & \frac{1}{2}\sigma & 0 & 0 & 0 & 0 & 0 \\
0 & \frac{1}{2}\sigma & \frac{-1-\sigma}{2} & 0 & \frac{1}{2} & \frac{1+\sigma}{2}+h\mu & \frac{1-\sigma}{2}-h\mu & -\frac{1}{2} & 0 & -\frac{1}{2} & 0 & 0 \\
0 & 0 & -\frac{1}{2} & 0 & -\frac{1}{2} & \frac{1-\sigma}{2}-h\mu & \frac{1+\sigma}{2}+h\mu & \frac{1}{2} & 0 & \frac{-1-\sigma}{2} & \frac{1}{2}\sigma & 0 \\
0 & 0 & 0 & 0 & 0 & \frac{1}{2}\sigma & -\frac{1}{2}\sigma & \frac{2}{15} & \frac{1}{30} & 0 & 0 & 0
\end{array}\right] .$$

For the Poisson equation on the uniform grid, in both cases the discretization matrix appears to be a block-Toeplitz matrix. This matrix is described by the repetition of either stencil (2.10) or stencil (2.11).

2.2.3 The MG algorithm

Our main interest lies in the application of the DG method in the *hp*-self-adaptive MG algorithm. Therefore we use an adaptive MG algorithm [19], where local refinements yield corrections for the coarser discretizations. In the linear case, if the total grid is refined, the *hp*-adaptive algorithm corresponds to the classical MG [16], combined with nested iteration. Its convergence is best studied by means of the two-level algorithm (TLA). The amplification operator of the error is given by

$$M_h^{\mathrm{TLA}} = (M_h^{\mathrm{REL}})^{\nu_2} M_h^{\mathrm{CGC}} (M_h^{\mathrm{REL}})^{\nu_1} , \tag{2.12}$$

ν_1 and ν_2 are the number of pre- (post-) relaxation sweeps, respectively, and

$$M_h^{\mathrm{CGC}} = I_h - P_{hH} L_H^{-1} \overline{R}_{Hh} L_h .$$

To each of the amplification operators of the error, M_h, corresponds an amplification operator for the residue $\overline{M}_h = L_h M_h L_h^{-1}$. In our analysis we are mainly interested in the convergence of the two-level iteration. Therefore we compute the spectral radius of the amplification operator $\rho(M_h^{\mathrm{TLA}}) = \rho(\overline{M}_h^{\mathrm{TLA}})$, which represents the final convergence factor per iteration step. We also compute the spectral norms $\|(M_h^{\mathrm{TLA}})^t\|_2$ and $\|(\overline{M}_h^{\mathrm{TLA}})^t\|_2$, which describe the worst possible convergence rate in t steps.

2.2.4 Restrictions and prolongations

As we are interested in MG methods for the solution of the discrete equations arising from DG discretization, we need proper restriction and prolongation operators. With piecewise polynomial approximations on the separate cells of the

partitioning Ω_h, a natural prolongation is immediately derived. For convenience we describe the grid transition operators for the one-dimensional case. Extension to higher dimensions follows immediately by means of the tensor-product principle (see Chapter 4 and [25]).

We consider a fine partitioning Ω_h and a coarse partitioning Ω_H, with $H = 2h$ and with nodal points jh and jH, respectively, and we denote the spaces of discontinuous piecewise polynomials by S_h and S_H. It is immediately clear that $S_H \subset S_h$. This defines the natural prolongation $P_{hH} : S_H \to S_h$ so that $(P_{hH}u_H)(x) = u_H(x)$ for all $x \in \mathbb{R} \setminus \mathbb{Z}_h$.[2] Given a polynomial basis, this prolongation is explicitly described by its stencil. For our basis $\{\phi_{i,e}\}$ the stencil reads

$$P_{hH} \approxeq \left[\begin{array}{cccc|cccc|cccc|cccc|cccc} 0 & 0 & 0 & \frac{-1}{8} & 0 & 0 & 0 & \frac{1}{4} & \frac{3}{8} & 0 & 0 & 0 & 0 & 0 & 0 & 0 & 0 & 0 & 0 & 0 \\ 0 & 0 & 0 & 0 & 0 & 0 & \frac{1}{2} & \frac{1}{8} & 0 & 1 & 0 & 0 & \frac{1}{8} & \frac{1}{2} & 0 & 0 & 0 & 0 & 0 & 0 \\ 0 & 0 & 0 & 0 & 0 & 0 & \frac{1}{2} & \frac{1}{8} & 0 & 0 & 1 & 0 & \frac{1}{8} & \frac{1}{2} & 0 & 0 & 0 & 0 & 0 & 0 \\ 0 & 0 & 0 & 0 & 0 & 0 & 0 & 0 & 0 & 0 & 0 & \frac{3}{8} & \frac{1}{4} & 0 & 0 & 0 & \frac{-1}{8} & 0 & 0 & 0 \end{array}\right] .$$

Different from the prolongation, a natural restriction is not uniquely determined. However, we recognize a natural restriction for the residue, associated with the weighted-residual character of the Galerkin discretization. This restriction is the adjoint of the natural prolongation; i.e., the Toeplitz operator for this restriction is the transpose of the Toeplitz operator for the natural prolongation. We denote this restriction as $\overline{R}_{Hh} = (P_{hH})^T$. It follows from the Galerkin construction of the discretization and from the nesting of the spaces S_h and S_H that the Galerkin relation exists between the discretization on the coarse grid and the finer grid,

$$L_H = \overline{R}_{Hh} L_h P_{hH} \ . \tag{2.13}$$

For the chosen basis $\{\phi_{i,e}\}$, which is essentially based on the function values and corrections for the derivatives at the cell endpoints, we can construct another pointwise restriction (the injective restriction). This restriction is constructed such that

$$\begin{aligned} (d/dx)(R_{Hh}u_h)(jH)|_{\Omega_{H,j-1}} &= (d/dx)u_h(2jh)|_{\Omega_{h,2j-1}} \ , \\ (R_{Hh}u_h)(jH)|_{\Omega_{H,j-1}} &= u_h(2jh)|_{\Omega_{h,2j-1}} \ , \\ (R_{Hh}u_h)(jH)|_{\Omega_{H,j}} &= u_h(2jh)|_{\Omega_{h,2j}} \ , \\ (d/dx)(R_{Hh}u_h)(jH)|_{\Omega_{H,j}} &= (d/dx)u_h(2jh)|_{\Omega_{h,2j}} \ . \end{aligned}$$

[2] $\mathbb{Z}_h$ is the infinite regular one-dimensional grid, defined by $\mathbb{Z}_h = \{jh \,|\, j \in \mathbb{Z}, h > 0\}$.

The stencil related to this restriction reads

$$R_{Hh} \approxeq \left[\begin{array}{cccc|cccc|cccc|cccc|cccc} 0 & 0 & 0 & 1 & 0 & 0 & 0 & 0 & 3 & 0 & 0 & 0 & 0 & 0 & 0 & 0 & 0 & 0 & 0 & 0 \\ 0 & 0 & 0 & 0 & 0 & 0 & 0 & 0 & 0 & 1 & 0 & 0 & 0 & 0 & 0 & 0 & 0 & 0 & 0 & 0 \\ 0 & 0 & 0 & 0 & 0 & 0 & 0 & 0 & 0 & 0 & 1 & 0 & 0 & 0 & 0 & 0 & 0 & 0 & 0 & 0 \\ 0 & 0 & 0 & 0 & 0 & 0 & 0 & 0 & 0 & 0 & 0 & 3 & 0 & 0 & 0 & 0 & 1 & 0 & 0 & 0 \end{array}\right].$$

We see that the prolongation P_{hH} and this restriction R_{Hh} satisfy the relation $R_{Hh}P_{hH} = I_H$, i.e., the identity operator on S_H. This implies that the operator $P_{hH}R_{Hh}$ is a projection operator from S_h into itself. Its image, Range$(P_{hH}) \subset S_h$, comprises the *fine grid functions representable* on the coarse grid. The range of the complementary projection $I_h - P_{hH}R_{Hh}$ is the set of *fine grid functions* that are *not representable* on the coarse grid.

2.3 Fourier analysis tools

2.3.1 Fourier analysis for vector grid functions

In order to apply Fourier analysis methods for the convergence study of our solution process, we introduce some elementary tools. We first introduce (vector valued) grid functions defined on the regular, unbounded, one-dimensional grid $\mathbb{Z}_h = \{jh \,|\, j \in \mathbb{Z}, h > 0\}$.

The Hilbert space of square summable scalar grid functions, defined on $\mathbb{Z}_h$, with inner product $(u_h, v_h) = \sum_j h\, u_h(jh)v_h(jh)$, is denoted by $\ell^2(\mathbb{Z}_h)$. We will use the Fourier transform $\widehat{u_h}$ of $u_h \in l_h^2(\mathbb{Z}_h)$, which is the complex function defined on $\mathbb{T}_h = [-\pi/h, +\pi/h]$, defined by

$$\widehat{u_h}(\omega) = \frac{h}{\sqrt{2\pi}} \sum_{j\in\mathbb{Z}} e^{-ijh\omega}\, u_h(jh)\,. \tag{2.14}$$

We see that the function $\widehat{u_h}(\omega)$ is $(2\pi/h)$-periodic and that by Parseval's equality we have

$$\|u_h\|_{\ell^2(\mathbb{Z}_h)} = \|\widehat{u_h}\|_{L^2(\mathbb{T}_h)}\,. \tag{2.15}$$

In an obvious manner we can extend this definition of the Fourier transform $\ell^2(\mathbb{Z}_h) \to L^2(\mathbb{T}_h)$ to the Fourier transform of a four-dimensional vector function $\mathbf{u}_h \in \left[\ell^2(\mathbb{Z}_h)\right]^4 \to \widehat{\mathbf{u}_h} \in \left[L^2(\mathbb{T}_h)\right]^4$.

The transform (2.14), its inverse, as well as Parseval's equality (2.15), also hold if we replace u_h by the vector valued grid function $\mathbf{u}_h \in \left[\ell^2(\mathbb{Z}_h)\right]^4$ and

$\widehat{u_h}$ by $\widehat{\mathbf{u}_h} \in \left[L^2(\mathbb{T}_h)\right]^4$, provided that we use the corresponding norms for the vector spaces

$$\|\mathbf{u}_h\|^2_{[\ell^2(\mathbb{Z}_h)]^4} = \sum_{i=1}^{4} \|u_{h,i}\|^2_{\ell^2(\mathbb{Z}_h)} \quad \text{and} \quad \|\widehat{\mathbf{u}_h}\|^2_{[L^2(\mathbb{T}_h)]^4} = \sum_{i=1}^{4} \|\widehat{u_{h,i}}\|^2_{\mathbb{T}_h}. \tag{2.16}$$

We apply this to the vector grid functions of coefficients, either for the cell-centered (*cellwise*) coefficients $u_h = \{[c_{e,0}, c_{e,2}, c_{e,3}, c_{e,1}]^T\}_{e\in\mathbb{Z}}$ or for the cell-corner (*pointwise*) coefficients $u_h = \{[c_{e-1,3}, c_{e-1,1}, c_{e,0}, c_{e,2}]^T\}_{e\in\mathbb{Z}}$. Cellwise vector grid functions are obtained from $H^2(\Omega_h)$ functions, with $\Omega = \mathbb{R}$, by the restriction operator $R^{\text{cell}}_{h,0} : H^2(\mathbb{R}_h) \to [\ell^2(\mathbb{Z}_h)]^4$ defined by

$$\begin{aligned} \mathbf{u}_h(jh) &= (R^{\text{cell}}_{h,0}u)(jh) \\ &= \begin{bmatrix} & u((j-1)h)|_{\Omega_j} \\ h & u'((j-1)h)|_{\Omega_j} + u((j-1)h)|_{\Omega_j} - u(jh)|_{\Omega_j} \\ -h & u'(jh)|_{\Omega_j} - u((j-1)h)|_{\Omega_j} + u(jh)|_{\Omega_j} \\ & u(jh)|_{\Omega_j} \end{bmatrix}, \end{aligned} \tag{2.17}$$

where $u(jh)|_{\Omega_i}$ is the function value in grid point jh for the function u restricted to cell Ω_i. Pointwise vector grid functions are obtained by a restriction operator $R_{h,0} : H^2(\mathbb{R}_h) \to [\ell^2(\mathbb{Z}_h)]^4$ defined by

$$\begin{aligned} \mathbf{u}_h(jh) &= (R_{h,0}u)(jh) \\ &= \begin{bmatrix} -h & u'(jh)|_{\Omega_{j-1}} - u\left((j-1)h\right)|_{\Omega_{j-1}} + u(jh)|_{\Omega_{j-1}} \\ & u(jh)|_{\Omega_{j-1}} \\ & u(jh)|_{\Omega_j} \\ h & u'(jh)|_{\Omega_j} + u(jh)|_{\Omega_j} - u\left((j+1)h\right)|_{\Omega_j} \end{bmatrix}. \end{aligned} \tag{2.18}$$

In both cases the restriction determines the function values and the correction for the derivatives at the cell boundaries. Only the ordering in the vector function is different: the discrete data are either cellwise or pointwise collected. These two representations correspond to the representations (2.10) and (2.11) of the block-Toeplitz matrix obtained for the DG discretization.

2.3.2 Fourier analysis for a block-Toeplitz operator

For a block-Toeplitz matrix of the type as encountered in Section 2.2.2 we can compute the Fourier transform and the eigenvalues as follows. Let $A_h = (\mathbf{a}_{m,j}) \in \mathbb{R}^{4\mathbb{Z}\times 4\mathbb{Z}}$ be an infinite Toeplitz operator, i.e., an operator with a block

structure $\mathbf{a}_{m,j} \in \mathbb{R}^{4\times 4}$, $m, j \in \mathbb{Z}$, satisfying $\mathbf{a}_{m,m+k} = \mathbf{a}_{-k}$ for all $m, k \in \mathbb{Z}$, and let $e_{h,\omega}$ be an elementary mode, i.e., a complex function defined on the grid $\mathbb{Z}_h$ with $e_{h,\omega}(jh) = e^{ijh\omega}$. Then

$$\begin{aligned} &\sum_{j\in\mathbb{Z}} \mathbf{a}_{m,j} e_{h,\omega}(jh) = \widehat{A}_h(\omega) e_{h,\omega}(mh) \\ &\Leftrightarrow \widehat{A}_h(\omega) = \sum_{j\in\mathbb{Z}} \mathbf{a}_{m,j} e^{i(j-m)h\omega} = \sum_{k\in\mathbb{Z}} \mathbf{a}_{-k} e^{ikh\omega} = \sum_{k\in\mathbb{Z}} \mathbf{a}_k e^{-ikh\omega} \end{aligned} \tag{2.19}$$

for all $\omega \in \mathbb{T}_h \equiv [-\frac{\pi}{h}, \frac{\pi}{h}]$.

Now, let $V_h \in \mathbb{R}^{4\mathbb{Z}\times 4\mathbb{Z}}$ be an arbitrary diagonal block-Toeplitz matrix, with blocks $\mathbf{v}_{j,j} = \mathbf{v} \in \mathbb{R}^{4\times 4}$ for all $j \in \mathbb{Z}$. Then

$$\left(A_h V_h e_{h,\omega}\right)(mh) = \sum_{j\in\mathbb{Z}} \mathbf{a}_{m,j}\mathbf{v}_{j,j} e^{ijh\omega} = \left(\sum_{j\in\mathbb{Z}} \mathbf{a}_{m,j} e^{ijh\omega}\right)\mathbf{v} = \widehat{A}_h(\omega) e^{imh\omega}\mathbf{v}\,,$$

with $\widehat{A}_h(\omega) = \sum_{j\in\mathbb{Z}} \mathbf{a}_j e^{-ijh\omega}$. If we choose $\mathbf{v} = \mathbf{v}(\omega)$ to be the matrix of eigenvectors of $\widehat{A}_h(\omega)$ such that

$$\widehat{A}_h(\omega)\mathbf{v} = \mathbf{v}\Lambda_h(\omega), \tag{2.20}$$

then we have

$$\left(A_h V_h e_{h,\omega}\right)(mh) = \widehat{A}_h(\omega)\mathbf{v} e_{h,\omega}(mh) = e_{h,\omega}(mh)\mathbf{v}\Lambda_h(\omega). \tag{2.21}$$

Hence, the columns of $\mathbf{v}(\omega)e_{h,\omega}(mh)$ are the eigenvectors of A_h. Also $\Lambda_h(\omega)$ is a family of 4×4 diagonal matrices with the eigenvalues of A_h at the diagonal entries.

COROLLARY. *The spectrum of the block-Toeplitz operator A_h is found as $\{\lambda_i(\omega)\}_{i=1,\ldots,4}$, $\omega \in \mathbb{T}_h$, where $\lambda_i(\omega)$ is an eigenvalue of $\widehat{A}_h(\omega)$.*

2.3.3 Fourier analysis for prolongations and restrictions

Key to the Fourier analysis of prolongations and restrictions are the flat prolongation and restriction operators $P^0_{hH} : [\ell^2(\mathbb{Z}_H)]^4 \to [\ell^2(\mathbb{Z}_h)]^4$ and $R^0_{Hh} : \ell^2(\mathbb{Z}_h) \to \ell^2(\mathbb{Z}_H)$ that are defined by

$$\mathbf{u}_h(jh) = \left(P^0_{hH}\mathbf{u}_H\right)(jh) = \begin{cases} \mathbf{u}_H(Hj/2) & \text{if } j \text{ even} \\ \mathbf{0} & \text{if } j \text{ odd} \end{cases} \tag{2.22}$$

and

$$\left(R^0_{Hh}\mathbf{u}_h\right)(jH) = \mathbf{u}_h(2jh). \tag{2.23}$$

General, arbitrary constant coefficient prolongations (restrictions) can be constructed as a combination of a Toeplitz operator and a flat operator. Any prolongation P_{hH} can be written as $P_{hH} = P_h P^0_{hH}$ and any restriction R_{Hh} can be written as $R_{Hh} = R^0_{Hh} R_h$, with P_h (or R_h) a Toeplitz operator $[\ell^2(\mathbb{Z}_h)]^4 \to [\ell^2(\mathbb{Z}_h)]^4$.

A simple computation [18] shows

$$\widehat{P^0_{hH}\mathbf{u}_H}(\omega) = \frac{1}{2}\widehat{\mathbf{u}_H}(\omega), \quad \omega \in \mathbb{T}_h, \tag{2.24}$$

(notice the periodicity of $\widehat{u_H}(\omega)$ with period π/h !) and

$$\widehat{R^0_{Hh}\mathbf{u}_h}(\omega) = \sum_{p=0,1} \widehat{\mathbf{u}_h}\left(\omega + \frac{\pi p}{h}\right) \quad \forall \omega \in T_H = T_{2h}. \tag{2.25}$$

Here we see that $\widehat{P_{hH}u_H}$ is defined on $\mathbb{T}_h = [-\pi/h, +\pi/h]$, whereas $\widehat{u_H}$ is defined on the smaller $\mathbb{T}_H = [-\pi/2h, \pi/2h]$. This motivates us to introduce a different notation for the same Fourier transform $\widehat{v_h}(\omega)$, with $\omega \in \mathbb{T}_h$. We introduce the new notation

$$\begin{pmatrix} \widehat{v_h}(\omega) \\ \widehat{v_h}(\omega + \pi/h) \end{pmatrix}, \quad \omega \in \mathbb{T}_H \ ,$$

with exactly the same meaning as $\widehat{v_h}$, $\omega \in \mathbb{T}_h$.

Having introduced this notation, we may write (2.24) as

$$\widehat{P_{hH}\mathbf{u}_H}(\omega) = \left(P_h\widehat{P^0_{hH}\mathbf{u}_H}\right)(\omega) = \frac{1}{2}\begin{bmatrix} \widehat{P_h}(\omega) \\ \widehat{P_h}\left(\omega + \frac{\pi}{h}\right) \end{bmatrix} \widehat{\mathbf{u}_H}(\omega), \quad \omega \in \mathbb{T}_H, \tag{2.26}$$

and (2.23) as

$$\begin{aligned} \widehat{R_{Hh}\mathbf{u}_h}(\omega) &= \widehat{R^0_{Hh}R_h\mathbf{u}_h}(\omega) \\ &= \begin{bmatrix} \widehat{R_h}(\omega), & \widehat{R_h}\left(\omega + \frac{\pi}{h}\right) \end{bmatrix} \begin{bmatrix} \widehat{\mathbf{u}_h}(\omega) \\ \widehat{\mathbf{u}_h}\left(\omega + \frac{\pi}{h}\right) \end{bmatrix}, \end{aligned} \tag{2.27}$$

with $\omega \in \mathbb{T}_H$.

2.3.4 Filtering the true high frequency functions

On the one hand, we can define low and high frequency grid functions in $\ell^2(\mathbb{Z}_h)$ as the functions that are linear combinations of modes $e^{ijh\omega}$ with, respectively, $\omega \in \mathbb{T}_{2h}$ and $\omega \in \mathbb{T}_h \setminus \mathbb{T}_{2h}$. On the other hand, having introduced a prolongation P_{hH} and a restriction R_{Hh} in the solution space S_h, we may define low frequency components in the error as those components that lie in the range of the projection $P_{hH}R_{Hh}$, and high frequency components as the complementary functions, i.e., those in the range of $I_h - P_{hH}R_{Hh}$. In view of the MG algorithm, the latter approach is more relevant.

Since a low frequency grid function can be represented on the coarser grid, we obtain this grid function by considering a "slowly varying" (4-valued) grid function $\mathbf{u}_h$,

$$P_{hH}R_{Hh}\mathbf{u}_h = P_h P^0_{hH} R^0_{Hh} R_h \mathbf{u}_h. \tag{2.28}$$

Since $P_{hH}R_{Hh}$ is a projection, we have for a high frequency grid function $\mathbf{u}_h$:

$$(I - P_h P^0_{hH} R^0_{Hh} R_h)\mathbf{u}_h = \mathbf{u}_h\,. \tag{2.29}$$

In view of this we want our MG smoothers (the relaxation methods) to damp the contributions (2.29). In other words, those eigenvalues of the amplification operator M_h^{REL} that correspond to high frequency contributions (2.29) must be small. So we are interested in whether the eigenvalues are small for

$$\mathbf{FT}\left((I - P_h P^0_{hH} R^0_{Hh} R_h)\; M^{\mathrm{REL}}\right)(\omega), \quad \omega \in T_H\,, \tag{2.30}$$

where **FT** denotes the Fourier transform.

2.3.5 Fourier transform of the two-level operator

Now, with these tools available, we write, for the amplification operator of the coarse-grid correction operator

$$M_h^{\mathrm{CGC}} = I_h - P_{hH} L_H^{-1} \overline{R}_{Hh} L_h,$$

its Fourier transform

$$\widehat{M_h^{\mathrm{CGC}}}(\omega) = \left(\widehat{I_h} - \widehat{P_{hH}}\,\widehat{L_H^{-1}}\,\widehat{\overline{R}_{Hh}}\,\widehat{L_h}\right)(\omega) = \begin{pmatrix} 1 & 0 \\ 0 & 1 \end{pmatrix}$$
$$- \begin{pmatrix} \widehat{P_h}(\omega) \\ \widehat{P_h}(\omega + \pi/h) \end{pmatrix} (\widehat{L_H}(\omega))^{-1} \begin{pmatrix} \widehat{R_h}(\omega) & \widehat{R_h}(\omega + \pi/h) \end{pmatrix} \begin{pmatrix} \widehat{L_h}(\omega) & 0 \\ 0 & \widehat{L_h}(\omega + \pi/h) \end{pmatrix}.$$

In view of Parseval's equality (2.15) and (2.21) the eigenvalues of the 8×8-matrix $\widehat{M_h^{\mathrm{CGC}}}(\omega)$ for $\omega \in \mathbb{T}_H$ yield the eigenvalues of the coarse-grid correction operator M_h^{CGC} and, similarly, $\widehat{M_h^{\mathrm{TLA}}}(\omega) = (\widehat{M_h^{\mathrm{REL}}}(\omega))^{\nu_2} \widehat{M_h^{\mathrm{CGC}}}(\omega)(\widehat{M_h^{\mathrm{REL}}}(\omega))^{\nu_1}$ yield the eigenvalues for the two-level operator M_h^{TLA}.

2.4 Smoothing analysis

One of the main ingredients of an MG solver is the smoother. It is used to damp the high frequencies of the error on the finer grid, while the low frequency errors are damped by the coarse-grid correction. For this, the smoother should have an amplification operator with a proper eigenvalue spectrum. That is, an eigenvalue spectrum in which most eigenvalues are in absolute value less than one, where the larger eigenvalues correspond to low frequency eigenfunctions. In this section we apply Fourier analysis to study the amplification operator of the damped block-Jacobi (JOR) and the damped block-Gauss–Seidel (DGS) relaxation for both stencils (2.10) and (2.11). So, we distinguish between cellwise block- and pointwise block-relaxations.

We will observe that with cellwise relaxations the amplification operators have a complex eigenvalue spectrum with many eigenvalues close to one. This indicates that this relaxation shows a poor and oscillating convergence. However, for pointwise block-relaxations the amplification operators show much better spectra.

For the discrete system $A_h x = b$ we consider the iterative process

$$x^{(i+1)} = x^{(i)} - B_h(A_h x^{(i)} - b)\,, \tag{2.31}$$

with B_h an approximate inverse of A_h. Decomposing A_h as

$$A_h = L + D + U, \tag{2.32}$$

into a strict block-lower, block-diagonal; and strict block-upper matrix, the different relaxation methods are uniquely described either by B_h or by the amplification matrix $M_h^{\mathrm{REL}} = I_h - B_h A_h$. These operators are shown in Table 2.1. Because A_h is a block-Toeplitz operator, the amplification matrix M_h also is block-Toeplitz. Notice that the meaning of the block decomposition (2.32) is different for stencils (2.10) and (2.11). The stencils corresponding to the decomposition $A_h = (\mathbf{a}_{m,j})$ are given in Table 2.2.

The difference between cellwise and pointwise block decomposition is that the eigenvectors $e_{h,\omega}(mh)\mathbf{v}$ of the cellwise stencil correspond to 4-valued grid

Table 2.1: The relaxation methods using $\alpha > 0$ as the relaxation parameter.

	B_h	M_h^{REL}
JOR	αD^{-1}	$D^{-1}((1-\alpha)D - \alpha(L+U))$
DGS_L	$\alpha(D+L)^{-1}$	$(D+L)^{-1}((1-\alpha)(D+L) - \alpha U)$
DGS_U	$\alpha(D+U)^{-1}$	$(D+U)^{-1}((1-\alpha)(D+U) - \alpha L)$

Table 2.2: The stencils in the diagonal decomposition.

Cellwise		Pointwise
$\begin{bmatrix} -\frac{1}{2} & 0 & -\frac{1}{2} & \frac{1-\sigma}{2} - h\mu \\ 0 & 0 & 0 & \frac{1}{2}\sigma \\ 0 & 0 & 0 & 0 \\ 0 & 0 & 0 & \frac{1}{2}\sigma \end{bmatrix}$	L	$\begin{bmatrix} 0 & 0 & 0 & \frac{1}{30} \\ 0 & \frac{1}{2}\sigma & \frac{-1-\sigma}{2} & 0 \\ 0 & 0 & -\frac{1}{2} & 0 \\ 0 & 0 & 0 & 0 \end{bmatrix}$
$\begin{bmatrix} \frac{1+\sigma}{2} + h\mu & \frac{1}{2} & 0 & \frac{-1-\sigma}{2} \\ -\frac{1}{2}\sigma & \frac{2}{15} & \frac{1}{30} & 0 \\ 0 & \frac{1}{30} & \frac{2}{15} & -\frac{1}{2}\sigma \\ \frac{-1-\sigma}{2} & 0 & \frac{1}{2} & \frac{1+\sigma}{2} + h\mu \end{bmatrix}$	D	$\begin{bmatrix} \frac{2}{15} & -\frac{1}{2}\sigma & \frac{1}{2}\sigma & 0 \\ \frac{1}{2} & \frac{1+\sigma}{2} + h\mu & \frac{1-\sigma}{2} - h\mu & -\frac{1}{2} \\ -\frac{1}{2} & \frac{1-\sigma}{2} - h\mu & \frac{1+\sigma}{2} + h\mu & \frac{1}{2} \\ 0 & \frac{1}{2}\sigma & -\frac{1}{2}\sigma & \frac{2}{15} \end{bmatrix}$
$\begin{bmatrix} \frac{1}{2}\sigma & 0 & 0 & 0 \\ 0 & 0 & 0 & 0 \\ \frac{1}{2}\sigma & 0 & 0 & 0 \\ \frac{1-\sigma}{2} - h\mu & -\frac{1}{2} & 0 & -\frac{1}{2} \end{bmatrix}$	U	$\begin{bmatrix} 0 & 0 & 0 & 0 \\ 0 & -\frac{1}{2} & 0 & 0 \\ 0 & \frac{-1-\sigma}{2} & \frac{1}{2}\sigma & 0 \\ \frac{1}{30} & 0 & 0 & 0 \end{bmatrix}$

functions associated with the cell interiors (in fact independent of the chosen basis), whereas for the pointwise stencil, they correspond to the 4-valued grid function (2.18) associated with *the nodal points* between the cells. This makes the cellwise stencil less suited for the MG analysis because it is less natural to define flat prolongations and flat restrictions for the staggered information than from the pointwise information in coarse and fine cells.

Using (2.19) we find the Fourier transforms of the basic Toeplitz operators:

$$\widehat{L}(\omega) = L\, e^{-i\omega h}, \quad \widehat{D}(\omega) = D, \quad \widehat{U}(\omega) = U\, e^{i\omega h}. \tag{2.33}$$

This yields the Fourier transform for the amplification operators of JOR and

DGS:

$$\widehat{M_{JOR}^{REL}} = \widehat{D}^{-1}\left((1-\alpha)\,\widehat{D} - \alpha\left(\widehat{L}+\widehat{U}\right)\right),$$

$$\widehat{M_{DGS_L}^{REL}} = \left(\widehat{D}+\widehat{L}\right)^{-1}\left((1-\alpha)\left(\widehat{D}+\widehat{L}\right) - \alpha\,\widehat{U}\right),$$

$$\widehat{M_{DGS_U}^{REL}} = \left(\widehat{D}+\widehat{U}\right)^{-1}\left((1-\alpha)\left(\widehat{D}+\widehat{U}\right) - \alpha\,\widehat{L}\right).$$

Because of (2.21), computing the eigenvalues of $\widehat{M_h^{REL}}(\omega)$ for $\omega \in \mathbb{T}_h$ we find the eigenvalues of M_h^{REL}. The eigenvalues corresponding to the high frequencies (i.e., the frequencies $|\omega| > \pi/2h$ that cannot be represented on the coarser grid) are found to be $\widehat{M_h^{REL}}(\omega)$ for $\omega \in \mathbb{T}_h \setminus \mathbb{T}_H$. For the various DG methods, viz., for Baumann's method, $\sigma = 1$, $\mu = 0$; for the symmetric DG method, $\sigma = -1$, $\mu = 0$; and for the IP DG method, $\sigma = -1$, $\mu = C/h$, Figures 2.2–2.10 show the eigenvalue spectra of JOR, DGS, and SGS relaxation amplification operators, the last amplification operator being defined by $M_{SGS}^{REL} = M_{DGS_L}^{REL} M_{DGS_U}^{REL}$.

We notice that the spectra of the amplification operators *for pointwise ordering* of the block-relaxations appear to be the same for the Baumann and symmetric DG methods ($\sigma = 1$ or $\sigma = -1$).

Although in the figures we distinguish between the behavior of low and high frequencies (LF: $|\omega| < \pi/2h$ and HF: $|\omega| \geq \pi/2h$), this does not precisely correspond to the meaning of LF and HF in the context of MG. Typical LF components in an MG algorithm are those functions that are invariant under the projection $P_{hH}R_{Hh}$ (they are in the range of the prolongation), whereas the HF components are those in the kernel of the restriction. Therefore, we take into account the properties of the restriction and prolongation to determine optimal relaxation parameters and also determine the spectra of the operator $M^{\mathrm{REL}}(I_h - P_{hH}R_{Hh})$.

Because Figures 2.2–2.10 show clearly that the convergence behavior for pointwise relaxation is much better than for cellwise relaxation, we further restrict our study to the former.

Figures 2.11–2.13 show the spectra of the operator $M^{\mathrm{REL}}(I_h - P_{hH}R_{Hh})$, again applied to the three different types of DG methods. From these results we can determine optimal damping parameters for relaxation. This parameter, minimizing the spectral radius $\rho(M_h^{REL}(I_h - P_{hH}R_{Hh}))$ is given by

$$\alpha_{opt} = \frac{2}{2 - (\lambda_{\min} + \lambda_{\max})},$$

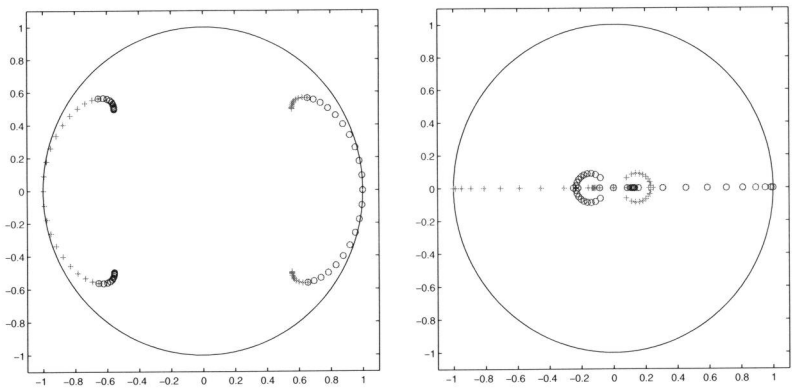

Cellwise order Pointwise order

$\circ : \omega_{low} \in [-\pi/2h, \pi/2h]; \quad + : \omega_{high} \in [-\pi/h, -\pi/2h] \cup [\pi/2h, \pi/h]$

Figure 2.2: Eigenvalue spectra of $\widehat{M^{REL}_{JOR}}(\omega)$ for Baumann's DG method (without damping: $\sigma = 1$, $\mu = 0$, $\alpha = 1$) relative to the unit circle.

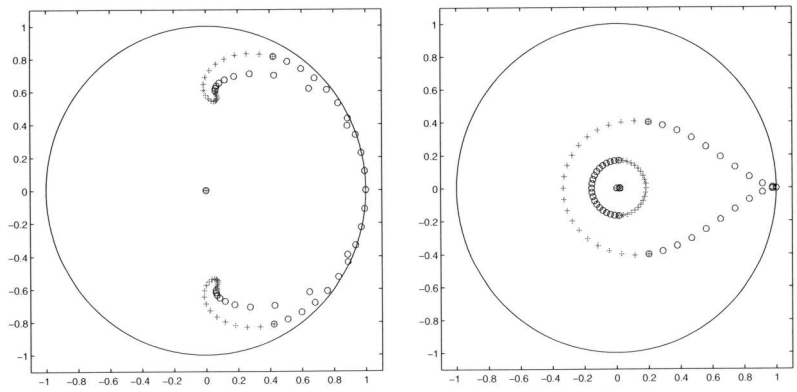

Cellwise order Pointwise order

$\circ : \omega_{low} \in [-\pi/2h, \pi/2h]; \quad + : \omega_{high} \in [-\pi/h, -\pi/2h] \cup [\pi/2h, \pi/h]$

Figure 2.3: Eigenvalue spectra of $\widehat{M^{REL}_{DGS}}(\omega)$ for Baumann's DG method (without damping: $\sigma = 1$, $\mu = 0$, $\alpha = 1$) relative to the unit circle.

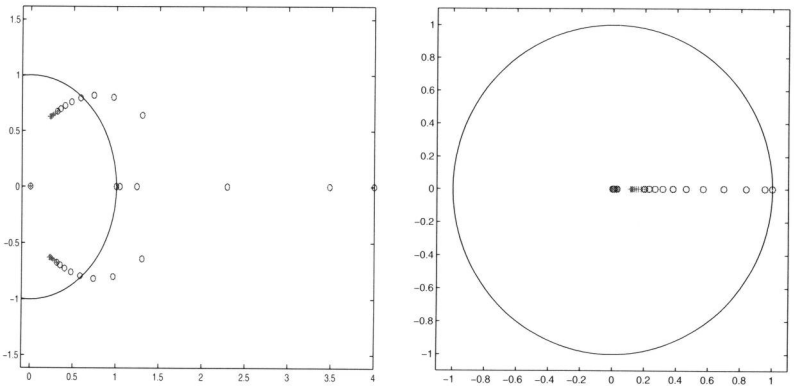

Cellwise order Pointwise order

$\circ : \omega_{low} \in [-\pi/2h, \pi/2h]; \quad + : \omega_{high} \in [-\pi/h, -\pi/2h] \cup [\pi/2h, \pi/h]$

Figure 2.4: Eigenvalue spectra of $\widehat{M^{REL}_{SGS}(\omega)}$ for Baumann's DG method (without damping: $\sigma = 1$, $\mu = 0$, $\alpha = 1$) relative to the unit circle.

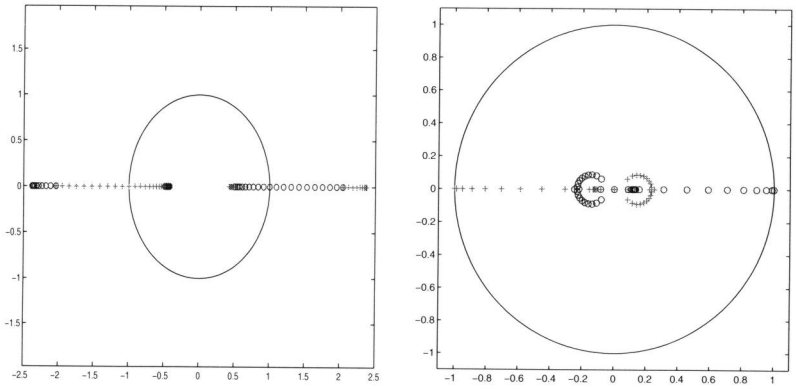

Cellwise order Pointwise order

$\circ : \omega_{low} \in [-\pi/2h, \pi/2h]; \quad + : \omega_{high} \in [-\pi/h, -\pi/2h] \cup [\pi/2h, \pi/h]$

Figure 2.5: Eigenvalue spectra of $\widehat{M^{REL}_{JOR}(\omega)}$ for symmetric DG method (without damping: $\sigma = -1$, $\mu = 0$, $\alpha = 1$) relative to the unit circle.

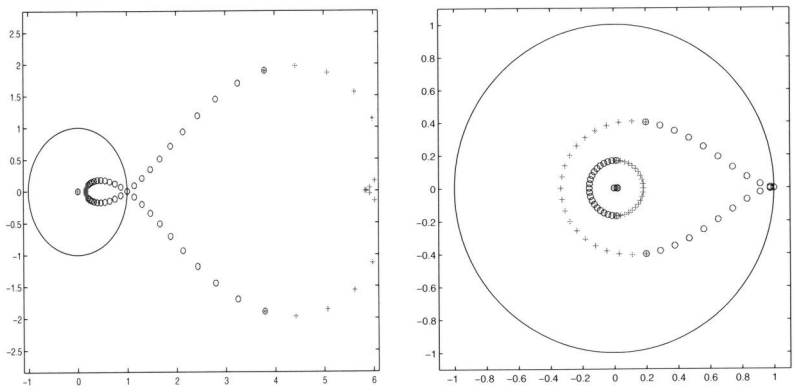

Cellwise order Pointwise order

$\circ : \omega_{low} \in [-\pi/2h, \pi/2h]; \quad + : \omega_{high} \in [-\pi/h, -\pi/2h] \cup [\pi/2h, \pi/h]$

Figure 2.6: Eigenvalue spectra of $\widehat{M^{REL}_{DGS}(\omega)}$ for the symmetric DG method (without damping: $\sigma = -1$, $\mu = 0$, $\alpha = 1$) relative to the unit circle.

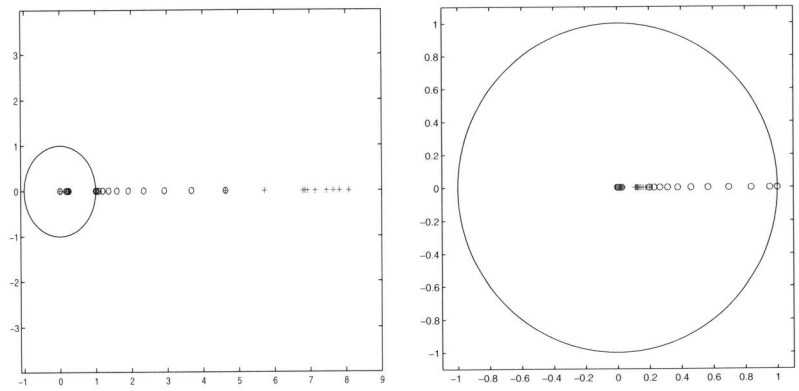

Cellwise order Pointwise order

$\circ : \omega_{low} \in [-\pi/2h, \pi/2h]; \quad + : \omega_{high} \in [-\pi/h, -\pi/2h] \cup [\pi/2h, \pi/h]$

Figure 2.7: Eigenvalue spectra of $\widehat{M^{REL}_{SGS}(\omega)}$ for the symmetric DG method (without damping: $\sigma = -1$, $\mu = 0$, $\alpha = 1$) relative to the unit circle.

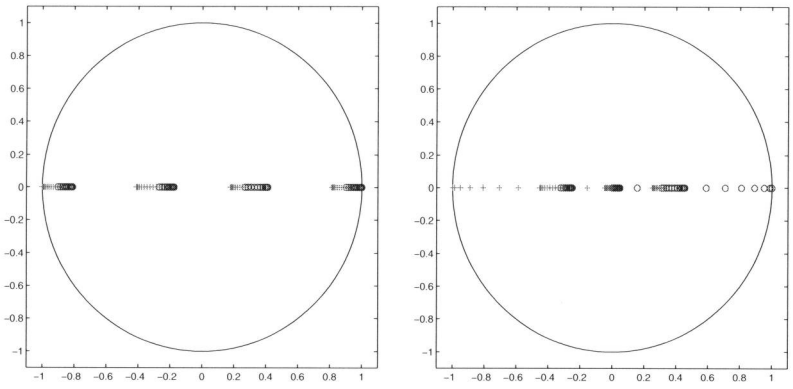

Cellwise order Pointwise order

$\circ : \omega_{low} \in [-\pi/2h, \pi/2h]; \quad + : \omega_{high} \in [-\pi/h, -\pi/2h] \cup [\pi/2h, \pi/h]$

Figure 2.8: Eigenvalue spectra of $\widehat{M_{JOR}^{REL}}(\omega)$ for the IP method (without damping: $\sigma = -1$, $\mu = 10/h$, $\alpha = 1$) relative to the unit circle.

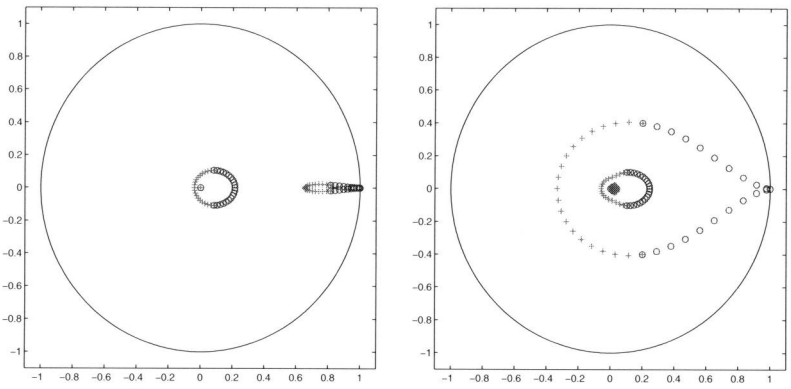

Cellwise order Pointwise order

$\circ : \omega_{low} \in [-\pi/2h, \pi/2h]; \quad + : \omega_{high} \in [-\pi/h, -\pi/2h] \cup [\pi/2h, \pi/h].$

Figure 2.9: Eigenvalue spectra of $\widehat{M_{DGS}^{REL}}(\omega)$ for the IP method (without damping: $\sigma = -1$, $\mu = 10/h$, $\alpha = 1$) relative to the unit circle.

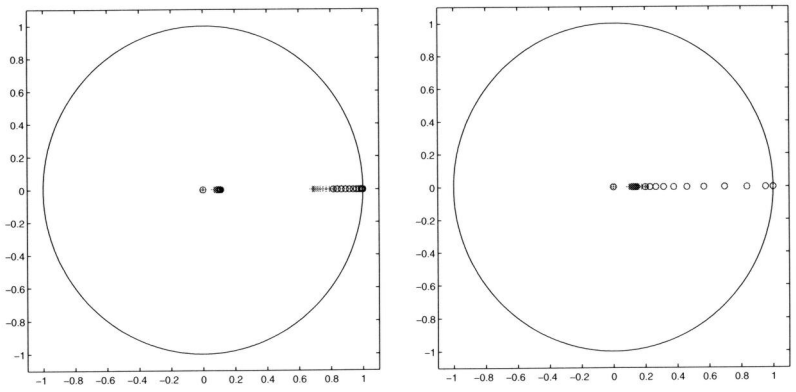

Cellwise order Pointwise order

$\circ : \omega_{low} \in [-\pi/2h, \pi/2h]; \quad + : \omega_{high} \in [-\pi/h, -\pi/2h] \cup [\pi/2h, \pi/h]$

Figure 2.10: Eigenvalue spectra of $\widehat{M_{SGS}^{REL}}(\omega)$ for the IP method (without damping: $\sigma = -1$, $\mu = 10/h$, $\alpha = 1$) relative to the unit circle.

where $\lambda_{\min}$ and $\lambda_{\max}$ are, respectively, the minimum and maximum (real) eigenvalues of the spectrum without damping. The damping parameters are given in Table 2.3. In Table 2.4 we show the spectral radii for the corresponding operators $M_h^{\mathrm{REL}}(I_h - P_{hH}R_{Hh})$. For the spectral radius of symmetric damped Gauss-Seidel (DGS) the damping parameter for DGS is used. In the next section we use a similar approach to optimize the TLA.

Table 2.3: Damping parameters for the relaxation.

α	Baumann/symmetric DG	IP DG ($\mu = 10/h$)
JOR	8/11	0.773
DGS	15/16	1.024

2.5 Two-level analysis

In this section we study the convergence behavior of a TLA for both the error and the residue. In a fashion similar to how we determined relaxation parameters for the smoothing operators, we determine optimal relaxation parameters

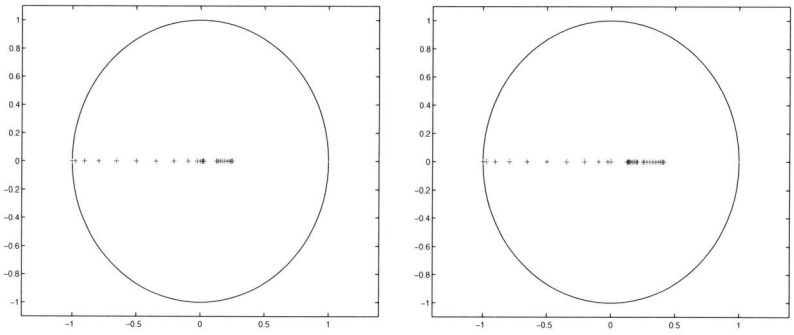

Baumann/symmetric DG penalized symmetric DG

Figure 2.11: Eigenvalue spectra of $\mathbf{FT}(M_{JOR}^{REL}(I_h - P_{hH}R_{Hh}))(\omega)$ without damping ($\alpha = 1$).

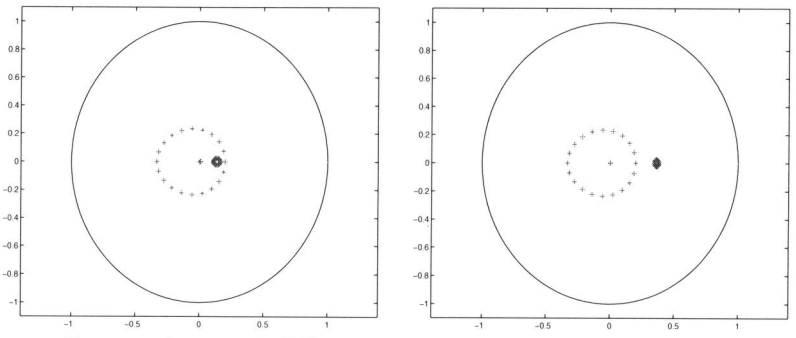

Baumann/symmetric DG penalized symmetric DG

Figure 2.12: Eigenvalue spectra of $\mathbf{FT}(M_{DGS}^{REL}(I_h - P_{hH}R_{Hh}))(\omega)$ without damping ($\alpha = 1$).

Table 2.4: Spectral radii of $M^{REL}(I_h - P_{hH}R_{Hh})$ for damping parameters as in Table 2.3.

$\rho(M^{REL}(I_h - P_{hH}R_{Hh}))$	Baumann/symmetric DG	IP DG ($\mu = 10/h$)
JOR	0.455	0.591
DGS	0.250	0.365
Symm-DGS	0.203	0.200

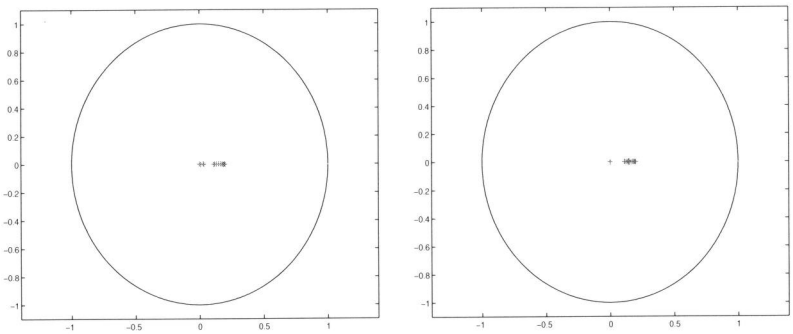

Baumann/symmetric DG penalized symmetric DG

Figure 2.13: Eigenvalue spectra of $\mathbf{FT}(M^{REL}_{DGS_U}(I_h - P_{hH}R_{Hh})M^{REL}_{DGS_L})(\omega)$ without damping ($\alpha = 1$).

for the two-level operators in order to minimize the spectral radii. The amplification of the error for the TLA is given by the operator

$$\begin{aligned} M_h^{TLA} &= \left(M_h^{\mathrm{REL}}\right)^{\nu_2} M_h^{\mathrm{CGC}} \left(M_h^{\mathrm{REL}}\right)^{\nu_1} \\ &= \left(M_h^{\mathrm{REL}}\right)^{\nu_2} \left(I - P_{hH} L_H^{-1} \overline{R}_{Hh} L_h\right) \left(M_h^{\mathrm{REL}}\right)^{\nu_1}, \end{aligned}$$

where ν_1 and ν_2 are the number of pre- (post-) relaxation sweeps, respectively, and M_h^{CGC} is the amplification operator of the coarse-grid correction. The amplification operator for the residue is

$$\begin{aligned} \overline{M}_h^{TLA} &= (\overline{M}_h^{REL})^{\nu_2} \overline{M}_h^{CGC} (\overline{M}_h^{REL})^{\nu_1} \\ &= \left(L_h M_h^{\mathrm{REL}} L_h^{-1}\right)^{\nu_2} L_h M_h^{\mathrm{CGC}} L_h^{-1} \left(L_h M_h^{\mathrm{REL}} L_h^{-1}\right)^{\nu_1}. \end{aligned}$$

In Section 2.2.4 we already noticed the Galerkin relation (2.13) between the discretization on the finer and the coarser grids and that, because test and trial spaces are the same, the residual restriction $\overline{R}_{Hh}$ is given by $\overline{R}_{Hh} = P_{hH}^T$, i.e., the adjoint of the prolongation. The consequence is that $M_h^{CGC} P_{hH} = 0$ for the solution and that $\overline{R}_{Hh} \overline{M}_h^{CGC} = 0$ for the residue. With the tools developed in the previous sections we now study the eigenvalue spectra of the two-level operators and their spectral norms.

2.5.1 Spectrum of the two-level iteration operator

The difference between the coarse-grid correction on the error and that on the residue is that the former splits an HF-error mode into an HF-mode and an LF-mode on the finer grid. This is in contrast to the coarse-grid correction on the residue, in which an LF-residual mode is split into an HF-mode and an LF-mode on the finer grid [20].

This implies that if we are interested in the error reduction, we should apply the smoothing operator M_h^{REL} *before* the coarse-grid correction. On the other hand, if we are interested in residue reduction we should apply the smoothing *after* the coarse-grid correction operator $\overline{M}_h^{CGC}$. Therefore, for the error, we are particularly interested in the behavior of the spectrum and the two-norm of

$$M_h^{\mathrm{CGC}} M_h^{\mathrm{REL}} = \left(I - P_{hH} L_H^{-1} \overline{R}_{Hh} L_h\right) M_h^{\mathrm{REL}},$$

whereas for the residue we want to study

$$\overline{M}_h^{REL}\, \overline{M}_h^{CGC} = \left(L_h M_h^{\mathrm{REL}} L_h^{-1}\right) \left(I - L_h P_{hH} L_H^{-1} \overline{R}_{Hh}\right).$$

It is clear that the spectra of these operators are the same, but the norms may be different. For different types of DG methods, viz. for Baumann's method ($\sigma = 1$, $\mu = 0$), the symmetric DG method ($\sigma = -1$, $\mu = 0$), and for the IP method ($\sigma = -1$, $\mu = C/h$), the spectra of the two-level operators can be studied as in Section 2.4 for the smoothing operators. The spectral radii of the two-level operators are shown in Table 2.5.

We see that the two-level amplification operators for the symmetric DG method have the smallest spectral radii, which indicates that the final convergence rate will be faster, compared with the Baumann and IP DG methods.

Table 2.5: Spectral radii $\rho(M_h^{CGC} M_h^{REL}) = \rho(\overline{M}_h^{REL} \overline{M}_h^{CGC})$ for optimal damping parameters.

$\rho(M_h^{CGC} M_h^{REL})$	Baum DG	Symm DG	IP DG ($\mu = 10/h$)
$M_h^{CGC} M_{JOR}^{REL}$	0.401	0.314	0.422
$M_h^{CGC} M_{DGS}^{REL}$	0.220	0.143	0.189
$M_{DGS_U}^{REL} M_h^{CGC} M_{DGS_L}^{REL}$	0.119	0.073	0.139

Table 2.6: The spectral norm ($\sigma_{\max}$) after one iteration for the residue with optimal damping.

	$\overline{M}_{JOR}^{REL}\overline{M}_h^{CGC}$	$\overline{M}_{DGS}^{REL}\overline{M}_h^{CGC}$	$\overline{M}_{DGS_L}^{REL}\overline{M}_h^{CGC}\overline{M}_{DGS_U}^{REL}$
Baum DG	1.762	1.364	0.557
Symm DG	1.282	0.506	0.104
IP DG ($\mu = 10/h$)	1.518	0.699	0.301

2.5.2 Spectral norm of the iteration operator for the error and residue

From Section 2.5.1 we know that all TLAs will converge rapidly after a sufficient number of iterations. However, since we want to minimize the total amount of iteration sweeps, we need to be sure also that the spectral norms of the iteration operators are sufficiently small. In order to check this we apply the singular value decomposition (SVD) to the Fourier transform of the amplification operators,

$$\mathbf{FT}\left(\left(M_h^{\mathrm{TLA}}\right)^t\right)(\omega) = U(\omega)\Sigma(\omega)V^T(\omega), \tag{2.34}$$

where, in view of our function basis, $U(\omega)$ and $V(\omega)$ are 8×8 unitary matrices and $\Sigma(\omega)$ is a real 8×8 diagonal matrix with singular values. The number of iterations is denoted by t. So, if we consider the error of the approximation, then according to (2.34), this error is first expressed on the basis $V(\omega)$, damped/amplified by $\Sigma(\omega)$, and then transformed to the basis $U(\omega)$. Since the spectral norm of the operator is the maximum singular value, this norm tells us how well the error (resp., the residue) is damped after t sweeps. The column of $V(\omega)$ determines the corresponding error/residual component.

The spectral norms after one iteration of the optimized two-level operators on the residue for the different types of DG methods are shown in Table 2.6. We see that not all two-level operators immediately converge. However, the situation changes if we look at the spectral norm of the two-level operators after two iterations (see Table 2.7). Then all methods converge, even by a significant factor. The spectral norms of the iteration operators on the error are the same as for the residual, except for Baumann's DG method. For this method the error-amplification norm becomes even unbounded (for vanishing frequency ω). This is related to the lack of adjoint consistency as indicated in [3]. We show the singular values of $\widehat{M_h^{\mathrm{TLA}}}(\omega)$ and $\widehat{\overline{M}_h^{\mathrm{TLA}}}(\omega)$ in Figures 2.14–2.16. We see that (as expected) in all cases four singular values vanish and that all singular values

Table 2.7: The spectral norm ($\sigma_{\max}$) after two iterations for the residue with optimal damping.

	$\overline{M}_{JOR}^{REL}\overline{M}_h^{CGC}$	$\overline{M}_{DGS}^{REL}\overline{M}_h^{CGC}$	$\overline{M}_{DGS_L}^{REL}\overline{M}_h^{CGC}\overline{M}_{DGS_U}^{REL}$
Baum DG	0.684	0.447	0.064
Symm DG	0.403	0.083	0.007
IP DG ($\mu = 10/h$)	0.640	0.284	0.038

(except for $\widehat{M_h^{\mathrm{TLA}}}(\omega)$ for Baumann's method) are much smaller than one.

2.6 Galerkin relation and consistency

By the nature of the DG method, it is clear that the Galerkin relation,

$$L_H = \overline{R}_{Hh} L_h P_{hH} ,$$

exists between the discrete operators on the fine grid and the coarse grid, provided that $\overline{R}_{Hh} = P_{hH}^T$ and that P_{hH} satisfies the requirement that $\mathbf{u}_h$ and $P_{hH}\mathbf{u}_H$ represent the same piecewise polynomial. For the prolongation introduced in Section 2.2.4 this holds true by construction.

The Galerkin relation, the order of consistency, and the order of convergence are easily verified by Fourier analysis. In order to see this in detail and to compute the corresponding order constants, we show some results of this analysis, which also yields some additional insight with respect to the lack of adjoint consistency of Baumann's method (see [3]).

For the analysis we use the four functions in the basis (2.8) with $p = 2$ and consider the related pointwise stencil (2.11). First, we are interested in the truncation error operator

$$\tau_h = L_h R_h - \overline{R}_h L , \tag{2.35}$$

and the operator corresponding to the discrete convergence, $C_h = L_h^{-1}\tau_h$. In (2.35) $R_h : C^1(\Omega_h) \to \mathbb{R}^{4\mathbb{Z}_h}$ is the injective restriction similar to (2.18), whereas the second restriction is the Galerkin restriction $\overline{R}_h : C^1(\Omega_h) \to \mathbb{R}^{4\mathbb{Z}_h}$, defined such that for all $f \in C^1(\Omega_h)$,

$$\left(\overline{R}_h f\right)(jh) = \begin{bmatrix} \int_{(j-1)h}^{jh} \phi_k(x) f(x) dx, & k \in \{1,2\} , \\ \int_{jh}^{(j+1)h} \phi_k(x) f(x) dx, & k \in \{3,4\} , \end{bmatrix}$$

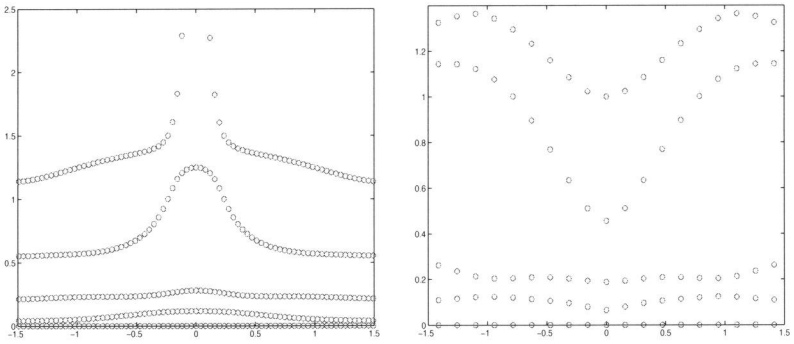

Baumann, $\widehat{M_h^{\mathrm{TLA}}}(\omega)$ Baumann, $\widehat{\overline{M}_h^{\mathrm{TLA}}}(\omega)$

Figure 2.14: Singular values $\Sigma(\omega)$, $\omega \in [-\pi/2, \pi/2]$, for a TLA iteration operator: $\widehat{M_h^{\mathrm{TLA}}}(\omega) = \widehat{M_h^{\mathrm{CGC}}}(\omega)\widehat{M_{\mathrm{DGS}}^{\mathrm{REL}}}(\omega)$ and $\widehat{\overline{M}_h^{\mathrm{TLA}}}(\omega) = \widehat{\overline{M}_{\mathrm{DGS}}^{\mathrm{REL}}}(\omega)\widehat{\overline{M}_h^{\mathrm{CGC}}}(\omega)$.

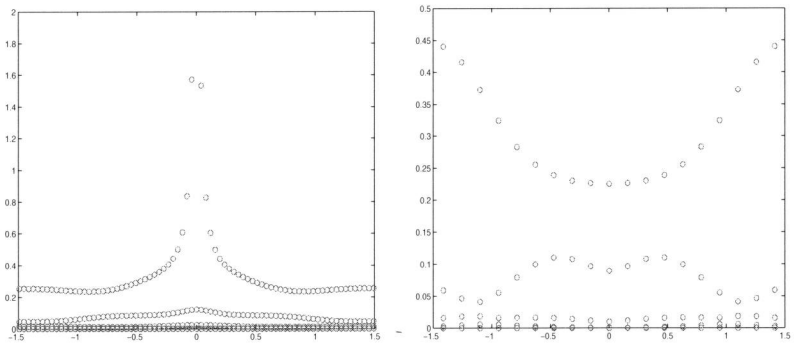

Baumann, $\left(\widehat{M_h^{\mathrm{TLA}}}\right)^2(\omega)$ Baumann, $\left(\widehat{\overline{M}_h^{\mathrm{TLA}}}\right)^2(\omega)$

Figure 2.15: Singular values $\Sigma(\omega)$, $\omega \in [-\pi/2, \pi/2]$, for two steps of the TLA-iteration operator.

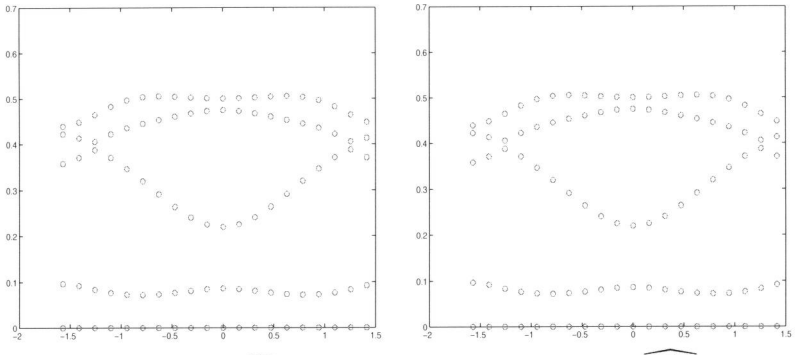

Symmetric DG, $\widehat{M_h^{\mathrm{TLA}}}(\omega)$ Symmetric DG, $\widehat{\overline{M}_h^{\mathrm{TLA}}}(\omega)$

Figure 2.16: Singular values $\Sigma(\omega)$, $\omega \in [-\pi/2, \pi/2]$, for one step of the symmetric DG TLA iteration operator.

where ϕ_k are the basis functions in pointwise ordering. With $P_h : \mathbb{R}^{4\mathbb{Z}_h} \to \mathrm{Span}(\phi_{j,e}) \subset C^1(\Omega_h)$ the interpolation with $R_h P_h = I_h$, it is clear that, by construction, $P_h = P_{hH} P_H$ and $\overline{R}_H = \overline{R}_{Hh} \overline{R}_h$, and the discrete operator is characterized by $L_h = \overline{R}_h L P_h$. Hence, $L_H = \overline{R}_H L P_H = \overline{R}_{Hh} \overline{R}_h L P_h P_{hH} = \overline{R}_{Hh} L_h P_{hH}$. Furthermore, we write for the truncation error:

$$\tau_h e^{i\omega x} = \tau_h e_\omega(x) = (L_h R_h e_\omega - \overline{R}_h L e_\omega)(x).$$

Using (2.18) and the definition of $\overline{R}_h$, we find

$$\tau_h e_\omega = L_h e^{i\omega jh} \begin{bmatrix} 1 - e^{-i\omega h} - i\omega h \\ 1 \\ 1 \\ 1 - e^{i\omega h} + i\omega h \end{bmatrix} - \omega^2 h e^{i\omega jh} \begin{bmatrix} \int_0^1 e^{i\omega h(t-1)} t^2 (1-t) dt \\ \int_0^1 e^{i\omega h(t-1)} t dt \\ \int_0^1 e^{i\omega ht} (1-t) dt \\ \int_0^1 e^{i\omega ht} t (1-t)^2 dt \end{bmatrix},$$

where the basis functions are scaled to the master element $\widehat{\Omega} = [0, 1]$. Hence,

$$\begin{aligned} \tau_h e_\omega &= \left(\widehat{L_h}(\omega) \begin{bmatrix} 1 - e^{-i\omega h} - i\omega h \\ 1 \\ 1 \\ 1 - e^{i\omega h} + i\omega h \end{bmatrix} - \omega^2 h \begin{bmatrix} \int_0^1 e^{i\omega h(t-1)} t^2 (1-t) dt \\ \int_0^1 e^{i\omega h(t-1)} t dt \\ \int_0^1 e^{i\omega ht} (1-t) dt \\ \int_0^1 e^{i\omega ht} t (1-t)^2 dt \end{bmatrix} \right) e^{i\omega jh} \qquad (2.36) \\ &= \left(\widehat{L_h}(\omega) \widehat{R_h}(\omega) - \widehat{\overline{R}}_h(\omega) \widehat{L}(\omega) \right) e^{i\omega jh}, \end{aligned}$$

Table 2.8: The expansion of *(2.38)* for $\omega h \to 0$, i.e., the order of convergence: pointwise values ($\widehat{v}_2$ and $\widehat{v}_3$) and pointwise derivatives ($\widehat{v}_1$ and $\widehat{v}_4$) at the nodal points.

Baumann	Symmetric	IP
$\sigma = 1$	$\sigma = -1$	$\sigma = -1$
$\mu = 0$	$\mu = 0$	$\mu = 1/h$
$\begin{pmatrix} \frac{1}{120}h^4\omega^4 + O(h^5\omega^5) \\ \frac{1}{840}h^4\omega^4 + O(h^5\omega^5) \\ \frac{1}{840}h^4\omega^4 + O(h^5\omega^5) \\ \frac{1}{120}h^4\omega^4 + O(h^5\omega^5) \end{pmatrix}$	$\begin{pmatrix} \frac{1}{120}h^4\omega^4 + O(h^5\omega^5) \\ \frac{1}{3360}h^5\omega^5 + O(h^6\omega^6) \\ \frac{1}{3360}h^5\omega^5 + O(h^6\omega^6) \\ \frac{1}{120}h^4\omega^4 + O(h^5\omega^5) \end{pmatrix}$	$\begin{pmatrix} \frac{1}{120}h^4\omega^4 + O(h^5\omega^5) \\ \frac{1}{2800}h^5\omega^5 + O(h^6\omega^6) \\ \frac{1}{2800}h^5\omega^5 + O(h^6\omega^6) \\ \frac{1}{120}h^4\omega^4 + O(h^5\omega^5) \end{pmatrix}$

where $\widehat{L_h}(\omega)$ is the Fourier transform of the block-Toeplitz matrix L_h. Now we find the expansion of the truncation error for $h \to 0$ from (2.36). Both for Baumann's method ($\sigma = 1, \mu = 0$) and for the symmetric DG method without penalty ($\sigma = -1, \mu = 0$) and with IP ($\sigma = -1, \mu = 1/h$), (the absolute value of) the truncation error is

$$\tau e_\omega = \begin{bmatrix} \frac{1}{720}h^3\omega^4 + O(h^4\omega^5) \\ 0 \\ 0 \\ \frac{1}{720}h^3\omega^4 + O(h^4\omega^5) \end{bmatrix}. \tag{2.37}$$

Taking into account the factor h^{d-2}, typical for the FEM difference stencil (with $d = 1$ the dimension of cell Ω_e), we recognize in (2.37) the fourth order consistency of the discretization.

Similarly, we study the discrete convergence (where no such factor exists) by

$$C_h\, e_\omega = L_h^{-1}\tau_h\, e_\omega = \widehat{L_h}^{-1}(\omega)\, \left(\widehat{L_h}(\omega)\widehat{R_h}(\omega) - \widehat{R_h}(\omega)\widehat{L}(\omega)\right) e^{i\omega jh}. \tag{2.38}$$

The results for the different methods are given in Table 2.8. We see that the symmetric DG methods, with and without IP, are more accurate with respect to the pointwise function values than Baumann's method. However, there is no difference in the order of accuracy with respect to the pointwise derivatives.

2.7 Numerical results

In this section we show by numerical experiments the convergence behavior of the two-level iteration operator for the error with the Baumann and symmetric DG methods for the smoothers JOR, DGS, and symmetric DGS with the

optimal damping parameters. For this purpose we solve Poisson's equation

$$-u_{xx} = \frac{e^{x/\epsilon}}{\epsilon^2(\epsilon^{1/\epsilon} - 1)} \text{ with } u(0) = 0,\ u(1) = 0.$$

The choice of the right-hand side is unimportant, but starting with zero, in this example both low and high frequencies are present in the error. To obtain the discrete system we use the fourth order polynomial basis (2.1) and we set the meshwidth $h = 2^{-N}$. We start with an initial function $u_h^0 = u_{h,\mathrm{PRE}}^0$ on the finer grid. We apply ν_1 prerelaxation sweeps

$$u_{h,\mathrm{PRE}}^{i+1} = u_{h,\mathrm{PRE}}^{i} + B_h \left(f_h - L_h u_{h,\mathrm{PRE}}^{i}\right),$$

where B_h is an approximate inverse of L_h as given in Table 2.1. We update the solution by a coarse-grid correction step, solving the problem once on grid $H = 2^{1-N}$,

$$u_{h,\mathrm{POST}}^{0} = u_{h,\mathrm{PRE}}^{\nu_1} + P_{hH} L_H^{-1} \overline{R}_{Hh} (f_h - L_h u_{h,\mathrm{PRE}}^{\nu_1}),$$

and eventually we apply ν_2 postrelaxation sweeps,

$$u_{h,\mathrm{POST}}^{i+1} = u_{h,\mathrm{POST}}^{i} + B_h (f_h - L_h u_{h,\mathrm{POST}}^{i}),$$

to compute $u_h^{i+1} = u_{h,\mathrm{PRE}}^{0} = u_{h,\mathrm{POST}}^{\nu_2}$. For the initial function u_h^0 we choose $u_h^0 = R_h u_0 = R_h \sin(2\pi/h)$. To show the convergence of the different methods we measure the residue in the vector norm (2.16). Hence we write

$$\|d_h\|_2 = \|f_h - L_h u_h\|_2 = \left(\sum_{e=1}^{64} \sum_{j=1}^{4} d_{he,j}^2 \right)^{1/2}.$$

Since the spectral radii of the two-level operators for the Baumann and symmetric DG methods calculated by Fourier analysis are smaller than those of the IP DG method, we only show results for the first two methods. The convergence of the residue for the two-level operator with different smoothers is shown in Figure 2.17.

We observe that both DG methods methods show immediately convergence, starting from the first iteration sweep. We see from Figure 2.17 and Table 2.9 that the spectral radii obtained from the numerical experiments coincide very well with spectral radii obtained by Fourier analysis (Table 2.5).

We further remark that the symmetric DG method converges somewhat faster than Baumann's DG method. In spite of the phenomenon related to the lack of adjoint consistency of Baumann's method, the observed convergence of the error shows in practice the same behavior as the convergence of the residual.

Table 2.9: Numerically obtained convergence factors corresponding to $\rho(M_h^{CGC} M_h^{REL}) = \rho(\overline{M}_h^{REL} \overline{M}_h^{CGC})$.

$\rho(M_h^{CGC} M_h^{REL})$	Baum DG	Symm DG
$M_h^{CGC} M_{JOR}^{REL}$	0.38	0.30
$M_h^{CGC} M_{DGS}^{REL}$	0.22	0.14
$M_{DGS_U}^{REL} M_h^{CGC} M_{DGS_L}^{REL}$	0.11	0.07

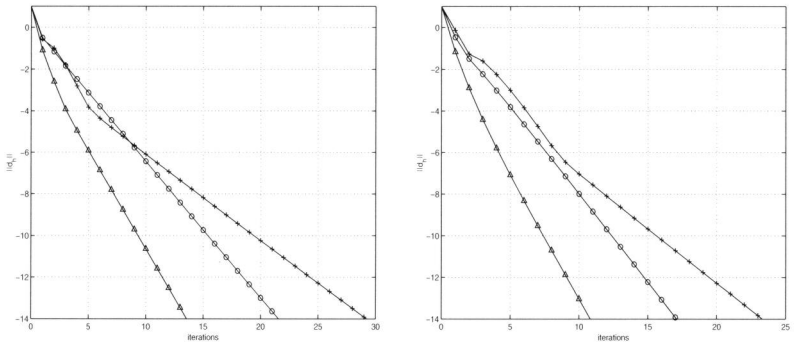

Baumann DG Symmetric DG

+: JOR; ○: DGS; △: SGS.

Figure 2.17: $\log(||d_h||_2)$ as function of iterations for the two-level iteration operator on the error.

2.8 Conclusion

In this chapter we analyze the convergence of the MG algorithm for various DG methods. For convenience we restrict ourselves to the one-dimensional Poisson problem. We consider the (asymmetric) Baumann–Oden discretization and the symmetric DG discretization, with and without IP.

By the choice of a suitable basis in the space of the discontinuous piecewise polynomials that are used for the trial and test spaces, we are able to introduce a point-wise block-partitioning of the discrete operators. It appears that block-relaxation methods based on this pointwise partitioning show completely different convergence properties from those found with classical, cellwise partitionings. Pointwise block-relaxations have much better convergence and smoothing properties. This is most significant for the symmetric DG discretiza-

tion without IP. Here, cellwise block-Jacobi and block-Gauss–Seidel relaxations diverge, whereas the pointwise block-relaxations converge.

For the three discretization methods studied we compute optimal damping parameters for Jacobi, Gauss–Seidel, and SGS relaxations. The resulting smoothing factors lie between 0.6 (JOR for IP discretization) and 0.2 (symmetric DG). A two-level analysis with optimal damping parameter shows even better convergence: with spectral radius from 0.4 (JOR for IP discretization) to 0.075 (for symmetric GS and symmetric DG). An analysis of the spectral norm of the two-level amplification for the residue shows that a very small number of iteration steps (usually not more than two) is indeed sufficient to reduce the error by an order of magnitude.

The lack of adjoint consistency of Baumann's method and the resulting loss of accuracy for the solution (and *not* for its derivative) could be analyzed by means of Fourier analysis, and was also reflected in the spectral norm of the two-level amplification operator for the error.

Chapter 3

Two-level analysis for DG discretization with linear elements

Summary

In this chapter we study the convergence of a multigrid method for the solution of a linear second order elliptic equation, discretized by discontinuous Galerkin (DG) methods, and we give a detailed analysis of the convergence for different block-relaxation strategies. To complement the analysis in Chapter 2 (see also [24]) where higher-order methods were studied, here we restrict ourselves to methods using piecewise linear approximations. It is well-known that these methods are unstable if no additional interior penalty is applied.

As for the higher-order methods, we find that point-wise block-relaxations give much better results than the classical cell-wise relaxations. Both for the Baumann-Oden and for the symmetric DG method, with a sufficient interior penalty, the block-relaxation methods studied (Jacobi, Gauss-Seidel and symmetric Gauss-Seidel) all make excellent smoothing procedures in a classical multigrid setting. Independent of the mesh size, simple MG cycles give convergence factors 0.2 – 0.4 per iteration sweep for the different discretizations studied.

3.1 Introduction

Since thus far relatively little attention has been paid to optimally efficient solution methods for the algebraic systems arising from the discretization of the stationary problems, we study the possible use of a multigrid algorithm for this purpose. We concentrate on the Baumann DG, the symmetric DG methods [3]. It is well-known [2, 43, 50] that these methods are not stable for the lowest order of approximation ($p = 1$), if no additional stabilization is applied by means of an interior penalty (IP) parameter. All these methods can be described by the same formulas [3, 24], where the distinction between the various methods is made by two parameters: σ, the sign ($\sigma = +1$ for Baumann and $\sigma = -1$ for symmetric DG), and $\mu = \nu/h$, the interior penalty parameter.

Whereas in the previous chapter we studied the convergence of a multigrid method for the solution of the systems arising from higher-order methods ($p \geq 3$), in this chapter we focus on the convergence of the multigrid method for the case $p = 1$, because this case may be used to accelerate the solution for $p > 1$ in the p-hierarchical structure of the hp-adaptive approximation process.

For the higher-order methods we showed that excellent convergence was obtained when blockwise relaxation (Jacobi or Gauss-Seidel) is applied as a smoother, if the blocks are formed by the degrees of freedom (dofs) associated with cell-vertices. This motivates us to study the smoothing abilities for the IP-DG method with a well chosen penalty parameter μ.

The outline of this chapter is as follows. In Section 3.2 we give a unified description of the DG discretizations so that the different symmetric forms, Baumann's variant and the Internal Penalty (IP) variants follow from the values of specific parameters (σ and μ) in the formulation. For the linear trial functions that we restrict ourselves to, we give a description of the resulting discrete operator in the form of a stencil that defines the resulting block-Toeplitz matrix.

In Section 3.3 we apply Fourier analysis to this discrete operator in order to study its stability properties. We observe that both the symmetric DG and Baumann's variant have a double zero eigenvalue, one of which has an eigenfunction that is not constant (the spurious eigenvalue responsible for the instability of the methods). If a large enough penalty parameter is chosen, then it is seen that the instability disappears. However, for a too large value of the penalty parameter we see that the discrete system becomes ill-conditioned.

In Section 3.4 we give a smoothing analysis of the point-wise and cell-wise block-relaxations and a convergence analysis of the two-level algorithm. As in the case of higher degree trial polynomials, dealt with in Chapter 2, we see also here that the use of point-wise relaxation gives much faster convergence. By

determining the spectral norm of the error-amplification operator it is shown that the observed 'good convergence' is guaranteed from the second iteration step on; we find convergence with a rate of about 0.2 – 0.4 per iteration.

In Section 3.5 we report on numerical results for the solution of a one-dimensional Poisson problem on the unit interval, where the solution has a thin boundary layer, its thickness depending on a parameter ε. The results confirm the theoretical analysis.

3.2 The linear discontinuous Galerkin discretization

For the Poisson equation (2.1), defined on the unit cube Ω, we consider the variational form (2.3), associated with the DG-methods [3, 24]: find $u \in H^1(\Omega_h)$ such that:

$$B(u,v) = L(v) \quad \forall v \in H^1(\Omega_h), \tag{3.1}$$

where the bilinear form $B(u,v)$ is defined by (2.4).

In this chapter we study the one-dimensional equation, which we consider as an essential building block for the higher dimensional case where we use tensor product polynomials. For test and trial space $S_h \subset H^1(\Omega_h)$ we use the space of discontinuous piecewise polynomials on the partitioning Ω_h. Then the discrete equations read: find $u_h \in S_h$ such that

$$B(u_h, v_h) = L(v_h) \qquad \forall v_h \in S_h\,. \tag{3.2}$$

With a basis $\{\phi_{i,e}\}$ for the space S_h this leads to the linear system

$$\begin{aligned}
&\sum_{e=1}^{N}\sum_{i=0}^{1} c_{i,e} \left(\int_{\Omega_e} \phi'_{i,e}(x)\phi'_{j,e}(x)dx - \langle \phi'_{i,e}(x)\rangle \cdot [\phi_{j,e}(x)]\,|_{\Gamma_{\mathrm{Dint}}} \right. \\
&\qquad \left. + \sigma\,[\phi_{i,e}(x)] \cdot \langle \phi'_{j,e}(x)\rangle\,|_{\Gamma_{\mathrm{Dint}}} + \mu\,[\phi_{i,e}(x)] \cdot [\phi_{j,e}(x)]\,|_{\Gamma_{\mathrm{Dint}}} \right) \qquad (3.3)\\
&= \sum_{e=1}^{N}\sum_{i=0}^{1} \int_{\Omega_e} f\phi_{j,e}(x)dx + \sigma\,[u_0] \cdot \langle \phi'_{j,e}(x)\rangle\,|_{\Gamma_{\mathrm{D}}} \\
&\qquad + \mu\,[u_0] \cdot [\phi_{j,e}(x)]\,|_{\Gamma_{\mathrm{D}}} + g\phi_{j,e}(x)|_{\Gamma_N}\,,
\end{aligned}$$

which we briefly denote by $L_h u_h = f_h$. In this chapter we restrict ourselves to S_h consisting of piecewise linear polynomials on a uniform partitioning for

which we use the element basis functions $\phi_j(\xi) = \xi^j(1-\xi)^{1-j}$, $j = 0, 1$, so that we have $2N$ basis functions $\phi_j((x-x_e)/h) = \phi_{j,e}(t)$; $j = 0, 1$; $e = 1, \cdots, N$. For this basis of piecewise linear polynomials the linear system (3.3) has a 2×2-block-tridiagonal structure, with the discretization stencil:

$$\left[\begin{array}{cc|cc|cc} -\frac{1}{2} & \frac{1-\sigma}{2} - h\mu & \frac{1+\sigma}{2} + h\mu & \frac{-1-\sigma}{2} & \frac{1}{2}\sigma & 0 \\ 0 & \frac{1}{2}\sigma & \frac{-1-\sigma}{2} & \frac{1+\sigma}{2} + h\mu & \frac{1-\sigma}{2} - h\mu & -\frac{1}{2} \end{array}\right], \tag{3.4}$$

if the equations (the weighting functions $\phi_{e,j}$) and coefficients are ordered *cell-wise* as $[c_{e,0}, c_{e,1}]_{e=1}^{N}$. As we emphasized in Chapter 2 we can also order the equations and coefficients *pointwise*, according to function values at the cell-interfaces, $[c_{e-1,1}, c_{e,0}]_{e=2}^{N}$, which leads to the stencil:

$$\left[\begin{array}{cc|cc|cc} \frac{1}{2}\sigma & \frac{-1-\sigma}{2} & \frac{1+\sigma}{2} + h\mu & \frac{1-\sigma}{2} - h\mu & -\frac{1}{2} & 0 \\ 0 & -\frac{1}{2} & \frac{1-\sigma}{2} - h\mu & \frac{1+\sigma}{2} + h\mu & \frac{-1-\sigma}{2} & \frac{1}{2}\sigma \end{array}\right]. \tag{3.5}$$

Thus, with the possible exception for the equations at the boundaries, the discretization matrix appears to be a block-Toeplitz matrix and is described by the repetition of either stencil (3.4) or stencil (3.5). Both stencils describe one and the same matrix, but the distinction between cell-wise and point-wise blocks materializes as soon as we consider block-relaxation methods.

3.3 Fourier analysis of the discrete operator L_h

Having introduced in Section 2.3.2 the Fourier transform of a block-Toeplitz operator, we describe the spectrum of the discrete operator L_h on an infinite domain, and we discuss its stability properties. We notice the difference between this operator for piecewise cubic approximations, as described in Chapter 2, and the corresponding operator for piecewise linears. We recognize that for the latter a sufficiently large interior penalty parameter has to be chosen in order to obtain a stable scheme. Then, for the stable schemes, we compute the order of accuracy.

3.3.1 Eigenvalues spectra of the discrete operator L_h

We study the eigenvalue spectra of the discrete operator L_h of (i) Baumann's, (ii) the symmetric-, and (iii) the internal penalty (IP) DG-method, all with linear

elements. It is well known that in this case Baumann's and the symmetric DG-method are unstable and that an additional penalty parameter $\mu = \nu/h$ (IP DG-method) can be introduced in order to stabilize the discrete operator L_h.

To study the behavior of the three different DG-methods we look at the eigenvalue spectra of $\widehat{L_h}(\omega)$. Considering the point-wise stencil (3.5) we write for $\widehat{L_h}(\omega)$, using (2.19),

$$\widehat{L_h}(\omega) = \frac{1}{2h} \begin{pmatrix} 1+\sigma+2\nu-e^{i\omega h}+\sigma e^{-i\omega h} & 1-\sigma-2\nu-(1+\sigma)e^{-i\omega h} \\ 1-\sigma-2\nu-(1+\sigma)e^{i\omega h} & 1+\sigma+2\nu-e^{-i\omega h}+\sigma e^{i\omega h} \end{pmatrix}, \tag{3.6}$$

for all $\omega \in \mathbb{T}_h \equiv [-\pi/h, \pi/h]$. If further $\widehat{L_h}(\omega)$ allows for an eigenvalue decomposition

$$\widehat{L_h}(\omega)\mathbf{v} = \mathbf{v}\Lambda_h(\omega), \tag{3.7}$$

then, because of (2.21), the columns of $\mathbf{v}(\omega)e_{h,\omega}(mh)$ are the eigenvectors of L_h and $\Lambda_h(\omega)$ is a family of 2×2 diagonal matrices with the eigenvalues of L_h at the diagonal entries. The eigenvalues $\lambda_h(\omega)$ of $\widehat{L_h}(\omega)$ for respectively Baumann's, the symmetric and the IP DG-method are shown in Table 3.1. Note that the same eigenvalues are obtained if the cell-wise stencil (3.4) is used instead of the point-wise stencil (3.5). Only the coefficients of the eigenvectors $\mathbf{v}(\omega)e_{h,\omega}(mh)$ are collected either point-wise ($[c_{e-1,1}, c_{e,0}]$) or cell-wise ($[c_{e,0}, c_{e,1}]$).

Table 3.1: Eigenvalues of $\widehat{L_h}(\omega)$.

$\lambda_h(\omega)$	Baum-DG $\sigma = 1,\ \mu = 0$	symm-DG $\sigma = -1,\ \mu = 0$	IP-DG $\sigma = -1,\ \mu = \nu/h$
$\lambda_1(\omega)$	$\frac{1+\cos(\omega h)}{h}$	$\frac{1-\cos(\omega h)}{h}$	$\frac{\nu-\cos(\omega h)+\lvert\nu-1\rvert}{h}$
$\lambda_2(\omega)$	$\frac{1-\cos(\omega h)}{h}$	$\frac{-1-\cos(\omega h)}{h}$	$\frac{\nu-\cos(\omega h)-\lvert\nu-1\rvert}{h}$

If we study the eigenvalues $\lambda_h(\omega)$ of $\widehat{L_h}(\omega)$ for Baumann's DG-method, we see in Table 3.1 that they are real and non-negative: $\lambda_1(\omega), \lambda_2(\omega) \in [0, 2/h]$. Furthermore we see that $\lambda_2 = 0$ for $\omega = 0$, which is the eigenvalue corresponding to the constant eigenfunction. This eigenfunction corresponds to the equivalent eigenfunction for the continuous operator and is controlled by the boundary conditions. However, we see that there also is an additional zero eigenvalue $\lambda_1 = 0$ for $\omega = \pm\pi/h$, and the corresponding eigenvalue is oscillating piecewise constant. This spurious zero eigenvalue causes the Baumann DG-method to be singular for linear basis functions in the test and trial space.

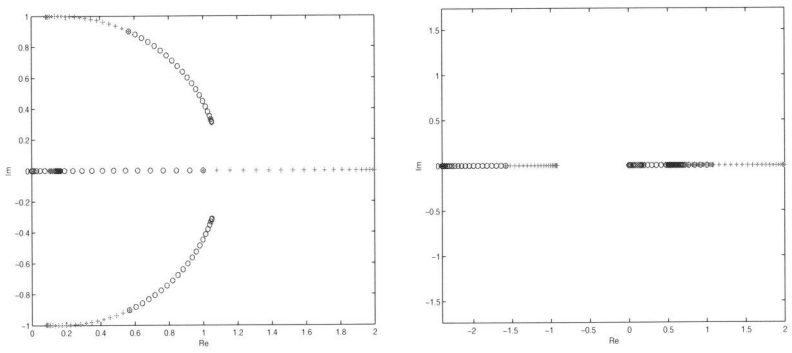

Baumann-DG symmetric-DG

$\circ : \omega_{low} \in [-\pi/2h, \pi/2h], \quad + : \omega_{high} \in [-\pi/h, -\pi/2h] \cup [\pi/2h, \pi/h]$

Figure 3.1: Eigenvalue spectra of discrete operator $\widehat{L_h}(\omega)$ for cubic stencil.

The same oscillating piecewise constant function is an additional eigenfunction, with $\lambda_2 = 0$, for the discrete operator L_h for the symmetric DG-method. Furthermore, for this DG-method we recognize the saddle-point behavior $\lambda_1(\omega) \in [0, 2/h]$, $\lambda_2(\omega) \in [-2/h, 0]$.

If we study the eigenvalue spectrum $\lambda_h(\omega)$ for the IP DG-method, then we may still choose the penalty parameter ν. If we choose $\nu < 0$, the method is stable in the sense that the unique zero eigenvalue corresponds to the constant eigenfunction. However, the method is indefinite. If we choose the parameter $0 \leq \nu < 1$ the method is indefinite *and* unstable (since then there is a spurious zero eigenvalue with a corresponding oscillating piecewise constant eigenfunction). For $\nu \geq 1$ the method is stable (the eigenvalues have non-negative sign). On the other hand, for a large parameter ν the discrete operator is ill-conditioned.

Whereas, for linear polynomials in the test and trial space, Baumann's non-symmetric DG-method has positive real eigenvalues, this is not the case for higher-order piecewise polynomials (although they have positive real parts). Figure 3.1 shows the eigenvalue spectra the Baumann and the symmetric DG-methods for piecewise cubics, as analyzed in Chapter 2 and [24]. The spectrum of Baumann's method shows complex eigenvalues; in the case of the symmetric DG-method the spectrum is real but indefinite.

Notice the distinction between eigenvalues for low and high frequencies which is useful in the context of multigrid. (Low frequency functions can also be

represented on a twice coarser grid.)

3.3.2 Consistency of the IP DG-method

In the previous section we have seen that the IP DG-method for the piecewise linear basis is stable if $\nu \geq 1$. In this section we study the accuracy and the discrete convergence of this method. For the analysis we use the point-wise stencil (3.5) and proceed analogously to the treatment in Section 2.6. We study the truncation operator

$$\tau_h = L_h R_h - \overline{R}_h L, \tag{3.8}$$

and the operator corresponding with the discrete convergence, $C_h = L_h^{-1}\tau_h$. In (3.8) $R_h : C^1(\Omega_h) \to \mathbb{R}^{2\mathbb{Z}_h}$ is the injective restriction defined by

$$\mathbf{u}_h(jh) = (R_h u)(jh) = \begin{bmatrix} u(jh)|_{\Omega_{j-1}} \\ u(jh)|_{\Omega_j} \end{bmatrix}.$$

The second restriction, $\overline{R}_h : C^1(\Omega_h) \to \mathbb{R}^{2\mathbb{Z}_h}$, is the Galerkin restriction defined by

$$\left(\overline{R}_h f\right)(jh) = \begin{bmatrix} \int_{(j-1)h}^{jh} \phi_{1,j-1}(x) f(x)\, dx\,, \\ \int_{jh}^{(j+1)h} \phi_{0,j}(x) f(x)\, dx\,, \end{bmatrix}$$

for all $f \in L^2(\Omega)$. Using $\tau_h e_\omega$ for the truncation error

$$\tau_h e_\omega(x) = \tau_h e^{i\omega x} = (L_h R_h e_\omega - \overline{R}_h L e_\omega)(x),$$

and with the definition of R_h, we find

$$\tau_h e_\omega = L_h e^{i\omega jh} \begin{bmatrix} 1 \\ 1 \end{bmatrix} - \omega^2 h e^{i\omega jh} \begin{bmatrix} \int_0^1 e^{i\omega h(t-1)} t\, dt \\ \int_0^1 e^{i\omega ht}(1-t)\, dt \end{bmatrix},$$

where the basis functions are scaled to the master element $\hat{\Omega} = [0,1]$. So,

$$\begin{aligned} \tau_h e_\omega &= \left(\widehat{L_h}(\omega) \begin{bmatrix} 1 \\ 1 \end{bmatrix} - h \begin{bmatrix} \int_0^1 e^{i\omega h(t-1)} t\, dt \\ \int_0^1 e^{i\omega ht}(1-t)\, dt \end{bmatrix} \omega^2 \right) e^{i\omega jh} \\ &=: \left(\widehat{L_h}(\omega)\widehat{R_h}(\omega) - \widehat{\overline{R}}_h(\omega)\widehat{L}(\omega) \right) e^{i\omega jh}, \end{aligned} \tag{3.9}$$

where $\widehat{L_h}(\omega)$ is the Fourier transform of the block Toeplitz matrix L_h for the point-wise stencil. The order of the truncation error is found by expansion of

(3.9) for $h \to 0$. Since $e_\omega = e^{i\omega x}$ is continuous, both for Baumann's method ($\sigma = 1, \mu = 0$), and for the symmetric DG-method without penalty ($\sigma = -1, \mu = 0$) and with interior penalty ($\sigma = -1, \mu = \nu/h$), the absolute value of the truncation error is

$$|\tau e_\omega| = \begin{bmatrix} \frac{1}{6}h^2\omega^3 + O(h^3\omega^4) \\ \frac{1}{6}h^2\omega^3 + O(h^3\omega^4) \end{bmatrix}. \tag{3.10}$$

However, from the previous section we know that only the IP DG-method is stable and definite, provided we choose $\nu \geq 1$. So, for that method we can derive the discrete convergence from

$$L_h^{-1}\tau_h e_\omega = \widehat{L_h}^{-1}(\omega)\ \left(\widehat{L_h}(\omega)\widehat{R_h}(\omega) - \widehat{R_h}(\omega)\widehat{L}(\omega)\right)\ e^{i\omega jh}. \tag{3.11}$$

The results are summarized in Table 3.2, distinguishing between penalty parameters $\mu = 1/h$ and $\mu = \nu/h$ with $\nu > 1$.

Table 3.2: The expansion of (3.11) for $h \to 0$, i.e., the order of convergence of pointwise values at the nodal points.

IP, $\mu = 1/h$	IP, $\mu = \nu/h$, $\nu > 1$
$\begin{pmatrix} -\frac{1}{3}h\omega + O(h^2\omega^2) \\ +\frac{1}{3}h\omega + O(h^2\omega^2) \end{pmatrix}$	$\begin{pmatrix} -\frac{1}{12(\nu-1)}h^3\omega^3 + O(h^4\omega^4) \\ +\frac{1}{12(\nu-1)}h^3\omega^3 + O(h^4\omega^4) \end{pmatrix}$

We see that we loose two orders of accuracy if $\mu = 1/h$. The IP DG-method is more accurate for a larger constant ν, but on the other hand, the method becomes less attractive due to the worse condition number of the discrete operator L_h.

3.4 Smoothing analysis and convergence of the two-level algorithm

In this section we consider three block-relaxation methods: Jacobi-, Gauss-Seidel-, and symmetric Gauss-Seidel block relaxations. If we want to apply these relaxations to the unstable operators (Baumann or symmetric DG with $\mu = 0$) with *cell-wise blocks*, then we notice that (i) it is impossible to apply Jacobi relaxation because of the singular diagonal blocks, and (ii) that block GS doesn't converge because all eigenvalues of the iteration operator have absolute value equal to 1. *Point-wise* block relaxation can be used. However, as can be expected, spurious modes remain and no smoothing is achieved.

For the stabilized methods, with $\mu \geq 1/h$, all block relaxations are smoothers, but for $\mu > 1/h$ point-wise block methods perform much better than the cell-wise block equivalents.

Because of this result, later in this section we drop the *cell-wise* relaxation and analyze two-level convergence for each of the three *point-wise* block relaxations. We determine the spectrum of the two-level iteration operator (for different values of μ) and compute for each of the relaxations the optimal damping parameter and the corresponding convergence rate.

Finally, in order to show that fast convergence is not only an asymptotic property after many iterations, but can be expected already in the first steps, we determine the spectral norms for the iteration operators at the end of Section 3.4.2.

3.4.1 Smoothing analysis

Having shown in Chapter 2 for piecewise cubics that the smoothing properties of the damped block-Jacobi (JOR) and the damped block-Gauss Seidel (DGS) are better for point-wise ordering than for cell-wise ordering, we see the same for piecewise linear basis functions. In this section we analyze the different smoothers for the linear case, again distinguishing between the cell-wise (3.4) and point-wise (3.5) approach.

Analogous to the treatment in Section 2.4 we consider the iterative process for the discrete system $A_h x = b$

$$x^{(i+1)} = x^{(i)} - B_h(A_h x^{(i)} - b)\,, \tag{3.12}$$

with B_h an approximate inverse of A_h. Decomposing A_h

$$A_h = L + D + U, \tag{3.13}$$

into a strictly block-lower, a block-diagonal and a strictly block-upper matrix, the different relaxation methods are uniquely described either by B_h or by the amplification matrix $M_h^{\mathrm{REL}} = I_h - B_h A_h$. These operators are shown in Table 2.1 in Section 2.4. Because A_h is a block Toeplitz operator, also the amplification matrix M_h is block Toeplitz. Notice, that the meaning of the block decomposition (3.13) is different for the stencils (3.4) and (3.5). The stencils corresponding to the decomposition (3.13) are given in Table 3.3.

As we emphasized in the previous chapter, the difference between cell-wise and point-wise decomposition is that the eigenvectors $e_{h,\omega}(mh)\mathbf{v}$ of the cell-wise stencil correspond to 2-valued grid functions associated with the cell interiors

Table 3.3: The stencils in the diagonal decomposition

Cellwise		Pointwise
$\frac{1}{h}\begin{bmatrix} -\frac{1}{2} & \frac{1-\sigma}{2} - h\mu \\ 0 & \frac{1}{2}\sigma \end{bmatrix}$	L	$\frac{1}{h}\begin{bmatrix} \frac{1}{2}\sigma & \frac{-1-\sigma}{2} \\ 0 & -\frac{1}{2} \end{bmatrix}$
$\frac{1}{h}\begin{bmatrix} \frac{1+\sigma}{2} + h\mu & \frac{-1-\sigma}{2} \\ \frac{-1-\sigma}{2} & \frac{1+\sigma}{2} + h\mu \end{bmatrix}$	D	$\frac{1}{h}\begin{bmatrix} \frac{1+\sigma}{2} + h\mu & \frac{1-\sigma}{2} - h\mu \\ \frac{1-\sigma}{2} - h\mu & \frac{1+\sigma}{2} + h\mu \end{bmatrix}$
$\frac{1}{h}\begin{bmatrix} \frac{1}{2}\sigma & 0 \\ \frac{1-\sigma}{2} - h\mu & -\frac{1}{2} \end{bmatrix}$	U	$\frac{1}{h}\begin{bmatrix} -\frac{1}{2} & 0 \\ \frac{-1-\sigma}{2} & \frac{1}{2}\sigma \end{bmatrix}$

(in fact independently of the basis chosen), whereas for the point-wise stencil they correspond to the 2-valued grid function associated with *the nodal points* between the cells. This makes the point-wise stencil better suited for analyzing the multi-grid algorithm. Using (2.19) we find the Fourier transform of the basic Toeplitz operators: $\widehat{L}(\omega) = L\, e^{-i\omega h}$, $\widehat{D}(\omega) = D$, $\widehat{U}(\omega) = U\, e^{i\omega h}$. This yields the Fourier transform for the amplification operators for JOR, DGS and SGS:

$$\begin{aligned}
\widehat{M^{REL}_{JOR}} &= \widehat{D}^{-1}\left((1-\alpha)\,\widehat{D} - \alpha\left(\widehat{L}+\widehat{U}\right)\right), \\
\widehat{M^{REL}_{DGS_L}} &= \left(\widehat{D}+\widehat{L}\right)^{-1}\left((1-\alpha)\left(\widehat{D}+\widehat{L}\right) - \alpha\,\widehat{U}\right), \\
\widehat{M^{REL}_{DGS_U}} &= \left(\widehat{D}+\widehat{U}\right)^{-1}\left((1-\alpha)\left(\widehat{D}+\widehat{U}\right) - \alpha\,\widehat{L}\right), \\
\widehat{M^{REL}_{SGS}} &= \widehat{M^{REL}_{DGS_L}}\,\widehat{M^{REL}_{DGS_U}}\,.
\end{aligned}$$

As shown in Section 2.3.2, we find, in view of (2.21), the eigenvalues of M_h^{REL} by computing the eigenvalues of $\widehat{M_h^{REL}}(\omega)$ for $\omega \in \mathbb{T}_h$. The eigenvalues corresponding with the high frequencies ($|\omega| > \pi/2h$), that determine the smoothing properties of the relaxation, are found as $\widehat{M_h^{REL}}(\omega)$ for $\omega \in \mathbb{T}_h \setminus \mathbb{T}_{2h}$. The spectra for the three different smoothers, applied on the DG method of Baumann ($\sigma = 1$, $\mu = 0$), the symmetric DG-method ($\sigma = -1$, $\mu = 0$) and the IP DG-method ($\sigma = -1$, $\mu = \nu/h$) are shown in the Figures 3.2–3.5 respectively.

The IP DG-method is stable for penalty parameters $\mu = \nu/h$, $\nu \geq 1$, which is reflected in the fact that the only undamped mode is the constant (eigen) function. In the Figures 3.2, 3.3 and 3.5 we see that the Baumann and the

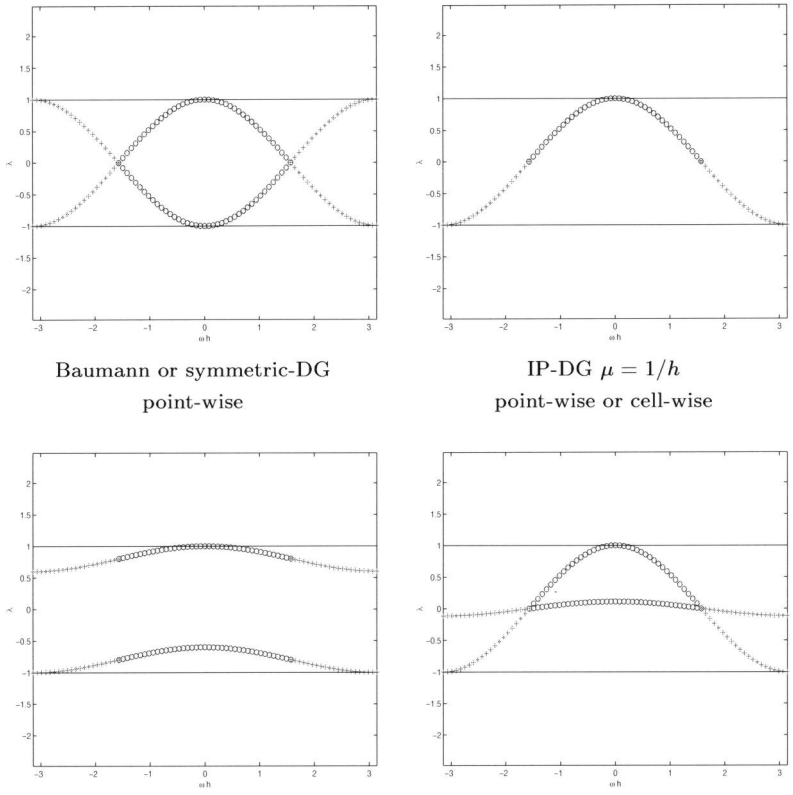

Baumann or symmetric-DG
point-wise

IP-DG $\mu = 1/h$
point-wise or cell-wise

IP-DG $\mu = 5/h$
cell-wise

IP-DG $\mu = 5/h$
point-wise

$\circ : \omega_{low} \in [-\pi/2h, \pi/2h], \quad + : \omega_{high} \in [-\pi/h, -\pi/2h] \cup [\pi/2h, \pi/h]$

Figure 3.2: Eigenvalue spectra of $\widehat{M_{JOR}^{\mathrm{REL}}}(\omega)$.

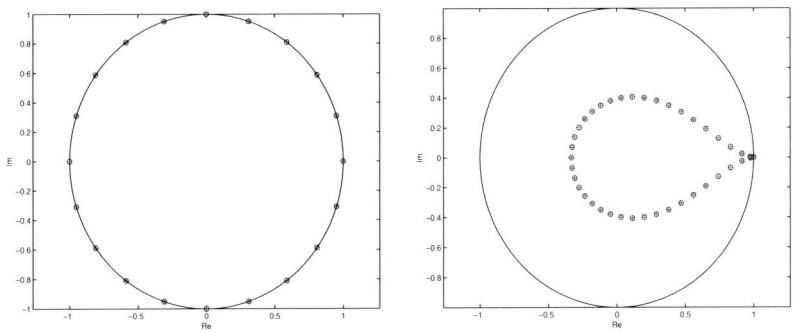

Baumann or symmetric-DG cell-wise

Baumann or symmetric-DG point-wise

$\circ : \omega_{low} \in [-\pi/2h, \pi/2h], \quad + : \omega_{high} \in [-\pi/h, -\pi/2h] \cup [\pi/2h, \pi/h]$

Figure 3.3: Eigenvalue spectra of $\widehat{M^{\mathrm{REL}}_{DGS}}(\omega)$, without damping ($\alpha = 1$) relative to unit circle, for the Baumann and the symmetric-DG.

symmetric DG method (both with $\mu = 0$) show their instability by not damping the highest frequencies $|\omega| \approx \pi/h$. The high frequencies appear to be handled similarly as the low frequencies. We see that the IP-DG methods allow smoothing by the various relaxation methods, and that (the case $\mu = 1/h$ excluded) the point-wise relaxations are better than the cell-wise relaxations (high frequencies are better damped).

In Table 3.4 we summarize the damping of the high-frequencies and we show the corresponding optimal damping factors, α, and smoothing factors for the damped relaxation methods in point-wise setting. We conclude that the pointwise block-relaxation methods are excellent smoothers. This brings us to focus more on their behavior in a multigrid algorithm in the next section.

3.4.2 The two-level analysis

Now we study the two-level operator for the IP DG-method with three choices of μ, viz. $\mu = 1/h$, $\mu = 2/h$ and $\mu = 5/h$, and we will compute optimal damping parameters for the smoothers JOR, DGS and SGS in combination with the coarse-grid correction, for the different choices of the parameter μ.

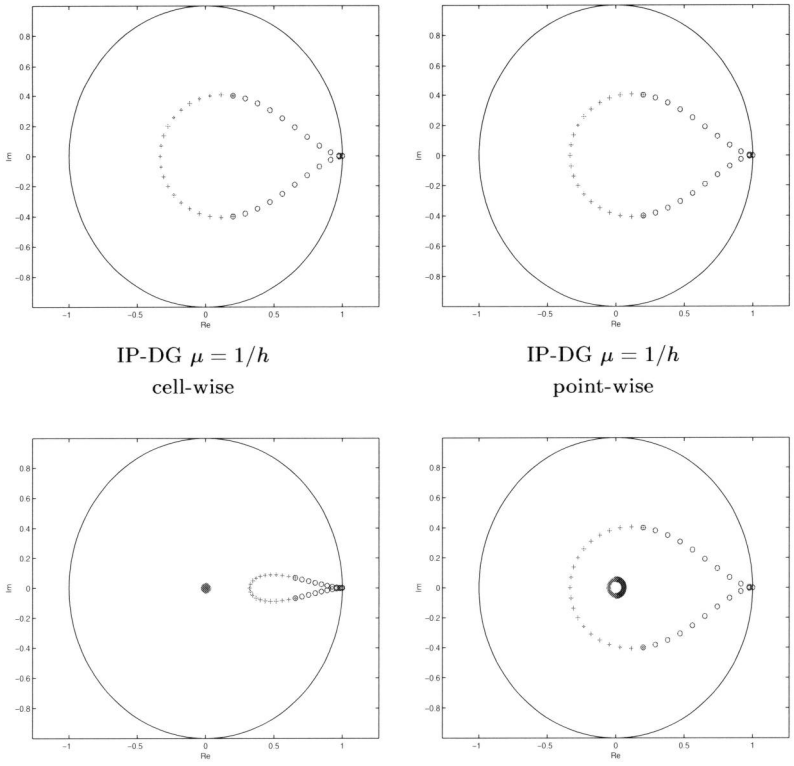

IP-DG $\mu = 1/h$ cell-wise

IP-DG $\mu = 1/h$ point-wise

IP-DG $\mu = 5/h$ cell-wise

IP-DG $\mu = 5/h$ point-wise

$\circ : \omega_{low} \in [-\pi/2h, \pi/2h], \quad + : \omega_{high} \in [-\pi/h, -\pi/2h] \cup [\pi/2h, \pi/h]$

Figure 3.4: Eigenvalue spectra of $\widehat{M_{DGS}^{\mathrm{REL}}}(\omega)$, without damping ($\alpha = 1$) relative to unit circle, for the IP-DG.

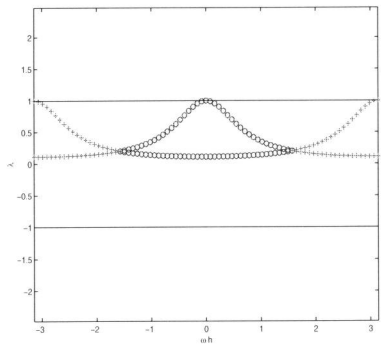

Baumann or symmetric-DG
point-wise

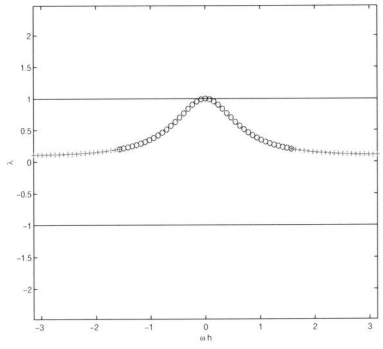

IP-DG $\mu = 1/h$
point- or cell-wise

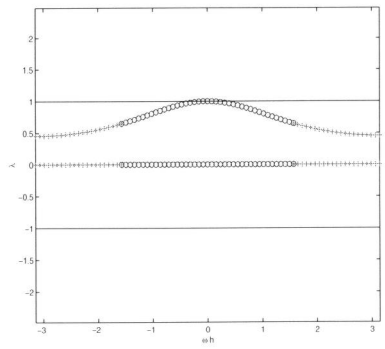

IP-DG $\mu = 5/h$
cell-wise

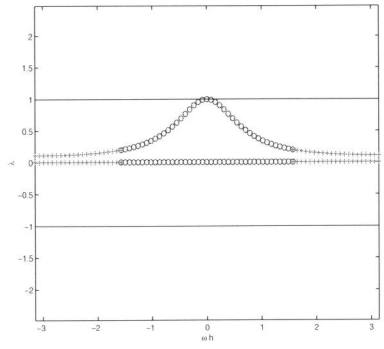

IP-DG $\mu = 5/h$
point-wise

$\circ : \omega_{low} \in [-\pi/2h, \pi/2h], \quad + : \omega_{high} \in [-\pi/h, -\pi/2h] \cup [\pi/2h, \pi/h]$

Figure 3.5: Eigenvalue spectra of $\widehat{M_{SGS}^{\mathrm{REL}}}(\omega)$.

Table 3.4: Smoothing factors (sf $= \max_{\pi/2h \le |\omega| \le \pi/h} |\lambda(\omega)|$) for the undamped (top) and the damped (bottom) relaxation methods. The damped relaxations are shown only for their point-wise ordered versions, and the damping factor (α) is shown.

$\max_\omega \lvert\lambda(\omega)\rvert$	JOR		DGS		SDGS	
$\pi/2h \le \lvert\omega\rvert \le \pi/h$	cell	point	cell	point	cell	point
Baumann	–	1.0	1.0	1.0	1.0	1.0
symmetric DG	–	1.0	1.0	1.0	1.0	1.0
IP $\mu = 1/h$	1.0	1.0	0.447	0.447	0.200	0.200
IP $\mu = 5/h$	1.0	1.0	0.659	0.447	0.647	0.200

IP point-wise	α	sf	α	sf	α	sf
$\mu = 2/h$	0.667	0.333	1.0	0.447	1.0	0.200
$\mu = 5/h$	0.667	0.333	1.0	0.447	1.0	0.200

The amplification operator of the two-level algorithm for the error is given by

$$\begin{aligned} M_h^{TLA} &= \left(M_h^{\mathrm{REL}}\right)^{\nu_2} M_h^{\mathrm{CGC}} \left(M_h^{\mathrm{REL}}\right)^{\nu_1} \\ &= \left(M_h^{\mathrm{REL}}\right)^{\nu_2} \left(I - P_{hH} L_H^{-1} \overline{R}_{Hh} L_h\right) \left(M_h^{\mathrm{REL}}\right)^{\nu_1}, \end{aligned}$$

where ν_1 and ν_2 are the number of pre- (post-) relaxation sweeps respectively. M_h^{CGC} is the amplification operator of the coarse grid correction. The amplification operator for the residue is

$$\begin{aligned} \overline{M}_h^{TLA} &= (\overline{M}_h^{REL})^{\nu_2} \overline{M}_h^{CGC} (\overline{M}_h^{REL})^{\nu_1} \\ &= \left(L_h M_h^{\mathrm{REL}} L_h^{-1}\right)^{\nu_2} L_h M_h^{\mathrm{CGC}} L_h^{-1} \left(L_h M_h^{\mathrm{REL}} L_h^{-1}\right)^{\nu_1}. \end{aligned}$$

From the analysis in Section 2.3.5, we find that the Fourier transform of the coarse grid correction M_h^{CGC} is

$$\widehat{M_h^{\mathrm{CGC}}}(\omega) = \left(\widehat{I_h} - \widehat{P_{hH}} \widehat{L_H^{-1}} \widehat{\overline{R}_{Hh}} \widehat{L_h}\right)(\omega) = \begin{pmatrix} 1 & 0 \\ 0 & 1 \end{pmatrix} -$$

$$\begin{pmatrix} \widehat{P_h}(\omega) \\ \widehat{P_h}(\omega + \pi/h) \end{pmatrix} (\widehat{L_H}(\omega))^{-1} \begin{pmatrix} \widehat{\overline{R}_h}(\omega) & \widehat{\overline{R}_h}(\omega + \pi/h) \end{pmatrix} \begin{pmatrix} \widehat{L_h}(\omega) & 0 \\ 0 & \widehat{L_h}(\omega + \pi/h) \end{pmatrix}.$$

For our piecewise linear basis $\phi_{i,e}$, the interpolation $P_{hH} : S_H \to S_h$ so that $(P_{hH} u_H)(x) = u_H(x)$ for all $x \in \mathbb{R} \setminus \mathbb{Z}_h$, is given by the stencil (for pointwise ordering):

$$P_{hH} \approx \left[\begin{array}{cc|cc|cc} 0 & \frac{1}{2} & 1 & 0 & \frac{1}{2} & 0 \\ 0 & \frac{1}{2} & 0 & 1 & \frac{1}{2} & 0 \end{array}\right].$$

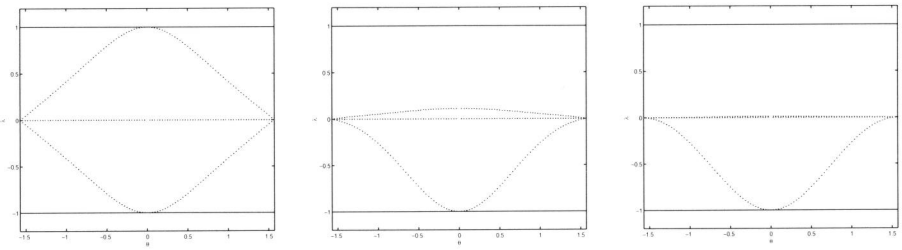

IP-DG $\mu = 1/h$ IP-DG $\mu = 2/h$ IP-DG $\mu = 5/h$

Figure 3.6: Eigenvalue spectra of $\mathbf{FT}(M_h^{CGC} M_{JOR}^{REL})(\omega) = \mathbf{FT}(\overline{M}_{JOR}^{REL} \overline{M}_h^{CGC})(\omega)$, without damping ($\alpha = 1$).

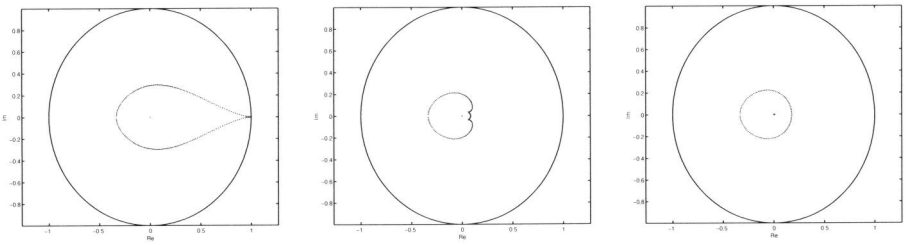

IP-DG $\mu = 1/h$ IP-DG $\mu = 2/h$ IP-DG $\mu = 5/h$

Figure 3.7: Eigenvalue spectra of $\mathbf{FT}(M_h^{CGC} M_{DGS}^{REL})(\omega) = \mathbf{FT}(\overline{M}_{DGS}^{REL} \overline{M}_h^{CGC})(\omega)$, without damping ($\alpha = 1$).

Because the DG discretization is of Galerkin type with equal test and trial space, the restriction of the residue, $\overline{R}_{Hh}$, is the adjoint of the prolongation, $\overline{R}_{Hh} = (P_{hH})^T$. For the different penalty parameters μ and different smoothers JOR, DGS and SGS, the eigenvalue spectra of the two-level operator for the IP DG-method are computed from (2.21) and shown in the Figures 3.6–3.8.

We see that none of the methods converge for $\mu = 1/h$. However, for $\mu = 2/h$ or $\mu = 5/h$ all pointwise relaxations are excellent smoothers and we see fast convergence for the two-level algorithm.

Having found the spectra and having computed the largest and smallest real eigenvalue $\lambda_{\min}$ and $\lambda_{\max}$ we can determine the optimal damping parameter and the corresponding convergence rate for the damped relaxation method. The

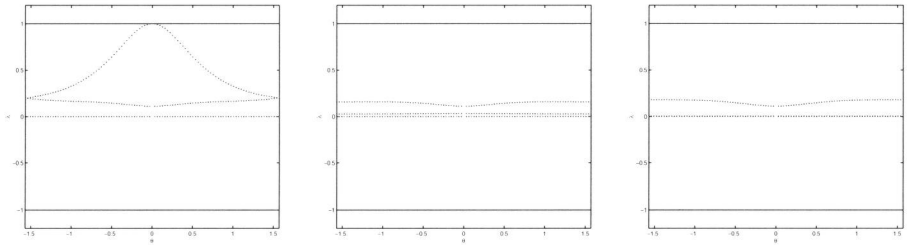

IP-DG $\mu = 1/h$ IP-DG $\mu = 2/h$ IP-DG $\mu = 5/h$

Figure 3.8: Eigenvalue spectra of two-level iteration with symmetric block-GS relaxation: $\mathbf{FT}(M_{DGS_U}^{REL} M_h^{CGC} M_{DGS_L}^{REL})(\omega) = \mathbf{FT}(\overline{M}_{DGS_L}^{REL} \overline{M}_h^{CGC} \overline{M}_{DGS_U}^{REL})(\omega)$, without damping ($\alpha = 1$).

parameter, minimizing the spectral radius $\rho(M_h^{CGC} M_h^{REL})$ is given by:

$$\alpha_{opt} = \frac{2}{2 - (\lambda_{\min} + \lambda_{\max})},$$

Seeing that the case $\nu = 1$ will not show h-independent convergence, we show in the Tables 3.5 and 3.6 the damping parameters and the convergence rates for the cases $\nu = 2$ and $\nu = 5$.

Table 3.5: Damping parameters for the two-level operators $\rho(M_h^{CGC} M_h^{REL}) = \rho(\overline{M}_h^{REL} \overline{M}_h^{CGC})$.

α_{opt}	IP-DG $\mu = 2/h$	IP-DG $\mu = 5/h$
$M_h^{CGC} M_{JOR}^{REL}$	0.692	0.669
$M_h^{CGC} M_{DGS}^{REL}$	0.897	0.928

In order not only to know the asymptotic convergence rate but also the guaranteed converge behavior after one or two iteration sweeps, we also compute the spectral norms $\left\|M_h^{TLA}\right\|$, $\left\|\overline{M}_h^{TLA}\right\|$, $\left\|\left(\overline{M}_h^{TLA}\right)^2\right\|$. The results are shown in the Tables 3.7 – 3.9. We see that the two-level algorithm (and hence the multi-level algorithm) converges with a rate of about 0.2 – 0.4 per iteration step and that reduction of the error and the residual is guaranteed, starting from the 2nd iteration step.

Table 3.6: Spectral radii $\rho(M_h^{CGC} M_h^{REL}) = \rho(\overline{M}_h^{REL} \overline{M}_h^{CGC})$ for damping parameters in Table 3.5.

$\rho(M_h^{CGC} M_h^{REL})$	IP-DG $\mu = 2/h$	IP-DG $\mu = 5/h$
$M_h^{CGC} M_{JOR}^{REL}$	0.385	0.339
$M_h^{CGC} M_{DGS}^{REL}$	0.217	0.238
$M_{DGS_U}^{REL} M_h^{CGC} M_{DGS_L}^{REL}$	0.156	0.180

Table 3.7: The spectral norm ($\sigma_{\max}$) after 1 iteration for the error with optimal damping.

	$M_h^{CGC} M_{JOR}^{REL}$	$M_h^{CGC} M_{DGS}^{REL}$	$M_{DGS_U}^{REL} M_h^{CGC} M_{DGS_L}^{REL}$
IP-DG ($\mu = 2/h$)	0.543	0.392	0.207
IP-DG ($\mu = 5/h$)	0.478	0.417	0.250

Table 3.8: The spectral norm ($\sigma_{\max}$) after 1 iteration for the residue with optimal damping.

	$\overline{M}_h^{CGC} \overline{M}_{JOR}^{REL}$	$\overline{M}_h^{CGC} \overline{M}_{DGS}^{REL}$	$\overline{M}_{DGS_U}^{REL} \overline{M}_h^{CGC} \overline{M}_{DGS_L}^{REL}$
IP-DG ($\mu = 2/h$)	1.071	1.019	0.340
IP-DG ($\mu = 5/h$)	1.056	1.028	0.343

Table 3.9: The spectral norm ($\sigma_{\max}$) after 2 iterations for the residue with optimal damping.

	$\overline{M}_h^{CGC} \overline{M}_{JOR}^{REL}$	$\overline{M}_h^{CGC} \overline{M}_{DGS}^{REL}$	$\overline{M}_{DGS_U}^{REL} \overline{M}_h^{CGC} \overline{M}_{DGS_L}^{REL}$
IP-DG ($\mu = 2/h$)	0.411	0.200	0.030
IP-DG ($\mu = 5/h$)	0.357	0.244	0.035

3.5 Numerical results

In this section we check by numerical experiments the spectral radii of the two-level operators with damped Jacobi-, $M_h^{CGC} M_{JOR}^{REL}$, Gauss-Seidel-, $M_h^{CGC} M_{DGS}^{REL}$, and symmetric Gauss-Seidel relaxation, $M_{DGS_U}^{REL} M_h^{CGC} M_{DGS_L}^{REL}$, for the IP-DG method with the penalty parameters $\mu = 2/h$ and $\mu = 5/h$. For that purpose, we consider the inhomogeneous Poisson equation

$$-u_{xx} = \frac{e^{x/\epsilon}}{\epsilon^2(\epsilon^{1/\epsilon} - 1)}, \qquad \text{with } u(0) = 0,\ u(1) = 0,\ \epsilon = 1/64,$$

which has a sharp boundary layer type solution. We set the meshwidth to $h = 2^{-6}$ and we take for our initial approximation the grid-function $u_h^0 = u_{h,\mathrm{PRE}}^0 = \sin(1/2\pi j)$. We apply a pre-relaxation sweep

$$u_{h,\mathrm{PRE}}^{i+1} = u_{h,\mathrm{PRE}}^{i} + B_h \left(f_h - L_h u_{h,\mathrm{PRE}}^{i}\right),$$

with B_h the approximate inverse of L_h as given in Table 2.1 in Section 2.4, and the coarse grid correction

$$u_{h,\mathrm{POST}}^{0} = u_{h,\mathrm{PRE}}^{\nu_1} + P_{hH} L_H^{-1} \overline{R}_{Hh} (f_h - L_h u_{h,\mathrm{PRE}}^{\nu_1}).$$

In case of symmetric damped Gauss-Seidel we apply an additional post relaxation sweep

$$u_{h,\mathrm{POST}}^{i+1} = u_{h,\mathrm{POST}}^{i} + B_h^T (f_h - L_h u_{h,\mathrm{POST}}^{i}).$$

To be consistent with the Fourier analysis we measure the residue in the 2-norm

$$\|d_h\|_2 = \|f_h - L_h u_h\|_2 = \left(\sum_{e=1}^{64} \sum_{j=1}^{2} d_{he,j}^2 \right)^{\frac{1}{2}}.$$

The convergence of the residue is shown in Figure 3.9. The convergence factors as observed, are given in Table 3.10.

Both for $\mu = 2/h$ and for $\mu = 5/h$ we see convergence, starting from the first iteration sweep. Furthermore, for the IP-DG method with $\mu = 5/h$ the observed convergence factors correspond very well to the spectral radii shown in Table 3.6. Only for the IP-DG method with $\mu = 2/h$ the spectral radii of the Fourier analysis seem too optimistic compared with the convergence factors in Table 3.10. This is clearly caused by a boundary effect (as can be seen if we study the slowest converging component, which is exponentially growing towards the boundary). This is related to the fact that, as μ approaches $1/h$, the two-level algorithm becomes singular. This singularity effect disappears for larger values of $\nu = h\mu$.

Table 3.10: Numerically obtained convergence factors corresponding with $\rho(M_h^{CGC} M_h^{REL}) = \rho(\overline{M}_h^{REL} \overline{M}_h^{CGC})$ for damping parameters as in Table 3.5.

$\rho(M_h^{CGC} M_h^{REL})$	IP-DG $\mu = 2/h$	IP-DG $\mu = 5/h$
$M_h^{CGC} M_{JOR}^{REL}$	0.48	0.34
$M_h^{CGC} M_{DGS}^{REL}$	0.24	0.23
$M_{DGS_U}^{REL} M_h^{CGC} M_{DGS_L}^{REL}$	0.17	0.18

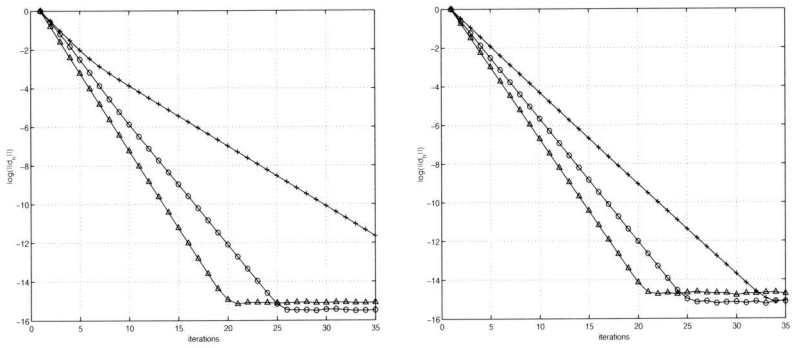

IP-DG $\mu = 2/h$ IP-DG $\mu = 5/h$

+: JOR; ○: DGS; △: SGS.

Figure 3.9: $\log(||d_h||_2)$ as function of iterations for the two-level iteration operator on the error.

3.6 Conclusion

In the previous chapter we have shown that multigrid iteration can be quite efficient for the solution of elliptic equations that are discretized by higher-order discontinuous Galerkin discretization, provided that a block (Jacobi or Gauss-Seidel) relaxation is used, based on a pointwise (instead of a cell-wise) ordering.

In this Chapter we have studied the solution of the discrete equations for the discontinuous Galerkin method with piecewise linear test- and trial functions. It is well-known [2, 43] that in this case the DG method requires an interior penalty (IP) parameter $\mu > 1$ in order to guarantee that the discrete equations are stable.

We show that in this case, again, a multigrid method can be used to solve

the corresponding discrete equations if block relaxation is used, based on the pointwise ordering. If a suitable IP parameter $\mu > 1$ is chosen, the block Jacobi or (symmetric) block Gauss-Seidel relaxation have a good smoothing property.

Using Fourier analysis, for feasible μ-values, we compute optimal damping parameters for the relaxation methods and the corresponding two-level convergence rates. In view of the hierarchical structure of the DG multigrid-algorithm proposed in the previous chapter, the present results can also be used to justify the use of a low order discretization in the hierarchical scale of methods, if needed.

Chapter 4

Two-level analysis for higher dimensional DG discretization

Summary

In this chapter we study the convergence of a multigrid method for the solution of a two-dimensional linear second order elliptic equation, discretized by discontinuous Galerkin (DG) methods. For the Baumann-Oden and for the symmetric DG method, we give a detailed analysis of the convergence for cell- and point-wise block-relaxation strategies.

We show that, for a suitably constructed two-dimensional polynomial basis, point-wise block partitioning gives much better results than the classical cell-wise partitioning.

Independent of the mesh size, for Poisson's equation, simple MG cycles with block-Gauss-Seidel or symmetric block-Gauss-Seidel smoothing, yield a convergence rate of 0.4 - 0.6 per iteration sweep for both DG-methods studied.

4.1 Introduction

In this chapter we describe and analyze a multigrid method for the solution of discrete systems arising from discontinuous Galerkin (DG) discretization. Since

recent work by Baumann-Oden [37], discontinuous Galerkin discretization has become more popular for discretization of elliptic problems, in particular for application in *hp*-adaptive solvers.

Originally, DG methods, based on constrained optimization [13, 26, 36], suffered from stability problems inherent in the saddle-point character of the Lagrange multiplier formulation. In [2, 50] these problems were overcome by introducing a penalization of the discontinuity that stabilizes the scheme. The method by Baumann-Oden modifies the saddle-point character of the problem and results in a definite (but asymmetric) discretization for the Poisson problem. Because the diffusion part is often combined with a convection term, the asymmetry is generally not considered as a disadvantage in practice. For a comprehensive survey of recent variants of DG methods and their properties we refer to [3].

In the present analysis we restrict ourselves to the Baumann-Oden and the symmetric DG method. Looking for an optimal efficient solution procedure that can also be applied conveniently in an *hp*-adaptive context, we are led to the solution of DG discretization by a multigrid (MG) technique. To our knowledge, the first paper on multigrid in combination with DG was [15], who give an abstract convergence theorem for the symmetric case along the lines of [7].

In [4] the use of MG with DG for application in groundwater flow by means of ILU-decomposition is mentioned. However, no analysis was given.

In the present chapter we analyze not only the symmetric but also the Baumann-Oden discretization for the two-dimensional Poisson equation and we derive two-level convergence rates by local mode Fourier analysis. An analysis for the one-dimensional case was given in [23, 24]. In this chapter we show that multigrid can be a an $\mathcal{O}(N)$ solver indeed, provided that the right block-relaxation methods are used. The block-relaxation should *not* be based on grouping the degrees of freedom according to their cells, but –for a suitably selected polynomial base– on a grouping of degrees of freedom that can be associated with cell vertices. Both for the Baumann-Oden and for the symmetric DG method, this strategy leads to an efficient MG method.

For the treatment of solution methods for systems arising from DG discretization of arbitrary high order, we consider the fourth-order approximation the generic case, where the solution is approximated by cubics. With tensor-product piecewise cubics on each rectangular cell, the trace of a function and its normal derivative can be approximated sufficiently well on each cell boundary segment to determine the fourth order discrete DG operator. All additional accuracy can be considered as corrections on a hierarchical basis, which can

be dealt with by a combination of static condensation and defect correction iteration. This is the motivation why we study here only the cubic case, and why we introduce the basis (4.3), or a variant (see also Section 2.2.2) with the Jacobi polynomials $P_n^{(4,4)}(x)$, that satisfy an L_2-orthogonality condition on the cell interior [1, p.774].

The outline of this chapter is as follows. Starting with the variational DG form (2.3), introduced in Chapter 2, we describe the discretization stencils that occur for the discretization of the two-dimensional Poisson equation. As a preparation for the MG-method we also describe the stencils for the grid-transfer-operators. In Section 4.3 we treat the Fourier analysis tools used for the systems of grid functions that correspond with DG discretization with piecewise cubics. In Section 4.4 we first treat the smoothing analysis. We show that block-relaxation is stable on a reduced basis of cubic polynomials, whereas the straightforward tensor product representation is *not*. In Section 4.5 we treat the two-level analysis and we compute optimal damping parameters for the smoothing, and the spectral radii for the two-level methods, with block-Jacobi, block-Gauss-Seidel or symmetric block-Gauss-Seidel relaxation.

In the last section we show by a numerical example that the actual convergence rates correspond very well with those derived by Fourier analysis. Both for the Baumann-Oden and for the symmetric DG method, this strategy leads to an h-independent convergence rate of at least 0.4 - 0.6 per two-level cycle.

4.2 The two-dimensional DG discretization

4.2.1 The discrete formulation in tensor product form

In order to describe the two-dimensional discretization methods studied in this chapter, we return to the special weak formulation (2.3) for the Poisson equation (2.1) defined on the unit cube Ω: Find $u \in H^1(\Omega_h)$ such that

$$B(u,v) = L(v) \quad \forall v \in H^1(\Omega_h), \tag{4.1}$$

where the bilinear form $B(u,v)$ is defined by (2.4).

The next step is to define the finite dimensional test and trial function spaces, $S_h, V_h \subset H^1(\Omega_h)$ in order to derive a discrete version of the weak formulation (4.1). To simplify the analysis we restrict ourselves to the two-dimensional Poisson's equation on a regular uniform partitioning, as given by (2.2). The treatment of the three-dimensional equation is analogous, but less convenient considering the notation.

Taking the same space for the test and trial functions ($S_h = V_h$), we have: find $u_h \in S_h$ such that,

$$B(u_h, v_h) = L(v_h), \qquad \forall v_h \in S_h\,. \tag{4.2}$$

We take for the finite dimensional trial and test space $S_h \subset H^1(\Omega_h)$ the space of piecewise polynomials of degree less than $2p$ in each of the coordinate directions on the partitioning Ω_h:

$$S_h = \left\{\phi_{i,e} \in P^{2p-1}(\Omega_e), \quad \Omega_e \in \Omega_h\right\}\,,$$

and, as motivated in Section 2.2.2, we further provide S_h with a tensor product basis of polynomials, defined on the unit interval by

$$\phi_{2n+k}(t) = t^{n+k}(1-t)^{n+1-k}, \quad n = 0, 1, \cdots, p-1;\ k = 0, 1. \tag{4.3}$$

Thus, on the unit square, $\hat{\Omega} \subset \mathbb{R}^2$, we use a basis of tensor-product polynomials based on (4.3). A basis for $P^{2p-1}(\Omega_e)$ is obtained by the usual affine mapping $\hat{\Omega} \to \Omega_e$. Hence, on a regular rectangular grid Ω_h with cells Ω_e of size $h_x \times h_y$ the approximate solution reads:

$$\begin{aligned} u_h(x,y) &= \sum_{1\le e\le N} \sum_{0\le i,j<2p} c_{e,i,j}\, \phi_i(\frac{x-x_e}{h_x})\phi_j(\frac{y-y_e}{h_y}) \\ &\equiv \sum_{1\le e\le N} \sum_{0\le i,j<2p} c_{e,i,j}\, \phi_{e,i}(\xi)\phi_{e,j}(\eta). \end{aligned} \tag{4.4}$$

After substitution of (4.4) into (4.2), and because of the tensor product structure of our basis, we can express the discrete system $L_h u_h = f_h$ in explicit form as:

$$\sum_{1\le e\le N}\sum_{0\le i,j<2p} c_{e,i,j}\left\{\left(\frac{1}{h_x}\int_0^1 \phi'_{e,i}\phi'_{e,\tilde{i}}d\xi - \frac{1}{h_x}\langle\nabla\phi_{e,i}\rangle\cdot\left[\phi_{e,\tilde{i}}\right]|_{\Gamma_{\mathrm{Dint}}}\right.\right. \tag{4.5}$$
$$\left.+\sigma\frac{1}{h_x}[\phi_{e,i}]\cdot\left\langle\nabla\phi_{e,\tilde{i}}\right\rangle|_{\Gamma_{\mathrm{Dint}}} + \mu[\phi_{e,i}]\cdot\left[\phi_{e,\tilde{i}}\right]|_{\Gamma_{\mathrm{Dint}}}\right) h_y\int_0^1 \phi_{e,j}\phi_{e,\tilde{j}}d\eta$$
$$+h_x\int_0^1 \phi_{e,i}\phi_{e,\tilde{i}}d\xi\left(\frac{1}{h_y}\int_0^1 \phi'_{e,j}\phi'_{e,\tilde{j}}d\eta - \frac{1}{h_y}\langle\nabla\phi_{e,j}\rangle\cdot\left[\phi_{e,\tilde{j}}\right]|_{\Gamma_{\mathrm{Dint}}}\right.$$
$$\left.\left.+\sigma\frac{1}{h_y}[\phi_{e,j}]\cdot\left\langle\nabla\phi_{e,\tilde{j}}\right\rangle|_{\Gamma_{\mathrm{Dint}}} +\mu[\phi_{e,j}]\cdot\left[\phi_{e,\tilde{j}}\right]|_{\Gamma_{\mathrm{Dint}}}\right)\right\}$$
$$\sum_{1\le e\le N}\sum_{0\le i,j<2p}\int_{\Omega_e} f(x,y)\phi_{\tilde{i}}(\frac{x-x_e}{h_x})\phi_{\tilde{j}}(\frac{y-y_e}{h_y})d\Omega_e$$
$$+\sigma\int_{\Gamma_D}\left\langle\nabla\left(\phi_{\tilde{i}}(\frac{x-x_e}{h_x})\phi_{\tilde{j}}(\frac{y-y_e}{h_y})\right)\right\rangle\cdot[u_0]\,ds$$
$$+\mu\int_{\Gamma_D}[u_0]\cdot\left[\phi_{\tilde{i}}(\frac{x-x_e}{h_x})\phi_{\tilde{j}}(\frac{y-y_e}{h_y})\right]ds + \int_{\Gamma_N} g\phi_{\tilde{i}}(\frac{x-x_e}{h_x})\phi_{\tilde{j}}(\frac{y-y_e}{h_y})ds,$$
$$\forall\tilde{i},\tilde{j}.$$

We see that the left-hand side of (4.5) is an extension of a one-dimensional stiffness and mass matrix. If we define

$$\mathbf{M} = (\mathbf{M}_{e,i,\tilde{i}}) = h_x\int_0^1 \phi_{e,i}\phi_{e,\tilde{i}}d\xi,$$

and

$$\mathbf{S} = (\mathbf{S}_{e,i,\tilde{i}}) = \frac{1}{h_x}\int_0^1 \phi'_{e,i}\phi'_{e,\tilde{i}}d\xi - \frac{1}{h_x}\langle\nabla\phi_{e,i}\rangle\cdot\left[\phi_{e,\tilde{i}}\right]|_{\Gamma_{\mathrm{Dint}}}$$
$$+\sigma\frac{1}{h_x}[\phi_{e,i}]\cdot\left\langle\nabla\phi_{e,\tilde{i}}\right\rangle|_{\Gamma_{\mathrm{Dint}}} + \mu[\phi_{e,i}]\cdot\left[\phi_{e,\tilde{i}}\right]|_{\Gamma_{\mathrm{Dint}}},$$

we may write:

$$L_h u_h = \sum_{1\le e\le N}\sum_{0\le i,j<2p} c_{e,i,j}\left(\mathbf{S}_{e,i,\tilde{i}}\mathbf{M}_{e,j,\tilde{j}} + \mathbf{M}_{e,i,\tilde{i}}\mathbf{S}_{e,j,\tilde{j}}\right), \qquad \forall\tilde{i},\tilde{j}.$$

Or briefly, in tensor product notation we have:

$$L_h u_h = \sum_{1\le e\le N}\sum_{0\le i,j<2p} c_{e,i,j}\left(\mathbf{S}\otimes\mathbf{M} + \mathbf{M}\otimes\mathbf{S}\right)_{e,i,\tilde{i},j,\tilde{j}}, \qquad \forall\tilde{i},\tilde{j}. \tag{4.6}$$

In our one-dimensional analysis [23, 24] we explained that if we associate the first four polynomials of basis (4.3) with function values and corrections on derivatives at the cell corners, the discrete system can be partitioned in *point-wise blocks*, each of which can be associated with a nodal point of a cell. We showed by Fourier analysis, that the relaxation methods (damped block-Gauss-Seidel (DGS) and damped block Jacobi (JOR)), based on that partitioning, show better smoothing properties than the classical cell-wise partitioning. We further emphasized that higher order polynomials can be introduced as genuine bubble functions. They correspond to interior cell corrections. So, if we are interested in fast convergence of the discrete system the coefficients of these bubble functions are of less importance. They can be eliminated by static condensation or dealt with by defect correction. So, in this two-dimensional analysis, we again restrict ourselves to the case $p = 2$ and we distinguish between cell-wise and point-wise stencils of the discrete system.

4.2.2 Implementational details

A slightly better alternative basis than (4.3), but still satisfying our purposes, is defined on [-1,+1] as follows. We take the first four basis functions as in (4.3), i.e., the functions $(x-1)^p(x+1)^q$, with $(p,q) = (1,0),\ (0,1),\ (2,1),\ (1,2)$, but for the higher order contributions we take $(x-1)^2(x+1)^2 P_n^{(4,4)}(x)$, with $n = 0, 1, \cdots$, and $P_n^{(4,4)}$ the Jacobi polynomials (see [1, p.774]). The first four basis functions are essential for our purpose, because they represent function values and first derivatives at the cell boundaries. The higher order polynomials, constructed by means of the Jacobi polynomials, satisfy the useful L_2-orthogonality property. In addition to the orthogonality, this new basis relieves the restriction to odd degree k for $k > 4$.

Notice that for higher order accuracy not *all* tensor product basis functions have to be included. Higher order cross-products of total degree higher than $2p-1$ can be neglected. This gives a significant reduction of computational work, viz., in two dimensions asymptotically a factor 2, in three dimensions a factor 6.

4.2.3 The two-dimensional cell-wise and point-wise stencil

Whereas for the one-dimensional discrete system the point-wise and the cell-wise stencils are both three-point block stencils, this is not the case for the two dimensional discrete system described above. To see this, consider (4.5) and (4.6). If we order the equations and coefficients of the stiffness and mass matrices

cell-wise over the two coordinate directions ($[\phi_{e,0}(.), \phi_{e,2}(.), \phi_{e,3}(.), \phi_{e,1}(.)]$), we have the following stencil contributions (see also (2.10)):

$$\mathbf{S}_L^C = \begin{bmatrix} -\frac{1}{2} & 0 & -\frac{1}{2} & \frac{1-\sigma}{2} - h\mu \\ 0 & 0 & 0 & \frac{1}{2}\sigma \\ 0 & 0 & 0 & 0 \\ 0 & 0 & 0 & \frac{1}{2}\sigma \end{bmatrix}, \quad \mathbf{S}_C^C = \begin{bmatrix} \frac{1+\sigma}{2} + h\mu & \frac{1}{2} & 0 & \frac{-1-\sigma}{2} \\ -\frac{1}{2}\sigma & \frac{2}{15} & \frac{1}{30} & 0 \\ 0 & \frac{1}{30} & \frac{2}{15} & -\frac{1}{2}\sigma \\ \frac{-1-\sigma}{2} & 0 & \frac{1}{2} & \frac{1+\sigma}{2} + h\mu \end{bmatrix},$$

$$\mathbf{S}_R^C = \begin{bmatrix} \frac{1}{2}\sigma & 0 & 0 & 0 \\ 0 & 0 & 0 & 0 \\ \frac{1}{2}\sigma & 0 & 0 & 0 \\ \frac{1-\sigma}{2} - h\mu & -\frac{1}{2} & 0 & -\frac{1}{2} \end{bmatrix}, \quad \mathbf{M}_C^C = \begin{bmatrix} \frac{1}{3} & \frac{1}{20} & \frac{1}{30} & \frac{1}{6} \\ \frac{1}{20} & \frac{1}{105} & \frac{1}{140} & \frac{1}{30} \\ \frac{1}{30} & \frac{1}{140} & \frac{1}{105} & \frac{1}{20} \\ \frac{1}{6} & \frac{1}{30} & \frac{1}{20} & \frac{1}{3} \end{bmatrix},$$

where the superscript 'C' denotes 'cell-wise' and the subscript 'L','C','R', respectively 'left', 'center' and 'right'. If we now, with the notation of (4.6), write:

$$\mathbf{L}_{\cdot\cdot}^C = \left(\mathbf{S}_{\cdot}^C \otimes \mathbf{M}_{\cdot}^C + \mathbf{M}_{\cdot}^C \otimes \mathbf{S}_{\cdot}^C\right)_{i,\tilde{i},j,\tilde{j}}, \quad i,\tilde{i},j,\tilde{j} \in \{1,2,..,4\}, \tag{4.7}$$

the result is a five-points block stencil, with for each block a 16×16 matrix. We denote the stencil by:

$$L_h \approxeq \begin{array}{|c|c|c|} \hline & \mathbf{L}_{CL}^C & \\ \hline \mathbf{L}_{LC}^C & \mathbf{L}_{CC}^C & \mathbf{L}_{RC}^C \\ \hline & \mathbf{L}_{CR}^C & \\ \hline \end{array}. \tag{4.8}$$

Re-ordering the equations and coefficients of the mass and stiffness matrices in a *point-wise* manner (collecting $[\phi_{e-1,3}, \phi_{e-1,1}, \phi_{e,0}, \phi_{e,2}]$) over the two coordinate directions, yields the following stencil contributions (see also (2.11)):

$$\mathbf{S}_L^P = \begin{bmatrix} 0 & 0 & 0 & \frac{1}{30} \\ 0 & \frac{1}{2}\sigma & \frac{-1-\sigma}{2} & 0 \\ 0 & 0 & -\frac{1}{2} & 0 \\ 0 & 0 & 0 & 0 \end{bmatrix}, \quad \mathbf{M}_L^P = \begin{bmatrix} 0 & 0 & \frac{1}{30} & \frac{1}{140} \\ 0 & 0 & \frac{1}{6} & \frac{1}{30} \\ 0 & 0 & 0 & 0 \\ 0 & 0 & 0 & 0 \end{bmatrix},$$

$$\mathbf{S}_C^P = \begin{bmatrix} \frac{2}{15} & -\frac{1}{2}\sigma & \frac{1}{2}\sigma & 0 \\ \frac{1}{2} & \frac{1+\sigma}{2} + h\mu & \frac{1-\sigma}{2} - h\mu & -\frac{1}{2} \\ -\frac{1}{2} & \frac{1-\sigma}{2} - h\mu & \frac{1+\sigma}{2} + h\mu & \frac{1}{2} \\ 0 & \frac{1}{2}\sigma & -\frac{1}{2}\sigma & \frac{2}{15} \end{bmatrix}, \quad \mathbf{M}_C^P = \begin{bmatrix} \frac{1}{105} & \frac{1}{20} & 0 & 0 \\ \frac{1}{20} & \frac{1}{3} & 0 & 0 \\ 0 & 0 & \frac{1}{3} & \frac{1}{20} \\ 0 & 0 & \frac{1}{20} & \frac{1}{105} \end{bmatrix},$$

$$\mathbf{S}_R^P = \begin{bmatrix} 0 & 0 & 0 & 0 \\ 0 & -\frac{1}{2} & 0 & 0 \\ 0 & \frac{-1-\sigma}{2} & \frac{1}{2}\sigma & 0 \\ \frac{1}{30} & 0 & 0 & 0 \end{bmatrix}, \quad \mathbf{M}_R^P = \begin{bmatrix} 0 & 0 & 0 & 0 \\ 0 & 0 & 0 & 0 \\ \frac{1}{30} & \frac{1}{6} & 0 & 0 \\ \frac{1}{140} & \frac{1}{30} & 0 & 0 \end{bmatrix},$$

where the superscript 'P' stands for 'point-wise'. Then evaluation of (4.7) yields the nine-points block stencil:

$$L_h \approxeq \begin{array}{|c|c|c|} \hline \mathbf{L}^P_{LL} & \mathbf{L}^P_{CL} & \mathbf{L}^P_{RL} \\ \hline \mathbf{L}^P_{LC} & \mathbf{L}^P_{CC} & \mathbf{L}^P_{RC} \\ \hline \mathbf{L}^P_{LR} & \mathbf{L}^P_{CR} & \mathbf{L}^P_{RR} \\ \hline \end{array} . \tag{4.9}$$

Every block is a 16×16 matrix containing information about the 4 cells around the point in the computational domain. The cell-wise and point-wise stencils represent the same discretization. The different ordering, only results in different relaxation behavior of the block-relaxation procedures.

4.2.4 Restrictions and Prolongations

As we are interested in multigrid solution methods we have to define restrictions and prolongations. In Section 2.2.4 we derived the natural prolongation, the injective restriction and the Galerkin restriction operator for the one-dimensional polynomial basis. We further stated that extension to more dimensions is easily made by means of the tensor product principle. However, for convenience we give in this section an overview of the conclusions.

For the two-dimensional analysis, we consider a uniform fine partitioning of cells Ω_h with size $h_1 \times h_2$ and a uniform coarse cell partitioning Ω_H of cells $H_1 \times H_2 = 2h_1 \times 2h_2$. With $jh = (j_1 h_1, j_2 h_2)$ and $jH = (j_1 H_1, j_2 H_2)$, we denote the nodal points of respectively the fine and coarse partitioning. We further denote the spaces of discontinuous piecewise polynomials by S_h and S_H. Since, by nesting we have $S_H \subset S_h$, the natural prolongation $P_{hH} : S_H \to S_h$ is defined[1] such that $(P_{hH} u_H)(x) = u_H(x)$ for all $x \in (\mathbb{R} \setminus \mathbb{Z}_h)^2$. For our piecewise cubics ($p = 2$) the one-dimensional prolongation stencil

$$[\mathbf{P}_{LL}, \mathbf{P}_L, \mathbf{P}_C, \mathbf{P}_R, \mathbf{P}_{RR}]$$

reads (see Section 2.2.4):

[1] $\mathbb{Z}_h$, with $0 < h \in \mathbb{R}$, is the regular infinite grid, defined by $\mathbb{Z}_h = \{jh \mid j \in \mathbb{Z}\}$.

$$\mathbf{P}_{LL} = \begin{bmatrix} 0 & 0 & 0 & -\frac{1}{8} \\ 0 & 0 & 0 & 0 \\ 0 & 0 & 0 & 0 \\ 0 & 0 & 0 & 0 \end{bmatrix}, \mathbf{P}_{L} = \begin{bmatrix} 0 & 0 & 0 & \frac{1}{4} \\ 0 & 0 & \frac{1}{2} & \frac{1}{8} \\ 0 & 0 & \frac{1}{2} & \frac{1}{8} \\ 0 & 0 & 0 & 0 \end{bmatrix}, \mathbf{P}_{C} = \begin{bmatrix} \frac{3}{8} & 0 & 0 & 0 \\ 0 & 1 & 0 & 0 \\ 0 & 0 & 1 & 0 \\ 0 & 0 & 0 & \frac{3}{8} \end{bmatrix},$$

$$\mathbf{P}_{R} = \begin{bmatrix} 0 & 0 & 0 & 0 \\ \frac{1}{8} & \frac{1}{2} & 0 & 0 \\ \frac{1}{8} & \frac{1}{2} & 0 & 0 \\ \frac{1}{4} & 0 & 0 & 0 \end{bmatrix}, \quad \mathbf{P}_{RR} = \mathbf{P}_{LL}^{T}.$$

Then, we derive the two-dimensional prolongation stencil from (cf. (4.6)):

$$P_{hH} \approxeq (\mathbf{P}_{\cdot} \otimes \mathbf{P}_{\cdot})_{i,\tilde{i},j,\tilde{j}} \quad i,\tilde{i},j,\tilde{j} \in \{1,2,..,4\}, \tag{4.10}$$

where the dot-subscript (LL,L,C,R,RR) denotes 'outer-left, left, center' etc.. The result is a 25-points block-stencil, with each block a 16×16 matrix, associated with a neighboring nodal point.

Whereas the prolongation P_{hH} is uniquely defined, the restriction operator is not. However, we recognize two natural restriction operators. The first one is the restriction for the residual, characterized as the Galerkin restriction. Due to the weighed residual character of the Galerkin discretization, this restriction operator is the adjoint of the prolongation: $\overline{R}_{Hh} = (P_{hH})^T$. The Toeplitz operator of the Galerkin restriction is the transpose of the Toeplitz operator for the prolongation. Because of the Galerkin construction of the discretization and the nesting of the spaces S_H and S_h, the Galerkin relation holds for the discretization on the coarser and finer grid:

$$L_H = \overline{R}_{Hh} L_h P_{hH} . \tag{4.11}$$

The stencil representation of $\overline{R}_{Hh}$ is the same as for P_{hH}.

The second natural restriction is the injective restriction, applied in the solution space. This restriction is based on function values and corrections on derivatives at the cell corners (see Section 2.2.4). Because of our basis (4.3), the one-dimensional restriction operator is constructed such that:

$$\begin{aligned} (d/dx)(R_{Hh}u_h)(jH)|_{\Omega_{H,j-1}} &= (d/dx)u_h(2jh)|_{\Omega_{h,2j-1}}, \\ (R_{Hh}u_h)(jH)|_{\Omega_{H,j-1}} &= u_h(2jh)|_{\Omega_{h,2j-1}}, \\ (R_{Hh}u_h)(jH)|_{\Omega_{H,j}} &= u_h(2jh)|_{\Omega_{h,2j}}, \\ (d/dx)(R_{Hh}u_h)(jH)|_{\Omega_{H,j}} &= (d/dx)u_h(2jh)|_{\Omega_{h,2j}}, \end{aligned}$$

yielding the block-stencil $[\mathbf{R}_{LL}, \mathbf{R}_L\mathbf{R}_C, \mathbf{R}_R\mathbf{R}_{RR}]$:

$$\mathbf{R}_{LL} = \begin{bmatrix} 0 & 0 & 0 & 1 \\ 0 & 0 & 0 & 0 \\ 0 & 0 & 0 & 0 \\ 0 & 0 & 0 & 0 \end{bmatrix}, \mathbf{R}_L = \mathbf{R}_R = \begin{bmatrix} 0 & & & \\ & \cdot & & \\ & & \cdot & \\ & & & 0 \end{bmatrix},$$

$$\mathbf{R}_C = \begin{bmatrix} 3 & 0 & 0 & 0 \\ 0 & 1 & 0 & 0 \\ 0 & 0 & 1 & 0 \\ 0 & 0 & 0 & 3 \end{bmatrix}, \qquad \mathbf{R}_{RR} = \begin{bmatrix} 0 & 0 & 0 & 0 \\ 0 & 0 & 0 & 0 \\ 0 & 0 & 0 & 0 \\ 1 & 0 & 0 & 0 \end{bmatrix}.$$

This operator R_{Hh} is the left-inverse of P_{hH}, i.e. $I_H = R_{Hh}P_{hH}$.

4.3 Two-dimensional Fourier analysis tools

4.3.1 The Fourier transform of an n-valued two-dimensional grid function

In Section 2.3 we introduced some Fourier analysis tools in order to analyze the eigenvalue spectra of the one-dimensional discrete system and its relaxation methods. In this section we extend this analysis for a more-dimensional discrete system. Therefore we define the regular two-dimensional grid $\mathbb{Z}_h^2$ as:

$$\mathbb{Z}_h^2 = \{jh | j \in \mathbb{Z}^2\}, \tag{4.12}$$

where

$$jh = (j_1 h_1, j_2 h_2), \tag{4.13}$$

and we denote $h^2 = h_1 \cdot h_2$. Further we introduce the two-dimensional torus

$$\mathbb{T}_h^2 = (-\pi/h_1, \pi/h_1] \times (-\pi/h_2, \pi/h_2].$$

Following [18], an n-valued two-dimensional grid function is denoted by $\mathbf{u}_h \in [l^2(\mathbb{Z}_h^2)]^n$ and is provided with the norm

$$\|\mathbf{u}_h\|^2_{[l^2(\mathbb{Z}_h^2)]^n} = \sum_{1 \le i \le n} \|u_{h,i}\|^2_{l^2(\mathbb{Z}_h^2)};$$

$l^2(\mathbb{Z}_h^2)$ is the Hilbert space of square summable two-dimensional complex grid-functions defined on $\mathbb{Z}_h^2$, with innerproduct

$$(u_h, v_h) = h^2 \sum_{j \in \mathbb{Z}^2} u_h(jh)\overline{v_h(jh)}.$$

The Fourier transform $\widehat{\mathbf{u}_h} \in [L^2(\mathbb{T}_h^2)]^n$ of $\mathbf{u}_h \in [l^2(\mathbb{Z}_h^2)]^n$ is the complex n-vector valued function $\mathbb{T}_h^2 \to \mathbb{C}^n$, defined by:

$$\widehat{\mathbf{u}_h}(\omega) = \left(\frac{h}{\sqrt{2\pi}}\right)^2 \sum_{j\in\mathbb{Z}^2} e^{-i(jh)\cdot\omega}\mathbf{u}_h(jh). \tag{4.14}$$

Its inverse transform is given by:

$$\mathbf{u}_h(jh) = \left(\frac{1}{\sqrt{2\pi}}\right)^2 \int_{\omega\in\mathbb{T}_h^2} e^{+i(jh)\cdot\omega}\widehat{\mathbf{u}_h}(\omega)d\omega. \tag{4.15}$$

Furthermore we have by Parseval's equality:

$$\|\mathbf{u}_h\|_{[l^2(\mathbb{Z}_h^2)]^n} = \|\widehat{\mathbf{u}_h}\|_{[L^2(\mathbb{T}_h^2)]^n} = \sqrt{\sum_{1\le i\le n} \|\widehat{u}_{h,i}\|_{\mathbb{T}_h^2}^2}, \tag{4.16}$$

where $\widehat{\mathbf{u}_h} = \{\widehat{u}_{h,i}\}$, $i \in \{1, 2, .., n\}$.

4.3.2 The Toeplitz operator on n-valued two-dimensional grid functions

Following the same approach as in Section 2.3.2, for an infinite block operator obtained from a two-dimensional discretization we write $A_h : [l^2(\mathbb{Z}_h^2)]^n \to [l^2(\mathbb{Z}_h^2)]^n$, where $A_h = (\mathbf{a}_{m,j})_{m,j\in\mathbb{Z}^2}$ with $\mathbf{a}_{m,j} \in \mathbb{R}^{n\times n}$. For a block Toeplitz operator A_h we have by definition $\mathbf{a}_{m,j} = \mathbf{a}_{m-j}$ and its Fourier transform $\widehat{A_h}(\omega)$ is determined by:

$$A_h e_{h,\omega} = \sum_{j\in\mathbb{Z}^2} \mathbf{a}_{m,j} e^{i(jh)\cdot\omega} = \widehat{A_h} e^{i(mh)\cdot\omega},$$

hence,

$$\widehat{A_h}(\omega) = \sum_{j\in\mathbb{Z}^2} \mathbf{a}_{m,j} e^{i([j-m]h)\cdot\omega} = \sum_{k\in\mathbb{Z}^2} \mathbf{a}_{-k} e^{i(kh)\cdot\omega} = \sum_{k\in\mathbb{Z}^2} \mathbf{a}_k e^{-i(kh)\cdot\omega}, \tag{4.17}$$

for all $\omega = (\omega_1, \omega_2) \in \mathbb{T}_h^2$. Here $e_{h,\omega} = e^{i(jh)\cdot\omega}$ is an elementary mode defined on the regular infinite two-dimensional grid (4.12) and $\widehat{A_h}(\omega)$ is the $n \times n$ Fourier transform matrix of A_h. In the eigenvalue decomposition of $\widehat{A_h}$:

$$\widehat{A_h}(\omega)V_h(\omega) = (V_h\Lambda_h)(\omega), \tag{4.18}$$

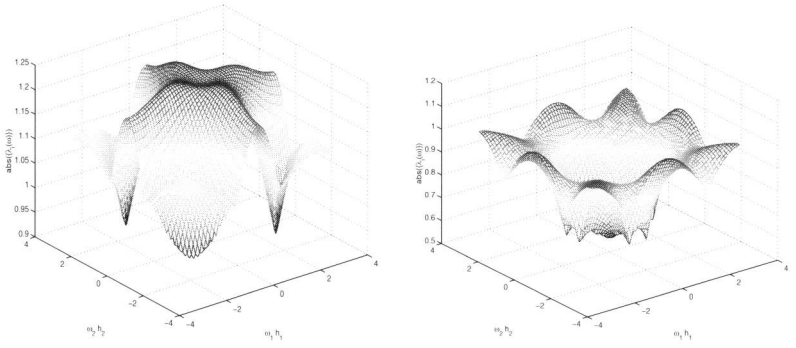

Symm-DG, $\sigma = -1$, $\mu = 0$ Baum-DG, $\sigma = 1$, $\mu = 0$

Figure 4.1: Spectral radius ($\max_j(|\lambda_i(\omega)|)$, $j \in \{1, 2, .., 16\}$) of $\widehat{L_h}(\omega)$ for the symmetric and Baumann's DG-method.

$V_h(\omega)$ is the $n \times n$ matrix of eigenvectors $\mathbf{v}(\omega)$ of $\widehat{A_h}(\omega)$. And with

$$(V_h \otimes e_{h,\omega})(jh) = V_h(\omega) e^{i(jh)\cdot\omega},$$

we have:

$$A_h (V_h \otimes e_{h,\omega}) = \widehat{A_h}(\omega)(V_h \otimes e_{h,\omega}) = (V_h \otimes e_{h,\omega}) \Lambda_h(\omega), \quad \omega \in \mathbb{T}_h^2. \tag{4.19}$$

Hence the columns $\mathbf{v}(\omega)e_{h,\omega}$ of $V_h \otimes e_{h,\omega}$ are n-valued eigen (grid) functions of A_h, while $\Lambda_h(\omega)$ is the family of $n \times n$ diagonal matrices containing the eigenvalues of A_h on its diagonal.

As an example we determine the eigenvalue spectra of the Toeplitz operators associated with the stencil (4.8) or (4.9) for respectively the symmetric DG-method ($\sigma = -1$, $\mu = 0$) and Baumann's DG-method ($\sigma = 1$, $\mu = 0$). Considering the cell-wise stencil (4.8), using (4.17) we write:

$$\widehat{L_h}(\omega) = \mathbf{L}_{LC}^C e^{-\omega_1 h_1} + \mathbf{L}_{RC}^C e^{\omega_1 h_1} + + \mathbf{L}_{CC}^C + \mathbf{L}_{CL}^C e^{-\omega_2 h_2} + \mathbf{L}_{CR}^C e^{\omega_2 h_2}, \tag{4.20}$$

where $\widehat{L_h}(\omega)$ is now a 16×16 matrix. By (4.19), $\Lambda_h(\omega)$ is the family of 16×16 matrices containing the set $\{\lambda_j(\omega)\}$, $j \in \{1, 2, .., 16\}$ eigenvalues of L_h for the mode $e_{h,\omega}$. Figure 4.1 shows the in absolute value largest eigenvalue ($\max_j(|\lambda_j(\omega)|)$) of (4.20) as function of $\omega \in \mathbb{T}_h^2$.

4.3.3 Fourier analysis for prolongations and restrictions on two-dimensional n vector valued grid functions

Having introduced the Fourier analysis for prolongations and restrictions on one dimensional (four)-vector valued grid functions (see Section 2.3.3), the same Fourier analysis is easily applied on two-dimensional n-valued grid functions. Key to the Fourier analysis of prolongations and restrictions are the flat prolongation and restriction operators. In the framework of this chapter, we may define the flat-prolongation: $P^0_{hH} : [\ell^2(\mathbb{Z}^2_H)]^n \to [\ell^2(\mathbb{Z}^2_h)]^n$ simply by:

$$\mathbf{u}_h(jh) = \left(P^0_{hH}\mathbf{u}_H\right)(jh) = \begin{cases} \mathbf{u}_H(Hj/2) & \text{if } j_1 \text{ and } j_2 \text{ even} \\ \mathbf{0} & \text{if } j_1 \text{ and } j_2 \text{ odd} \end{cases} \tag{4.21}$$

where j and h are multi-indices as in (4.13).

The flat-restriction: $R^0_{Hh} : [\ell^2(\mathbb{Z}^2_h)]^n \to [\ell^2(\mathbb{Z}^2_H)]^n$ is given by:

$$\left(R^0_{Hh}\mathbf{u}_h\right)(jH) = \mathbf{u}_h(2jh). \tag{4.22}$$

Then, according to [18] we have the relation:

$$\widehat{P^0_{hH}\mathbf{u}_H}(\omega) = \frac{1}{4}\widehat{\mathbf{u}_H}(\omega), \quad \omega_1, \omega_2 \in \mathbb{T}^2_h, \tag{4.23}$$

whereas the Fourier transform of the flat-restriction on a two-dimensional n-valued grid function is computed as:

$$\widehat{R^0_{Hh}\mathbf{u}_h}(\omega) = \sum_{p_1,p_2=0,1} \widehat{\mathbf{u}_h}\left(\omega_1 + \frac{\pi p_1}{h_1}, \omega_2 + \frac{\pi p_2}{h_2}\right), \tag{4.24}$$

for all $\omega_1, \omega_2 \in T^2_H = T^2_{2h}$. Any constant coefficient prolongation/restriction can be constructed as a combination of a Toeplitz operator and a flat operator. Using (4.23) the Fourier transform of a prolongation on a two-dimensional n-valued grid function is given by:

$$\widehat{P_{hH}\mathbf{u}_H}(\omega) = \left(\widehat{P_h P^0_{hH}\mathbf{u}_H}\right)(\omega) = \frac{1}{4}\begin{bmatrix} \widehat{P_h}(\omega_1, \omega_2) \\ \widehat{P_h}\left(\omega_1, \omega_2 + \frac{\pi}{h_2}\right) \\ \widehat{P_h}\left(\omega_1 + \frac{\pi}{h_1}, \omega_2\right) \\ \widehat{P_h}\left(\omega_1 + \frac{\pi}{h_1}, \omega_2 + \frac{\pi}{h_2}\right) \end{bmatrix} \widehat{\mathbf{u}_h}(\omega), \tag{4.25}$$

$\omega_1, \omega_2 \in \mathbb{T}_H$.

For the restriction operator, using (4.24) we have:

$$\widehat{R_{Hh}\mathbf{u}_h}(\omega) = R^0_{H_h}\widehat{R_h}\mathbf{u}_h(\omega)$$
$$= \begin{bmatrix} \widehat{R_h}(\omega_1,\omega_2), \\ \widehat{R_h}\left(\omega_1,\omega_2+\frac{\pi}{h_2}\right) \\ \widehat{R_h}\left(\omega_1+\frac{\pi}{h_1},\omega_2\right) \\ \widehat{R_h}\left((\omega_1+\frac{\pi}{h_1},\omega_2+\frac{\pi}{h_2}\right) \end{bmatrix}^T \begin{bmatrix} \widehat{\mathbf{u}_h}(\omega_1,\omega_2) \\ \widehat{\mathbf{u}_h}\left(\omega_1,\omega_2+\frac{\pi}{h_2}\right) \\ \widehat{\mathbf{u}_h}\left(\omega_1+\frac{\pi}{h_1},\omega_2\right) \\ \widehat{\mathbf{u}_h}\left(\omega_1+\frac{\pi}{h_1},\omega_2+\frac{\pi}{h_2}\right) \end{bmatrix}, \tag{4.26}$$

with $\omega_1, \omega_2 \in \mathbb{T}^2_H$.

4.4 Two-dimensional smoothing analysis

4.4.1 Smoothing analysis for the full polynomial basis

Having introduced the Fourier analysis tools, we can study the convergence of the block-relaxation methods: damped block Jacobi (JOR), damped block-Gauss-Seidel (DGS), and symmetric damped block-Gauss-Seidel, either with cell-wise or point-wise blocks. For an efficient multigrid method it is essential that the block-relaxation methods show good smoothing ability. This implies that all high frequency components of the error (or residual) are damped before (or after) the approximate solution (or residual) is restricted to the coarser grid. So, for the system $A_h x = b$, we are interested in the convergence behavior of the iterative process:

$$x^{(i+1)} = x^{(i)} - B_h\left(A_h x^{(i)} - b\right),$$

where B_h is an approximate inverse of A_h. Decomposing A_h into a strictly block-lower, a block-diagonal and a strictly block-upper matrix,

$$A_h = L + D + U, \tag{4.27}$$

we find the relaxation methods as described in Section 2.4. Table 2.1 shows the meaning of the approximate inverse B_h and the meaning of the amplification matrix $M_h^{\mathrm{REL}} = I_h - B_h A_h$. Because A_h is a block-Toeplitz operator, also the amplification matrix M_h is block-Toeplitz. By (4.17) and (4.8), we determine the Fourier transform of the different block-matrices in *cell-wise* ordering:

$$\widehat{L} = \mathbf{L}^C_{CL}\, e^{-i\omega_2 h_2} + \mathbf{L}^C_{LC}\, e^{-i\omega_1 h_1},$$
$$\widehat{D} = \mathbf{L}^C_{CC},$$
$$\widehat{U} = \mathbf{L}^C_{RC}\, e^{i\omega_1 h_1} + \mathbf{L}^C_{CR}\, e^{i\omega_2 h_2},$$

whereas the Fourier Transform of the different block-matrices in *point-wise* ordering yields (4.9):

$$\begin{aligned}
\widehat{L} &= \mathbf{L}^P_{LL}\, e^{-i(\omega_1 h_1+\omega_2 h_2)} + \mathbf{L}^P_{CL}\, e^{-i\omega_2 h_2} + \mathbf{L}^P_{RL}\, e^{i(\omega_1 h_1-\omega_2 h_2)} + \mathbf{L}^P_{LC}\, e^{-i\omega_1 h_1},\\
\widehat{D} &= \mathbf{L}^P_{CC},\\
\widehat{U} &= \mathbf{L}^P_{RC}\, e^{i\omega_1 h_1} + \mathbf{L}^P_{LR}\, e^{i(-\omega_1 h_1+\omega_2 h_2)} + \mathbf{L}^P_{CR}\, e^{i\omega_2 h_2} + \mathbf{L}^P_{RR}\, e^{i(\omega_1 h_1+\omega_2 h_2)}.
\end{aligned}$$

Both cell-wise and point-wise, this yields the Fourier transform for the amplification operators for JOR, DGS and SGS:

$$\widehat{M^{REL}_{JOR}} = \widehat{D}^{-1}\left((1-\alpha)\,\widehat{D} - \alpha\left(\widehat{L}+\widehat{U}\right)\right), \tag{4.28}$$

$$\widehat{M^{REL}_{DGS_L}} = \left(\widehat{D}+\widehat{L}\right)^{-1}\left((1-\alpha)\left(\widehat{D}+\widehat{L}\right) - \alpha\,\widehat{U}\right), \tag{4.29}$$

$$\widehat{M^{REL}_{DGS_U}} = \left(\widehat{D}+\widehat{U}\right)^{-1}\left((1-\alpha)\left(\widehat{D}+\widehat{U}\right) - \alpha\,\widehat{L}\right), \tag{4.30}$$

$$\widehat{M^{REL}_{SGS}} = \widehat{M^{REL}_{DGS_L}}\,\widehat{M^{REL}_{DGS_U}}\,. \tag{4.31}$$

By (4.19) we find the eigenvalues of M^{REL}_h by computing the eigenvalues of $\widehat{M^{REL}_h}(\omega)$ for $\omega \in \mathbb{T}^2_h$. So, both for cell-wise and point-wise relaxation methods, the Fourier transform of the amplification matrix $\widehat{M^{REL}_h}(\omega)$ yields a 16×16 matrix with for each $\omega \in \mathbb{T}^2_h$ sixteen eigenvalues. The spectral radii of $\widehat{M^{REL}_h}(\omega)$ for $\omega \in \mathbb{T}^2_h$ for the different relaxation methods (JOR, DGS, SGS) are shown in Table 4.1 for respectively the symmetric and Baumann's DG-method.

Table 4.1: The in absolute value largest eigenvalue of $\widehat{M^{REL}_h}(\omega)$ for the different relaxation methods for respectively the symmetric and Baumann's DG-method ($\alpha = 1$). On the empty spots (–) in the table, $\widehat{M^{REL}_h}(\omega)$ is singular.

$\max_\omega \lvert\lambda(\omega)\rvert$	JOR		DGS		SDGS	
$\omega \in \mathbb{T}^2_h$	cell-wise	point-wise	cell-wise	point-wise	cell-wise	point-wise
Baumann DG	1.10	1.22	1.20	1.00	4.91	1.00
symmetric DG	–	2.98	–	–	–	–

We see that, except for block-Gauss-Seidel applied on Baumann's DG-method, the smoothers are unstable, or show singular behavior. Figure 4.2 shows the spectral radius: $\max_j(|\lambda(\omega)|)$, $j \in \{1, 2, .., 16\}$ of block-Gauss-Seidel for Baumann's DG-method in point-wise ordering.

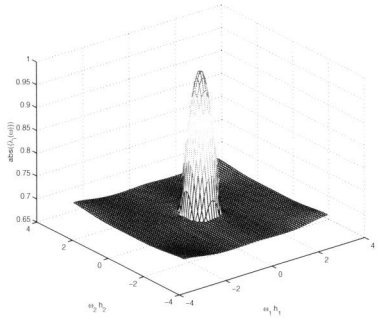

Baum-DG, $\sigma = 1$, $\mu = 0$

Figure 4.2: Spectral radius $\max_j(|\lambda_j(\omega)|)$, $j \in \{1, 2, .., 16\}$ of $\widehat{M^{REL}_{DGS_L}}(\omega)$ for Baumann's DG-method in point-wise ordering, without damping ($\alpha = 1$).

4.4.2 The reduced polynomial basis for the space S_h.

Since we want convergence in a few iteration sweeps, we see that this block-relaxation method is not suitable for multi-grid. A smoothing factor of 0.67 for $\widehat{M^{REL}_{DGS_L}}$, i.e. the largest eigenvalue corresponding to the high frequencies $|\omega| > \pi/2h$, is not sufficiently small.

An easy heuristic explanation for the divergence of the various smoothers, is not at hand. However, an idea is that cell-wise relaxation methods mainly correct the polynomial coefficients corresponding to the cell interior, while point-wise relaxation methods efficiently correct the coefficients corresponding to cell-boundaries. If we consider the two-dimensional tensor product basis (4.3) for $p = 2$, we associate the 16 coefficients to function values, (corrections on) x and y derivatives, and (corrections on) cross-derivatives at the cell-corners. So we expect that this polynomial basis is suited for point-wise relaxation. However the functions associated with (corrections on) cross-derivatives,

$$\{\phi_{e,2}(x)\phi_{e,2}(y), \phi_{e,2}(x)\phi_{e,3}(y), \phi_{e,3}(x)\phi_{e,2}(y), \phi_{e,3}(x)\phi_{e,3}(y)\}$$

have small cell-boundary contributions compared with the jump and flux operators in the discrete weak form (4.5). So they belong more to the class of genuine bubble functions, like the higher-order corrections in the hierarchical base. If we remove these cross-derivative contributions, we restore the typical cell boundary contribution concept of the low-order polynomial basis. We will see that the

introduction of the reduced polynomial basis will lead to good smoothing properties for the point-wise relaxation methods similar as shown in the previous chapters. for the one-dimensional case.

4.4.3 The accuracy of the reduced polynomial basis

In this section we show that the reduced polynomial basis has the same accuracy as the tensor-product polynomial basis. The 12 basis-functions in the reduced basis correspond with function values and (corrections to) the x- and y-derivatives at the two-dimensional cell corners. In the three-dimensional case the equivalent modification reduces $4^3 = 64$ functions of the tensor-product basis to a 32-function basis representing function-values and x-, y- and z-derivatives at the 8 corners of the three-dimensional cell. We call this basis the reduced polynomial basis. As mentioned in Section 4.2.2, the use of the reduced polynomial basis essentially reduces the amount of work for the DG-method without reducing the order of accuracy.

Considering the two-dimensional tensor product basis (4.3), for $p = 2$, polynomials up to degree three in the two coordinate directions are interpolated exactly over the cells Ω_e. So, for cells with size $h_1 \times h_2$, the approximation introduces an error of

$$\epsilon_h = O(h_1^4) + O(h_2^4).$$

Removing the basis functions

$$\{\phi_{e,2}(x)\phi_{e,2}(y), \phi_{e,2}(x)\phi_{e,3}(y), \phi_{e,3}(x)\phi_{e,2}(y), \phi_{e,3}(x)\phi_{e,3}(y)\}$$

from the two-dimensional tensor product approximation (4.4), we lose the typical tensor product character of the approximation without affecting the order of the approximation. The removal of the basis functions responsible for the cross-derivatives introduces an extra error of order

$$\epsilon_{extra} = O(h_1^3)\,O(h_2^2) + O(h_1^2)\,O(h_2^3).$$

Now, considering the total error $\epsilon_{total} = \epsilon_h + \epsilon_{extra}$ on a cell Ω_e with size $h_1 \times h_2$, we distinguish the following three cases: (i) if $h_1 = h_2 = h$ then: $\epsilon_{total} = O(h^4) + O(h^3)\,O(h^2) + O(h^2)\,O(h^3) \approx \epsilon_h$; (ii) if $h_1 > h_2$ we find: $\epsilon_{total} = O(h_1^4) \approx \epsilon_h$; and (iii) if $h_1 < h_2$ we get: $\epsilon_{total} = O(h_2^4) \approx \epsilon_h$.

So, we can remove the test- and trial functions, representing the cross-derivatives at the cell corners of a cell Ω_e without reducing the order of (approximation) accuracy. In the remaining of this paper we study the convergence behavior of the various smoothers for the reduced polynomial basis, which is significantly better than that for the original tensor-product basis.

4.4.4 Smoothing analysis for the reduced polynomial basis

Having reduced the polynomial basis for the test/trial space S_h, we are interested in the spectral radii of the different amplification operators M_h^{REL} of damped block-Jacobi, damped block-Gauss-Seidel and symmetric block-Gauss-Seidel, both in point-wise and cell-wise ordering, applied to the symmetric and Baumann's DG-method. Because of the identity (4.19) the eigenvalues $\lambda(\omega)$ of the Fourier transform $\widehat{M_h^{REL}}(\omega)$ contain the eigenvalues of M_h^{REL}. We calculate the Fourier transform $\widehat{M_h^{REL}}(\omega)$ by either (4.28) or (4.29) or (4.31), now yielding a 12×12 matrix. So for every $\omega \in \mathbb{T}_h^2$ we find 12 eigenvalues. For the different relaxation methods (JOR, DGS, SGS), the spectral radii $\max_j(|\lambda_j(\omega)|)$, $j = \{1, 2, .., 12\}$ of $\widehat{M_h^{REL}}(\omega)$ as function of $\omega \in \mathbb{T}_h^2$, for respectively the symmetric and Baumann's DG-method are shown in the Figures 4.3 to 4.7.

The spectra of all shown relaxation methods, have an eigenvalue $|\lambda(\omega)| = 1$ for $\omega_1 = \omega_2 = 0$. This is the eigenvalue corresponding to the undamped mode, which is taken care of by the boundary conditions. The cell-wise relaxation methods cannot be applied for the symmetric-DG method, because the operator B_h is singular. However the corresponding point-wise relaxation methods are stable. For Baumann's DG-method, we see the better smoothing behavior of the point-wise relaxation methods.

4.5 Two-level analysis

4.5.1 The Fourier transform of the two-level amplification operator

Having determined the behavior of the amplification operators as a function of $\omega \in \mathbb{T}_h^2$ for the different relaxation methods, we are now interested in the convergence behavior of the two-level operator. Therefore, the amplification operator of the two-level algorithm for the error is given by

$$\begin{aligned} M_h^{TLA} &= \left(M_h^{\mathrm{REL}}\right)^{\nu_2} M_h^{\mathrm{CGC}} \left(M_h^{\mathrm{REL}}\right)^{\nu_1} \\ &= \left(M_h^{\mathrm{REL}}\right)^{\nu_2} \left(I - P_{hH} L_H^{-1} \overline{R}_{Hh} L_h\right) \left(M_h^{\mathrm{REL}}\right)^{\nu_1}, \end{aligned} \tag{4.32}$$

where ν_1 and ν_2 are the number of pre- (post-) relaxation sweeps respectively. M_h^{CGC} is the amplification operator of the coarse grid correction. The amplifi-

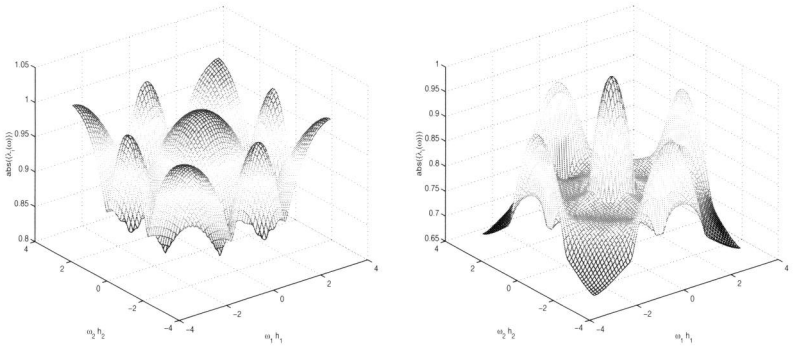

cell-wise point-wise

Figure 4.3: Spectral radii ($\max_j(|\lambda_j(\omega)|)$, $j \in \{1, 2, .., 12\}$) of the relaxation, $\widehat{M_{JOR}^{REL}}(\omega)$, for Baumann's DG-method ($\sigma = 1$) in point-wise and cell-wise ordering, without damping.

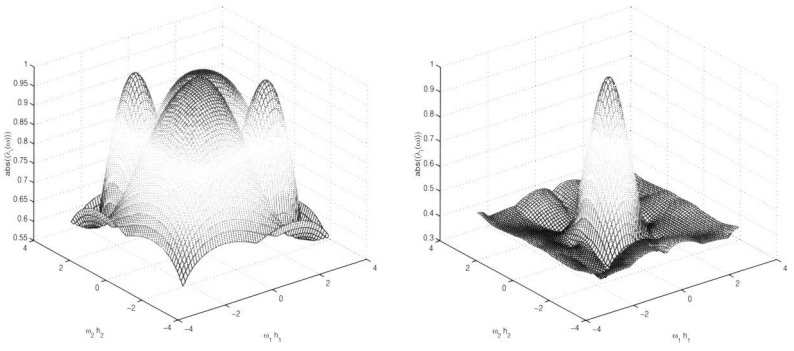

cell-wise point-wise

Figure 4.4: Spectral radii ($\max_j(|\lambda_j(\omega)|)$, $j \in \{1, 2, .., 12\}$) of the relaxation, $\widehat{M_{DGS}^{REL}}(\omega)$, for Baumann's DG-method ($\sigma = 1$) in point-wise and cell-wise ordering, without damping.

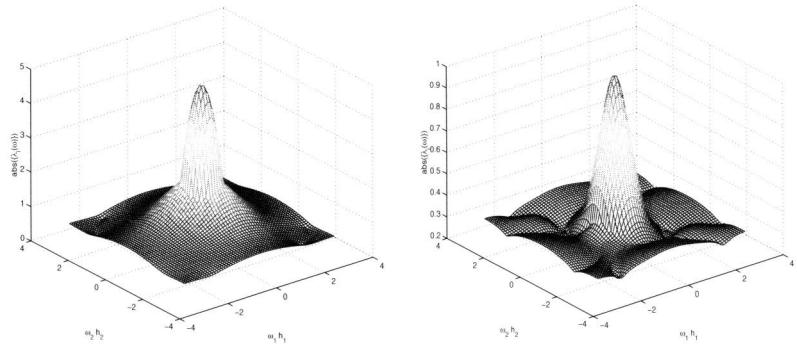

cell-wise point-wise

Figure 4.5: Spectral radii ($\max_j(|\lambda_j(\omega)|)$, $j \in \{1,2,..,12\}$) of the relaxation, $\widehat{M_{SGS}^{REL}}(\omega)$, for Baumann's DG-method ($\sigma = 1$) in point-wise and cell-wise ordering, without damping.

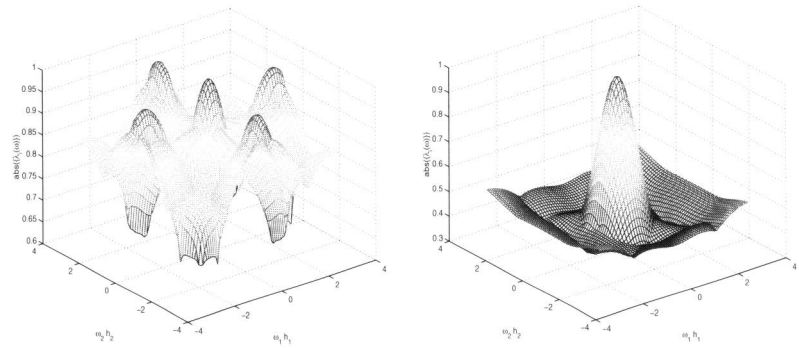

$\widehat{M_{JOR}^{REL}}(\omega)$ point-wise $\widehat{M_{DGS}^{REL}}(\omega)$ point-wise

Figure 4.6: Spectral radii ($\max_j(|\lambda_j(\omega)|)$, $j \in \{1,2,..,12\}$) of the relaxation, $\widehat{M_h^{REL}}(\omega)$, for the symmetric DG-method ($\sigma = -1$) in point-wise ordering, without damping.

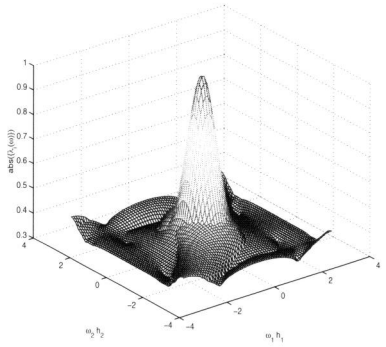

point-wise

Figure 4.7: Spectral radii ($\max_j(|\lambda_j(\omega)|)$, $j \in \{1,2,..,12\}$) of the relaxation, $\widehat{M_{SGS}^{REL}}(\omega)$, for the symmetric DG-method ($\sigma = -1$) in point-wise ordering, without damping.

cation operator for the residue is:

$$\begin{aligned} \overline{M}_h^{TLA} &= (\overline{M}_h^{REL})^{\nu_2}\, \overline{M}_h^{CGC}\, (\overline{M}_h^{REL})^{\nu_1} \\ &= \left(L_h M_h^{\mathrm{REL}} L_h^{-1}\right)^{\nu_2} L_h M_h^{\mathrm{CGC}} L_h^{-1} \left(L_h M_h^{\mathrm{REL}} L_h^{-1}\right)^{\nu_1}. \end{aligned} \tag{4.33}$$

Because of the definition of the restriction (4.25) and prolongation (4.26), it follows that the Fourier transform of the coarse grid correction M_h^{CGC} is:

$$\begin{aligned} \widehat{M_h^{\mathrm{CGC}}}(\omega) &= \left(\widehat{I_h} - \widehat{P_{hH}}\,\widehat{L_H^{-1}}\,\widehat{R_{Hh}}\,\widehat{L_h}\right)(\omega) \\ &= \begin{pmatrix} \mathbf{I} & 0 & 0 & 0 \\ 0 & \mathbf{I} & 0 & 0 \\ 0 & 0 & \mathbf{I} & 0 \\ 0 & 0 & 0 & \mathbf{I} \end{pmatrix} - \begin{pmatrix} \widehat{P_h}(\omega_1,\omega_2) \\ \widehat{P_h}(\omega_1,\omega_2+\frac{\pi}{h_2}) \\ \widehat{P_h}(\omega_1+\frac{\pi}{h_1},\omega_2) \\ \widehat{P_h}(\omega_1+\frac{\pi}{h_1},\omega_2+\frac{\pi}{h_2}) \end{pmatrix} (\widehat{L_H}(\omega_1,\omega_2))^{-1} \\ &\times \begin{pmatrix} \widehat{R_h}(\omega_1,\omega_2) & \widehat{R_h}(\omega_1,\omega_2+\frac{\pi}{h_2}) & \widehat{R_h}(\omega_1+\frac{\pi}{h_1},\omega_2) & \widehat{R_h}(\omega_1+\frac{\pi}{h_1},\omega_2+\frac{\pi}{h_2}) \end{pmatrix} \\ &\times \begin{pmatrix} \widehat{L_h}(\omega_1,\omega_2) & 0 & 0 & 0 \\ 0 & \widehat{L_h}(\omega_1,\omega_2+\frac{\pi}{h_2}) & 0 & 0 \\ 0 & 0 & \widehat{L_h}(\omega_1+\frac{\pi}{h_1},\omega_2) & 0 \\ 0 & 0 & 0 & \widehat{L_h}(\omega_1+\frac{\pi}{h_1},\omega_2+\frac{\pi}{h_2}) \end{pmatrix}. \end{aligned} \tag{4.34}$$

In view of the reduced polynomial basis, the Fourier transform of $\widehat{M_h^{\mathrm{CGC}}}(\omega)$ is an 48×48 matrix for each $\omega \in \mathbb{T}_H^2$. And because of the identity (4.19),

the eigenvalues $\lambda_i(\omega)$ of $\widehat{M_h^{\mathrm{CGC}}}(\omega)$ contain the eigenvalues of M^{CGC}, i.e., the block-Toeplitz operator of the two-level operator.

Because of the bad smoothing behavior of JOR, DGS and SDGS in cell-wise block-ordering, we abandon these block relaxation methods in the remainder of this chapter and in the next section we study the point-wise smoothers and derive optimal damping factors for the two-level algorithm.

4.5.2 Optimal block-smoothing factors for the coarse grid correction

In local mode analysis, low and high frequency grid functions in $[l^2(\mathbb{Z}_h^2)]^n$ are usually defined as the functions that are linear combinations of modes $e_{h,\omega} = e^{i(jh)\cdot\omega}$, with respectively $\omega \in \mathbb{T}_{2h}^2$ and $\omega \in \mathbb{T}_h^2 \setminus \mathbb{T}_{2h}^2$. However, to obtain optimal damping factors for the different relaxation methods in combination with the coarse grid correction, M_h^{CGC}, we have to redefine low and high frequency grid functions as follows. We consider the amplification operator of the coarse grid correction $M_h^{CGC} = I - P_{hH} L_H^{-1} \overline{R}_{Hh} L_h$. Because of the Galerkin relation (4.11), $P_{hH} L_H^{-1} \overline{R}_{Hh} L_h$ is a projection operator and we define low frequency components in the error as those components that lie in the range of $P_{hH} L_H^{-1} \overline{R}_{Hh} L_h$. Then the high frequency components are those in the range of $I - P_{hH} L_H^{-1} \overline{R}_{Hh} L_h$. So, for a "slowly varying" n-valued grid function $\mathbf{u}_h^{LF}$ we have:

$$P_{hH} L_H^{-1} \overline{R}_{Hh} L_h \mathbf{u}_h = \mathbf{u}_h^{LF}, \tag{4.35}$$

while for a "high frequency" grid function $\mathbf{u}_h^{HF}$:

$$(I - P_{hH} L_H^{-1} \overline{R}_{Hh} L_h)\mathbf{u}_h = \mathbf{u}_h^{HF}. \tag{4.36}$$

Since $M_h^{CGC} \mathbf{u}_h^{LF} = 0$, we want the relaxation methods to optimally damp the contributions (4.36). Therefore, for the different relaxation methods, we seek damping parameters α_{opt} such that the spectral radius of $M_h^{CGC} M_h^{REL}$ is minimal. Notice that according to (4.32), $M_h^{CGC} M_h^{REL}$ is just the two-level operator on the error M_h^{TLA} with $\nu_1 = 1$, $\nu_2 = 0$.

By (4.34) and by either (4.28), (4.29) or (4.31), we compute the eigenvalue spectra, of $M_h^{CGC} M_h^{REL}$, first without damping ($\alpha = 1$). We determine the optimal damping parameter for the relaxation by:

$$\alpha_{opt} = \frac{2}{2 - (\lambda_{\min} + \lambda_{\max})},$$

where $\lambda_{\min}$ and $\lambda_{\max}$ are respectively the minimum and maximum real eigenvalues of the spectrum without damping. It is clear that the spectral radius for the two-level operator on the residue is the same as that for the error: $\rho(M_h^{CGC} M_h^{REL}) = \rho(\overline{M}_h^{REL} \overline{M}_h^{CGC})$.

The optimal damping parameters for the different two-level operators are given in Table 4.2, the minimized spectral radii in Table 4.3. The spectral radii of $\widehat{M_h^{CGC}}(\omega)\widehat{M_h^{REL}}(\omega)$ as function of $\omega \in \mathbb{T}_H^2$, with optimal damping are shown in the Figures 4.8 and 4.9.

Table 4.2: Optimal damping parameters, α_{opt}, for the two-level operators $\rho(M_h^{CGC} M_h^{REL}) = \rho(\overline{M}_h^{REL} \overline{M}_h^{CGC})$.

α_{opt}	Baum-DG	symm-DG
$M_h^{CGC} M_{JOR}^{REL}$	0.95	1.03
$M_h^{CGC} M_{DGS}^{REL}$	1.22	1.44

Table 4.3: Spectral radii $\rho(M_h^{CGC} M_h^{REL}) = \rho(\overline{M}_h^{REL} \overline{M}_h^{CGC})$ for optimal damping parameters as in Table 4.2.

$\rho(M_h^{CGC} M_h^{REL})$	$M_h^{CGC} M_{JOR}^{REL}$	$M_h^{CGC} M_{DGS}^{REL}$	$M_{DGS_U}^{REL} M_h^{CGC} M_{DGS_L}^{REL}$
Baum-DG	0.74	0.44	0.36
symm-DG	0.89	0.62	0.38

Table 4.4: The spectral norm $\left\| \left(\overline{M}^{REL} \overline{M}_h^{CGC} \right)^k \right\|_2$ for the amplification operator of the residue with optimal damping, $k = 1, 3, 4$.

	$\left(\overline{M}_{JOR}^{REL} \overline{M}_h^{CGC} \right)^k$	$\left(\overline{M}_{DGS_L}^{REL} \overline{M}_h^{CGC} \right)^k$	$\left(\overline{M}_{DGS_L}^{REL} \overline{M}_h^{CGC} \overline{M}_{DGS_U}^{REL} \right)^k$
Baum-DG, $k = 1$	3.15	3.48	2.37
Baum-DG, $k = 3$	1.02	0.72	0.34
Baum-DG, $k = 4$	0.68	0.32	0.13
Symm-DG, $k = 1$	7.46	5.82	4.09
Symm-DG, $k = 3$	2.65	1.74	0.76
Symm-DG, $k = 4$	2.24	1.01	0.31

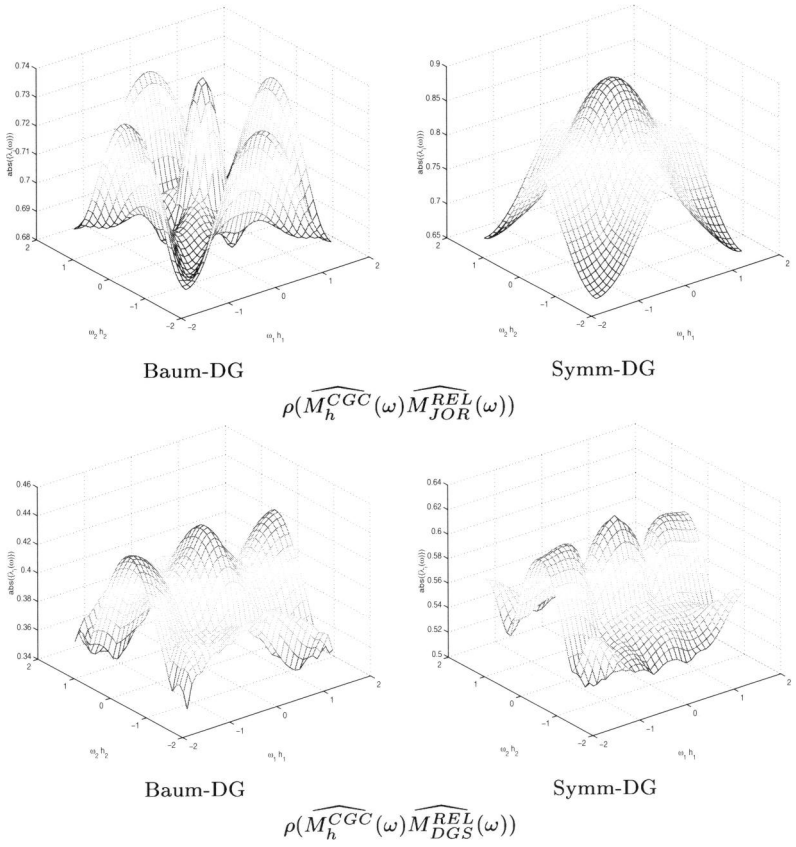

Figure 4.8: Spectral radii ($\max_j(|\lambda_j(\omega)|)$, $j \in \{1, 2, .., 12\}$) of as function of $\omega \in \mathbb{T}_h^2$ for the symmetric ($\sigma = -1$) and Baumann's DG-method ($\sigma = 1$) for damping parameters as in Table 4.2.

From Table 4.3, we see that all two-level algorithms converge. Baumann's DG-method converges faster than the symmetric DG-method. This is also reflected in the two-norm of the amplification operator of the two-level algorithm. Table 4.4 shows the two-norm of the amplification operator of the residue after respectively 1, 3 and 4 iteration(s). We see that, except for block-Jacobi on the symmetric DG-method, reduction of the residue is guaranteed within a small number of iteration steps. For the symmetric DG-method, the spectral norms of the iteration operator for the error are the same as for the residue. In case of

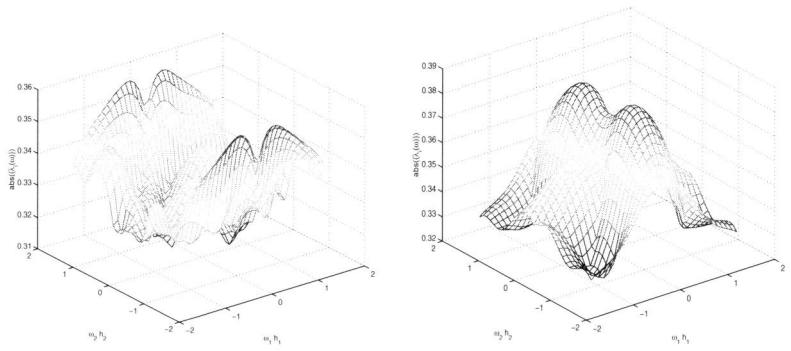

Baum-DG Symm-DG

$$\rho(\widehat{M^{REL}_{DGS_U}}(\omega)\widehat{M^{CGC}_h}(\omega)\widehat{M^{REL}_{DGS_L}}(\omega))$$

Figure 4.9: Spectral radii ($\max_j(|\lambda_j(\omega)|)$, $j \in \{1, 2, .., 12\}$) of as function of $\omega \in \mathbb{T}^2_h$ for the symmetric ($\sigma = -1$) and Baumann's DG-method ($\sigma = 1$) for damping parameters as in Table 4.2.

Baumann's DG-method, the norm of the error amplification operator becomes unbounded for vanishing frequency ω. This phenomenon was also observed in Section 2.5.2 for the the error amplification norm in case of the one-dimensional Poisson's equation and is due to the adjoint inconsistency of the method [3].

4.6 Numerical results

Having determined optimal damping parameters for the two-level algorithm, we want to check the results by a numerical experiment. For that purpose, we solve the following two-dimensional Poisson's equation on the unit square:

$$-(u_{xx} + u_{yy}) = \frac{e^{x/\epsilon} + e^{y/\epsilon}}{\epsilon^2 \left(e^{1/\epsilon} - 1\right)}, \text{ in } \Omega,$$

with on the Dirichlet boundary $\partial\Omega$

$$u(x, y) = \frac{2 - \left(e^{x/\epsilon} + e^{y/\epsilon}\right)}{e^{1/\epsilon} - 1} + x + y.$$

To obtain the discrete system we use the reduced polynomial basis for S_h as explained in Section 4.4.2. I.e. we use for each cell Ω_e a local basis consisting of

$\phi_{e,i}(\xi)\phi_{e,j}(\eta)$ as in (4.4), where $(i,j) \in \{(m.n), (m+2,n), (m,n+2) \mid m,n = 0,1\}$. We use a regular mesh with size $h \times h = 4^{-N}$ and we start with an initial function $u_h^0(x,y) = u_{PRE}^0$ on the finer grid. We apply ν_1 pre-relaxation sweeps

$$u_{h,\mathrm{PRE}}^{i+1} = u_{h,\mathrm{PRE}}^{i} + B_h\left(f_h - L_h u_{h,\mathrm{PRE}}^{i}\right),$$

where B_h is the approximate inverse of L_h as given in Table 2.1 in Section 2.4. Then, we update the solution by a coarse grid correction step, solving for e_H on the coarser grid with size $H \times H = 4^{1-N}$,

$$u_{h,\mathrm{POST}}^{0} = u_{h,\mathrm{PRE}}^{\nu_1} + P_{hH} L_H^{-1} \overline{R}_{Hh}(f_h - L_h u_{h,\mathrm{PRE}}^{\nu_1}). \tag{4.37}$$

and, eventually, we apply ν_2 post-relaxations sweeps

$$u_{h,\mathrm{POST}}^{i+1} = u_{h,\mathrm{POST}}^{i} + B_h(f_h - L_h u_{h,\mathrm{POST}}^{i}),$$

to compute $u_h^{i+1} = u_{h,\mathrm{POST}}^{\nu_2}$. The correction on the coarser grid at its turn, is solved by multigrid until the residue of the correction (in the L_2 norm) is less than an order of $O(10^{-6})$. To show convergence we measure the residue in the L_2 norm[2]

$$\|d_h\|_{L_2} = \|f_h - L_h u_h\|_{L_2} = \left(\sum_e \int_{\Omega_e} |\sum_{i=0}^{12} c_{e,i}\phi_{e,i}(x,y)|^2 dx\right)^{1/2}. \tag{4.38}$$

The observed convergence of the two-level solution method applied to Baumann's and the symmetric DG-method are shown in Figure 4.10. We observe that both methods show convergence, Baumann's DG-method converging faster. From the slope we determine the experimental convergence rates for the different two-level algorithms. Table 4.5 shows the results and we see that the observed rates in the numerical experiments coincide well with the spectral radii obtained by Fourier analysis as shown in Table 4.3.

4.7 Conclusion

In this chapter we analyze the convergence behavior of the two-level algorithm applied to the two-dimensional Poisson equation, discretized by two discontinuous Galerkin (DG) methods: the Baumann-Oden and the symmetric DG-method, each with a polynomial basis of piecewise cubics in each of the two

[2] According to (4.16) we would follow the Fourier analysis more precisely if we would measure the residue in the vector two-norm, however both norms are equivalent.

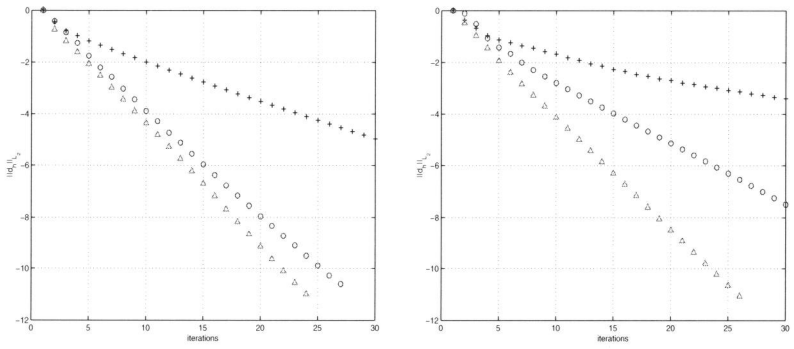

Baumann-DG Symmetric-DG

+: JOR; ○: DGS; △: SGS.

Figure 4.10: $\log(\|d_h\|_{L_2})$ as function of iterations for the two-level iteration operator on the error.

Table 4.5: Numerically obtained convergence rates observed for the different two-level block-relaxation methods with optimal damping parameters as in Table 4.2.

$\rho(M_h^{CGC} M_h^{REL})$	Baum-DG	symm-DG
$M_h^{CGC} M_{JOR}^{REL}$	0.7	0.9
$M_h^{CGC} M_{DGS}^{REL}$	0.4	0.6
$M_{DGS_U}^{REL} M_h^{CGC} M_{DGS_L}^{REL}$	0.3	0.4

coordinate directions. We studied the convergence behavior of different block-relaxation methods: damped block-Jacobi (JOR), damped block-Gauss-Seidel (DGS) and symmetric damped block-Gauss-Seidel (SDGS), where the blocks are chosen, based either on cell-wise or on point-wise ordering. We show that *point-wise block* relaxation has better smoothing properties than the classical *cell-wise* block relaxation methods. Moreover, point-wise block-relaxation for the symmetric DG-method is stable, whereas the classical cell-wise relaxation methods are not.

The smoothing behavior is further improved by reduction of the polynomial basis, i.e. removing tensor-basis functions that represent cross-derivatives at the cell corners, but do not contribute to the order of accuracy. Reduction of the basis not only improves the convergence behavior of the relaxation methods, it also makes the DG-method much more efficient than when it is based on a

tensor-product basis.

For the two-level algorithm we computed optimal damping parameters for the relaxation methods, and spectral radii of the corresponding iteration operators. With a spectral radius between 0.6 and 0.4 for DGS and SDGS smoothers, the two-level algorithms show good convergence. An analysis of the spectral norm on the residual shows that residual reduction is guaranteed within a few iteration steps.

Chapter 5

Two-level analysis for the convection-diffusion equation

Summary

In this chapter we study a multigrid method for the solution of a linear convection-diffusion equation that is discretized by a discontinuous Galerkin method. In particular we emphasize the convection-dominated case when the perturbation parameter, i.e., the inverse cell-Reynolds-number, is smaller than the finest mesh size.

We show that, if the diffusion term is discretized by the non-symmetric interior penalty method (NIPG) with feasible penalty term, multi-grid is sufficient to solve the convection-diffusion or the convection-dominated equation. Then, independent of the mesh-size, simple MG cycles with symmetric Gauss-Seidel smoothing give an error reduction factor of 0.2-0.3 per iteration sweep.

Without penalty term, for the Baumann-Oden (BO) method we find that only a robust (i.e., cell-Reynolds-number uniform) two-level error-reduction factor (0.4) is found if the point-wise block-Jacobi smoother is used.

5.1 Introduction

The present analysis is motivated by our interest in the *hp*-self-adaptive solution of elliptic problems that are discretized by discontinuous Galerkin (DG) methods

on dyadic grids.

DG-methods were traditionally introduced for the solution of hyperbolic equations, as methods that have a natural cell-wise upwind character [9, 30]. However, since renewed insights were obtained in their application to elliptic problems, DG-methods gain in popularity [3, 5, 36, 40], specially because of their convenient properties when combined with the *hp*-self-adaptive approach and with multigrid (MG) solvers [29, 42, 44].

In this framework, having studied the Poisson equation in one and more dimensions, [23, 24, 25] we now study the convergence of the MG method for the one-dimensional convection-diffusion equation. In particular we study the convection-dominated case, when the perturbation parameter, i.e., the inverse cell-Reynolds-number, is smaller than the finest mesh size.

To have a stable DG discretization, we consider for discretization of the diffusion term, the asymmetric DG variants, the Baumann-Oden method and the non-symmetric interior penalty method (NIPG) respectively. For both these methods the discrete operators are positive definite for polynomial discretizations of order higher than two [3]. The resulting linear system is block-tridiagonal and, as discussed in Chapter 2, can be partitioned in two distinct ways: *cell-wise* and *point-wise*. Each partitioning defines its own type of block-relaxation methods that can be used as smoothing procedure in the MG algorithm (e.g., block-Jacobi, block-Gauss-Seidel).

In our analysis we find that, in case of convection-diffusion and the convection-dominated situation and for the DG method where the diffusion term is discretized by the Baumann-Oden DG-method, only a good two-level error-reduction factor (0.4) is predicted if the *point-wise block Jacobi* smoother is used. Although with imperfect coarse grid corrections and for vanishing diffusion this block-relaxation method starts to diverge, the Baumann-Oden type DG-method still can be used in MG techniques when robustness is increased by introducing additional stabilization in the coarse grid correction, [11, 12, 38, 48].

Further, we show that in case of the DG method, where the diffusion term is discretized by the non-symmetric interior penalty (NIPG) method with feasible penalty term, simple multi-grid cycles with *cell-wise* symmetric Gauss-Seidel are sufficient to solve the convection-diffusion and the convection-dominated equation. Then an error reduction factor of 0.2-0.3 per iteration sweep is observed.

For our analysis, we consider the following outline. In Section 5.2 we give the discontinuous Galerkin formulation used for the discretization, and we specify the corresponding discrete system. Then, in Section 5.3, we describe the Fourier analysis for block-Toeplitz operators, where we distinguish between *cell-wise* and *point-wise* partitioned stencils. In case the block-Toeplitz operator is partitioned

cell-wise, the blocks are associated with the *cell-interiors*, while in a point-wise partitioned block-Toeplitz operator, the equations and coefficients are associated with the *cell-vertices*. In the latter partitioning, the coefficients correspond to (vector-valued) grid functions on a regular grid, for which, in view of our two-level analysis, it is natural and easy to define prolongation and restriction operators. This in contrast to cell-wise ordered coefficient, for which we would have to take care of staggered information in coarse and fine cells.

Important for the reliability of the Fourier analysis, is that the inverse of a block-Toeplitz operator is bounded. The consequences of this fact are explained in Section 5.3.2.

We continue with the smoothing analysis. In Section 5.4.1, we study the error-amplification operators of the cell- and point-wise block-relaxation methods (block-Jacobi, block-Gauss-Seidel). To ensure that the equations and coefficients are associated with the *cell-vertices*, i.e., the coefficients correspond to vector-valued grid functions, both the cell- and point-wise error-amplification operators are casted in *point-wise notation.*

For mixed convection-diffusion and pure convection, in 5.4.2, we study the eigenvalue spectra of the error-amplification operators of the cell- and point-wise block-relaxation methods. In Section 5.4.3, we take the MG coarse-grid correction into account and we determine smoothing factors and spectral norms of the block-relaxation methods. In the final section we show numerical experiments to illustrate the analysis. The present study shows that simple MG cycles with symmetric Gauss-Seidel smoothing are sufficient to solve the convection-diffusion equation efficiently, provided that the diffusion term is discretized by the non-symmetric interior penalty method.

5.2 The discontinuous Galerkin discretization

5.2.1 The weak formulation for the convection-diffusion equation

To describe the discontinuous Galerkin methods considered, we give the variational formulation used for the discretization of the convection-diffusion equation. On the unit cube $\Omega \subset \mathbb{R}^d$, we consider the following boundary value problem with Dirichlet and Neumann boundary conditions:

$$-\varepsilon\Delta u + \mathbf{b}\cdot\nabla u = f \text{ on } \Omega; \quad u = u_0 \text{ on } \Gamma_{\mathrm{D}}, \quad \mathbf{n}\cdot\nabla u = g \text{ on } \Gamma_{\mathrm{N}}, \tag{5.1}$$

where $\Gamma_D \cup \Gamma_N = \partial\Omega$, $\Gamma_D \cap \Gamma_N = \emptyset$, $\varepsilon \geq 0$ and $\mathbf{b} \in \mathbb{R}^d$. We further assume that $\mathbf{n} \cdot \mathbf{b} \geq 0$ on Γ_N, i.e., Γ_N is an outflow boundary. Next we consider a uniform partitioning of Ω. Therefore, we take a set of regular rectangular cells, Ω_e, all of the same size,

$$\Omega_h = \left\{ \Omega_e \mid \cup_e \overline{\Omega}_e = \overline{\Omega},\ \Omega_i \cap \Omega_j = \emptyset,\ i \neq j \right\}.$$

On this partitioning, we define the broken Sobolev space [5, 37] of piecewise H^1-functions, u,

$$H^1(\Omega_h) = \left\{ u \in L_2(\Omega) \mid u|_{\Omega_e} \in H^1(\Omega_e),\ \forall \Omega_e \in \Omega_h \right\}.$$

Then the DG formulation associated with (5.1) reads [3, 9]: find $u \in H^1(\Omega_h)$ such that:

$$B(u, v) = L(v), \quad \forall v \in H^1(\Omega_h), \tag{5.2}$$

where

$$\begin{aligned} B(u,v) = \sum_{\Omega_e \in \Omega_h} & (\varepsilon \nabla u, \nabla v)_{\Omega_e} - \langle \langle \varepsilon \nabla u \rangle, [v] \rangle_{\Gamma_{\text{int}} \cup \Gamma_D} + \\ & \sigma \langle \langle \varepsilon \nabla v \rangle, [u] \rangle_{\Gamma_{\text{int}} \cup \Gamma_D} + \mu \langle [u], \varepsilon [v] \rangle_{\Gamma_{\text{int}} \cup \Gamma_D} \\ & - \sum_{\Omega_e \in \Omega_h} (\nabla v, \mathbf{b} u)_{\Omega_e} + \left\langle \mathbf{n} \cdot \mathbf{b} u^-, v \right\rangle_{\Gamma_{\text{int}}^- \cup \Gamma_D} + \langle \mathbf{n} \cdot \mathbf{b} u, v \rangle_{\Gamma_{\text{int}}^+ \cup \Gamma_N}, \end{aligned} \tag{5.3}$$

and

$$L(v) = \sum_{\Omega_e \in \Omega_h} (f, v)_{\Omega_e} + \sigma \langle \langle \varepsilon \nabla v \rangle, [u_0] \rangle_{\Gamma_D} + \mu \langle [u_0], \varepsilon [v] \rangle_{\Gamma_D} + \langle g, \varepsilon v \rangle_{\Gamma_N}.$$

Here Γ_{int} is the union of all interior cell interfaces. With Γ_{int}^- we denote the set of all inflow boundaries, i.e., $\mathbf{n} \cdot \mathbf{b} < 0$, and with Γ_{int}^+ the set of all outflow boundaries. Notice that $u^-|_{\Gamma_D} = u_0$, i.e. the value of u at the Dirichlet boundary. The parameters σ and μ identify the different DG-methods; $\sigma = -1$ for symmetric DG; $\sigma = 1$ for the Baumann-Oden method; $\mu > 0$ for respectively the symmetric ($\sigma = -1$) and non-symmetric ($\sigma = 1$) interior penalty DG-method (i.e., IPG or NIPG respectively).

The jump operator $[\cdot]$ and the average operator $\langle \cdot \rangle$ are defined for the traces of functions $v(x)$ and vector functions $\tau(x)$ on the common interface $\Gamma_{i,j}$ between two adjacent[1] cells Ω_i, Ω_j The operators are defined in Section 2.2.1 by (2.5) and (2.6) respectively.

[1] At the Dirichlet boundary, the interface of a flat (virtual) adjacent cell is used.

To discretize (5.2), we introduce the finite dimensional space of piecewise polynomials of degree at most k,

$$S_h = \left\{ \phi_{i,e} \in \mathcal{P}^k(\Omega_e),\ \forall \Omega_e \in \Omega_h \right\}.$$

Taking test and trial space the same, we consider the discrete equations: find $u_h \in S_h$ such that

$$B(u_h, v_h) = L(v_h), \quad \forall v_h \in S_h. \tag{5.4}$$

5.2.2 The discrete system

To describe the linear system, $L_h u_h = f_h$, arising from the discrete form (5.4), we have to specify a base for the space S_h. For this purpose, on the unit interval we choose the polynomial basis (2.8), introduced in Section 2.2.2. On the unit cube, $\hat{\Omega} \subset \mathbb{R}^d$, we use a basis of tensor-product polynomials based on (2.8), and as usual, a basis for $\mathcal{P}^{2p-1}(\Omega_e)$ is obtained by the affine mapping $\hat{\Omega} \to \Omega_e$.

As we have discussed in Section 2.2.2, we consider the fourth-order discretization the relevant and generic one for studying iterative solution procedures. Further, for the initial study presented in this chapter, we restrict ourselves to the one-dimensional case. In view of the tensor product principle, this is an essential building block for higher-dimensional problems. So, taking $p = 2$ in (2.8), writing the approximate solution as

$$u_h = \sum_{e=1}^{N} \sum_{i=0}^{3} c_{i,e} \phi_i \left(\frac{x - x_e}{h} \right) = \sum_{e=1}^{N} \sum_{i=0}^{3} c_{i,e} \phi_{i,e}(t),$$

the coefficients being determined by the $4N \times 4N$ linear system

$$\begin{aligned}
&\sum_{e=1}^{N} \varepsilon \sum_{i=0}^{3} c_{i,e} \Big[(\phi'_{i,e}(x), \phi'_{j,e}(x))_{\Omega_e} - \langle \phi'_{i,e}(x) \rangle \cdot [\phi_{j,e}(x)]|_{\Gamma_{\mathrm{Dint}}} \\
&\qquad + \sigma \langle \phi'_{j,e}(x) \rangle \cdot [\phi_{i,e}(x)]|_{\Gamma_{\mathrm{Dint}}} + \mu [\phi_{j,e}(x)] \cdot [\phi_{i,e}(x)]|_{\Gamma_{\mathrm{Dint}}} \Big] \\
&\quad + b \sum_{i=0}^{3} c_{i,e} \left[-(\phi'_{j,e}(x), \phi_{i,e}(x)) + n \phi^{-}_{i,e}(x) \phi_{j,e}(x)]|_{\Gamma^{-}_{\mathrm{int}}} + n \phi_{i,e}(x) \phi_{j,e}(x)]|_{\Gamma^{+}_{\mathrm{int}} \cup \Gamma_{\mathrm{N}}} \right] \\
&= \sum_{e=1}^{N} \sum_{i=0}^{3} (f, \phi_{j,e}(x))_{\Omega_e} + \sigma [u_0] \cdot \langle \varepsilon \phi'_{j,e}(x) \rangle |_{\Gamma_{\mathrm{D}}} + \varepsilon g \phi_{j,e}(x)|_{\Gamma_{\mathrm{N}}} - n b u_0 \phi_{j,e}(x)]|_{\Gamma_{\mathrm{D}}}.
\end{aligned} \tag{5.5}$$

Here, n is the one-dimensional outward normal vector, i.e., $n = \pm 1$ and the sign of b determines the convection direction. The resulting matrix is block-tridiagonal and by the constant coefficients (neglecting the influence of the

boundary conditions) it can be formulated as a block-Toeplitz matrix, i.e, as a repetition of a lower-diagonal, diagonal and an upper-diagonal 4×4 block.

This repetition of lower-diagonal, diagonal and an upper-diagonal blocks, can be formulated in two distinct ways. The classical approach is to order the equations and coefficients *cell-wise*, i.e., $\{c_{e,0}, c_{e,2}, c_{e,3}, c_{e,1}\}$, then we obtain for the diffusion part of the stencil (see stencil (2.10) in Section 2.2.2)

$$L_{h_D} \approxeq \tag{5.6}$$
$$\left[\begin{array}{cccc|cccc|cccc}
-\frac{1}{2} & 0 & -\frac{1}{2} & \frac{1-\sigma}{2} - h\mu & \frac{1+\sigma}{2} + h\mu & \frac{1}{2} & 0 & \frac{-1-\sigma}{2} & \frac{1}{2}\sigma & 0 & 0 & 0 \\
0 & 0 & 0 & \frac{1}{2}\sigma & -\frac{1}{2}\sigma & \frac{2}{15} & \frac{1}{30} & 0 & 0 & 0 & 0 & 0 \\
0 & 0 & 0 & 0 & 0 & \frac{1}{30} & \frac{2}{15} & -\frac{1}{2}\sigma & \frac{1}{2}\sigma & 0 & 0 & 0 \\
0 & 0 & 0 & \frac{1}{2}\sigma & \frac{-1-\sigma}{2} & 0 & \frac{1}{2} & \frac{1+\sigma}{2} + h\mu & \frac{1-\sigma}{2} - h\mu & -\frac{1}{2} & 0 & -\frac{1}{2}
\end{array}\right],$$

while the stencil for the convection part reads ($b \geq 0$)

$$L_{h_C} \approxeq \left[\begin{array}{cccc|cccc|cccc}
0 & 0 & 0 & -1 & \frac{1}{2} & \frac{1}{12} & \frac{1}{12} & \frac{1}{2} & 0 & 0 & 0 & 0 \\
0 & 0 & 0 & 0 & -\frac{1}{12} & 0 & \frac{1}{60} & \frac{1}{12} & 0 & 0 & 0 & 0 \\
0 & 0 & 0 & 0 & -\frac{1}{12} & -\frac{1}{60} & 0 & \frac{1}{12} & 0 & 0 & 0 & 0 \\
0 & 0 & 0 & 0 & -\frac{1}{2} & -\frac{1}{12} & -\frac{1}{12} & \frac{1}{2} & 0 & 0 & 0 & 0
\end{array}\right]. \tag{5.7}$$

So, the discrete block-Toeplitz operator L_h for positive convection direction b reads

$$L_h \equiv \frac{\varepsilon}{h} L_{h_D} + L_{h_C}. \tag{5.8}$$

However, in view of the Fourier analysis for the multi-grid method, where prolongation and restriction operators are based on values at the cell-vertices (see Section 2.3.3), it is more convenient to represent the block-Toeplitz operator (5.8) as a repetition of *point-wise* partitioned stencils. Then, ordering the equations and coefficients as $\{c_{e-1,3}, c_{e-1,1}, c_{e,0}, c_{e,2}\}$, we find again that the matrix has a block-Toeplitz structure and we find for the diffusion part of the stencil (see also stencil (2.11))

$$L_{h_D} \approxeq \tag{5.9}$$
$$\left[\begin{array}{cccc|cccc|cccc}
0 & 0 & 0 & \frac{1}{30} & \frac{2}{15} & -\frac{1}{2}\sigma & \frac{1}{2}\sigma & 0 & 0 & 0 & 0 & 0 \\
0 & \frac{1}{2}\sigma & \frac{-1-\sigma}{2} & 0 & \frac{1}{2} & \frac{1+\sigma}{2} + h\mu & \frac{1-\sigma}{2} - h\mu & -\frac{1}{2} & 0 & -\frac{1}{2} & 0 & 0 \\
0 & 0 & -\frac{1}{2} & 0 & -\frac{1}{2} & \frac{1-\sigma}{2} - h\mu & \frac{1+\sigma}{2} + h\mu & \frac{1}{2} & 0 & \frac{-1-\sigma}{2} & \frac{1}{2}\sigma & 0 \\
0 & 0 & 0 & 0 & 0 & \frac{1}{2}\sigma & -\frac{1}{2}\sigma & \frac{2}{15} & \frac{1}{30} & 0 & 0 & 0
\end{array}\right],$$

whereas the stencil for the convection part now reads

$$L_{h_C} \approxeq \left[\begin{array}{cccc|cccc|cccc}
0 & 0 & -\frac{1}{12} & -\frac{1}{60} & 0 & \frac{1}{12} & 0 & 0 & 0 & 0 & 0 & 0 \\
0 & 0 & -\frac{1}{2} & -\frac{1}{12} & -\frac{1}{12} & \frac{1}{2} & 0 & 0 & 0 & 0 & 0 & 0 \\
0 & 0 & 0 & 0 & 0 & -1 & \frac{1}{2} & \frac{1}{12} & \frac{1}{12} & \frac{1}{2} & 0 & 0 \\
0 & 0 & 0 & 0 & 0 & 0 & -\frac{1}{12} & 0 & \frac{1}{60} & \frac{1}{12} & 0 & 0
\end{array}\right]. \tag{5.10}$$

The fact that point-wise ordering leads again to a block-tridiagonal structure is not automatic, but it is caused by the proper choice of basis functions as in (2.8). The choice makes that the coefficients $\{c_{e-1,3}, c_{e-1,1}, c_{e,0}, c_{e,2}\}$ correspond to function values and corrections on derivatives at the cell-vertices. Hence, we may interpret the coefficients as four-valued grid functions defined on a regular one-dimensional grid associated with the cell-vertices. These degrees of freedom are also used to define prolongation and restriction operators (see the Sections 2.2.4 and 2.3.3). This, in contrast to the coefficients $\{c_{e,0}, c_{e,2}, c_{e,3}, c_{e,1}\}$, grouped in the cell-wise partitioned stencils, where we would have to deal with staggered information in coarse and fine cells.

We emphasize that, either the repetition of (5.6) and (5.7) or the repetition of (5.9) and (5.10), represents the same block-Toeplitz matrix L_h.

5.3 Fourier analysis for block-Toeplitz operators

5.3.1 Eigenvalues and eigenvectors of a block-Toeplitz operator

To study the smoothing behavior of the different block-relaxation algorithms, we return to the Fourier analysis tools for block-Toeplitz operators, introduced in Section 2.3.2. So, we consider an elementary mode $e_{h,\omega}(jh) = e^{ijh\omega}$, for all $\omega \in \mathbb{T}_h \equiv [-\frac{\pi}{h}, \frac{\pi}{h}]$, defined on the regular infinite one-dimensional grid

$$\mathbb{Z}_h = \{jh \,|\, j \in \mathbb{Z}, h > 0\} \,. \tag{5.11}$$

Then, for an infinite block-Toeplitz operator $A_h = (\mathbf{a}_{m,j}) \in \mathbb{R}^{4\mathbb{Z}\times 4\mathbb{Z}}$, $m, j \in \mathbb{Z}$, i.e., $(\mathbf{a}_{m,m+k}) = (\mathbf{a}_{-k})$, for $k = j - m \in \mathbb{Z}$ and $\forall m \in \mathbb{Z}$, we find by (2.19) the Fourier transform $\widehat{A}_h(\omega)$. Hence, $\widehat{A}_h(\omega)$ is a 4×4 matrix, depending on $\omega \in \mathbb{T}_h$. If $\widehat{A}_h(\omega)$ allows for the eigenvalue decomposition (2.20), then the columns of $\mathbf{v}(\omega)e_{h,\omega}(mh)$ in (2.21) are four-valued grid functions defined on the grid (5.11) and correspond to the eigenvectors of A_h, while $\Lambda(\omega)$ is a family of 4×4 diagonal matrices with the eigenvalues of A_h at the diagonal entries.

As an example, we compute the eigenvalue spectra of the discrete Toeplitz operator (5.8), where, for diffusion stencil (5.6) (or (5.9)), we take the Baumann-Oden discretization ($\sigma = 1$ and $\mu = 0$). So, recognizing in (5.8) the different block contributions $(\mathbf{a}_{m,j})$, either in cell-wise ((5.6) and (5.7)) or in point-wise

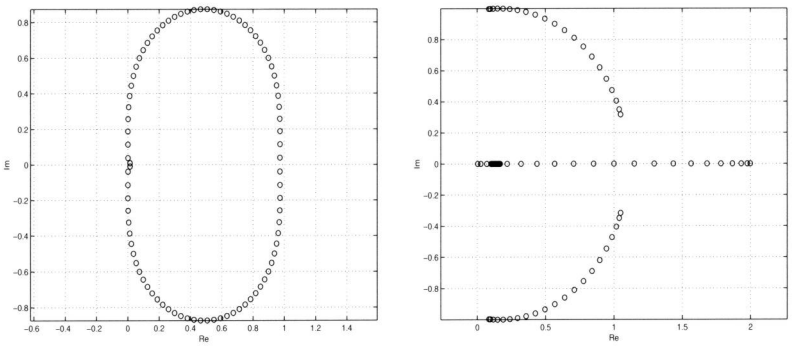

convection diffusion

Figure 5.1: Eigenvalue spectra of the operator $\widehat{L}_h(\omega)$, with $\sigma = 1$ and $\mu = 0$.

((5.9) and (5.10)) notation, we find $\widehat{L}_h(\omega)$ by (2.19). And because of (2.21), the four eigenvalues $\lambda_i(\omega)$ as function of $\omega \in \mathbb{T}_h$ correspond to the eigenvalues of L_h. Figure 5.1 shows the eigenvalue spectra for the case of pure convection and pure diffusion.

We see that in both cases the discrete operator is positive semi-definite and hence is also positive semi-definite for mixed convection-diffusion. The zero eigenvalue corresponds to the constant grid function $\mathbf{v}_0 = \mathbf{v}(\omega)e_{h,0}(mh)$, given in (2.21) as a column of $\mathbf{v}(\omega)e_{h,\omega}(mh)$. The difference in the cell-wise and point-wise partitioning of (5.8) is reflected in this grid function. Where for the cell-wise partitioned stencils, the constant grid function reads

$$\mathbf{v}_0 = \begin{bmatrix} c & 0 & 0 & c \end{bmatrix}^{\mathrm{T}} e_{h,0}(mh), \quad c \in \mathbb{R},$$

for the point-wise partitioned stencils, the constant grid-function is represented by

$$\mathbf{v}_0 = \begin{bmatrix} 0 & c & c & 0 \end{bmatrix}^{\mathrm{T}} e_{h,0}(mh), \quad c \in \mathbb{R}. \tag{5.12}$$

Because the fourth-order discretization (5.5), both for the Baumann-Oden DG method and for the NIPG method is coercive [3], in our block-relaxation analysis we use these methods for the discretization of the diffusion term.

5.3.2 Boundedness of an inverse block-Toeplitz operator

An important feature in our block-relaxation analysis is that the inverse of a given $n \times n$ block-Toeplitz operator is bounded. We show this by the following

simple example.

Let the stencil associated with a $n \times n$ block-Toeplitz operator be given by

$$A_h \widehat{=} \left[\begin{array}{ccc} -K & I & \mathbf{0} \end{array} \right], \qquad K \in \mathbb{R}^{n \times n}, \tag{5.13}$$

Now, writing the inverse of A_h as

$$A_h^{-1} \widehat{=} \left[\begin{array}{ccccccccccc} \cdot & K^k & K^{k-1} & \cdot & \cdot & K & I & \mathbf{0} & \cdot & \cdot & \mathbf{0} & \mathbf{0} & \cdot \end{array} \right], \tag{5.14}$$

we readily see that A_h^{-1} is bounded if and only if the n eigenvalues $|\lambda_j(K)| < 1$. Then, in view of (2.19), we write

$$\left(\widehat{A}_h(\omega)\right)^{-1} = \frac{I}{I - Ke^{-i\omega h}} = \sum_{k=0}^{\infty} K^k e^{-ikh\omega} = \left(\widehat{A}_h^{-1}\right)(\omega), \tag{5.15}$$

where, using (2.21), we find the eigenvalues of A_h^{-1}. We readily see that, in case $|\lambda_j(K)| \geq 1$, the finite dimensional discrete operator, corresponding with (5.13) is non normal.

5.4 Smoothing analysis

The aim of this study is to identify smoothing procedures which damp the frequencies that cannot be damped by the coarse grid correction in the multigrid process. So, to quantify the smoothing behavior of simple block-relaxation procedures, we are interested in the spectral radii and spectral norms of the two-level operator for the error. This operator reads

$$\begin{aligned} M_h^{\mathrm{TLA}} &= \left(M_h^{\mathrm{REL}}\right)^{\nu_2} M_h^{\mathrm{CGC}} \left(M_h^{\mathrm{REL}}\right)^{\nu_1} \\ &= \left(M_h^{\mathrm{REL}}\right)^{\nu_2} \left(I - P_{hH} L_H^{-1} \overline{R}_{Hh} L_h\right) \left(M_h^{\mathrm{REL}}\right)^{\nu_1}. \end{aligned} \tag{5.16}$$

Here, M_h^{REL} is the error-amplification operator of the smoother, ν_1 and ν_2 are the number of pre- (post-) relaxation sweeps respectively; M_h^{CGC} is the amplification operator of the coarse grid correction (CGC), see e.g., [45, 49]. P_{hH} and $\overline{R}_{Hh}$ are the grid transfer operators between the fine h-grid and the coarse H-grid, where $H = 2h$.

Because the prolongation should keep the piecewise cubics invariant, the operator $P_{hH} : S_H \to S_h$ is constructed so that $(P_{hH} u_H)(x) = u_H(x)$ for all $x \in \mathbb{R} \setminus \mathbb{Z}_h$. Its stencil in *point-wise* ordering is given by (see also Section 2.2.4):

$$P_{hH} \approx$$

$$\left[\begin{array}{cccc|cccc|cccc|cccc|cccc} 0 & 0 & 0 & \frac{-1}{8} & 0 & 0 & 0 & \frac{1}{4} & \frac{3}{8} & 0 & 0 & 0 & 0 & 0 & 0 & 0 & 0 & 0 & 0 & 0 \\ 0 & 0 & 0 & 0 & 0 & 0 & \frac{1}{2} & \frac{1}{8} & 0 & 1 & 0 & 0 & \frac{1}{8} & \frac{1}{2} & 0 & 0 & 0 & 0 & 0 & 0 \\ 0 & 0 & 0 & 0 & 0 & 0 & \frac{1}{2} & \frac{1}{8} & 0 & 0 & 1 & 0 & \frac{1}{8} & \frac{1}{2} & 0 & 0 & 0 & 0 & 0 & 0 \\ 0 & 0 & 0 & 0 & 0 & 0 & 0 & 0 & 0 & 0 & 0 & \frac{3}{8} & \frac{1}{4} & 0 & 0 & 0 & \frac{-1}{8} & 0 & 0 & 0 \end{array}\right].$$

Since test and trial space are the same, the restriction of the residue, $\overline{R}_{Hh}$, is the adjoint of the prolongation, $\overline{R}_{Hh} = (P_{hH})^T$.

For different ν_1 and ν_2 in (5.16) the convergence can be studied. However, essential for the coarse grid correction operator for the error, M_h^{CGC}, is that it splits the high frequency modes into a low and high frequency modes on the fine grid [20]. Therefore, we better use the smoother *before* the coarse grid correction (this, in contrast to the correction operator for the residual, for which the smoothing should be applied *after* the coarse grid correction). So, we restrict ourself to a representative and simple case, where, to quantify the smoothing behavior of the various block-relaxation methods, we study the spectral radii and spectral norms of $M_h^{\mathrm{CGC}} M_h^{\mathrm{REL}}$.

In the next section we specify the block-Jacobi (JOR) and damped block-Gauss-Seidel (DGS) smoothers both for point-wise and for cell-wise relaxation. We further derive Fourier transforms of the error-amplification operators in order to study their eigenvalue spectra. Then we compute the Fourier transforms of the two-level operator $M_h^{\mathrm{TLA}} = M_h^{\mathrm{CGC}} M_h^{\mathrm{REL}}$ to obtain spectral radii and spectral norms, and we quantify the smoothing behavior of the various block-relaxation methods.

5.4.1 Block-relaxation analysis

A good smoother damps all frequencies in the error that cannot be damped by the coarse grid correction operator M_h^{CGC}. Therefore, the spectrum of the amplification operator M_h^{REL} must be such, that at least the eigenvalues corresponding with these frequencies are in absolute value less than one. In this section we use Fourier analysis to study the amplification operators of both the cell-wise and point-wise block-Jacobi (JOR) and the damped block-Gauss-Seidel (DGS) relaxation methods. In view of the two-level amplification operator M_h^{TLA}, studied in Section 5.4.3, it is of importance that for both the cell-wise and point-wise relaxation procedures the eigenvectors are represented as point-wise grid-functions (i.e., are associated with the cell vertices).

Since we have shown in the previous chapters, that, in the case of pure diffu-

sion, the point-wise smoothers show much better smoothing behavior than the cell-wise block-relaxation methods [23, 24, 25], and also because for dominant diffusion ($\varepsilon/h > 1$ in (5.8)), the point-wise smoothers appear to be better in the case when the convection term acts as a small perturbation of the diffusion, we restrict ourselves here mainly to the case of convection diffusion, $\varepsilon/h \in (0, 1]$ and the case of pure convection, $\varepsilon/h = 0$.

After the introduction of the Fourier transforms for the various amplification operators in this section, in Section 5.4.2 we study their eigenvalue spectra for two distinct cases: convection-diffusion ($\varepsilon/h = 1$) and pure convection ($\varepsilon/h = 0$).

For the DG-method with diffusion term discretized by the Baumann-Oden method we will observe that, in case of convection-diffusion, the point-wise amplification operators have eigenvalue spectra with many eigenvalues in absolute value smaller than one, whereas the spectra of the cell-wise amplification operators show eigenvalues in absolute value larger than one. The cell-wise amplification operators can be stabilized if an interior penalty $\mu > 0$ is used, i.e., if we consider the NIPG discretization instead of BO discretization for the diffusion term. For pure convection, the cell-wise amplification operators show better smoothing behavior.

For the discrete system $A_h x = b$ we study block-relaxation methods of the type

$$x^{(i+1)} = x_h^{(i)} - B_h(A_h x^{(i)} - b), \tag{5.17}$$

where B_h is an approximate inverse of the matrix A_h. Analogous to the treatment in Section 2.4, we decompose

$$A_h = L + D + U, \tag{5.18}$$

into a strictly block-lower, a block-diagonal and a strictly block-upper matrix and we easily recognize the block-Jacobi (JOR) and block Gauss-Seidel (DGS) relaxation methods. The different methods and their amplification operators are shown in Table 2.1 in Section 2.4.

We first consider the decomposition (5.18) *for the point-wise stencils* (5.9) and (5.10). The stencils corresponding with this decomposition of $A_h = (\mathbf{a}_{m,j})$ are given in Table 5.1.

Table 5.1: The stencils of the point-wise decomposition (5.9)-(5.10).

diffusion	convection
$L_D \cong \begin{bmatrix} 0 & 0 & 0 & \frac{1}{30} \\ 0 & \frac{1}{2}\sigma & \frac{-1-\sigma}{2} & 0 \\ 0 & 0 & -\frac{1}{2} & 0 \\ 0 & 0 & 0 & 0 \end{bmatrix}$	$L_C \cong \begin{bmatrix} 0 & 0 & -\frac{1}{12} & -\frac{1}{60} \\ 0 & 0 & -\frac{1}{2} & -\frac{1}{12} \\ 0 & 0 & 0 & 0 \\ 0 & 0 & 0 & 0 \end{bmatrix}$
$D_D \cong \begin{bmatrix} \frac{2}{15} & -\frac{1}{2}\sigma & \frac{1}{2}\sigma & 0 \\ \frac{1}{2} & \frac{1+\sigma}{2} + h\mu & \frac{1-\sigma}{2} - h\mu & -\frac{1}{2} \\ -\frac{1}{2} & \frac{1-\sigma}{2} - h\mu & \frac{1+\sigma}{2} + h\mu & \frac{1}{2} \\ 0 & \frac{1}{2}\sigma & -\frac{1}{2}\sigma & \frac{2}{15} \end{bmatrix}$	$D_C \cong \begin{bmatrix} 0 & \frac{1}{12} & 0 & 0 \\ -\frac{1}{12} & \frac{1}{2} & 0 & 0 \\ 0 & -1 & \frac{1}{2} & \frac{1}{12} \\ 0 & 0 & -\frac{1}{12} & 0 \end{bmatrix}$
$U_D \cong \begin{bmatrix} 0 & 0 & 0 & 0 \\ 0 & -\frac{1}{2} & 0 & 0 \\ 0 & \frac{-1-\sigma}{2} & \frac{1}{2}\sigma & 0 \\ \frac{1}{30} & 0 & 0 & 0 \end{bmatrix}$	$U_C \cong \begin{bmatrix} 0 & 0 & 0 & 0 \\ 0 & 0 & 0 & 0 \\ \frac{1}{12} & \frac{1}{2} & 0 & 0 \\ \frac{1}{60} & \frac{1}{12} & 0 & 0 \end{bmatrix}$

By (2.19) the Fourier transforms of the block-diagonal operators read

$$\begin{aligned} \widehat{L}(\omega) &= \left(\frac{\varepsilon}{h} L_D + L_C\right) e^{-i\omega h}, \\ \widehat{D}(\omega) &= \left(\frac{\varepsilon}{h} D_D + D_C\right), \\ \widehat{U}(\omega) &= \left(\frac{\varepsilon}{h} U_D + U_C\right) e^{i\omega h}. \end{aligned} \tag{5.19}$$

So we find the Fourier transform for the amplification operators

$$\begin{aligned} \widehat{M^{\mathrm{REL}}_{\mathrm{JOR}}} &= \widehat{D}^{-1}\left((1-\alpha)\,\widehat{D} - \alpha\,\left(\widehat{L}+\widehat{U}\right)\right), \\ \widehat{M^{\mathrm{REL}}_{\mathrm{DGS}_L}} &= \left(\widehat{D}+\widehat{L}\right)^{-1}\left((1-\alpha)\left(\widehat{D}+\widehat{L}\right) - \alpha\,\widehat{U}\right), \\ \widehat{M^{\mathrm{REL}}_{\mathrm{DGS}_U}} &= \left(\widehat{D}+\widehat{U}\right)^{-1}\left((1-\alpha)\left(\widehat{D}+\widehat{U}\right) - \alpha\,\widehat{L}\right). \end{aligned} \tag{5.20}$$

Decomposing $\widehat{M^{\mathrm{REL}}_h}(\omega)$ according to (2.21), we find the eigenvalues $\lambda_i(\omega)$, $i = 1,..,4$, $\omega \in \mathbb{T}_h$ of M^{REL}_h and the set of vector-valued eigenfunctions $\mathbf{v}(\omega)e_{h,\omega}(mh)$, defined on the regular infinite one-dimensional grid associated with the cell-vertices.

The same procedure can be applied *for the cell-wise stencils* (5.6) and (5.7). However, then the eigenvectors $\mathbf{v}e_{h,\omega}(mh)$ are 4-valued grid functions associated

Table 5.2: The stencils of the cell-wise diagonal decomposition (5.6) to (5.7) in point-wise ordering (i.e., grouped as $\{c_{e-1,3}, c_{e-1,1}, c_{e,0}, c_{e,2}\}$). The operator E denotes a grid-shift so that $\widehat{\mathrm{E}} = e^{i\omega h}$.

diffusion	convection
$L_D \cong \begin{bmatrix} 0 & 0 & 0 & 0 \\ 0 & \frac{1}{2}\sigma & 0 & 0 \\ -\frac{1}{2}\mathrm{E} & (\frac{1-\sigma}{2} - h\mu)\mathrm{E} & -\frac{1}{2} & 0 \\ 0 & \frac{1}{2}\sigma\mathrm{E} & 0 & 0 \end{bmatrix}$	$L_C \cong \begin{bmatrix} 0 & 0 & -\frac{1}{12} & -\frac{1}{60} \\ 0 & 0 & -\frac{1}{2} & -\frac{1}{12} \\ 0 & 0 & 0 & 0 \\ 0 & 0 & 0 & 0 \end{bmatrix}$
$D_D \cong \begin{bmatrix} \frac{2}{15} & -\frac{1}{2}\sigma & 0 & \frac{1}{30}\mathrm{E}^{-1} \\ \frac{1}{2} & \frac{1+\sigma}{2} + h\mu & \frac{-1-\sigma}{2}\mathrm{E}^{-1} & 0 \\ 0 & \frac{-1+\sigma}{2}\mathrm{E} & \frac{1+\sigma}{2} + h\mu & \frac{1}{2} \\ \frac{1}{30}\mathrm{E} & 0 & -\frac{1}{2}\sigma & \frac{2}{15} \end{bmatrix}$	$D_C \cong \begin{bmatrix} 0 & \frac{1}{12} & 0 & 0 \\ -\frac{1}{12} & \frac{1}{2} & 0 & 0 \\ 0 & -\mathrm{E} & \frac{1}{2} & \frac{1}{12} \\ 0 & 0 & -\frac{1}{12} & 0 \end{bmatrix}$
$U_D \cong \begin{bmatrix} 0 & 0 & \frac{1}{2}\sigma\mathrm{E}^{-1} & 0 \\ 0 & -\frac{1}{2} & (\frac{1-\sigma}{2} - h\mu)\mathrm{E}^{-1} & -\frac{1}{2}\mathrm{E}^{-1} \\ 0 & 0 & \frac{1}{2}\sigma & 0 \\ 0 & 0 & 0 & 0 \end{bmatrix}$	$U_C \cong \begin{bmatrix} 0 & 0 & 0 & 0 \\ 0 & 0 & 0 & 0 \\ \frac{1}{12} & \frac{1}{2} & 0 & 0 \\ \frac{1}{60} & \frac{1}{12} & 0 & 0 \end{bmatrix}$

with the *cell-interiors*. This is most inconvenient if we want to transfer this information to the coarser grid. Therefore, to also have for the cell-wise amplification operators eigenvectors associated with the *cell-vertices* instead, we rewrite the cell-wise decomposition in *point-wise* notation, by grouping the equations and coefficients as $\{c_{e-1,3}, c_{e-1,1}, c_{e,0}, c_{e,2}\}$. The stencils corresponding with this decomposition are shown in Table 5.2, where E denotes the grid-shift operator for which $\widehat{\mathrm{E}} = e^{i\omega h}$.

Now, with (5.19) and (5.20), we find the cell-wise $\widehat{M_h^{\mathrm{REL}}}(\omega)$, and the representation is associated with the *cell-vertices* as needed for the two-level analysis.

5.4.2 Eigenvalue spectra of pure smoothers

Having found the Fourier transforms of the cell- and point-wise block-relaxation operators M_h^{REL} in (5.20), we can compute their eigenvalue spectra by (2.21). In order to have the block-relaxation methods independent of the convection direction, we restrict ourselves to Jacobi and symmetric Gauss-Seidel relaxation procedures.

For the discretization of the diffusion term (5.8), we choose the asymmetric DG-methods; the Baumann-Oden ($\sigma = 1$, $\mu = 0$) and the NIPG ($\sigma = 1$, $\mu > 0$)

formulation, because these methods, in contrast to the symmetric IPG-method, do not suffer from saddle-point behavior, i.e., the discrete operators do not have eigenvalues with negative real part.

In the Figures 5.2 to 5.7, we show the eigenvalue spectra of Jacobi (JOR) and symmetric Gauss-Seidel, $M^{\mathrm{REL}}_{\mathrm{SGS}_{UL}} = M^{\mathrm{REL}}_{\mathrm{DGS}_U} M^{\mathrm{REL}}_{\mathrm{DGS}_L}$, relaxation amplification operators, for DG-methods with the diffusion term discretized by the Baumann-Oden DG-method and the NIPG-method with $\mu = 10/h$ (this, to see the influence of the penalty term on the relaxation).

We first consider the DG-method with the diffusion term discretized by the Baumann-Oden DG-method (Figures 5.2 and 5.3). We see that, similar to the pure diffusion case (see Chapter 2), also for convection-diffusion the point-wise relaxation methods show much better eigenvalue spectra than the cell-wise relaxation methods. Both the eigenvalues corresponding with low frequency modes (i.e., the frequencies $|\omega| < \frac{\pi}{2h}$) and high frequency modes ($|\omega| \geq \frac{\pi}{2h}$ that cannot be represented on the coarse grid), lie within the unit circle in the complex plane. For the point-wise relaxation, the only mode, which cannot be damped, corresponds with the constant grid function (5.12). This in contrast to the cell-wise relaxation methods, which may show amplification, especially for the low frequency modes.

Next we consider the DG-method with the diffusion term discretized by the NIPG-method. We choose $\mu = 10/h$ to see the influence of the penalty term on the relaxation (Figures 5.4 and 5.5). There is a minor influence of the penalty term on the point-wise relaxation operators, but we clearly see a stabilizing effect on the cell-wise relaxation operators.

For the pure convection case (Figures 5.6 and 5.7), we see that the cell-wise block-relaxation methods do better than the point-wise relaxation methods. Whereas no amplification occurs in case of the Jacobi relaxation, the problem is solved at once by the cell-wise symmetric block Gauss-Seidel relaxation. This is an immediate consequence of the cell-wise upwind character of the DG-method. In this situation, the point-wise block-Jacobi diverges (Figure 5.6). Although all the eigenvalues of the point-wise symmetric block Gauss-Seidel relaxation (Figure 5.7) lie within the in the unit circle (except for the constant mode), in practice, no convergence is seen. This divergence for the non-periodic, finite dimensional case is caused by the operator $B_h^{-1} = L + D \equiv G_h$ in the downwind Gauss-Seidel algorithm losing its normality. It can also be checked that the inverse of the corresponding Toeplitz operator is unbounded so that the eigenvalue spectrum of $\widehat{G_h^{-1}}$ does not correspond to the spectrum of $(\widehat{G_h})^{-1}$, since (5.15) is not satisfied.

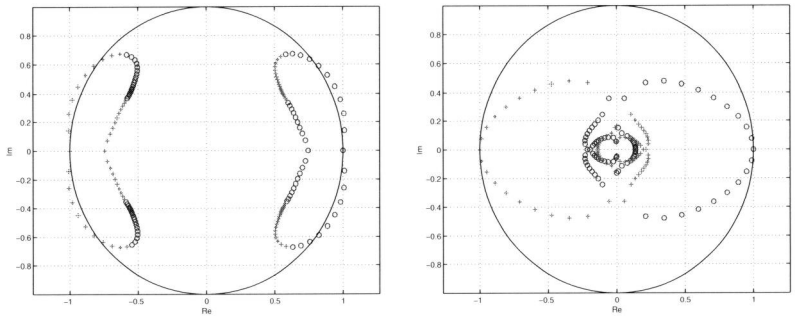

cell-wise relaxation point-wise relaxation

$\circ : \omega_{low} \in [-\pi/2h, \pi/2h], \quad + : \omega_{high} \in [-\pi/h, -\pi/2h] \cup [\pi/2h, \pi/h].$

Figure 5.2: Eigenvalue spectra of $\widehat{M^{\text{REL}}_{\text{JOR}}}(\omega)$, without damping ($\alpha = 1$), with $\sigma = 1$, $\mu = 0$ and $\varepsilon/h = 1$.

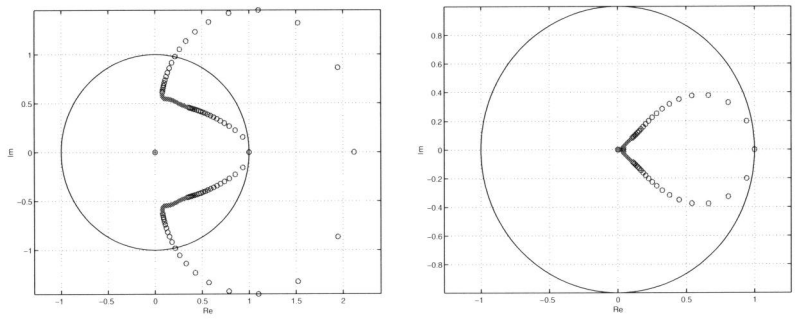

cell-wise relaxation point-wise relaxation

$\circ : \omega_{low} \in [-\pi/2h, \pi/2h], \quad + : \omega_{high} \in [-\pi/h, -\pi/2h] \cup [\pi/2h, \pi/h].$

Figure 5.3: Eigenvalue spectra of $\widehat{M^{\text{REL}}_{\text{SGS}_{UL}}}(\omega) = \widehat{M^{\text{REL}}_{\text{DGS}_U}}(\omega)\widehat{M^{\text{REL}}_{\text{DGS}_L}}(\omega)$, without damping ($\alpha = 1$), with $\sigma = 1$, $\mu = 0$ and $\varepsilon/h = 1$.

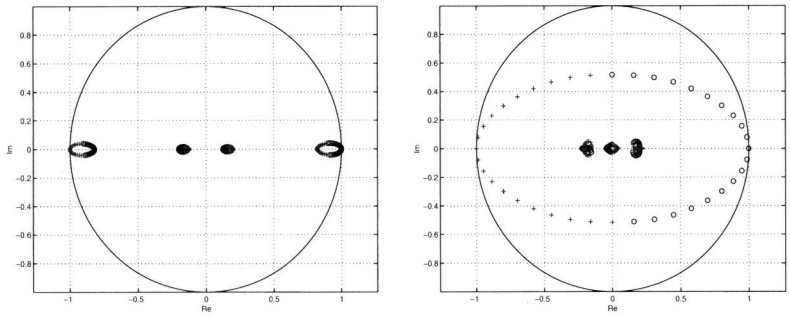

cell-wise relaxation point-wise relaxation

$\circ$: $\omega_{low} \in [-\pi/2h, \pi/2h]$, $+$: $\omega_{high} \in [-\pi/h, -\pi/2h] \cup [\pi/2h, \pi/h]$.

Figure 5.4: Eigenvalue spectra of $\widehat{M^{\mathrm{REL}}_{\mathrm{JOR}}}(\omega)$, without damping ($\alpha = 1$), with $\sigma = 1$, $\mu = 10/h$ and $\varepsilon/h = 1$.

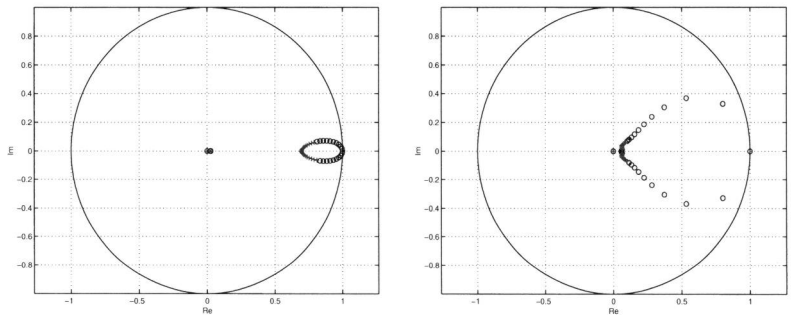

cell-wise relaxation point-wise relaxation

$\circ$: $\omega_{low} \in [-\pi/2h, \pi/2h]$, $+$: $\omega_{high} \in [-\pi/h, -\pi/2h] \cup [\pi/2h, \pi/h]$.

Figure 5.5: Eigenvalue spectra of $\widehat{M^{\mathrm{REL}}_{\mathrm{SGS}_{UL}}}(\omega) = \widehat{M^{\mathrm{REL}}_{\mathrm{DGS}_U}}(\omega)\widehat{M^{\mathrm{REL}}_{\mathrm{DGS}_L}}(\omega)$, without damping ($\alpha = 1$), with $\sigma = 1$, $\mu = 10/h$ and $\varepsilon/h = 1$.

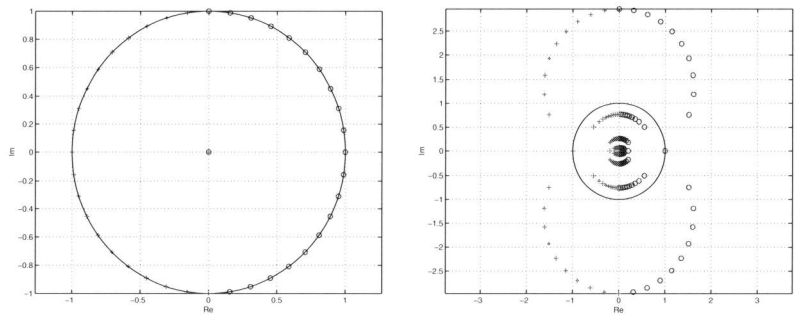

cell-wise relaxation point-wise relaxation

$\circ : \omega_{low} \in [-\pi/2h, \pi/2h], \quad + : \omega_{high} \in [-\pi/h, -\pi/2h] \cup [\pi/2h, \pi/h].$

Figure 5.6: Eigenvalue spectra of $\widehat{M^{\mathrm{REL}}_{\mathrm{JOR}}}(\omega)$, without damping ($\alpha = 1$), with $\varepsilon/h = 0$.

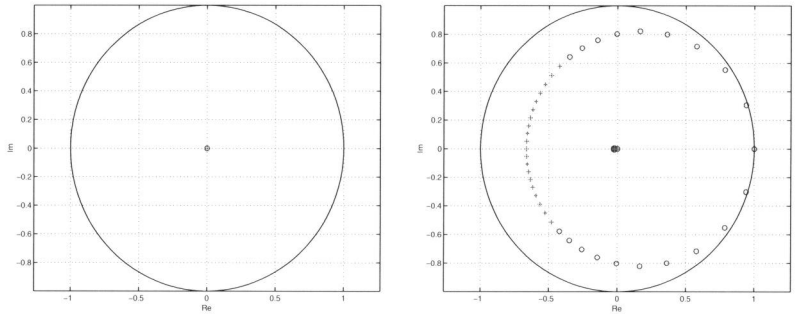

cell-wise relaxation point-wise relaxation

$\circ : \omega_{low} \in [-\pi/2h, \pi/2h], \quad + : \omega_{high} \in [-\pi/h, -\pi/2h] \cup [\pi/2h, \pi/h].$

Figure 5.7: Eigenvalue spectra of $\widehat{M^{\mathrm{REL}}_{\mathrm{SGS}_{UL}}}(\omega) = \widehat{M^{\mathrm{REL}}_{\mathrm{DGS}_U}}(\omega)\widehat{M^{\mathrm{REL}}_{\mathrm{DGS}_L}}(\omega)$, without damping ($\alpha = 1$), with $\varepsilon/h = 0$.

In the next section, we study the two-level behavior of the cell- and point-wise block-relaxation methods. We will observe that, in case of the DG-method with diffusion term discretized by the Baumann-Oden, only the point-wise Jacobi relaxation method is a promising smoother, while, in case of the DG-method, with diffusion term discretized by the NIPG method, the cell-wise symmetric Gauss-Seidel relaxation methods show good smoothing behavior.

5.4.3 Two-level analysis

Having studied the eigenvalue spectra of the various block-relaxation algorithms, we are now interested in the convergence of the two-level operator (5.16), i.e., the cell- and point-wise JOR and SGS block-relaxation algorithms in combination with the coarse-grid correction. From Section 2.3.5 it follows that the Fourier transform of the coarse grid correction for the error M_h^{CGC} reads

$$\widehat{M_h^{\mathrm{CGC}}}(\omega) = \left(\widehat{I_h} - \widehat{P_{hH}}\widehat{L_H^{-1}}\widehat{R_{Hh}}\widehat{L_h}\right)(\omega) = \begin{pmatrix} 1 & 0 \\ 0 & 1 \end{pmatrix}$$
$$- \begin{pmatrix} \widehat{P_h}(\omega) \\ \widehat{P_h}(\omega + \pi/h) \end{pmatrix} (\widehat{L_H}(\omega))^{-1} \begin{pmatrix} \widehat{R_h}(\omega) & \widehat{R_h}(\omega + \pi/h) \end{pmatrix} \begin{pmatrix} \widehat{L_h}(\omega) & 0 \\ 0 & \widehat{L_h}(\omega + \pi/h) \end{pmatrix},$$

for $\omega \in \mathbb{T}_H = \mathbb{T}_{2h} \equiv \left[-\frac{\pi}{2h}, \frac{\pi}{2h}\right]$. Hence, $\widehat{M_h^{\mathrm{CGC}}}(\omega)$ is a 8×8 matrix of which, in view of (2.21), the eigenvalues $\lambda_i(\omega)$ correspond with the eigenvalues of M_h^{CGC}.

Interested in the asymptotic convergence of the two-level algorithm, we compute spectral radii of $M_h^{\mathrm{CGC}} M_h^{\mathrm{REL}}$ for the cell- and point-wise $M_{\mathrm{JOR}}^{\mathrm{REL}}$, $M_{\mathrm{SGS}_{UL}}^{\mathrm{REL}} = M_{\mathrm{DGS}_U}^{\mathrm{REL}} M_{\mathrm{DGS}_L}^{\mathrm{REL}}$ and $M_{\mathrm{SGS}_{LU}}^{\mathrm{REL}} = M_{\mathrm{DGS}_L}^{\mathrm{REL}} M_{\mathrm{DGS}_U}^{\mathrm{REL}}$ block-relaxation methods as function of the diffusion parameter $\varepsilon/h \in [0, 1]$. Notice that here $M_h^{\mathrm{REL}}(\omega)$ is an 8×8-matrix and $\omega \in \mathbb{T}_H$, which is equivalent with $M_h^{\mathrm{REL}}(\omega) \in \mathbb{R}^{4\times4}$ and $\omega \in \mathbb{T}_h$. We find the spectral radii of $M_h^{\mathrm{CGC}} M_h^{\mathrm{REL}}$ by computing $\max_\omega \rho\left(\widehat{M_h^{\mathrm{CGC}}}\widehat{M_h^{\mathrm{REL}}}(\omega)\right)$, with M_h^{REL} in point-wise notation. The asymptotic convergence factors as function of the diffusion parameter are shown in the Figures 5.8 and 5.9 for the Baumann-Oden and NIPG-method respectively.

If we consider the convergence for the Baumann-Oden method (Figure 5.8), we see that the two-level operator with the *point-wise* Jacobi smoother shows good convergence ($\rho < 0.5$) in the range of $\varepsilon/h > 0.1$. Furthermore, this two-level algorithm is stable on the whole interval $\varepsilon/h \in [0, \infty]$. With the *cell-wise* Jacobi smoother the two-level operator shows good convergence in case of pure convection and convection-dominated problems, $\varepsilon/h \in [0, 0.1]$, however, the convergence is very poor in case of convection-diffusion ($\varepsilon/h > 0.1$).

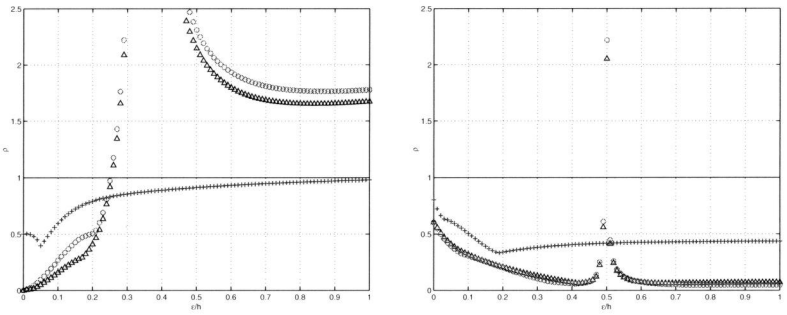

cell-wise relaxation point-wise relaxation

+: JOR; ∘: SGS_{UL}; △: SGS_{LU}.

Figure 5.8: Spectral radii $\rho\left(\widehat{M_h^{\mathrm{CGC}}}\widehat{M_h^{\mathrm{REL}}}(\omega)\right)$ as function of $\varepsilon/h \in [0,1]$ for the case $\sigma = 1$ and $\mu = 0$. No damping ($\alpha = 1$).

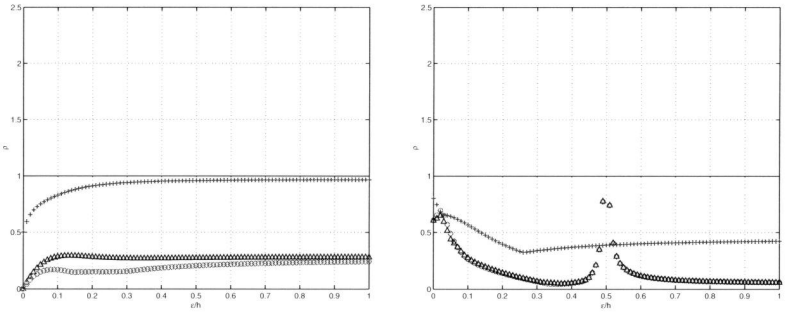

cell-wise relaxation point-wise relaxation

+: JOR; ∘: SGS_{UL}; △: SGS_{LU}.

Figure 5.9: Spectral radii $\rho\left(\widehat{M_h^{\mathrm{CGC}}}\widehat{M_h^{\mathrm{REL}}}(\omega)\right)$ as function of $\varepsilon/h \in [0,1]$ for the case $\sigma = 1$ and $\mu = 10/h$. No damping ($\alpha = 1$).

If we consider the symmetric Gauss-Seidel smoothers (Figure 5.8), in case of the cell-wise block-relaxation methods, we see that the spectral radius is generally larger than one and grows without bound in the neighborhood of $\epsilon/h \approx 0.35$.

We find $\rho < 1$ only for $\epsilon/h < 1/4$. In view of this result, we might expect that these two-level algorithms show acceptable convergence for the range of $\varepsilon/h \in \langle 0, 0.2]$. (In case of pure convection, the problem is solved at once, due to the cell-wise upwind character of the DG-method.) However, in practice, the two-level algorithms will diverge, because of the lack of normality of the finite dimensional operator $B_h^{-1} = L + D$ in the down-wind Gauss-Seidel relaxation method. It can readily be checked that the inverse of the corresponding Toeplitz operator $B_h^{-1} = L + D \equiv G_h$ is unbounded, so that the eigenvalue spectrum of $\widehat{G_h^{-1}}$ does not correspond with the spectrum of $(\widehat{G_h})^{-1}$, since (5.15) is not satisfied.

A similar situation occurs if we consider the two-level algorithms with the point-wise symmetric Gauss-Seidel smoothers (Figure 5.8). We may expect good convergence ($\rho < 0.1$) for the range $\varepsilon/h > 0.6$. However, in the range $\varepsilon/h \in [0, 0.5]$, the finite dimensional two level-algorithms diverge, again due to the lack of normality of the operator $B_h^{-1} = L + D$ in the down-wind Gauss-Seidel relaxation method.

Now, considering the convergence for the NIPG method in Figure 5.9, we clearly see the stabilizing effect of the penalty term ($\mu = 10/h$) on the cell-wise symmetric Gauss-Seidel smoothers. The transition point ($\varepsilon/h \approx 0.35$), after which the Toeplitz operator $B_h = (L + D)^{-1}$ is unbounded, has vanished and normality of the finite dimensional operator is restored. So we may expect an overall good convergence ($\rho < 0.3$) for the whole range $\varepsilon/h \in [0, \infty]$. However, the influence of the penalty term on the point-wise block-relaxation algorithms is small: the transition point $\varepsilon/h \approx 0.5$ does not vanish; for smaller values of ϵ/h the corresponding finite dimensional two-level algorithm diverges.

In view of the above analysis, we conclude that for the Baumann-Oden method, if no interior penalty term is used, the point-wise Jacobi algorithm is a good smoother, provided that for $\varepsilon/h \in [0, 0.5]$ the problem is solved with sufficient accuracy on the coarser mesh (since the smoother alone diverges). Overall good asymptotic convergence of multi-grid cycles is found when cell-wise symmetric Gauss-Seidel smoothers are used, and the discretization method is stabilized by the interior penalty term, i.e., if the NIPG discretization is used.

Given the above results, we further restrict ourselves to the more promising methods. The spectral radii, corresponding with the Figures 5.8 and 5.9, of the

Table 5.3: The spectral radii $\rho\left(M_h^{\mathrm{CGC}} M_{\mathrm{JOR}}^{\mathrm{REL}}\right)$, for different cases of the diffusion parameter ε/h, without damping ($\alpha = 1$). The diffusion term is discretized by the Baumann Oden DG-method.

point-wise relaxation					
ε/h	0	1/4	1/2	3/4	1
$\rho\left(M_h^{\mathrm{CGC}} M_{\mathrm{JOR}}^{\mathrm{REL}}\right)$	0.802	0.363	0.419	0.431	0.435

Table 5.4: The spectral radii $\rho\left(M_h^{\mathrm{CGC}} M_{\mathrm{SGS}_{UL}}^{\mathrm{REL}}\right)$ and $\rho\left(M_h^{\mathrm{CGC}} M_{\mathrm{SGS}_{LU}}^{\mathrm{REL}}\right)$, for different cases of the diffusion parameter ε/h, without damping ($\alpha = 1$). The diffusion term is discretized by the NIPG-method with $\mu = 10/h$.

cell-wise relaxation					
ε/h	0	1/4	1/2	3/4	1
$\rho\left(M_h^{\mathrm{CGC}} M_{\mathrm{SGS}_{UL}}^{\mathrm{REL}}\right)$	0.000	0.150	0.205	0.231	0.243
$\rho\left(M_h^{\mathrm{CGC}} M_{\mathrm{SGS}_{LU}}^{\mathrm{REL}}\right)$	0.000	0.274	0.273	0.279	0.281

point-wise $M_h^{\mathrm{CGC}} M_{\mathrm{JOR}}^{\mathrm{REL}}$ and cell-wise $M_h^{\mathrm{CGC}} M_{\mathrm{SGS}_{UL}}^{\mathrm{REL}}$ and $M_h^{\mathrm{CGC}} M_{\mathrm{SGS}_{LU}}^{\mathrm{REL}}$ (with $\mu = 10/h$) for $\varepsilon/h = 0, 1/4, 1/2, 3/4, 1$, are shown in the Tables 5.3 and 5.4.

We see that the point-wise two-level algorithm shows acceptable convergence ($\rho \approx 0.4$) for the various cases of mixed convection-diffusion. However in case of pure convection, the convergence is somewhat poor ($\rho \approx 0.8$). The cell-wise two-level algorithms show good convergence both for mixed convection-diffusion and for pure convection ($\rho < 0.3$).

Because the spectral radius only predicts the asymptotic rate of convergence, next we check if the methods achieve convergence within a few iteration steps. For this purpose, we compute the 2-norm of the two-level operator. Since both the asymmetric Baumann-Oden and the NIPG formulation are adjoint inconsistent [3, 24], which is reflected in Fourier analysis by unbounded $\|\widehat{M_h^{\mathrm{CGC}}}\,\widehat{M_h^{\mathrm{REL}}}(\omega)\|_2$ for vanishing ω (see Section 2.5.2), we compute the 2-norm of the two-level operator for the residue,

$$\overline{M}_h^{\mathrm{REL}} \overline{M}_h^{\mathrm{CGC}} = L_h M_h^{\mathrm{REL}} L_h^{-1} L_h M_h^{\mathrm{CGC}} L_h^{-1}.$$

The spectral norms of the point-wise unpenalized $\overline{M}_{\mathrm{JOR}}^{\mathrm{REL}} \overline{M}_h^{\mathrm{CGC}}$ and the penalized ($\mu = 10/h$) cell-wise $\overline{M}_{\mathrm{SGS}_{UL}}^{\mathrm{REL}} \overline{M}_h^{\mathrm{CGC}}$ and $\overline{M}_{\mathrm{SGS}_{UL}}^{\mathrm{REL}} \overline{M}_h^{\mathrm{CGC}}$ are shown in the

Table 5.5: The spectral norm $\sigma_{\max}$ after respectively one, two and three iterations for the residue, for different cases of the diffusion parameter ε/h, without damping ($\alpha = 1$). The diffusion term is discretized by the Baumann Oden DG-method.

point-wise relaxation					
ε/h	0	1/4	1/2	3/4	1
$\|\overline{M}_{\text{JOR}}^{\text{REL}}\overline{M}_h^{\text{CGC}}\|$	17.656	4.748	2.600	2.040	1.829
$\|\left(\overline{M}_{\text{JOR}}^{\text{REL}}\overline{M}_h^{\text{CGC}}\right)^2\|$	24.788	2.265	1.131	0.887	0.797
$\|\left(\overline{M}_{\text{JOR}}^{\text{REL}}\overline{M}_h^{\text{CGC}}\right)^3\|$	18.671	0.569	0.443	0.374	0.343

Table 5.6: The spectral norm $\sigma_{\max}$ after respectively one and two iterations for the residue, for different cases of the diffusion parameter ε/h, without damping ($\alpha = 1$). The diffusion term is discretized by the NIPG-method with $\mu = 10/h$.

cellwise relaxation					
ε/h	0	1/4	1/2	3/4	1
$\|\overline{M}_{\text{SGS}_{UL}}^{\text{REL}}\overline{M}_h^{\text{CGC}}\|$	0.000	1.972	1.798	1.804	1.793
$\|\left(\overline{M}_{\text{SGS}_{UL}}^{\text{REL}}\overline{M}_h^{\text{CGC}}\right)^2\|$	0.000	0.360	0.358	0.367	0.379
$\|\overline{M}_{\text{SGS}_{LU}}^{\text{REL}}\overline{M}_h^{\text{CGC}}\|$	0.000	1.370	1.459	1.557	1.601
$\|\left(\overline{M}_{\text{SGS}_{LU}}^{\text{REL}}\overline{M}_h^{\text{CGC}}\right)^2\|$	0.000	0.408	0.462	0.460	0.454

Tables 5.5 and 5.6 for the diffusion parameters $\varepsilon/h = 0, 1/4, 1/2, 3/4, 1$.

We see that, in case of convection-diffusion, for the point-wise Jacobi two-level algorithm the reduction of the residue is guaranteed, from the third iteration step on (Table 5.5), except for the case of pure convection, where the spectral norm is still large. However, in the next section, we see that this large 2-norm is a conservative upperbound. By the influence of the boundary condition, in the finite dimensional case the two-level algorithm already converges within a few iteration steps.

In Table 5.6, we see for the penalized cell-wise symmetric Gauss-Seidel smoothers that the reduction in the residue is guaranteed after two iteration steps.

5.5 Numerical results

In this section we check the theoretical convergence behavior by numerical experiments, where we restrict ourselves to the more promising two-level algorithms with the unpenalized point-wise Jacobi smoother and the cell-wise penalized symmetric Gauss-Seidel smoothers ($\mu = 10/h$). For this purpose, we consider the convection-diffusion equation on $[0,1]$,

$$-\varepsilon u_{xx} + u_x = 1\,, \qquad \text{with } u(0) = 0,\ u(1) = 0,\ \epsilon \geq 0,$$

which for $\varepsilon << 1$ has a sharp boundary layer-type solution, given by

$$u = x - \frac{e^{\frac{x}{\varepsilon}} - 1}{e^{\frac{1}{\varepsilon}} - 1}, \quad x \in [0,1]\,.$$

For the discrete system we use the polynomial basis (2.8) and we take $h = 2^{-7}$. As initial approximation we choose the vector $u_h^0 = [1000, .., .., 1000]$, i.e, a large constant grid function, not satisfying the boundary conditions. For respectively the point-wise Jacobi and the cell-wise symmetric Gauss-Seidel relaxation, we apply a single and a double pre-relaxation sweep

$$u_{h,\mathrm{PRE}}^{i+1} = u_{h,\mathrm{PRE}}^{i} + B_h\left(f_h - L_h u_{h,\mathrm{PRE}}^{i}\right),$$

where B_h is the approximate inverse of L_h as given in Table 2.1 in Section 2.4. We solve the problem on the coarse grid $H = 2^{-6}$, during the coarse grid correction

$$u_h^{i+1} = u_{h,\mathrm{PRE}}^{i+1} + P_{hH} L_H^{-1} \overline{R}_{Hh}(f_h - L_h u_{h,\mathrm{PRE}}^{i+1}).$$

To be consistent with the Fourier analysis (see Section 2.3), we measure the residue in the 2-norm

$$\|d_h\|_2 = \|f_h - L_h u_h\|_2 = \sqrt{\sum_{e=1}^{128}\sum_{j=1}^{4} d_{he,j}^2}\,.$$

The convergence plots for unpenalized point-wise $M_h^{\mathrm{CGC}} M_{\mathrm{JOR}}^{\mathrm{REL}}$ and the penalized cell-wise $M_h^{\mathrm{CGC}} M_{\mathrm{SGS}_{UL}}^{\mathrm{REL}}$ and $M_h^{\mathrm{CGC}} M_{\mathrm{SGS}_{LU}}^{\mathrm{REL}}$ with diffusion parameters $\varepsilon/h = 0, 1$ are shown in Figure 5.10. The convergence factors observed, for diffusion parameters $\varepsilon/h = 0, 1/4, 1/2, 3/4, 1$ are shown in the Tables 5.7 and 5.8.

We see that, in case of pure convection, the two-level operator with the point-wise Jacobi smoother converges from the first iteration step, regardless

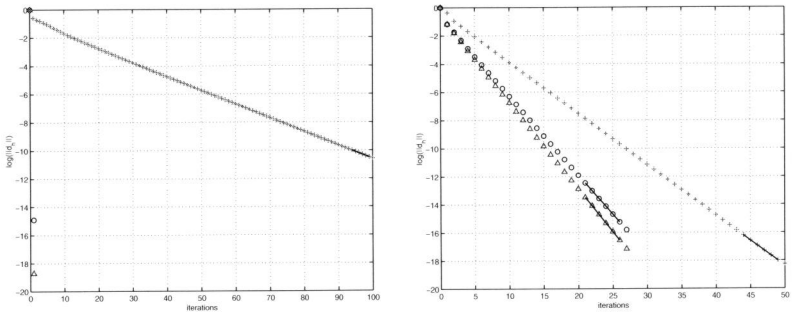

$\varepsilon/h = 0$ $\varepsilon/h = 1$

+: JOR; △: SGS_{UL}; ○: SGS_{LU}.

Figure 5.10: $\log(||d_h||_2)$ as function of iterations for the two-level operator on the error with the unpenalized point-wise Jacobi smoother and penalized cell-wise symmetric Gauss-Seidel smoothers $\mu = 10/h$.

Table 5.7: Numerically obtained convergence factors, corresponding with $\rho(M^{\text{CGC}} M^{\text{REL}}_{\text{JOR}})$, without damping ($\alpha = 1$), for different cases of ε/h. The diffusion term is discretized by the Baumann-Oden DG-method.

point-wise relaxation

ε/h	0	1/4	1/2	3/4	1
$M_h^{\text{CGC}} M^{\text{REL}}_{\text{JOR}}$	0.80	0.36	0.42	0.43	0.44

the large 2-norm shown in Table 5.5. The cell-wise symmetric Gauss-Seidel smoothers solve the problem at once, because of the cell-wise upwind character of the DG-method. Also in case of convection-diffusion, convergence is observed from the first iteration step on. Furthermore, in all cases of convection-diffusion, the observed convergence factors coincide very well with the spectral radii shown in the Tables 5.3 and 5.4.

5.6 Conclusion

Having shown in the previous chapters that straightforward multi-grid (MG) is quite effective for the solution of the Poisson equation discretized by higher order discontinuous Galerkin (DG) methods, we now study the convergence of MG for the solution of the convection-diffusion equation.

Table 5.8: Numerically obtained convergence factors, corresponding with $\rho\left(M^{\mathrm{CGC}} M^{\mathrm{REL}}_{\mathrm{SGS}_{UL}}\right)$ and $\rho\left(M^{\mathrm{CGC}} M^{\mathrm{REL}}_{\mathrm{SGS}_{LU}}\right)$, for different cases of the diffusion parameter ε/h, without damping ($\alpha = 1$). The diffusion term is discretized by the NIPG-method with $\mu = 10/h$.

	cell-wise relaxation				
ε/h	0	1/4	1/2	3/4	1
$M^{\mathrm{CGC}} M^{\mathrm{REL}}_{\mathrm{SGS}_{UL}}$	0.000	0.14	0.20	0.23	0.25
$M^{\mathrm{CGC}} M^{\mathrm{REL}}_{\mathrm{SGS}_{LU}}$	0.000	0.27	0.27	0.27	0.28

For the generic fourth-order discretization we consider DG-methods with the diffusion term discretized by the asymmetric Baumann-Oden (BO) or the non-symmetric interior penalty method (NIPG) because these methods yield positive definite discrete operators. We study classical multigrid iteration with simple block-relaxation (Jacobi or symmetric Gauss-Seidel) as smoothing procedure. We distinguish two essentially distinct types of block-relaxation algorithms: the classical block-relaxation methods based using a *cell-wise* partitioning of the discretization matrix, and the new block-relaxation methods based on *point-wise* partitioning.

By Fourier analysis we show that a robust method, applicable in the whole range of convection-diffusion, dominating convection and pure convection, with acceptable MG convergence, can only be achieved for the Baumann-Oden method if point-wise block Jacobi smoothing is applied and the problem is solved with sufficient accuracy on the coarser mesh.

However, MG with classical cell-wise symmetric Gauss-Seidel smoothing is quite effective for the NIPG method. Here convergence factors $\rho < 0.3$ are found for the whole range of convection-diffusion to pure convection. Moreover, an analysis of the two-level spectral norm shows that an reduction of the residue is guaranteed within two iteration steps.

Thus, the present analysis justifies the use of an interior penalty term in higher order DG-methods when MG is applied for the solution of the convection-diffusion equation.

Chapter 6

DG discretization with embedded boundary conditions

Summary

The purpose of this chapter is to introduce discretization methods of discontinuous Galerkin type for solving second order elliptic PDEs on a structured, regular grid, while the problem is defined on a curved boundary. The methods aim at high-order accuracy and the difficulty arises since the regular grid cannot follow the curved boundary.

Starting with the Lagrange multiplier formulation for the boundary conditions, we derive variational forms for the discretization of 2-D elliptic problems with embedded Dirichlet boundary conditions. Within the framework of structured, regular rectangular grids, we treat curved boundaries according to the principles that underlie the discontinuous Galerkin method. Thus, the high-order DG-discretization is adapted in the cells with embedded boundaries. We give examples of approximation with tensor products of cubic polynomials.

As an illustration, we solve a convection dominated boundary value problem on a complex domain. Although, of course, it is impossible to accurately represent a boundary layer with a complex structure by means of a cubic polynomial, the boundary condition treatment appears quite effective in handling

such complex situations.

6.1 Introduction

The purpose of this chapter is to introduce methods of discontinuous Galerkin type for solving second order elliptic PDEs on a structured, regular grid while the problem is defined on a curved boundary. The methods aim at high-order accuracy and the difficulty arises because the regular grid cannot follow the curved boundary.

Earlier, several techniques have been proposed to handle boundary conditions on irregular, curvilinear boundaries. The most convenient certainly is the FEM, where elements near the boundary are adapted to the shape of the boundary curve. Generally, this results in an unstructured grid. This relatively straightforward technique can be applied up to arbitrary high-order of accuracy and delivers good results.

In contrast, finite difference methods are usually applied on regular grids. Here, curved boundaries are treated by locally adapted finite differences as, e.g., Shortley-Weller approximation [17, Sect.4.8]. Generally, such discretizations are not used for higher orders of accuracy.

A more recent technique for treatment of complex boundaries on orthogonal grids, in two or three dimensions, is the Embedded Curved Boundary (ECB) method. Here –usually in the context of the discretization of conservation laws– piecewise linear segments are embedded in the grid to represent the boundary. Generalizations are used, e.g., to solutions across interfaces [27, 28]. In many cases the ECB method shows clear advantages compared to the traditional stair-step method [32] but no higher-order accuracy than order two can be expected.

A higher order may be obtained by Immersed Boundary Methods (IBM) [33, 34, 35, 46], e.g., in pseudo-spectral codes [14], where the presence of a boundary within the computational domain is simulated by specifying a body force term, without altering the computational grid. This technique is very flexible as it allows for bodies and interfaces of almost arbitrary shape. The method is quite popular in situations with rather complex geometries [31] and e.g., elastic boundaries [39]. Usually the method is applied as to maintain second order accuracy (first order near the boundaries). However, fourth-order convergence rates are reported in [10], where the same methodology is used with PDEs for thin flexible membranes in an incompressible fluid domain.

In contrast with the above methods, we take the Lagrange multiplier formulation of the boundary conditions as a starting point, in the same manner

as used in [36] or in the derivation of the discontinuous Galerkin discretization. Within the framework of structured, regular rectangular grids we introduce the treatment of curved boundaries in full agreement with the principles that lead to the discontinuous Galerkin method.

We apply a high-order DG-discretization in the interior and adapt the method in the cells with embedded boundaries. The order of approximation of the boundary condition corresponds with the accuracy of the DG-method. In the present chapter we give examples of approximation with tensor products of cubic polynomials.

In Chapter 2 we explained why the treatment of this cubic polynomial case is the basis for higher-order approximation. In the DG discretization, information exchange over the interior cell boundaries by function values and normal fluxes. On an interval, at the endpoints, function values and fluxes are determined by four independent parameters, that correspond with the four degrees of freedom in the cubic polynomial approximation on a cell. Higher-order approximation can be achieved by additional bubble functions with vanishing values and derivatives at the cell boundary. In the multi-dimensional case, on a structured rectangular grid, the same principle holds with tensor-products for approximation.

For the treatment of the embedded boundary conditions, we give in Section 6.2 of this chapter an exposition of the weak forms used for the different discretization alternatives. In Section 6.3 we start with simple experiments in one and two dimensions to see the differences between the various methods. In Section 6.4 we identify the discrete function spaces in which the approximate solution is found. In the last section we solve a convection-dominated equation on an irregular domain, partitioned in two cells only. We show how well a complex problem can be solved on this mesh with a piecewise cubic approximation.

6.2 Weak forms for the Poisson equation

6.2.1 The Lagrange multiplier form for the embedded boundary problem

To apply DG-methods for structured rectangular grids on complicated domains, we are interested in solving an elliptic second order problem $Lu = f$ on a fictitious open domain $\widehat{\Omega}$, which is larger than the open domain Ω on which the elliptic BVP is originally defined. The solution u on Ω is determined by the Dirichlet boundary condition $u = u_0$ on $\partial\Omega$, the boundary of Ω, and we want to

discretize the problem on a fictitious domain $\widehat{\Omega} \supseteq \Omega$. For this purpose we assume that the solution u on Ω allows a sufficiently smooth extension, u, defined on $\widehat{\Omega}$, solving $Lu = f$. Of course, this excludes certain types of singularities near the boundary.

For sake of simplicity, in this initial treatment we assume $\widehat{\Omega}$ to be the unit cube and we consider the Poisson equation with an embedded Dirichlet boundary condition as follows: let $\widehat{\Omega}$ be the open unit cube, with boundary $\partial\widehat{\Omega}$, which consists of two non-overlapping open sub-domains, Ω and $\widetilde{\Omega}$, such that

$$\overline{\widehat{\Omega}} = \overline{\Omega} \cup \overline{\widetilde{\Omega}}, \qquad \text{and} \qquad \Omega \cap \widetilde{\Omega} = \emptyset, \tag{6.1}$$

where $\widetilde{\Omega}$ is the fictitious part of the domain $\widehat{\Omega}$. We now consider the boundary value problem consisting of the Poisson equation defined on the whole of $\widehat{\Omega}$ and Dirichlet boundary conditions on $\partial\Omega$, the boundary of Ω:

$$Lu \equiv -\Delta u = f \ \text{ on } \ \widehat{\Omega}, \qquad \text{and} \qquad u = u_0 \ \text{ on } \ \Gamma_{\mathrm{D}} = \partial\Omega, \tag{6.2}$$

under the assumption that the solution u on Ω, has a sufficiently smooth continuation to $\widetilde{\Omega}$, satisfying the Poisson equation on the whole of $\widehat{\Omega}$.

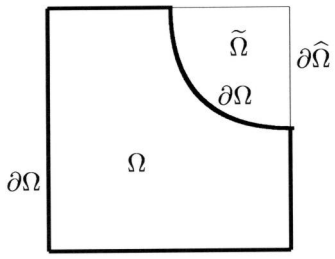

Figure 6.1: The domain of interest, Ω and the fictitious part, $\widetilde{\Omega}$, make the domain $\widehat{\Omega} = \Omega \cup \widetilde{\Omega}$.

To arrive at the corresponding weak formulation of the Poisson equation with 'embedded' Dirichlet boundary condition, we multiply the left- and right-hand side of (6.2) with a sufficiently smooth function v, and integrate over the domain $\widehat{\Omega}$, to get: find $u \in H^1(\widehat{\Omega})$ such that

$$(\nabla u, \nabla v)_{\widehat{\Omega}} - \langle \mathbf{n} \cdot \nabla u, v \rangle_{\partial\widehat{\Omega}} = (f, v)_{\widehat{\Omega}}\,, \qquad \forall v \in H^1(\widehat{\Omega}), \tag{6.3}$$

under the constraint that $u = u_0$ on $\partial\Omega$. By the Lagrange multiplier theorem, the following formulation is equivalent to (6.3): find $u \in H^1(\widehat{\Omega})$ and

$\overline{p} \in H^{-1/2}(\partial\Omega)$ such that

$$\begin{aligned}(\nabla u, \nabla v)_{\widehat{\Omega}} - \langle \mathbf{n}\cdot\nabla u, v\rangle_{\partial\widehat{\Omega}} + \langle \overline{p}, v\rangle_{\partial\Omega} &= (f,v)_{\widehat{\Omega}}, \qquad \forall v \in H^1(\widehat{\Omega}), \\ \langle q, u\rangle_{\partial\Omega} &= \langle q, u_0\rangle_{\partial\Omega}\,, \quad \forall q \in H^{-1/2}(\partial\Omega).\end{aligned} \tag{6.4}$$

We call this the *Lagrange multiplier form* of the embedded boundary problem. We see that, if u satisfies the Poisson equation (6.2) and the embedded Dirichlet boundary condition, the Lagrange multiplier $\overline{p}$ in (6.4) vanishes.

6.2.2 The weak form for boundaries along gridlines

In the classical case that $\widetilde{\Omega} = \emptyset$, we can combine the boundary terms in (6.4), in order to obtain

$$\begin{aligned}(\nabla u, \nabla v)_{\widehat{\Omega}} - \langle p, v\rangle_{\partial\widehat{\Omega}} &= (f,v)_{\widehat{\Omega}}, \qquad \forall v \in H^1(\widehat{\Omega}), \\ \langle q, u\rangle_{\partial\Omega} &= \langle q, u_0\rangle_{\partial\Omega}\,, \quad \forall q \in H^{-1/2}(\partial\Omega),\end{aligned}$$

with $p = \mathbf{n}\cdot\nabla u - \overline{p}$ on $\partial\Omega = \partial\widehat{\Omega}$. This leads to a *hybrid* form of (6.2) with Dirichlet BCs: find $u \in H^1(\widehat{\Omega})$ and $p \in H^{-1/2}(\partial\Omega)$ such that

$$\begin{aligned}(\nabla u, \nabla v)_{\widehat{\Omega}} - \langle p, v\rangle_{\partial\widehat{\Omega}} - \langle q, u\rangle_{\partial\Omega} &= (f,v)_{\widehat{\Omega}} - \langle q, u_0\rangle_{\partial\Omega}\,, \quad \forall v \in H^1(\widehat{\Omega}), \\ &\qquad\qquad \forall q \in H^{-1/2}(\partial\Omega).\end{aligned} \tag{6.5}$$

When u satisfies (6.2) we have $p = \mathbf{n}\cdot\nabla u$, the normal flux at the boundary $\partial\widehat{\Omega}$. Substituting this value for p, and replacing similarly the weighting function q by $q = -\sigma\mathbf{n}\cdot\nabla v$, with $\sigma = 1$ or $\sigma = -1$, this leads to the weak form used in DG-methods (viz., Baumann's and the symmetric DG-method respectively). Other DG-methods (viz., IPG, NIPG) are obtained by taking $q = -\sigma\mathbf{n}\cdot\nabla v - \mu v$ with parameters σ and μ. Thus, our DG weak form reads: find $u \in H^1(\widehat{\Omega})$ such that

$$\begin{aligned}(\nabla u, \nabla v)_{\widehat{\Omega}} - \langle \mathbf{n}\cdot\nabla u, v\rangle_{\partial\widehat{\Omega}} + \sigma\,\langle \mathbf{n}\cdot\nabla v, u\rangle_{\partial\Omega} & \\ = (f,v)_{\widehat{\Omega}} + \sigma\,\langle \mathbf{n}\cdot\nabla v, u_0\rangle_{\partial\Omega}\,, \quad \forall v \in H^1(\widehat{\Omega}).&\end{aligned} \tag{6.6}$$

6.2.3 The hybrid and the DG-form for the embedded boundary problem

Not only the Lagrange multiplier form (6.4) can be used for the embedded boundary problem, we can also apply (6.5) or (6.6). In the case $\widetilde{\Omega} \neq \emptyset$ the form

(6.5) reads: find $u \in H^1(\widehat{\Omega})$ and $p \in H^{-1/2}(\partial\widehat{\Omega})$ such that

$$(\nabla u, \nabla v)_{\widehat{\Omega}} - \langle p, v\rangle_{\partial\widehat{\Omega}} - \langle q, u\rangle_{\partial\Omega} = (f, v)_{\widehat{\Omega}} - \langle q, u_0\rangle_{\partial\Omega}, \quad \begin{array}{l}\forall v \in H^1(\widehat{\Omega}), \\ \forall q \in H^{-1/2}(\partial\Omega),\end{array} \tag{6.7}$$

which we call the *hybrid* form of the interior boundary problem. In the case $\widetilde{\Omega} \neq \emptyset$, equation (6.6) is written: find $u \in H^1(\widehat{\Omega})$ such that

$$\begin{aligned}(\nabla u, \nabla v)_{\widehat{\Omega}} - \langle \mathbf{n}\cdot\nabla u, v\rangle_{\partial\widehat{\Omega}} + \sigma \langle \mathbf{n}\cdot\nabla v, u\rangle_{\partial\Omega} & \\ = (f, v)_{\widehat{\Omega}} + \sigma \langle \mathbf{n}\cdot\nabla v, u_0\rangle_{\partial\Omega}, \quad \forall v \in H^1(\widehat{\Omega}),&\end{aligned} \tag{6.8}$$

which we call the *DG-form* (the Baumann-Oden weak form if $\sigma = 1$ or the symmetric form if $\sigma = -1$) of the interior boundary problem. Notice that this symmetric weak form is not symmetric anymore if $\Omega \neq \widehat{\Omega}$.

6.3 Numerical experiments in one and two dimensions

6.3.1 Numerical experiments on one-dimensional problems

To see the difference in practice, we first study the three weak forms (6.4), (6.7) and (6.8) for a simple one-dimensional problem. On the unit interval $\widehat{\Omega} = (0, 1)$ we consider the Poisson equation with homogeneous Dirichlet boundary conditions:

$$-\frac{d^2u}{dx^2} = f, \quad \text{on } \widehat{\Omega}, \quad \text{with } u(d) = 0, \quad u(1) = 0, \tag{6.9}$$

where $d \in [0, 1)$ and $\Omega = (d, 1)$. To discretize this problem we take for test and trial spaces the $(p+1)$-dimensional space $S_h(\widehat{\Omega}) = P^p(\widehat{\Omega}) \subset H^1(\widehat{\Omega})$, i.e., the space of polynomials of degree $\leq p$.

$$u_h = \sum_{0\leq i\leq p} c_i\phi_i(x), \quad \phi_i(x) \in S_h(\widehat{\Omega}).$$

Further, we provide the boundary spaces $Q_h(\partial\widehat{\Omega}) \subset H^{-1/2}(\partial\widehat{\Omega})$ and $Q_h(\partial\Omega) \subset H^{-1/2}(\partial\Omega)$, with the trace of polynomials on the boundary, hence

$$Q_h(\partial\widehat{\Omega}) = \left\{\psi_0(x) = (1-x)|_{x=(0,1)},\ \psi_1(x) = x|_{x=(0,1)})\right\},$$

and

$$Q_h(\partial\Omega) = \left\{ \psi_0(x) = \frac{x-1}{d-1}|_{x=(d,1)}, \psi_1(x) = \frac{x-d}{1-d}|_{x=(d,1)}) \right\}, \quad d \in [0,1).$$

Then we write for the approximation of the Lagrange multiplier:

$$p_h = \sum_{0 \le i \le 1} a_i \psi_i(x)|_{x=0,d,1}.$$

Because of the 1-D character of this example, boundary values are parameterized by only two values for both $\partial\widehat{\Omega}$ and $\partial\Omega$. Given the approximating spaces, the three forms (6.4), (6.7) and (6.8) become:
(i) In case of the *Lagrange multiplier formulation*: find $u_h \in S_h(\widehat{\Omega})$, $\overline{p}_h \in Q_h(\partial\Omega)$ such that

$$\int_0^1 u_h' v_h' dx - [u_h'(1)v_h(1) - u_h'(0)v_h(0)] + [\overline{p}_h(1)v_h(1) + \overline{p}_h(d)v_h(d)] \qquad (6.10)$$
$$+ [q_h(1)u_h(1) + q_h(d)u_h(d)] = \int_0^1 v_h f dx, \qquad \forall v_h \in S_h(\widehat{\Omega}),\ \forall q_h \in Q_h(\partial\Omega);$$

(ii) in case of the *hybrid form*: find $u_h \in S_h(\widehat{\Omega})$, $p_h \in Q_h(\partial\widehat{\Omega})$ such that

$$\int_0^1 u_h' v_h' dx - [p_h(1)v_h(1) + p_h(0)v_h(0)] - [q_h(1)u_h(1) + q_h(d)u_h(d)] \qquad (6.11)$$
$$= \int_0^1 v_h f dx, \qquad \forall v_h \in S_h(\widehat{\Omega}),\ \forall q_h \in Q_h(\partial\Omega);$$

(iii) whereas the *DG-formulation* reduces to: find $u_h \in S_h(\widehat{\Omega})$ such that

$$\int_0^1 u_h' v_h' dx - [u_h'(1)v_h(1) - u_h'(0)v_h(0)] + \sigma\,[v_h'(1)u_h(1) - v_h'(d)u_h(d)] \qquad (6.12)$$
$$= \int_0^1 v_h f dx, \qquad \forall v_h \in S_h(\widehat{\Omega}).$$

As a first experiment we check if the three discrete forms (6.10), (6.11) and (6.12) can solve for the exact solution, when we choose $f(x) = x$ in (6.9) and $d = 1/2$, and if we take $S_h(\widehat{\Omega}) = P^3(\widehat{\Omega})$. The result is shown in Figure 6.2. It appears that all three formulations compute the exact solution.

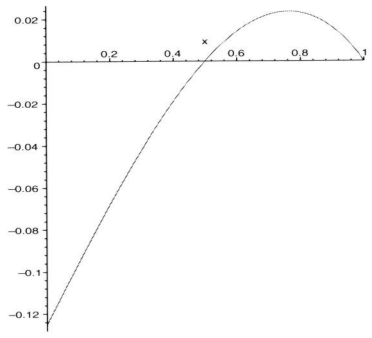

Figure 6.2: The solution $u(x) = -\frac{1}{6}x^3 + \frac{7}{24}x - \frac{1}{8}$ computed by the hybrid, Lagrange, symmetric and the Baumann method, $\sigma = \pm 1$.

The computed Lagrange-multipliers for the hybrid and Lagrange formulation are shown in Table 6.1. We see that, in case of the hybrid formulation, the Lagrange multipliers correspond with the fluxes at the boundaries, i.e., $p_h(0) = \frac{du}{dn}(0)$ and $p_h(1) = \frac{du}{dn}(1)$, whereas for the Lagrange formulation, the Lagrange multipliers vanish.

Table 6.1: The values of the Lagrange multipliers of hybrid and Lagrange methods for the solution as in Figure 6.2.

Lagrange method	(6.10)	$p_h(d) = 0$	$p_h(1) = 0$
hybrid method	(6.11)	$p_h(0) = -5/25$	$p_h(1) = -7/24$

Next we check if we can solve (6.2) for an arbitrary location $d \in [0, 1)$ of the interior Dirichlet boundary condition. Now we see that the dependencies on d and σ differ for the three methods. In case of the symmetric or Baumann-Oden method, we have to solve a full $(p+1) \times (p+1)$ linear system $L_{\sigma,d}\ u_h = f_h$, where the matrix depends on both the method parameter σ and the interior boundary location d.

In contrast, if we consider the coefficients of the linear system arising from the hybrid and the Lagrange methods we observe the following block-partitioning:

$$L_{\sigma,d}\ u_h = \begin{pmatrix} \mathbf{A} & \mathbf{B} \\ \mathbf{C} & \mathbf{0} \end{pmatrix} u_h = f_h,$$

where, for the Lagrange method, $\mathbf{A} \cong \int_0^1 u_h' v_h' dx - [u_h'(1,0)v_h(1,0)]$ is the $(p+$

$1)\times(p+1)$ leading submatrix, and $\mathbf{B} \cong [\overline{p}_h(d,1)v_h(d,1)]$ and $\mathbf{C} \cong [q_h(d,1)u_h(d,1)]$ have respectively dimensions $(p+1)\times 2$ and $2\times(p+1)$. The dependence on d is reflected in the elements of $\mathbf{B}$ and $\mathbf{C}$.

On the other hand, in case of the hybrid method, we have a $(p+1)\times(p+1)$ leading submatrix $\mathbf{A} \cong \int_0^1 u_h' v_h' dx$. Now the $(p+1)\times 2$ submatrix $\mathbf{B} \cong [p_h(0,1)v_h(0,1)]$ is independent of d. The dependence on d is only reflected in the $2\times(p+1)$ matrix $\mathbf{C} \cong [q_h(d,1)u_h(d,1)]$.

So we check if there are locations $d \in [0,1)$ in which any of the three methods may become singular. The results are shown in Table 6.2. We see that both the Lagrange and the symmetric Baumann methods have interior boundary locations where the methods become singular. The number of points where a singularity appears increases with the polynomial degree. The hybrid method, however, shows no singular points. This motivates us to continue mainly with the hybrid method for the two-dimensional numerical experiments.

Table 6.2: Values for d for which the discrete system becomes singular. The discretizations are made for $S_h(\widehat{\Omega}) = P^p(0,1)$, $p = 2,3,4$.

p	The Lagrange method			The symmetric Baumann method	
2	$1/3$	–	–	–	–
3	$2/5 - 1/10\sqrt{6}$	$2/5 + 1/10\sqrt{6}$	–	$2/5$	–
4	0.08858795951	0.4094668644	0.7876594618	$3/7 - 1/7\sqrt{2}$	$3/7 + 1/7\sqrt{2}$

6.3.2 Numerical experiments for the hybrid method on two-dimensional problems

Having studied the one-dimensional discretization for the various weak formulations with an embedded Dirichlet boundary condition, we now consider the two-dimensional Poisson equation on the unit square $\widehat{\Omega}$ as in (6.2) with an embedded Dirichlet boundary condition on a line parallel to a diagonal. For this line we use the following parametrization (See Figure 6.3):

$$\begin{cases} x(s) = 1 - d/\sqrt{2} + s, \\ y(s) = 1 - d/\sqrt{2} - s, \end{cases} \quad \text{with} \quad \begin{cases} |s| < d & \text{if } 0 \le d \le 1/\sqrt{2}, \\ |s| < 1 - d/\sqrt{2} & \text{if } 1/\sqrt{2} < d < \sqrt{2}. \end{cases}$$

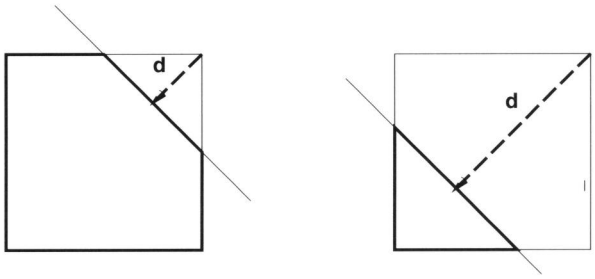

Figure 6.3: The domain Ω and its parametrization

Approximation with piecewise quadratics.

To discretize the hybrid formulation, we first introduce the quadratic polynomial basis on the unit interval

$$P^2([0,1]) = \text{Span}\{1-t,\ t,\ t(1-t)\}.$$

We provide the test and trial function spaces with the 9 dimensional subspace $S_h(\widehat{\Omega}) = P^{2\times 2}(\widehat{\Omega}) = P^2(x) \otimes P^2(y) \subset H^1(\widehat{\Omega})$, i.e., the tensor product set of polynomials of degree ≤ 2 in the two coordinate directions. Since we know that the Lagrange multiplier of the hybrid method corresponds with the flux $p = \mathbf{n} \cdot \nabla u$ on the boundary $\partial\widehat{\Omega}$, we choose to discretize the Lagrange multiplier as $p_h = n_x \psi_x(x,y)|_{\partial\widehat{\Omega}} + n_y \psi_y(x,y)|_{\partial\widehat{\Omega}}$, with $\psi \in P^{2\times 2}(\widehat{\Omega})$ which defines the polynomial subspace $Q_h(\partial\widehat{\Omega}) \subset H^{-1/2}(\partial\widehat{\Omega})$ and also $Q_h(\partial\Omega) \subset H^{-1/2}(\partial\Omega)$ by $p_h|_{\partial\Omega} = n_x \psi_x(x,y)|_{\partial\Omega} + n_y \psi_y(x,y)|_{\partial\Omega}$. Then the discrete formulation of the hybrid form is: find $u_h \in S_h(\widehat{\Omega})$, $p_h \in Q_h(\partial\widehat{\Omega})$ such that

$$\begin{aligned} \langle \nabla u_h, \nabla v_h \rangle_{S_h(\widehat{\Omega})} - \langle p_h, v_h \rangle_{Q_h(\partial\widehat{\Omega})} &= \langle f, v_h \rangle_{S_h(\widehat{\Omega})}, \quad \forall v_h \in S_h(\widehat{\Omega}), \\ \langle q_h, u_h \rangle_{Q_h(\partial\Omega)} &= \langle q, u_0 \rangle_{Q_h(\partial\Omega)}, \quad \forall q \in Q_h(\partial\Omega), \end{aligned} \tag{6.13}$$

where the approximations are given by (9 degrees of freedom describe the polynomial in the interior)

$$u_h(x,y) = \sum_{0 \leq i \leq 8} c_i \phi_i(x,y), \quad \phi_i \in S_h(\widehat{\Omega}),\ (x,y) \in \widehat{\Omega}, \tag{6.14}$$

and (note that 8 degrees of freedom describe the quadratic polynomials at the 4 boundaries)

$$p_h(x,y) = \sum_{0\le i\le 7} a_i \left[n_x \psi_{x,i}(x,y)|_{\partial\widehat{\Omega}} + n_y \psi_{y,i}(x,y)|_{\partial\widehat{\Omega}} \right], \tag{6.15}$$

$$\psi_{x,i}|_{\partial\widehat{\Omega}}, \psi_{y,i}|_{\partial\widehat{\Omega}} \in Q_h(\partial\widehat{\Omega}),\ (x,y) \in \partial\widehat{\Omega}.$$

The result is a 17×17 linear system depending on the diagonal distance of the embedded Dirichlet boundary to the origin. It is obvious that all methods will become ill-conditioned for values of d close to $\sqrt{2}$, when the region Ω vanishes. In order to see how the singularity develops for the hybrid method (6.13), we plot the 17 singular values as function of the diagonal distance d. The result is shown in Figure 6.4. We see that, as in the one-dimensional experiment, also for this experiment, there are no values of d for which the discretization matrix becomes singular. Furthermore the method is not ill-conditioned for values of d even larger than one.

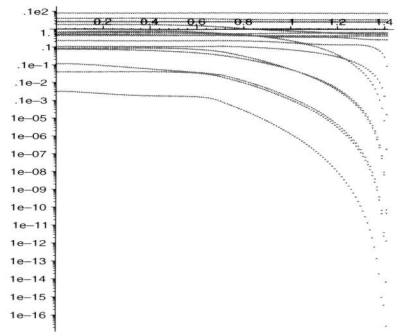

Figure 6.4: Singular values σ_i, $1 \le i \le 17$ as function of the diagonal distance $0 \le d < \sqrt{2}$ for the third order discretization of the hybrid method.

Approximation with piecewise cubics.

Next we want to study the regularity of a higher order discretization of the hybrid method (6.7), for the same two-dimensional model problem. To this end, we consider on the unit interval the cubic polynomial basis

$$P^3([0,1]) = \{1-t,\ t,\ t(1-t)^2, t^2(1-t)\ \}, \tag{6.16}$$

and we choose for the test- and trial function spaces the 16-dimensional subspace $S_h(\widehat{\Omega}) = P^{3\times 3}(\widehat{\Omega}) = P^3(x) \otimes P^3(y) \subset H^1(\widehat{\Omega})$, i.e., the tensor product polynomials of degree less than four in the two coordinate directions. We choose the polynomial subspaces $Q_h(\partial\widehat{\Omega}) = \gamma_1^{\partial\widehat{\Omega}}(S_h(\widehat{\Omega})) \subset H^{-1/2}(\partial\widehat{\Omega})$ and $Q_h(\partial\Omega) = \gamma_1^{\partial\Omega}(S_h(\widehat{\Omega})) \subset H^{-1/2}(\partial\Omega)$. The choice of the basis functions in $Q_h(\partial\Omega)$ will be explained in the next section, where we study the general case with a curved boundary.

As explained in Section 6.4, using (6.13) and (6.14) we obtain a 28×28 system depending on the diagonal distance d of the interior Dirichlet boundary to the origin. For this hybrid discretization, the 28 singular values as function of d are shown in Figure 6.5. Generally, we observe the same behavior as for the quadratic polynomials.

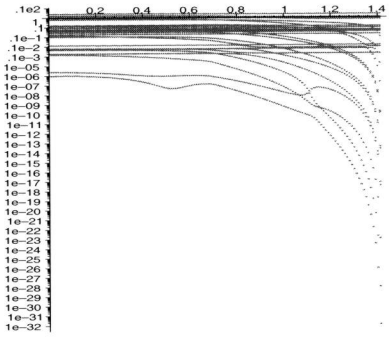

Figure 6.5: Singular values σ_i, $1 \leq i \leq 28$ as function of the diagonal distance $0 \leq d < \sqrt{2}$ for the fourth order discretization of the hybrid method.

6.4 Weak forms for embedded boundary conditions

6.4.1 The boundary condition on a curved embedded boundary

In this section we study the regularity and the accuracy of a fourth order hybrid discretization of the Poisson equation on the unit square, with a part of the

circular boundary embedded. So, we solve the equation

$$-\Delta u = f \quad \text{on} \quad \widehat{\Omega}, \qquad \text{with} \quad u = u_0 \quad \text{on} \quad \Gamma_D = \partial\Omega, \tag{6.17}$$

on the unit square from which a circle sector has been removed: i.e., $\widehat{\Omega}$ is the unit square and $\Gamma_{\text{int}} \subset \partial\Omega$, with $\Omega \subset \widehat{\Omega}$, is the circular curve

$$\Gamma_{\text{int}} = \left\{(x,y) \mid x^2 + y^2 = R^2 < \sqrt{2},\ x \geq 0,\ y \geq 0\right\}, \tag{6.18}$$

and the fictitious part is

$$\widetilde{\Omega} = \left\{(x,y) \mid x > 0,\ y > 0,\ x^2 + y^2 < R^2\right\}. \tag{6.19}$$

The corresponding discrete hybrid formulation reads: find $u_h \in S_h(\widehat{\Omega})$ and $\chi_h \in Q_h(\widehat{\Omega})$ such that

$$\begin{aligned} (\nabla u_h, \nabla v_h)_{\widehat{\Omega}} - \left\langle \gamma_1^{\widehat{\Omega}}(\chi_h), \gamma_0^{\widehat{\Omega}}(v_h) \right\rangle_{\partial\widehat{\Omega}} &= (f, v_h)_{\widehat{\Omega}}, && \forall v_h \in S_h(\widehat{\Omega}), \\ \left\langle \gamma_1^{\Omega}(q_h), \gamma_0^{\Omega}(u_h) \right\rangle_{\partial\Omega} &= \left\langle \gamma_1^{\Omega}(q_h), u_0 \right\rangle_{\partial\Omega}, && \forall q_h \in Q_h(\widehat{\Omega}), \end{aligned} \tag{6.20}$$

where $S_h(\widehat{\Omega}) \subset H^1(\widehat{\Omega})$ and $Q_h(\widehat{\Omega}) \subset H^1(\widehat{\Omega})$ are the proper finite dimensional polynomial subspaces, and γ_0^{Ω}, γ_1^{Ω} and $\gamma_0^{\widehat{\Omega}}$, $\gamma_1^{\widehat{\Omega}}$ are the usual trace operators on $\partial\Omega$ and $\partial\widehat{\Omega}$ respectively. To provide these subspaces with a basis, we choose cubic polynomials and consider the following polynomial basis on the unit interval:

$$\phi_1 = 1 - t, \quad \phi_2 = (1-t)^2 t, \quad \phi_3 = (1-t)t^2, \quad \phi_4 = t. \tag{6.21}$$

We recognize that $\phi_1(t)$ and $\phi_4(t)$ are associated with function values at $t = 0, 1$ respectively, while $\phi_2(t)$ and $\phi_3(t)$ can be associated with corrections for the derivatives at $t = 0, 1$. These facts help us to understand the structure behind the different polynomial subspaces that are constructed below.

First we choose for the test and trial function spaces a 16-dimensional subspace, i.e., $S_h(\widehat{\Omega}) = P^{3\times 3}(\widehat{\Omega}) = P^3(x) \otimes P^3(y) \subset H^1(\widehat{\Omega})$, the usual tensor product of polynomials of degree less than four in the two coordinate directions. Hence, on the unit square $\widehat{\Omega}$ we get the approximation $u_h \in S_h(\widehat{\Omega})$,

$$u_h = \sum_{1 \leq i,j \leq 4} c_{i,j} \phi_i(y) \phi_j(x). \tag{6.22}$$

Next we consider the usual trace operators, $\gamma_0^{\widehat{\Omega}} : H^1(\widehat{\Omega}) \to H^{1/2}(\partial\widehat{\Omega})$ and $\gamma_0^{\Omega} : H^1(\widehat{\Omega}) \to H^{1/2}(\partial\Omega)$ applied to the boundary of $\widehat{\Omega}$ and Ω respectively, and

similarly, $\gamma_1^{\widehat{\Omega}} : H^1(\widehat{\Omega}) \to H^{-1/2}(\partial\widehat{\Omega})$ and $\gamma_1^{\Omega} : H^1(\widehat{\Omega}) \to H^{-1/2}(\partial\Omega)$ the traces for the normal derivatives. We see that the approximating space of tensor product cubics, $S_h(\widehat{\Omega}) \subset H^1(\widehat{\Omega})$, is a 16-dimensional subspace. The trace of this space on $\partial\widehat{\Omega}$, the space $\gamma_0^{\widehat{\Omega}}(S_h(\widehat{\Omega}))$, however, is 12-dimensional, because the trace consists of independent cubics on the four edges, related by four continuity conditions at the vertices. Choosing the polynomial basis (6.21), in $S_h(\widehat{\Omega})$ the basis for $\gamma_0^{\widehat{\Omega}}(S_h(\widehat{\Omega}))$ can readily be found as a subset of the tensor product of the basis functions (6.21), by splitting $S_h(\widehat{\Omega})$ into two linearly independent subspaces:

$$S_h(\widehat{\Omega}) = \widetilde{Q}_h(\widehat{\Omega}) \oplus \widetilde{K}_h(\widehat{\Omega}) ,$$

with

$$\widetilde{K}_h(\widehat{\Omega}) = \ker(\gamma_0^{\widehat{\Omega}}) \cap S_h(\widehat{\Omega}) = \text{Span}\left(\phi_i(x)\phi_j(y) \mid i,j = 2,3 \right) ,$$

and

$$\widetilde{Q}_h(\widehat{\Omega}) = \text{Span}\left(\phi_1(x)\phi_j(y),\ \phi_4(x)\phi_j(y),\ \phi_i(x)\phi_1(y),\ \phi_i(x)\phi_4(y) \mid i,j = 1,2,3,4\right) .$$

For the approximating space for $\gamma_0^{\widehat{\Omega}}(H^1(\widehat{\Omega}))$ we take

$$Q_h^*(\partial\widehat{\Omega}) = \gamma_0^{\widehat{\Omega}}(S_h(\widehat{\Omega})) = \gamma_0^{\widehat{\Omega}}(\widetilde{Q}_h(\widehat{\Omega})) \subset H^{1/2}(\partial\widehat{\Omega}) .$$

Similarly we introduce the approximation space for the traces on $\partial\Omega$ as

$$Q_h^*(\partial\Omega) := \gamma_0^{\Omega}(\widetilde{Q}_h(\widehat{\Omega})) \subset H^{1/2}(\partial\Omega) .$$

On the other hand, for the approximation of the trace of the normal derivatives we split the space $S_h(\widehat{\Omega})$ as

$$S_h(\widehat{\Omega}) = \ Q_h(\widehat{\Omega}) \oplus K_h(\widehat{\Omega}) ,$$

with

$$K_h(\widehat{\Omega}) = \ker(\gamma_1^{\widehat{\Omega}}) \cap S_h(\widehat{\Omega}) = \text{Span}\left(\psi_i(x)\psi_j(y) \mid i,j = 1,4 \right) ,$$

with $\psi_k = \phi_k - \phi_2 - \phi_3$ and

$$Q_h(\widehat{\Omega}) = \text{Span}\left(\phi_2(x)\phi_j(y),\ \phi_3(x)\phi_j(y),\ \phi_i(x)\phi_2(y),\ \phi_i(x)\phi_3(y),\ i,j = 1,2,3,4\right) .$$

We see that $Q_h(\widehat{\Omega})$ is 12-dimensional and $K_h(\widehat{\Omega})$ is 4-dimensional. The normal derivatives on the four edges of $\widehat{\Omega}$ are all approximated by cubic polynomials

related by the condition that at the vertices $\frac{1}{\partial x}(\frac{\partial u_h}{\partial y}) = \frac{1}{\partial y}(\frac{\partial u_h}{\partial x})$. So we find the approximating space for the normal derivatives at the boundary of $\widehat{\Omega}$, viz., and at the boundary of Ω as

$$Q_h(\partial\Omega) = \gamma_1^{\Omega}(\, Q_h(\widehat{\Omega})) \subset H^{-1/2}(\partial\Omega)\,.$$

Considering the Lagrange multiplier function $p \in H^{-1/2}(\partial\widehat{\Omega})$ in (6.7), we know that, if u satisfies the Poisson equation (6.17) and also the Dirichlet boundary condition, the Lagrange multiplier p on $\partial\widehat{\Omega}$ represents the normal flux $\mathbf{n}\cdot\nabla u$ at the the boundary $\partial\widehat{\Omega}$, i.e., $p = \mathbf{n}\cdot\nabla u$. Thus, in the discrete hybrid formulation (6.20), we write for the Lagrange multiplier $p_h = \mathbf{n}\cdot\nabla\chi_h$ on $\partial\widehat{\Omega}$, where $\mathbf{n}$ is the unit outward normal vector and $\chi_h \in Q_h(\widehat{\Omega})$ is the master flux function given by

$$\chi_h = \sum_{1\le i,j\le 4} a_{i,j}\phi_i(x)\phi_j(y), \quad \text{with} \quad a_{i,j} = 0, \quad i,j = 1,4\,.$$

So we recognize the discrete hybrid formulation (6.20) as a $(16+12)\times(16+12)$ linear system.

To study the regularity of this hybrid formulation, we plot the singular values of the discrete 28×28 system as function of the circle radius, $0 < R \le \sqrt{2}$. The result is shown in Figure 6.6. In this figure we see 28 singular values as a function of the circle radius, R. The discrete formulation is sufficiently well-conditioned up to circle radii of $R \approx 1.1$. In that case more than 80% of the total domain $\widehat{\Omega}$ consists of the fictitious domain $\widetilde{\Omega}$. The reason for the cusps in the figure near $R = 0.4$ and $R = 0.9$ is unknown.

Next, we check how the cubic approximation will be solved for the exact solution by taking in (6.17) the right-hand side and the boundary conditions such that the solution is given by $u = x^3 + y^3 + xy$. The solution and the error for two possible domains ($R = 2/5$ and $R = 4/5$) are shown in the Figures 6.7 and 6.8. We see that the hybrid formulation finds the exact solution on the domain Ω, except for rounding errors corresponding to the condition of the linear system.

To check the approximation behavior of the method we repeat the experiment for the solution $u(x,y) = e^{x+y}$ in (6.17). The solution and the error for both domains ($R = 2/5$ and $R = 4/5$) are shown in the Figures 6.9 and 6.10.

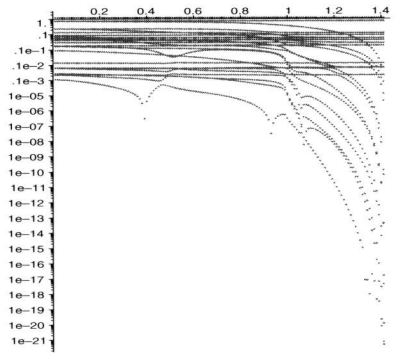

Figure 6.6: The singular values as function of the embedded circle bow radius for the fourth order hybrid discretization. On the fictitious part of the domain the solution and the error are set equal to zero.

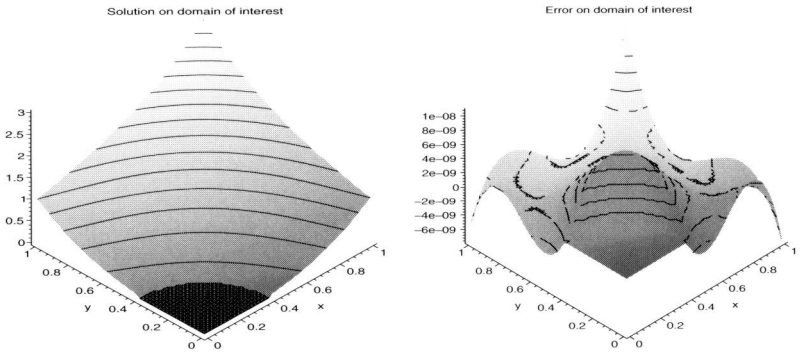

Figure 6.7: The solution $u = x^3 + y^3 + xy$ and the error on the domain Ω of the fourth order hybrid discretization ($R = 2/5$).

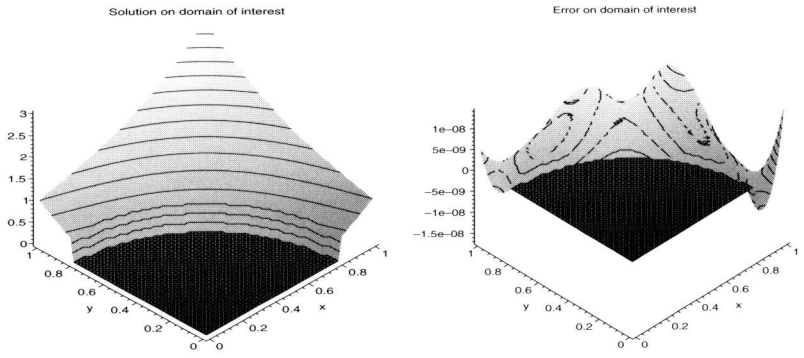

Figure 6.8: The solution $u = x^3 + y^3 + xy$ and the error on the domain Ω of the fourth order hybrid discretization ($R = 4/5$).

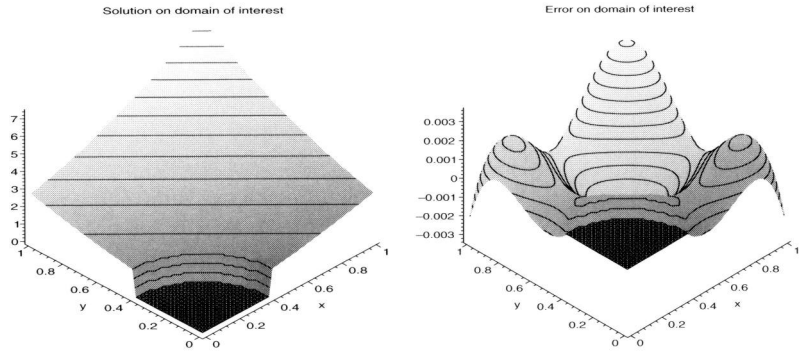

Figure 6.9: The solution $u = e^{x+y}$ and the error on the domain Ω of the fourth order hybrid discretization ($R = 2/5$).

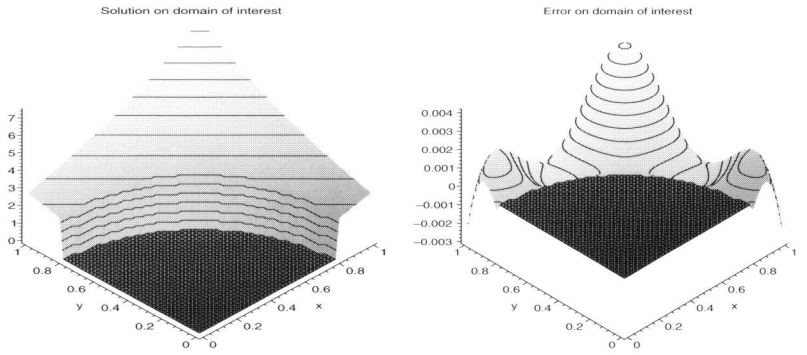

Figure 6.10: The solution $u = e^{x+y}$ and the error on the domain Ω of the fourth order hybrid discretization ($R = 4/5$).

6.4.2 The combination of the hybrid and the discontinuous Galerkin formulation

In the previous sections we have seen that the discretization of the hybrid form with an embedded Dirichlet boundary condition leads to a regular linear system, whereas the linear system of a discontinuous Galerkin discretization is not always invertible. On the other hand the discontinuous Galerkin method is cheaper, because the Lagrange multiplier has been eliminated and hence less degrees of freedom are involved. So, to reduce the computational costs, if we consider a large regular rectangular grid on which locally there exist cells with embedded Dirichlet boundary conditions, it is natural to treat these cells with the hybrid method, while the 'normal' rectangular cells are treated with a DG-Galerkin discretization.

To study such a method, we consider two adjacent rectangular cells $\widehat{\Omega}_1$ and $\widehat{\Omega}_2$, where only $\widehat{\Omega}_1$ has an embedded Dirichlet boundary condition. The cells have a common interface $\Gamma_{1,2}$. Because cell $\widehat{\Omega}_1$ has an embedded boundary condition, we treat this cell with a hybrid discretization. The cell $\widehat{\Omega}_2$ is discretized by DG discretization. So, on cell $\widehat{\Omega}_1$ we have

$$\int_{\widehat{\Omega}_1} \nabla u_h \cdot \nabla u_h dx - \int_{\Gamma_{1,2}} (\mathbf{n}_{1,2} \cdot \nabla \chi_h) v_h ds - \int_{\partial\widehat{\Omega}_1 \setminus \Gamma_{1,2}} (\mathbf{n} \cdot \nabla \chi_h) v_h ds - \tag{6.23}$$
$$\int_{\Gamma_{1,2}} (\mathbf{n}_{1,2} \cdot \nabla q_h) u_h ds - \int_{\partial\Omega_1 \setminus \Gamma_{1,2}} (\mathbf{n} \cdot \nabla q_h) u_h ds = \int_{\widehat{\Omega}_1} f v_h dx - \int_{\partial\Omega_1 \setminus \Gamma_{1,2}} \mathbf{n} \cdot \nabla q_h u_0 ds,$$

where $\mathbf{n}_{1,2}$ is the unit normal on the interface $\Gamma_{1,2}$ pointing from cell $\widehat{\Omega}_1$ towards cell $\widehat{\Omega}_2$. On the other hand, on cell $\widehat{\Omega}_2$ we consider (for simplicity) the symmetric DG discretization. Hence

$$\begin{aligned}&\int_{\widehat{\Omega}_2} \nabla u_h \cdot \nabla u_h dx - \int_{\Gamma_{1,2}} (\mathbf{n}_{2,1} \cdot \nabla u_h) v_h \, ds - \int_{\partial\widehat{\Omega}_2 \setminus \Gamma_{1,2}} (\mathbf{n} \cdot \nabla u_h) v_h \, ds - \\ &\int_{\Gamma_{1,2}} (\mathbf{n}_{2,1} \cdot \nabla v_h) u_h \, ds - \int_{\partial\widehat{\Omega}_2 \setminus \Gamma_{1,2}} (\mathbf{n} \cdot \nabla v_h) u_h \, ds = \int_{\widehat{\Omega}_2} f v dx - \int_{\partial\widehat{\Omega}_2 \setminus \Gamma_{1,2}} (\mathbf{n} \cdot \nabla v_h) u_0 \, ds.\end{aligned} \tag{6.24}$$

Now we have to couple the two cells at the interface $\Gamma_{1,2}$. Therefore, we have to satisfy the locality, consistency and conservation conditions as discussed in [3]. To meet these conditions we define the average fluxes across the interface by

$$\left\langle \widetilde{\nabla u_h} \right\rangle = \frac{1}{2} \left(\nabla \chi_h|_{\partial\widehat{\Omega}_1} + \nabla u_h|_{\partial\widehat{\Omega}_2} \right) \text{ and } \left\langle \widetilde{\nabla v_h} \right\rangle = \frac{1}{2} \left(\nabla q_h|_{\partial\widehat{\Omega}_1} + \nabla v_h|_{\partial\widehat{\Omega}_2} \right),$$

and the jumps by

$$[u_h] = u_h|_{\partial\widehat{\Omega}_1} \mathbf{n}_{1,2} + u_h|_{\partial\widehat{\Omega}_2} \mathbf{n}_{2,1}.$$

Then combining (6.23) and (6.24), together with the flux and jump relations, we arrive at the form

$$\begin{aligned}&\int_{\widehat{\Omega}_1 \cup \widehat{\Omega}_2} \nabla u_h \cdot \nabla v_h dx - \int_{\Gamma_{1,2}} \left\langle \widetilde{\nabla u_h} \right\rangle \cdot [v_h] \, ds - \int_{\Gamma_{1,2}} \left\langle \widetilde{\nabla v_h} \right\rangle \cdot [u_h] \, ds - \\ &\int_{\partial\widehat{\Omega}_1 \setminus \Gamma_{1,2}} (\mathbf{n} \cdot \nabla \chi_h) v_h ds - \int_{\partial\widehat{\Omega}_2 \setminus \Gamma_{1,2}} (\mathbf{n} \cdot \nabla u_h) v_h ds - \int_{\partial\Omega_1 \setminus \Gamma_{1,2}} (\mathbf{n} \cdot \nabla q_h) u_h ds - \\ &\int_{\partial\widehat{\Omega}_2 \setminus \Gamma_{1,2}} (\mathbf{n} \cdot \nabla v_h) u_h ds = \int_{\widehat{\Omega}_1 \cup \widehat{\Omega}_2} f v_h dx - \int_{\partial\Omega_1 \setminus \Gamma_{1,2}} (\mathbf{n} \cdot \nabla q_h) u_0 ds - \int_{\partial\widehat{\Omega}_2 \setminus \Gamma_{1,2}} (\mathbf{n} \cdot \nabla v_h) u_0 ds.\end{aligned}$$

This weak form can immediately be used for discretizations as described above. The solution and the error of such a combined discretization with cubic polynomials is shown in Figure 6.11.

6.4.3 An embedded boundary for the convection equation

Having studied the discretization of the Poisson equation, we now consider the convection equation with an interior Dirichlet boundary condition

$$\mathbf{b} \cdot \nabla u = f \text{ in } \widehat{\Omega}, \quad u = u_0 \text{ on } \partial\Omega_{\text{in}},$$

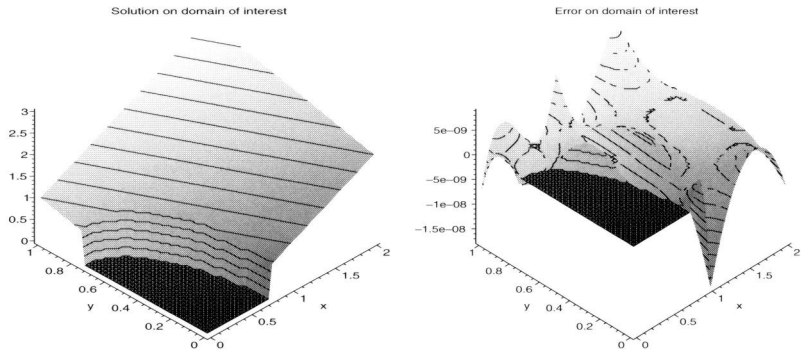

Figure 6.11: The approximate solution $u = x + y$ of $\Delta u = 0$, and the error on the domain $\Omega_1 \cup \widehat{\Omega}_2$ for a fourth order combined hybrid-symmetric DG discretization with embedded circle segment Dirichlet boundary condition ($R = 3/4$).

where $\mathbf{b}$ is a constant vector denoting the direction of the convection and $\partial\Omega_{\text{in}}$ is the inflow boundary of Ω such that this boundary is $\partial\Omega = \partial\Omega_{\text{in}} \cup \partial\Omega_{\text{out}}$. The inflow and outflow boundaries are defined by $\mathbf{b} \cdot \mathbf{n} < 0$ on $\partial\Omega_{\text{in}}$ and $\mathbf{b} \cdot \mathbf{n} > 0$ on $\partial\Omega_{\text{out}}$, respectively. Considering the boundary of the whole domain $\partial\widehat{\Omega}$, we also split this boundary in an upwind and downwind boundary such that $\partial\widehat{\Omega} = \partial\widehat{\Omega}_{\text{in}} \cup \partial\widehat{\Omega}_{\text{out}}$. Then, according to the Lagrange multiplier theorem we arrive for the boundary value problem at the following weak formulation: find $u \in H^1(\widehat{\Omega})$ and $\chi \in H^{1/2}(\partial\widehat{\Omega}_{\text{in}})$ such that

$$
\begin{aligned}
&-\int_{\widehat{\Omega}} \nabla v \cdot \mathbf{b} u \, dx + \int_{\partial\widehat{\Omega}_{\text{in}}} \mathbf{n} \cdot \mathbf{b} \, \chi v \, ds + \int_{\partial\widehat{\Omega}_{\text{out}}} \mathbf{n} \cdot \mathbf{b} \, uv \, ds + \\
&\int_{\partial\Omega_{\text{in}}} \mathbf{n} \cdot \mathbf{b} \, qu \, ds = \int_{\widehat{\Omega}} fv \, dx + \int_{\partial\Omega_{\text{in}}} \mathbf{n} \cdot \mathbf{b} \, qu_0 \, ds, \quad \forall v \in H^1(\widehat{\Omega}), \\
&\qquad\qquad\qquad\qquad\qquad\qquad\qquad\qquad\qquad\qquad \forall q \in H^{1/2}(\partial\Omega_{\text{in}}),
\end{aligned}
\tag{6.25}
$$

in which we assume that u on the fictitious domain $\widetilde{\Omega}$ satisfies the differential equation and is the continuation of the solution u on the domain Ω. Figure 6.12 shows the solution and the error if (6.25) is used as the starting point for a discretization with cubic polynomials, as discussed above.

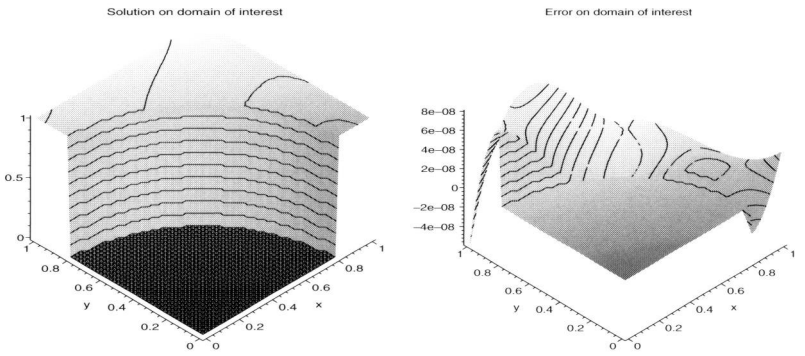

Figure 6.12: The approximate solution $u = 1$ of the convection equation $\mathbf{b} \cdot \nabla u = 0$ and the error on the domain Ω for a fourth order hybrid discretization with embedded circle segment Dirichlet boundary condition ($R = 8/10$).

6.4.4 Two adjacent cells with a common interior embedded boundary condition

In this section we study a finite element discretization of the convection diffusion equation

$$-\varepsilon \Delta u + \mathbf{b} \cdot \nabla u = 0\,, \tag{6.26}$$

discretized on two adjacent cells $\widehat{\Omega}_1$ and $\widehat{\Omega}_2$, with vertices $(-1,0)$, $(0,0)$, $(0,1)$, $(-1,1)$ and $(0,0)$, $(1,0)$, $(1,1)$, $(0,1)$ respectively. The embedded Dirichlet boundary condition is given on the half circle $x^2 + y^2 = R^2$, $0 \leq y \leq 1$, so that the domain of interest is given by

$$\Omega = (\widehat{\Omega}_1 \cup \widehat{\Omega}_2) \setminus \left\{(x,y) \mid x^2 + y^2 < R^2\right\}.$$

We first consider the diffusion part of the equation. Then the weak hybrid formulation of the problem reads: find $u \in H^1(\widehat{\Omega}_h)$ and $p \in H^{-1/2}(\partial\widehat{\Omega} \cup \widehat{\Gamma}_{\text{int}})$ such that:

$$\begin{aligned}(\nabla u, \nabla v)_{\widehat{\Omega}_h} - \langle p, v\rangle_{\partial\widehat{\Omega}} - \langle p, \mathbf{n}\cdot[v]\rangle_{\widehat{\Gamma}_{\text{int}}} - \langle q, u\rangle_{\partial\Omega} - \langle q, \mathbf{n}\cdot[u]\rangle_{\Gamma_{\text{int}}} = \\ (f, v)_{\widehat{\Omega}_h} - \langle q, u_0\rangle_{\partial\Omega}\,, \qquad \forall v \in H^1(\widehat{\Omega}_h),\ \forall q \in H^{-1/2}(\partial\Omega \cup \Gamma_{\text{int}}),\end{aligned} \tag{6.27}$$

where $H^1(\widehat{\Omega}_h)$ is the broken Sobolev space on $\widehat{\Omega}_1 \cup \widehat{\Omega}_2$ (see Section 2.2.1) and the common interface is given by $\widehat{\Gamma}_{\text{int}} = \widehat{\Omega}_1 \cap \widehat{\Omega}_2$, with $\mathbf{n}$ the normal vector. The interface Γ_{int}, not including the fictitious part, is defined by $\Gamma_{\text{int}} = \overline{\Omega}_1 \cap \overline{\Omega}_2$.

Recognizing in $p|_{\widehat{\Gamma}_{\text{int}}}$ a normal flux on the common interface $\widehat{\Gamma}_{\text{int}}$, we define the trace operators, $\widetilde{\gamma}_1^{\widehat{\Omega}} : H^1(\widehat{\Omega}) \cap C^1(\widehat{\Omega}) \to H^{-1/2}(\partial\widehat{\Omega} \cup \widehat{\Gamma}_{\text{int}})$ and $\widetilde{\gamma}_1^{\Omega} : H^1(\widehat{\Omega}) \cap C^1(\widehat{\Omega}) \to H^{-1/2}(\partial\Omega \cup \Gamma_{\text{int}})$. In order to approximate the normal derivatives on $\partial\widehat{\Omega} \cup \widehat{\Gamma}_{\text{int}}$ we proceed as in Section 6.4.1 and introduce the polynomial subspace $S_h(\widehat{\Omega}) \subset H^1(\widehat{\Omega}) \cap C^1(\widehat{\Omega})$. We split this space as:

$$S_h(\widehat{\Omega}) = Q_h(\widehat{\Omega}) \oplus K_h(\widehat{\Omega}),$$

with

$$K_h(\widehat{\Omega}) = \ker(\widetilde{\gamma}_1^{\widehat{\Omega}}) \cap S_h(\widehat{\Omega}).$$

Then the discrete version of (6.27) reads: find $u_h \in S_h(\widehat{\Omega}_h)$ and $\chi_h \in Q_h(\widehat{\Omega})$ such that

$$\begin{aligned}(\nabla u_h, \nabla v_h)_{\widehat{\Omega}_h} &- \left\langle \widetilde{\gamma}_1^{\widehat{\Omega}}(\chi_h), \gamma_0(v_h) \right\rangle_{\partial\widehat{\Omega}} - \left\langle \widetilde{\gamma}_1^{\widehat{\Omega}}(\chi_h), [v_h] \right\rangle_{\widehat{\Gamma}_{\text{int}}} \\ &- \langle \widetilde{\gamma}_1^{\Omega}(q_h), \gamma_0(u_h) \rangle_{\partial\Omega} - \langle \widetilde{\gamma}_1^{\Omega}(q_h), [u_h] \rangle_{\Gamma_{\text{int}}} \\ &= (f, v_h)_{\widehat{\Omega}_h} - \langle \widetilde{\gamma}_1^{\Omega}(q_h), u_0 \rangle_{\partial\Omega} \qquad \forall v_h \in S_h(\widehat{\Omega}_h),\ q_h \in Q_h(\widehat{\Omega}).\end{aligned} \tag{6.28}$$

(Note the polynomial spaces used!). For the polynomial space $S_h(\widehat{\Omega}_h)$ we can take the usual space of piecewise cubic polynomials in each coordinate direction on the partitioning $\widehat{\Omega}_1 \cup \widehat{\Omega}_2$. On the other hand, it is not trivial to find a cubic polynomial space for $Q_h(\widehat{\Omega}) \subset H^1(\widehat{\Omega}) \cap C^1(\widehat{\Omega})$. As we do not want to make our discretization unnecessary complicated and expensive, we eliminate the extra degrees of freedom for χ_h by identifying them with ∇u_h. Similarly, identifying q_h with $\sigma \nabla v_h$ on $\partial\Omega \cup \Gamma_{\text{int}}$ we arrive at a discontinuous Galerkin discretization: find $u_h \in S_h(\widehat{\Omega}_h)$ such that

$$\begin{aligned}&(\nabla u_h, \nabla v_h)_{\widehat{\Omega}_h} - \langle \nabla u_h, v_h \rangle_{\partial\widehat{\Omega}} - \langle\langle \nabla u_h \rangle, [v_h] \rangle_{\widehat{\Gamma}_{\text{int}}} + \sigma \langle \nabla v_h, u_h \rangle_{\partial\Omega} + \\ &\sigma \langle\langle \nabla v_h \rangle, [u] \rangle_{\Gamma_{\text{int}}} = (f, v_h)_{\widehat{\Omega}_h} + \sigma \langle \nabla v_h, u_0 \rangle_{\partial\Omega}, \qquad \forall v \in S_h(\widehat{\Omega}_h),\end{aligned} \tag{6.29}$$

with the usual choices for the normal flux functions.

Nevertheless, the use of DG discretization forces us to monitor for possible singularities. However, in the next chapter we show for the cubic discontinuous Galerkin discretization how possible singularities can be avoided by introducing an extra weighting term for the embedded Dirichlet boundary (see also [47]).

To continue we consider the convection part of (6.26). So, on the domain $\widehat{\Omega}$ we consider the equation

$$\mathbf{b} \cdot \nabla u = f, \quad u = u_0 \text{ on } \partial\Omega_{\text{in}}.$$

For simplicity we set $\mathbf{b} = (1,0)$. Then the embedded boundary is an outflow boundary for $\widehat{\Omega}_1$, whereas for $\widehat{\Omega}_2$ it is an inflow boundary. Hence, we can neglect this embedded boundary in $\widehat{\Omega}_1$, whereas in cell $\widehat{\Omega}_2$ we must introduce a Lagrange multiplier in order to satisfy the upwind boundary condition on the circle bow. Therefore we arrive at the following weak form for the convection part: find $u, \chi \in H^1(\widehat{\Omega}_h) = H^1(\widehat{\Omega}_1 \cup \widehat{\Omega}_2)$

$$
\begin{aligned}
&- \int_{\widehat{\Omega}} \nabla v \cdot \mathbf{b} u dx + \int_{\partial\widehat{\Omega}_{1,\text{out}}} (\mathbf{n} \cdot \mathbf{b} u) v ds + \int_{\partial\widehat{\Omega}_{2,\text{in}}} (\mathbf{n} \cdot \mathbf{b}\chi) v ds \\
&+ \int_{\partial\widehat{\Omega}_{2,\text{out}}} (\mathbf{n} \cdot \mathbf{b} u) v ds + \int_{\partial\Omega_{\text{in}}} (\mathbf{n} \cdot \mathbf{b} q) u ds - \int_{\Gamma_{\text{int}}} (\mathbf{n} \cdot \mathbf{b} q) u^- ds \\
&= \int_{\widehat{\Omega}} f v dx - \int_{\partial\widehat{\Omega}_{1,\text{in}}} (\mathbf{n} \cdot \mathbf{b} u_0) v ds + \int_{\Gamma_{\text{D}}} (\mathbf{n} \cdot \mathbf{b} q) u_0 ds \quad \forall v, q \in H^1(\widehat{\Omega}),
\end{aligned}
\tag{6.30}
$$

where $u^- = u|_{\partial\Omega_1} = u|_{\Gamma_{\text{int}}}$. If we want to eliminate in (6.30) the extra degrees of freedom, we set $\chi = u$ and $q = v$.

The linear combination of (6.29) and (6.30) gives a discretization of the convection diffusion equation

$$
-\Delta u + \mathbf{b} \cdot \nabla u = f \quad \text{in } \widehat{\Omega}, \qquad u = u_0 \quad \text{on } \partial\Omega. \tag{6.31}
$$

The Figures 6.13 and 6.14 show the solution and the error of the discretization of (6.31) by means of (6.29) and (6.30) with tensor-product cubics.

6.5 A singularly perturbed PDE on only two cells with a half circle excluded

In this section we are interested to solve the following convection diffusion problem (see Figure 6.15). More details about this problem can be found in [21].

$$
-\varepsilon\Delta u + u_x = f, \quad \text{on } \widehat{\Omega} = \{ (x,y) \mid -1 < x < 1,\ 0 < y < 1 \}, \tag{6.32}
$$

$$
\begin{aligned}
u &= 0 \quad \text{on } \partial\Omega = \{ (x,y) \mid x = -1,\ 0 < y < 1;\ -1 < x < 1, y = 1 \}, \\
u &= 1 \quad \text{on } \Gamma_{\text{D}} = \{ (x,y) \mid x^2 + y^2 = R^2, y > 0;\ R < 1 \}, \\
\mathbf{n} \cdot \varepsilon\nabla u &= 0 \quad \text{on } \Gamma_{\text{N}} = \{ (x,0) \mid R < |x| < 1 \} \cup \{ (1,y) \mid 0 < y < 1 \}.
\end{aligned}
\tag{6.33}
$$

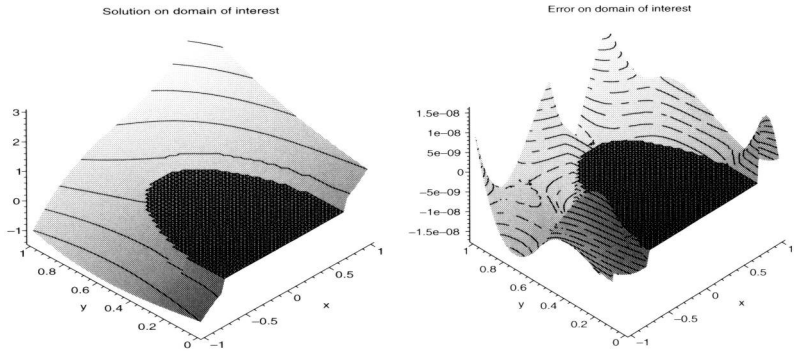

Figure 6.13: The approximate solution $u = x^3 + y^3 + xy$ of $-\Delta u + u_x = f$ and the error on the domain $\Omega = \Omega_1 \cup \Omega_2$ for a fourth order symmetric-DG discretization with embedded circle Dirichlet boundary condition ($R = 3/4$).

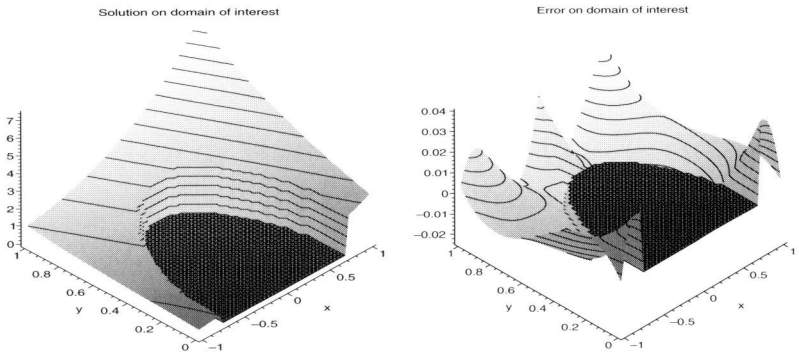

Figure 6.14: The approximate solution $u = e^{x+y}$ of $-\Delta u + u_x = f$ and the error on the domain $\Omega_1 \cup \Omega_2$ for a fourth order symmetric-DG discretization with embedded circle Dirichlet boundary condition ($R = 3/4$).

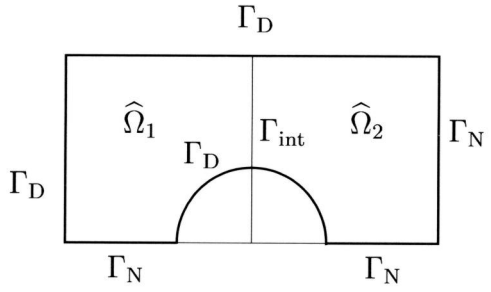

Figure 6.15: The domain for problem (6.32-6.33).

Let $\widehat{\Omega}_1$ and $\widehat{\Omega}_2$ be two unit cells with respectively vertices $(-1,0)$, $(0,0)$, $(0,1)$, $(-1,1)$ and $(0,0)$, $(1,0)$, $(1,1)$, $(0,1)$ so that $\widehat{\widetilde{\Omega}} = \widehat{\widetilde{\Omega}}_1 \cup \widehat{\widetilde{\Omega}}_2$. For this problem we want to study the symmetric and the Baumann-Oden DG-method.

First we study the diffusion part of (6.32) and replace the homogeneous Neumann boundary condition on $\Gamma_N = \{\ (x,y) \mid x = 1,\ 0 < y < 1\}$ with the homogeneous Dirichlet boundary condition, in order to obtain a symmetric problem around $x = 0$. Now the corresponding *hybrid* formulation (6.7) for (6.32) reads: find $u \in H^1(\widehat{\Omega}_h)$ and $p \in H^{-1/2}(\partial\widehat{\Omega} \cup \widehat{\Gamma}_{\rm int})$ such that

$$\begin{aligned}(\nabla u, \nabla v)_{\widehat{\Omega}} - \langle p, v\rangle_{\partial\widehat{\Omega}} - \langle q, u\rangle_{\partial\Omega\cup\Gamma_D} - \langle p, \mathbf{n}\cdot[v]\rangle_{\widehat{\Gamma}_{\rm int}} - \langle q, \mathbf{n}\cdot[u]\rangle_{\Gamma_{\rm int}} = \\ (f, v)_{\widehat{\Omega}} - \langle q, u_0\rangle_{\partial\Omega\cup\Gamma_D}\,, \quad \forall v \in H^1(\widehat{\Omega}_h),\ q \in H^{-1/2}(\partial\widehat{\Omega}\cup\Gamma_{\rm int}).\end{aligned} \tag{6.34}$$

Here $H^1(\widehat{\Omega}_h)$ is the broken Sobolev space on $\widehat{\Omega}_1 \cup \widehat{\Omega}_2$ and the jump operator is given by $[v] = \mathbf{n}_1 v|_{\partial\widehat{\Omega}_1} + \mathbf{n}_2 v|_{\partial\widehat{\Omega}_2}$. Further, $\Gamma_{\rm int} = \partial\Omega_1 \cap \partial\Omega_2$ is the interior wall on which the true solution is continuous. However, continuity is not required outside Ω and hence not on all of $\widetilde{\Gamma}_{\rm int} = \widehat{\Gamma}_{\rm int} \cap \widetilde{\Omega}$.

To arrive at the DG-discretization of (6.34) we take for the test and trial space, $S_h(\widehat{\Omega}) \subset H^1(\widehat{\Omega}_h)$, the tensor product of polynomials of degree $p < 4$ in each of the coordinate directions and we write for the approximation

$$u_h = \sum_{0\le e<2} \sum_{0\le i,j<4} c_{e,i,j}\ \phi_{e,i}(x)\ \phi_{e,j}(y)\,.$$

In practice we construct a basis from (6.21).

Next, for the DG discretization, we eliminate the extra equations and degrees of freedom for the Lagrange multiplier using the fact that p represents the normal

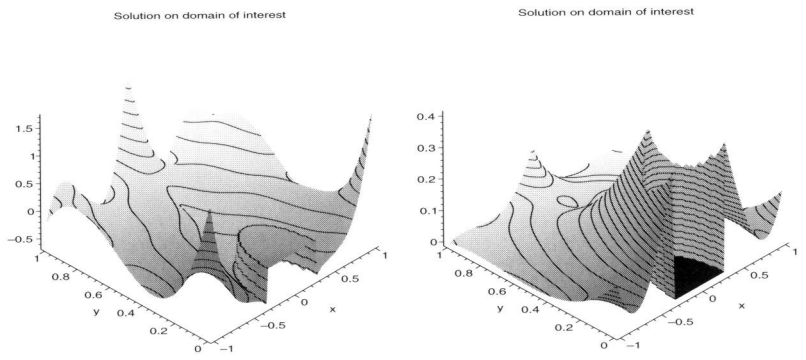

Figure 6.16: The approximate solution u_h of $\Delta u = 0$ on the domain Ω with symmetric boundary conditions and fourth order discretizations with embedded circle Dirichlet boundary condition ($R = 3/10$).

flux of u at $\partial\widehat{\Omega}$ and at the internal wall $\widehat{\Gamma}_{\text{int}}$. Thus, replacing p by $\mathbf{n} \cdot \nabla u_h$ on $\partial\widehat{\Omega}$ and by $\langle \mathbf{n} \cdot \nabla u_h \rangle$ on $\widehat{\Gamma}_{\text{int}}$ and replacing similarly q by $-\sigma \mathbf{n} \cdot \nabla v$, we get the DG discretization of (6.34): find $u_h \in S_h(\widehat{\Omega})$ such that

$$(\nabla u_h, \nabla v_h)_{\widehat{\Omega}} - \langle \mathbf{n} \cdot \nabla u_h, v_h \rangle_{\partial\widehat{\Omega}} + \sigma \langle \mathbf{n} \cdot \nabla v_h, u_h \rangle_{\partial\Omega \cup \Gamma_{\text{D}}} - \tag{6.35}$$
$$\langle \langle \nabla u_h \rangle, [v] \rangle_{\widehat{\Gamma}_{\text{int}}} + \sigma \langle \langle \nabla v_h \rangle, [u] \rangle_{\Gamma_{\text{int}}} = (f, v_h)_{\widehat{\Omega}} + \sigma \langle \mathbf{n} \cdot \nabla v_h, u_0 \rangle_{\partial\Omega \cup \Gamma_{\text{D}}},$$
$$\forall v_h \in S_h(\widehat{\Omega}).$$

Figure 6.16 shows the solution of the symmetric ($\sigma = -1$) and the Baumann-Oden ($\sigma = 1$) discretization. We see that both solutions are symmetric, indeed, because of the symmetric structure of the problem. On the other hand we recognize the unstable behavior of the symmetric DG method, which is of poor quality compared to the solution of the Baumann-Oden method.

We proceed by considering both methods for the diffusion part of the equation and boundary conditions as in (6.33). Then the discrete formulation is also given by (6.35), except that the Dirichlet boundary condition at $\{(1, y) \mid 0 < y < 1\}$ is replaced by the homogeneous Neumann boundary condition $\mathbf{n} \cdot \nabla u = 0$. The corresponding solutions of the symmetric and the Baumann-Oden method are shown in Figure 6.17. Now the solutions are not symmetric. Again, the solution of the symmetric DG-method is poor compared to the solution of the Baumann-Oden DG method.

Finally, we take the convection part of (6.32). The Lagrange weak for-

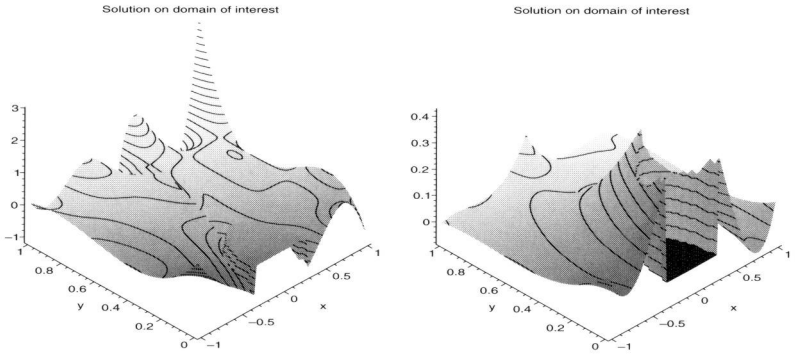

symmetric DG Baumann-Oden DG

Figure 6.17: The approximate solution u_h of $\Delta u = 0$ on the domain $\widehat{\Omega}$ with the boundary conditions (6.33) for a fourth-order symmetric and Baumann-Oden discontinuous Galerkin discretization. The embedded circle Dirichlet boundary condition is located at $R = 3/10$.

mulation of the convection term for the cell $\widehat{\Omega}_2$ reads: find $u \in H^1(\widehat{\Omega}_2)$ and $\overline{p} \in H^{1/2}(\partial\Omega_{\text{in}})$ such that

$$
\begin{aligned}
-(\nabla v \cdot \mathbf{b}, u)_{\widehat{\Omega}_2} + \oint_{\partial\widehat{\Omega}_2} v\mathbf{n}\cdot\mathbf{b}u \, ds + & \qquad (6.36)\\
\langle \overline{p}\ \mathbf{n}\cdot\mathbf{b}, v\rangle_{\partial\Omega_{\text{in}}} &= 0, \qquad \forall v \in H^1(\widehat{\Omega}_2),\\
\langle q\ \mathbf{n}\cdot\mathbf{b}, u\rangle_{\partial\Omega_{\text{in}}} &= \langle q\ \mathbf{n}\cdot\mathbf{b}, u_0\rangle_{\partial\Omega_{\text{in}}}, \quad \forall q \in H^{1/2}(\partial\Omega_{\text{in}}),
\end{aligned}
$$

with $\mathbf{b} = (1, 0)$ and $u_0 = 1$ on the embedded circle, $\Gamma_{\text{D}} \cap \partial\Omega_{\text{in}}$, while $u_0 = u^-$ on the common interior boundary, $\Gamma_{\text{int}} \cap \partial\Omega_{\text{in}}$, with u^- being the upwind value of u obtained from $\widehat{\Omega}_1$.

As for the diffusion term, we can rewrite (6.36) in a *hybrid* formulation, where the Lagrange multiplier is computed on $\partial\widehat{\Omega}_{\text{in}}$, the inflow edge of the domain $\widehat{\Omega}_2$. Thus, we obtain: find $u \in H^1(\widehat{\Omega}_2)$ and $\widetilde{p} \in H^{1/2}(\partial\widehat{\Omega}_{\text{in}})$ such that

$$
\begin{aligned}
-(\nabla v \cdot \mathbf{b}, u)_{\widehat{\Omega}_2} + \oint_{\partial\widehat{\Omega}_2} v\mathbf{n}\cdot\mathbf{b}u \, ds + & \qquad (6.37)\\
\langle \widetilde{p}\ \mathbf{n}\cdot\mathbf{b}, v\rangle_{\partial\widehat{\Omega}_{\text{in}}} &= 0, \qquad \forall v \in H^1(\widehat{\Omega}_2),\\
\langle q\ \mathbf{n}\cdot\mathbf{b}, u\rangle_{\partial\Omega_{\text{in}}} &= \langle q\ \mathbf{n}\cdot\mathbf{b}, u_0\rangle_{\partial\Omega_{\text{in}}}, \quad \forall q \in H^{1/2}(\partial\Omega_{\text{in}}),
\end{aligned}
$$

Next, the second term in (6.37) is split in an integration part over the inflow and a part over the outflow edge of $\partial\widehat{\Omega}_2$ so that we can combine the integration

of u and $\widetilde{p}$ over the inflow wall $\partial\widehat{\Omega}_{\text{in}}$. This yields: find $u \in H^1(\widehat{\Omega}_2)$ and $\widetilde{p} \in H^{1/2}(\partial\widehat{\Omega}_{\text{in}})$ such that

$$\begin{aligned} -(\nabla v \cdot \mathbf{b}, u)_{\widehat{\Omega}_2} + \langle (\widetilde{p}+u)\ \mathbf{n}\cdot\mathbf{b}, v\rangle_{\partial\widehat{\Omega}_{\text{in}}} + \langle u\ \mathbf{n}\cdot\mathbf{b}, v\rangle_{\partial\widehat{\Omega}_{\text{out}}} + \langle q\ \mathbf{n}\cdot\mathbf{b}, u\rangle_{\partial\Omega_{\text{in}}} \\ = \langle q\ \mathbf{n}\cdot\mathbf{b}, u_0\rangle_{\partial\Omega_{\text{in}}}, \qquad \forall v \in H^1(\widehat{\Omega}_2),\ \forall q \in H^{1/2}(\partial\Omega_{\text{in}}). \end{aligned}$$

Writing $p = \widetilde{p} + u$, this is simplified to: find $u \in H^1(\widehat{\Omega}_2)$ and $p \in H^{1/2}(\partial\widehat{\Omega}_{\text{in}})$ such that

$$\begin{aligned} -(\nabla v \cdot \mathbf{b}, u)_{\widehat{\Omega}_2} + \langle p\ \mathbf{n}\cdot\mathbf{b}, v\rangle_{\partial\widehat{\Omega}_{\text{in}}} + \langle u\ \mathbf{n}\cdot\mathbf{b}, v\rangle_{\partial\widehat{\Omega}_{\text{out}}} + \langle q\ \mathbf{n}\cdot\mathbf{b}, u\rangle_{\partial\Omega_{\text{in}}} \\ = \langle q\ \mathbf{n}\cdot\mathbf{b}, u_0\rangle_{\partial\Omega_{\text{in}}}, \qquad \forall v \in H^1(\widehat{\Omega}_2),\ \forall q \in H^{1/2}(\partial\Omega_{\text{in}}). \end{aligned} \tag{6.38}$$

To eliminate the Lagrange multiplier p, we recognize this function as the value of u at the boundary $\partial\widehat{\Omega}_{\text{in}}$. The corresponding equations are eliminated by taking $q = \sigma v$ on $\partial\Omega_{\text{in}}$, yielding the DG-formulation of the convection term: find $u \in H^1(\widehat{\Omega}_2)$ such that

$$\begin{aligned} -(\nabla v \cdot \mathbf{b}, u)_{\widehat{\Omega}_2} + \oint_{\partial\widehat{\Omega}_2} v\ \mathbf{n}\cdot\mathbf{b}u\ ds + \sigma\left\langle v\ \mathbf{n}\cdot\mathbf{b}, \left(u-u^-\right)\right\rangle_{\Gamma_{\text{int}}} \\ +\sigma\langle v\ \mathbf{n}\cdot\mathbf{b}, u\rangle_{\Gamma_{\text{D}}} = \sigma\langle v\ \mathbf{n}\cdot\mathbf{b}, u_0\rangle_{\Gamma_{\text{D}}}, \qquad \forall v \in H^1(\widehat{\Omega}_2). \end{aligned} \tag{6.39}$$

In cell Ω_1 the embedded boundary is an outflow boundary and, therefore, for the convection part there is no boundary condition. Hence, we may treat $\widehat{\Omega}_1$ as a normal convection DG-cell.

The discretization of problem (6.32) is obtained by combining (6.35) and (6.39) and reads: find $u_h \in S_h(\widehat{\Omega})$ such that

$$\begin{aligned} &(\varepsilon\nabla u_h, \nabla v_h)_{\widehat{\Omega}} - \langle \mathbf{n}\cdot\varepsilon\nabla u_h, v_h\rangle_{\partial\widehat{\Omega}} + \sigma\langle \mathbf{n}\cdot\varepsilon\nabla v_h, u_h\rangle_{\partial\Omega\cup\Gamma_{\text{D}}} \\ &- \langle\langle\varepsilon\nabla u_h\rangle, [v_h]\rangle_{\widehat{\Gamma}_{\text{int}}} + \sigma\langle\langle\varepsilon\nabla v_h\rangle, [u_h]\rangle_{\Gamma_{\text{int}}} - (\nabla v_h\cdot\mathbf{b}, u_h)_{\widehat{\Omega}} + \langle v_h\mathbf{n}\cdot\mathbf{b}, u_h\rangle_{\partial\widehat{\Omega}_{1,\text{out}}} \\ &+ \oint_{\partial\widehat{\Omega}_2} v_h\mathbf{n}\cdot\mathbf{b}u_h\ ds + \sigma\left\langle v_h\mathbf{n}\cdot\mathbf{b}, \left(u_h-u_h^-\right)\right\rangle_{\Gamma_{\text{int}}} + \sigma\langle v_h\mathbf{n}\cdot\mathbf{b}, u_h\rangle_{\Gamma_{\text{D}}\cap\partial\Omega_2} \\ &= \sigma\langle \mathbf{n}\cdot\varepsilon\nabla v_h, 1\rangle_{\Gamma_{\text{D}}} + \sigma\langle v_h\mathbf{n}\cdot\mathbf{b}, 1\rangle_{\Gamma_{\text{D}}\cap\partial\Omega_2}, \qquad \forall v_h \in S_h(\widehat{\Omega}). \end{aligned} \tag{6.40}$$

Figure 6.18 shows the solutions of the fourth order discretization of (6.40) for $R = 3/10$, for the different values of $\varepsilon = 1,\ 1/10,\ 1/50,\ 1/100$. We see that in all cases the solution is stable. For values of $\varepsilon = O(1)$ we clearly see the approximation of the boundary condition $u_0 = 1$ on the circle bow,

while for small values of ε, when the true solution shows a thin boundary layer, typical effects of the weak boundary requirement show up. Figure 6.19 shows the solution for $\varepsilon = 1/50$. Although it seems that the solution is not able to catch the boundary layer in Ω at the upwind side of the circle, we clearly see a boundary layer arising in the fictitious part of the domain if we consider the total $\widehat{\Omega}$. Clearly, the cubics are not able to represent the thin circular boundary layer. Note, in particular, that at $x = 0$, $y < R$, there is a discontinuity in the fictitious part $\widetilde{\Omega}$. For small values of $\varepsilon << 1$ the boundary layer disappears.

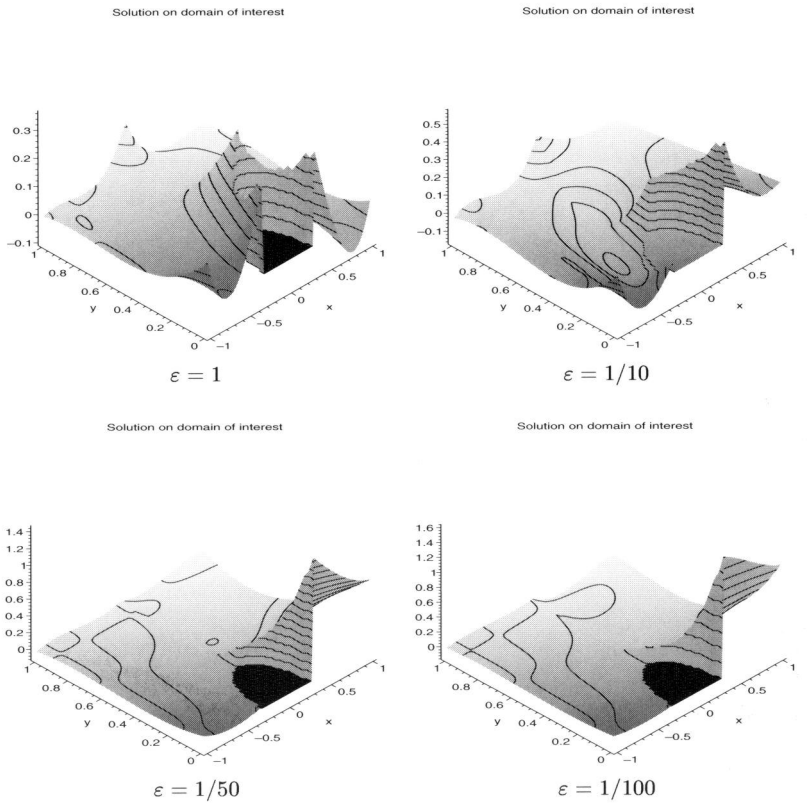

Figure 6.18: The approximate solution u_h of $-\varepsilon\Delta u + u_x = 0$, on the domain exterior of the circle for a fourth order Baumann-Oden DG discretization with Dirichlet boundary condition $u_0 = 1$ on the circle, $(R = 3/10)$.

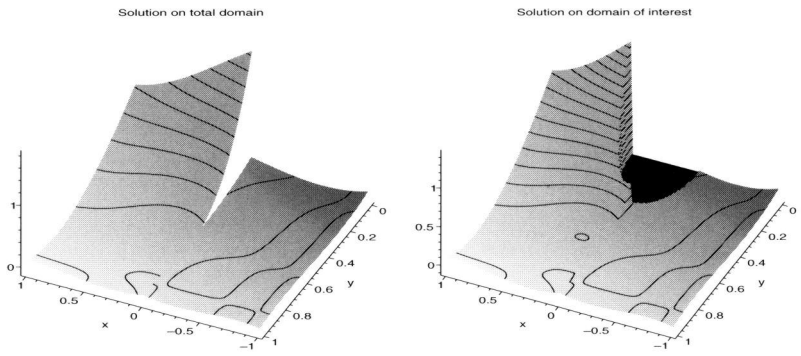

Total domain Domain of interest

Figure 6.19: The approximate solution u_h for the same problem as in Figure 6.18, with $\varepsilon = 1/50$. At the right, the approximate solution on Ω, the domain of interest. Left, the approximate solution on $\widehat{\Omega}$, the whole domain where the approximation is constructed, including the fictitious part.

6.6 Conclusion

In this chapter we propose a technique for the treating second-order elliptic PDEs with complex Dirichlet boundary conditions in combination with a discontinuous Galerkin discretization. The aim is to maintain a structured, regular rectangular grid while solving problems with irregular curved boundary conditions.

The complex domain on which the solution is sought, is covered by a fictitious domain with the structured, regular rectangular grid. An embedded boundary is the transition between the domain of interest and the fictitious part of the computational domain.

We present and compare several weak forms for the diffusion part of the equation: the Lagrange multiplier form, the hybrid form and the DG-form. The hybrid form shows regularity for an arbitrary location of the embedded boundary, whereas for the other forms the discretization may become singular for particular locations of the Dirichlet BC. The problem is studied, first for a single cell and then for a couple of adjacent cells, either sharing or not sharing the embedded boundary. We also describe the treatment of a convection part in the equation.

As an example, we solve a singularly perturbed boundary value problem on a complex domain by means of a fourth-order DG-discretization on only two cells.

Although –as expected– it appears to be impossible to accurately represent sharp boundary layers with a complex structure by means of a few cubic polynomials, the boundary condition treatment is quite effective in handling such complex situations.

Chapter 7

A feasibility study for DG discretization with embedded Dirichlet boundary condition

Summary

In this chapter we introduce a discretization of discontinuous Galerkin (DG) type for solving 2-D second order elliptic PDEs on a regular rectangular grid, while the boundary value problem has a curved Dirichlet boundary. According to the same principles that underlie DG-methods, we adapt the discretization in the cell in which the (embedded) Dirichlet boundary cannot follow the gridlines of the orthogonal grid.

The DG-discretization aims at a high order of accuracy. We discretize with tensor products of cubic polynomials and we parameterize the embedded boundary by cubic polynomials. Then, by construction, such a DG discretization is fourth order consistent, both in the interior and at the boundaries. The proposed discretization technique is motivated by the fact that it results in only a slight modification of DG discretization at embedded boundaries and requires a much simpler mesh generation than needed for boundary conforming meshes. In particular the method can show its use in cases where regular rectangular grids are preferred.

To illustrate the possibilities of our DG-discretization, we solve a convection

dominated boundary value problem on a regular rectangular grid with a circular embedded boundary condition [21]. We show how accurately the boundary and shear layer, emanating from the curved embedded boundary, can be captured by means of the tensor product polynomials on the structured orthogonal mesh.

7.1 Introduction

In the previous chapter (see also [22]), we introduced weak-formulations of discontinuous Galerkin (DG) type for the solution of second-order elliptic PDEs on a structured, regular rectangular grid, while the problem is defined on a curved boundary and we studied fourth order discretizations on a single cell and on a pair of cells. In this chapter, we introduce a DG-discretization technique for solving 2-D second order elliptic PDEs with curved Dirichlet boundary conditions on a complete regular rectangular grid. This discretization technique is motivated by the fact that it results in a high order discretization and a significantly simplified mesh generation in comparison to discretizations using boundary conforming meshes.

Since renewed insights into discontinuous Galerkin methods for elliptic PDEs were obtained, [3, 5, 36, 40], these methods gain in popularity. Especially, because of their convenient properties when combined with the *hp*-adaptive approach and multi-grid solvers [29, 42, 44]. In view of such applications we want to solve elliptic PDEs by a DG-method on a regular rectangular grid, while the embedded boundary is typically not aligned with the grid, but rather intersects the edges of the grid.

For this purpose, we introduce a domain $\widehat{\Omega}$ slightly larger than the domain Ω on which the BVP is defined and we straightforwardly discretize the PDE on the structured orthogonal mesh with tensor products of cubic polynomials. The part of the Dirichlet boundary, which is not aligned with the grid, i.e., the embedded boundary, is parameterized by cubic polynomials in each cell, while the Dirichlet boundary value constraint is incorporated by the use of a Lagrange multiplier. Then, according to the typical DG setting, DG-formulations for the embedded boundary are derived by elimination of this Lagrange multiplier. By construction, such a DG discretization is fourth order consistent, both in the interior and at the boundaries.

Certainly, the most classical technique in treating complex boundaries is the FEM, where elements near the boundary are adapted to the shape of the boundary curve. Although this method is convenient for high order discretizations, the advantage of having a structured grid is lost, while 3D grid generation still

remains an extremely challenging problem.

In the field of finite difference methods, the finite differences can be locally adapted to the curved boundary while the total domain is a regular structured grid. A recent example is the Embedded Curved Boundary (ECB) Method for higher dimensions, in which the curved boundary is approximated by piecewise linear segments [28, 32]. This method is fast and has all the advantages of having a regular structured grid, however no order of accuracy can be expected higher than two.

Another method which treats complex geometries on orthogonal meshes, is the immersed boundary (IB) method. This method was introduced by Peskin [39, 46] as a method to study biofluid dynamics problems. Examples of applications are the coupled motion of the blood filling the ventricles of the heart and the interaction between flexible elastic membranes in combination with an incompressible fluid in two dimensions [10]. This approach results in a very flexible method and even a variant with fourth order convergence is reported [10]. Nevertheless, we believe that it can be valuable to have a simple method at hand that fits with the discontinuous Galerkin discretization.

We present the technique in this chapter according to the following outline: in Section 7.2 we derive the DG-formulation for the Poisson equation with an embedded boundary. We briefly discuss by a simple 1D model problem that the discrete operator, associated with the DG-formulation, may become singular for certain locations of the embedded boundary condition (see also Section 6.3), i.e., we identify the Singular Embedded Boundary condition (SEB). We show for this 1D model problem that the discrete operator becomes regular if a regularization term is introduced, by weighting the embedded boundary with the traces of two linear polynomials.

Since the Baumann-Oden DG formulation is positive and stable for polynomial discretizations of order larger than two [3] without the use of an interior penalty term, we continue to study this form for the 2D Poisson equation with an embedded boundary condition. We show by 2D numerical experiments that the cubic Baumann-Oden DG-discretization for the embedded boundary problem can be regularized as in 1D, by a similar regularization term, now weighting the embedded boundary with the traces of four bilinear polynomials. Then, using this regularization term, on halving the gridsize, an average error reduction of about a factor 12 can be expected. This sub-optimal convergence can be improved, without introducing more complexity in the discretization, if for vanishing cut cells, i.e., vanishing local domains of interest Ω_e, the surface of the fictitious part of the cell is downsized, while keeping Ω_e unchanged and the cell $\widehat{\Omega}_e$ rectangular.

It is straightforward to extend the use of the above DG-technique for the embedded boundary condition to the convection equation. This is explained in Section 7.4.

In the last section we solve a singularly perturbed convection dominated boundary value problem with an embedded circular boundary. We show how accurately the boundary layer and shear layer, emanating from the curved embedded boundary, can be captured by means of the tensor product polynomials on the structured orthogonal mesh.

The present discretization technique can be applied in combination with a full multigrid algorithm.

7.2 The discontinuous Galerkin forms

7.2.1 The discontinuous Galerkin formulation for the embedded boundary condition

In order to solve a second order elliptic problem $Lu = f$ on a complex domain by means of a DG-discretization type, we consider the equation on an open domain $\widehat{\Omega}$, which is slightly larger than the open domain Ω on which the elliptic BVP is originally defined. On this fictitious domain $\widehat{\Omega} \supseteq \Omega$ we discretize the problem $Lu = f$. The solution u is determined by a Dirichlet boundary condition $u = u_0$ on $\partial\Omega$, the boundary of Ω which is smooth enough in order to be parameterized. Further, we assume that the solution u allows for a sufficiently smooth continuation on the whole of $\widehat{\Omega}$, i.e., u can be approximated by the trial functions. For this treatment we consider a piecewise rectangular domain $\widehat{\Omega}$ with boundary $\partial\widehat{\Omega}$ as in Figure 7.1.

In this domain we distinguish two non-overlapping open sub-domains, Ω and $\widetilde{\Omega}$, such that

$$\overline{\widehat{\Omega}} = \overline{\Omega} \cup \overline{\widetilde{\Omega}}, \qquad \text{and} \qquad \Omega \cap \widetilde{\Omega} = \emptyset, \tag{7.1}$$

where Ω is the domain of interest and $\widetilde{\Omega}$ is the fictitious part. On the whole domain $\widehat{\Omega}$, we now apply the differential equation, while the Dirichlet boundary conditions are (weakly) imposed on $\partial\Omega$, the boundary of Ω. So, for the Poisson equation our boundary value problem reads:

$$Lu \equiv -\Delta u = f \ \text{ on } \ \widehat{\Omega}, \qquad \text{and} \qquad u = u_0 \ \text{ on } \ \Gamma_D = \partial\Omega, \tag{7.2}$$

under the assumption that the solution u on Ω, has a sufficiently smooth con-

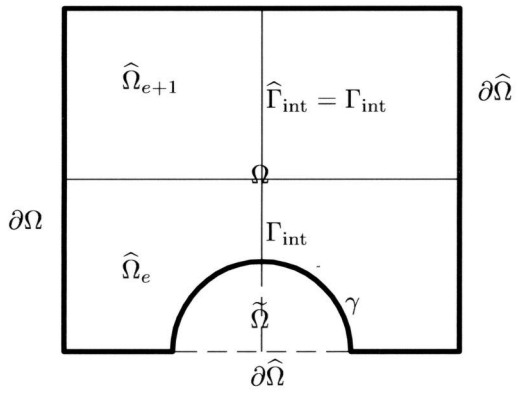

Figure 7.1: The partitioning $\widehat{\Omega}_h$, the domain of interest Ω and the fictitious part $\widetilde{\Omega}$. The fictitious domain $\overline{\widehat{\Omega}} = \overline{\Omega} \cup \overline{\widetilde{\Omega}}$.

tinuation into $\widetilde{\Omega}$, satisfying the Poisson equation on the whole of $\widehat{\Omega}$. [1]

To arrive at a mesh-dependent variational formulation of the Poisson equation, we consider a partitioning, $\widehat{\Omega}_h$, of $\widehat{\Omega}$ in regular rectangular cells, such that

$$\widehat{\Omega}_h = \left\{ \widehat{\Omega}_e \quad | \ \cup_e \overline{\widehat{\Omega}}_e = \overline{\widehat{\Omega}},\ \widehat{\Omega}_i \cap \widehat{\Omega}_j = \emptyset,\ i \neq j \right\}. \tag{7.3}$$

By the partitioning (7.3), we introduce the set of common interfaces between adjacent cells, $\widehat{\Gamma}_{\text{int}} = \overline{\widehat{\Omega}}_i \cap \overline{\widehat{\Omega}}_j$. In this way, cells $\widehat{\Omega}_e$ which contain part of the embedded boundary $\gamma_e \subset \partial\Omega$ are split into two disjoint parts, $\Omega_e = \widehat{\Omega}_e \cap \Omega$ and $\widetilde{\Omega}_e = \widehat{\Omega}_e \cap \widetilde{\Omega}$, so that $\widetilde{\Gamma}_{\text{int}} = \overline{\widetilde{\Omega}}_i \cap \overline{\widetilde{\Omega}}_j$, $i \neq j$, and $\Gamma_{\text{int}} = \widehat{\Gamma}_{\text{int}} \setminus \widetilde{\Gamma}_{\text{int}}$ is the interface not including the fictitious part. (See also Figure 7.1.) On the partitioning (7.3), we consider the broken Sobolev space [5, 6, 37] for non-negative integer k, defined by

$$H^k(\widehat{\Omega}_h) = \left\{ u \in L_2(\widehat{\Omega}) \mid u|_{\widehat{\Omega}_e} \in H^k(\widehat{\Omega}_e),\ \forall \widehat{\Omega}_e \in \widehat{\Omega}_h \right\}.$$

Now the weak DG formulation for the Poisson equation with an embedded Dirichlet boundary condition reads (see also (6.29) in Section 6.4.4): find $u \in$

[1] If this is not the case, the weak formulation should be taken as starting point.

$H^1(\widehat{\Omega}_h)$, such that

$$\begin{aligned}\sum_{\widehat{\Omega}_e \in \widehat{\Omega}_h} (\nabla u, \nabla v)_{\widehat{\Omega}_e} &- \langle\langle \nabla u \rangle, [v] \rangle_{\widehat{\Gamma}_{\text{int}} \cup \partial\widehat{\Omega}} + \sigma \langle\langle \nabla v \rangle, [u] \rangle_{\Gamma_{\text{int}}} \\ &+ \sigma \langle \mathbf{n} \cdot \nabla v, u \rangle_{\partial\Omega} + \mu \langle [v], [u] \rangle_{\Gamma_{\text{int}}} + \mu \langle v, u \rangle_{\partial\Omega} = \\ \sum_{\widehat{\Omega}_e \in \widehat{\Omega}_h} (f, v)_{\widehat{\Omega}_e} &+ \sigma \langle \mathbf{n} \cdot \nabla v, u_0 \rangle_{\partial\Omega} + \mu \langle v, u_0 \rangle_{\partial\Omega}, \qquad \forall v \in H^1(\widehat{\Omega}_h).\end{aligned} \tag{7.4}$$

Here, we define the jump operator $[\,\cdot\,]$ at the common interfaces $\widehat{\Gamma}_{\text{int}}$ and Γ_{int} between two adjacent [2] cells $\widehat{\Omega}_i$ and $\widehat{\Omega}_j$ by

$$\begin{aligned}\widehat{\Gamma}_{\text{int}}: &\quad [w(x)] = w(x)|_{\partial\widehat{\Omega}_i} \mathbf{n}_i + w(x)|_{\partial\widehat{\Omega}_j} \mathbf{n}_j, \\ \Gamma_{\text{int}}: &\quad [w(x)] = w(x)|_{\partial\Omega_i} \mathbf{n}_i + w(x)|_{\partial\Omega_j} \mathbf{n}_j,\end{aligned} \tag{7.5}$$

and, for the average operator $\langle\,\cdot\,\rangle$, we distinguish between

$$\begin{aligned}\widehat{\Gamma}_{\text{int}}: &\quad \langle \tau(x) \rangle = \frac{1}{2} \left(\tau(x)|_{\partial\widehat{\Omega}_i} + \tau(x)|_{\partial\widehat{\Omega}_j} \right) \text{ and} \\ \Gamma_{\text{int}}: &\quad \langle \tau(x) \rangle = \frac{1}{2} \left(\tau(x)|_{\partial\Omega_i} + \tau(x)|_{\partial\Omega_j} \right).\end{aligned} \tag{7.6}$$

Notice, that the terms $\sigma \langle\langle \nabla v \rangle, [u] \rangle_{\Gamma_{\text{int}}}$ and $\mu \langle [v], [u] \rangle_{\Gamma_{\text{int}}}$ are also computed at interfaces of cells $\widehat{\Omega}_e$ not containing part of the embedded boundary γ, since we then have $\widetilde{\Gamma}_{\text{int}} = \emptyset$ and hence $\widehat{\Gamma}_{\text{int}} = \Gamma_{\text{int}}$. In this way, we only require continuity of the solution u at the internal boundaries inside Ω, the domain of interest.

7.2.2 The singular embedded boundary condition (SEB) for the discontinuous Galerkin formulation

To explain a characteristic difficulty that can be encountered if (7.4) is used, we first consider the following simple one-dimensional problem. On a single cell, the unit interval $\widehat{\Omega}_h = \widehat{\Omega} = (0, 1)$, we consider the Poisson equation with homogeneous boundary conditions,

$$-\frac{d^2 u}{dx^2} = f, \quad \text{on } \widehat{\Omega}, \quad \text{with } u(d) = 0,\ u(1) = 0, \tag{7.7}$$

[2] At the boundary $\partial\widehat{\Omega}$ the interface with a virtual (flat, exterior) adjacent cell is used.

where $d \in (0,1)$ and $\Omega = (d,1)$. To discretize (7.7), we take for test and trial spaces the $(p+1)$-dimensional subspace $S_h(\widehat{\Omega}) = P^p(\widehat{\Omega}) \subset H^1(\widehat{\Omega})$, the polynomials of degree $\leq p$. So, we seek the approximation

$$u_h = \sum_{0 \leq i \leq p} c_i \phi_i(x), \ \phi_i(x) \in S_h(\widehat{\Omega}).$$

For (7.7), the general DG-formulation with the embedded boundary condition reduces to: find $u_h \in S_h(\widehat{\Omega})$ such that

$$\int_0^1 u_h' v_h' dx - [u_h'(1)v_h(1) - u_h'(0)v_h(0)] + \sigma [u_h(1)v_h'(1) - u_h(d)v_h'(d)] \quad (7.8)$$
$$+ \mu [u_h(1)v_h(1) + u_h(d)v_h(d)] = \int_0^1 v_h f dx, \qquad \forall v_h \in S_h(\widehat{\Omega}_h).$$

It is obvious that (7.8) is $(p+1)$-st order consistent. However, the matrix associated with the discrete system of (7.8) can be singular for some location $d \in (0,1)$ of the embedded boundary condition. For the given polynomial basis in $S_h(\widehat{\Omega})$ we have to solve a $(p+1)\times(p+1)$ linear system $L_{\sigma,\mu,d} u_h = f_h$, in which the matrix depends on the method parameter $\sigma = \pm 1$, the penalty parameter $\mu \geq 0$ and the location of the interior Dirichlet boundary condition d. The locations for which the matrix associated with the Baumann-Oden-DG ($\sigma = 1, \mu = 0$), the symmetric-DG ($\sigma = -1, \mu = 0$) and the non-symmetric interior penalty-method (NIPG) ($\sigma = 1, \mu > 0$), is not invertible, are shown in Table 7.1. We call these locations, d, the singular embedded boundary conditions (SEBs).

Table 7.1: Locations d of the embedded boundary condition (SEBs) for which the discrete system becomes singular. The discretizations are made for $S_h(\widehat{\Omega}) = P^p(0,1)$, $p = 2,3,4$.

p	The symmetric or Baumann method		NIPG ($\mu = 5$)		
2	–	–	11/21	–	–
3	2/5	–	0.2820018914	0.8313042416	–
p	$3/7 - 1/7\sqrt{2}$	$3/7 + 1/7\sqrt{2}$	0.1786866021	0.5490461868	0.934889434

We see that the number of locations of the interior Dirichlet boundary condition for which the discrete system becomes singular (SEBs), increases with the polynomial degree p. The use of the penalty parameter $\mu > 0$ does not stabilize the method. We discuss this below.

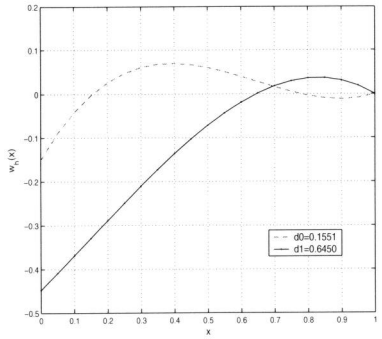

Figure 7.2: The two spurious modes of a fourth order NIPG discretization, according to (7.8) with $\sigma = 1$ and large penalty parameter $\mu = 10^6$. We see that, since $u_h(d) = u_h(1) = O(1/\mu)$, the functions satisfy (7.10) by approximation.

Considering the NIPG formulation in (7.8), with $\sigma = 1$ and $\mu >> 0$, we see that, there remain values of d, for which a spurious mode appears in (7.8):

$$0 \neq u_h \in S_h(\widehat{\Omega}_h) \mid \int_0^1 |u_h'|^2 dx + u_h'(0)u_h(0) - u_h(d)u_h'(d) + \mu[u_h^2(1) + u_h^2(d)] = 0. \tag{7.9}$$

For $\mu \to \infty$ equation (7.9) simplifies to

$$u_h(d) = u_h(1) = 0 \text{ and } \int_0^1 |u_h'|^2 dx = -u_h'(0)u_h(0), \tag{7.10}$$

and we can find a $u_h \in S_h(\widehat{\Omega})$ with $u_h'(0)u_h(0) \neq 0$. By a continuity argument the SEBs of the NIPG method in (7.8) with large penalty parameter μ satisfy (7.10) by approximation. The two spurious modes, corresponding with the SEBs $d \approx 0.1551$ and $d \approx 0.6450$, of a fourth order NIPG discretization according to (7.8), with $\sigma = 1$ and large penalty parameter $\mu = 10^6$, are shown in Figure 7.2. We see that, since $u_h(d) = u_h(1) = O(1/\mu)$, the functions satisfy (7.10) by approximation.

In the next section we show that (7.8) can be regularized.

7.2.3 Regularization of the SEB for the one-dimensional Baumann-Oden DG-discretization

Our main interest for higher-order discretizations lies in the Baumann-Oden (BO) method, since this DG-method is positive definite for polynomial spaces of degree $k \geq 2$ without the use of an interior penalty term [3]. Therefore, in spite of its adjoint consistency which leads to non-optimal L_2-accuracy, we use this DG variant for the embedded boundary problem, i.e., $\sigma = 1$ and $\mu = 0$ in (7.4).

However, in the previous Section 7.2.2 we have seen that, in view of a cubic discretization of the 1D problem (7.7), there is a location of the embedded boundary ($d = 2/5$), for which the corresponding linear system is singular (see Table 7.1). And hence, also for the two-dimensional case, we may expect locations of the embedded boundary for which the corresponding linear system is singular (SEBs). Therefore, to regularize the discrete system, we slightly modify the BO-discretization, by introducing an extra weight at the embedded boundary.

For this purpose, we first consider a modified cubic BO-discretization of the one-dimensional problem defined in (7.7). For the finite dimensional test and trial space $S_h(\widehat{\Omega}) = \text{Span}\{\phi_i(x)\} \subset H^1(\widehat{\Omega})$, $i = \{0, 1, .., 3\}$, we take on the unit interval the polynomials

$$\phi_{2n+k} = t^{n+k}(1-t)^{n+1-k}, \quad n = 0, 1, \quad k = 0, 1. \tag{7.11}$$

And, with $P^1(\widehat{\Omega}) = \text{Span}\{1 - x,\ x\}$, we introduce the following trace operator at the embedded boundary at $x = d$:

$$\widetilde{\gamma}_d \ : \ S_h(\widehat{\Omega}) \to P^1(d) \subset H^{-1/2}(d) \ : \ \widetilde{\gamma}_d(v_h) = \widetilde{\gamma}_d(v_{0,h} + v_{1,h}) = v_{0,h}(d), \tag{7.12}$$

with $v_{0,h} \in P^1(\widehat{\Omega})$ and $v_{1,h} \in S_h(\widehat{\Omega}) \backslash P^1(\widehat{\Omega})$. The present notation is used to see the correspondence with the 2D-case below. Next, with the approximation $u_h = \sum_{0 \leq i < 4} c_i \phi_i(x)$, we introduce the following *modified Baumann-Oden variant* for (7.7), i.e. $\sigma = 1$ and $\mu = 0$ in (7.8): find $u_h \in S_h(\widehat{\Omega})$ such that

$$\int_0^1 u_h' v_h' dx - [u_h'(1)v_h(1) - u_h'(0)v_h(0)] + u_h(1)v_h'(1) - u_h(d)v_h'(d) \tag{7.13}$$

$$+ \mu u_h(d)\widetilde{\gamma}_d(v_h) = \int_0^1 v_h f dx, \qquad \forall v_h \in S_h(\widehat{\Omega}_h),\ \mu \geq 0.$$

It is obvious that this discretization is fourth-order consistent for arbitrary $d \in (0, 1)$ and $\mu \geq 0$. Hence, (7.13) reduces to a 4×4 linear system $L_h u_h = f_h$,

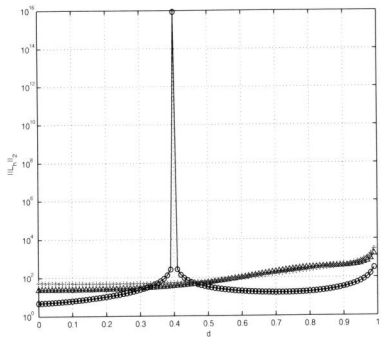

Figure 7.3: The spectral condition number $\kappa = \sigma_{\max}/\sigma_{\min}$ of the discrete operator (7.13) as function of $d \in (0,1)$, the location of the interior boundary condition for the cases $o:\ \mu = 0$, $+:\ \mu = 5$ and $\diamond:\ \mu = 10$. If the regularization term is used, the location of the embedded boundary for which the discrete operator is singular ($d = 2/5$) vanishes.

in which the discrete operator still depends on d, the location of the embedded boundary. The spectral condition number $\kappa = \sigma_{\max}/\sigma_{\min}$ as function of d, for the regularization term in (7.13), with $\mu = 0$, 5 and 10, is shown in Figure 7.3.

In case $\mu = 0$, i.e., the regularization term in (7.13) is not used, we find the singular embedded boundary condition (SEB) at $d = 2/5$ of the cubic BO-discretization, corresponding with the SEB as shown in Table 7.1. However, this SEB vanishes for the cases $\mu = 5$ and 10, i.e., if the regularization term is introduced. So, the regularization term makes the fourth-order discrete operator invertible for arbitrary $d \in (0,1)$. Notice that, as a consequence of the vanishing domain of interest, only in the limit for $d \to 1$, the system becomes singular. This, however, is intrinsic for the approach and is no restriction in practice.

7.2.4 Motivation for the use of the regularization term

The use of the regularization term in (7.13) is motivated by the following observation. Let us consider the space $V(\widehat{\Omega}) = H^1(\widehat{\Omega})$, $\widehat{\Omega} = (0,1)$, which we split as

$$V(\widehat{\Omega}) = P^1(\widehat{\Omega}) \oplus H_0^1(\widehat{\Omega}), \tag{7.14}$$

where $P^1(\widehat{\Omega}) = \text{Span}\{1-x,\ x\}$. According to (7.12), we now consider the trace operator at the embedded boundary at $x = d$:

$$\widetilde{\gamma}_d\ :\ V(\widehat{\Omega}) \to P^1(d) \subset H^{-1/2}(d)\ :\ \widetilde{\gamma}_d(v) = \widetilde{\gamma}_d(v_0 + v_1) = v_0(d), \tag{7.15}$$

with $v_0 \in P^1(\widehat{\Omega})$ and $v_1 \in H_0^1(\widehat{\Omega})$. Next, we assume that the weak formulation (7.13), for large regularization parameter μ, may be simplified by neglecting the influence of the term $u_h(d)v_h'(d)$. So we consider the weak form: find $u \in V(\widehat{\Omega})$ such that

$$B(u,v) \equiv \int_0^1 u'v'dx - [u'(1)v(1) - u'(0)v(0)] + u(1)v'(1) \tag{7.16}$$
$$+\mu u(d)\widetilde{\gamma}_d(v) = \int_0^1 fvdx, \qquad \forall v \in V(\widehat{\Omega}),\ \mu > 0.$$

It is obvious that, for arbitrary $d \in (0,1)$ a solution $u \in V$ satisfying (7.7), also satisfies (7.16). Next we show that the solution $u \in V(\widehat{\Omega})$ of (7.16) is unique and hence satisfies (7.7).

Theorem 1. *Consider the bilinear form $B(u,v)$ given in (7.16) on the functions space $V(\widehat{\Omega})$ as in (7.14). The linear system associated with (7.16) is regular in the sense that, for arbitrary $d \in (0,1)$, from $B(u,v) = 0$, $\forall v \in V(\widehat{\Omega})$ it follows that $u \equiv 0$.*

Proof. Let $0 \neq u \in V(\widehat{\Omega})$ be arbitrary and select first $v_1 \in D(\widehat{\Omega}) = \{v \in H_0^1(\widehat{\Omega}), v'(1) = 0\}$. From

$$\int_0^1 u'v_1'dx = 0, \qquad \forall v_1 \in D(\widehat{\Omega}) \subset H_0^1(\widehat{\Omega}), \tag{7.17}$$

we conclude that u is a linear polynomial on $\widehat{\Omega}$. Next, for arbitrary $v_1 \in H_0^1(\widehat{\Omega})$,

$$\int_0^1 u'v_1'dx + u(1)v_1'(1) = 0, \tag{7.18}$$

so that $u = a_0(1-x) \in P^1(\widehat{\Omega}) \subset V(\widehat{\Omega})$, $a_0 \in \mathbb{R}$, satisfying the homogeneous Dirichlet boundary condition $u(1) = 0$. Now, we consider the function $u = a_0(1-x)$, which has to satisfy

$$\int_0^1 u'v_0'dx - [u'(1)v_0(1) + u'(0)v_0(0)] + \mu v_0(d)u(d) = 0, \quad \forall v_0 \in P^1(\widehat{\Omega}). \tag{7.19}$$

Notice that for $u = a_0(1-x)$ and $v_0 = 1-x$ or $v_0 = x$, the first three terms in (7.19) vanish. Hence we are left with the condition that $\mu u(d)v_0(d) = 0$, $\forall v_0 \in P^1(\widehat{\Omega})$, and hence $u \equiv 0$. In other words $B(u,v) = 0$, $\forall v \in V(\widehat{\Omega})$ implies that $u \equiv 0$. □

7.3 The two-dimensional discretization

Next we continue with the two-dimensional Baumann-Oden variant for the embedded boundary problem, i.e., $\sigma = 1$ and $\mu = 0$ in (7.4).

The idea is to straightforwardly discretize (7.4) by means of cubic tensor product-polynomials and to parameterize the embedded boundary segment in each cell by means of cubic polynomials. Then by computing the boundary integrals with four-point Lobatto quadrature on the parameterized boundary, a fourth-order consistent discretization is obtained both in the interior and at the boundaries.

However, as seen in Section 7.2.2, also for the two-dimensional case we may expect locations of the embedded boundary for which the corresponding linear system is singular (SEBs). To avoid this difficulty, as in Section 7.2.3 we introduce a similar regularization term as (7.12) for cells having an embedded boundary segment, to regularize the corresponding discrete system.

7.3.1 Regularization of the SEBs for the two-dimensional Baumann-Oden DG-discretization

We take (7.4) with $\sigma = 1$ and $\mu = 0$ as a starting point. (I.e., the BO-formulation for the Poisson equation with embedded boundary conditions.) The idea is to stabilize cells with an interior boundary segment by means of an extra weight in order to arrive at a linear system which is non-singular for arbitrary locations of the embedded boundary condition.

For this purpose, consider the following BVP. On a single unit square $\widehat{\Omega}$, we define the Poisson equation with Dirichlet boundary condition on Γ_{D} and on the interior boundary part γ,

$$-\Delta u = f \quad \text{on} \quad \widehat{\Omega}, \text{ and } u = u_0 \quad \text{on } \partial\Omega = \Gamma_{\mathrm{D}} \cup \gamma, \tag{7.20}$$

where the Dirichlet boundary conditions are defined with $d \in (0,1)$ on

$$\begin{aligned} \Gamma_{\mathrm{D}} &= \{(x,y) \mid 0 < x < d,\ y = 0,1;\ x = 0,\ 0 < y < 1\}, \\ \gamma &= \{(x,y) \mid x = d,\ 0 < y < 1\}. \end{aligned}$$

To discretize (7.20), we take for the finite dimensional test and trial space $S_h(\widehat{\Omega}) \subset H^1(\widehat{\Omega})$ the space of cubic tensor-product polynomials in each of the two coordinate directions, based on (7.11). Hence, with

$$S_h(\widehat{\Omega}_h) = \left\{ \phi_{j,e}(y)\phi_{i,e}(x) \in P^{3\times 3}(\widehat{\Omega}) \right\}, \tag{7.21}$$

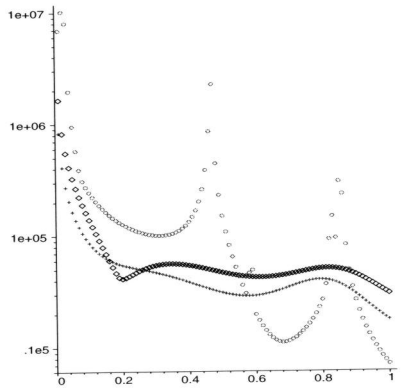

Figure 7.4: The spectral condition number $\kappa = \sigma_{\max}/\sigma_{\min}$ of the discrete operator (7.23) as function of d, the location of the interior boundary condition for the cases o : $\mu = 0$, $+$: $\mu = 5$ and $\diamond$: $\mu = 10$. It shows, that, if the regularization term is used, the locations of the embedded boundary for which the discrete operator is singular vanish. The discrete operator with regularization term is well conditioned for $d \in (0.2, 1]$. For a vanishing domain of interest Ω, it is natural that the discrete operator becomes ill-conditioned.

Furthermore, we see in Figure 7.4 that, for a vanishing domain of interest Ω with respect to the fictitious part of the domain $\widetilde{\Omega}$, $d \in (0, 0.2)$, the discrete operator becomes ill-conditioned. The suboptimal behavior in the case of a large fictitious part with a very small domain of interest in the computational cell, is quite natural because the smooth continuation of the solution in the fictitious part of the domain becomes the dominating factor. Then we have a *vanishing cut cell.* However, without changing the complexity in the discretization (7.23), a vanishing cut cell can easily be avoided, by reducing the surface of the fictitious part $\widetilde{\Omega}_e$ while keeping the domain of interest unchanged and keeping the computational cell $\widehat{\Omega}_e$ rectangular.

In the next section we study this discretization technique for more complex domains partitioned according to (7.3), where the cells with interior boundary segments are discretized by the fourth-order discrete form (7.23) and other cells are discretized by means of the corresponding Baumann-Oden's DG form. In this initial study, we do not take special measures for vanishing cut cells, in order not to obscure the convergence behavior of the approximate solution.

7.3.2 Application of the Poisson equation with a half circle excluded

In this section we study a fourth order discretization of the Baumann-Oden DG formulation (7.4), with $\sigma = 1$, $\mu = 0$, for the two-dimensional Poisson equation on a rectangular domain with a half circle excluded, where we apply on the interior boundary the extra regularization term as in (7.23).

For this purpose, we consider the (initial) computational domain $\widehat{\Omega}$ with vertices $(x, y) = (0, 0)$, $(2, 0)$, $(2, 1)$ and $(0, 1)$. The circular embedded boundary is described by

$$\gamma = \{ \ (x, y) \mid (x-1)^2 + y^2 = R^2 < 1; \ x, y \geq 0 \ \}, \tag{7.25}$$

and is in each cut cell parameterized by means of cubic polynomials. Then, the fictitious part of the domain $\widehat{\Omega}$ is given by

$$\widetilde{\Omega} = \{ \ (x, y) \mid x, y \geq 0; \ (x-1)^2 + y^2 < R^2 \ \}.$$

Next, according to (7.3), we partition the domain $\widehat{\Omega}$ in a set of regular square dyadic grids $\{g(i), \ i = 0, 1, 2, 3\}$, with mesh size $h = h_x = h_y = (\frac{1}{2})^i$. An example of such partitionings is shown in Figure 7.5.
In this figure, we see the coarse and finer partitionings, where the radius of the embedded boundary is $R = \sqrt{0.13}$. We take the radius in (7.25) such that the parameterized curve segments γ_e in cells $\widehat{\Omega}_e$ intersect two edges. (No two intersection points on one edge.)

On meshes as in Figure 7.5, we consider the discrete Baumann-Oden DG formulation for the embedded boundary (7.4) with regularization term at the curved boundary as in (7.23): find $u_h \in S_h(\widehat{\Omega}_h)$ such that

$$\begin{aligned}
&\sum_{\widehat{\Omega}_e \in \widehat{\Omega}_h} (\nabla u_h, \nabla v_h)_{\widehat{\Omega}_e} - \langle \mathbf{n} \cdot \nabla u_h, v_h \rangle_{\partial\widehat{\Omega}} + \langle \mathbf{n} \cdot \nabla v_h, u_h \rangle_{\partial\Omega} - \langle \langle \nabla u_h \rangle, [v_h] \rangle_{\widehat{\Gamma}_{\text{int}}} \\
&+ \langle \langle \nabla v_h \rangle, [u_h] \rangle_{\Gamma_{\text{int}}} + \mu \langle \widetilde{\gamma}_{\text{D}}(v_h), u_h \rangle_{\gamma} = \sum_{\widehat{\Omega}_e \in \widehat{\Omega}_h} (f, v_h)_{\widehat{\Omega}_e} + \langle \mathbf{n} \cdot \nabla v_h, u_0 \rangle_{\partial\Omega} \\
&+ \mu \langle \widetilde{\gamma}_{\text{D}}(v_h), u0 \rangle_{\gamma}, \qquad \forall v_h \in S_h(\widehat{\Omega}_h),
\end{aligned} \tag{7.26}$$

where $\mu = \nu / |\gamma_e|$, $\nu > 0$ and $\gamma = \sum_e \gamma_e$ with γ_e the parameterized boundary segment in cell $\widehat{\Omega}_e$ with length $|\gamma_e|$.

Next, we take for the finite dimensional test and trial space $S_h(\widehat{\Omega}_h) \subset H^1(\widehat{\Omega}_h)$ the space of piecewise cubic tensor-product polynomials as in (7.21).

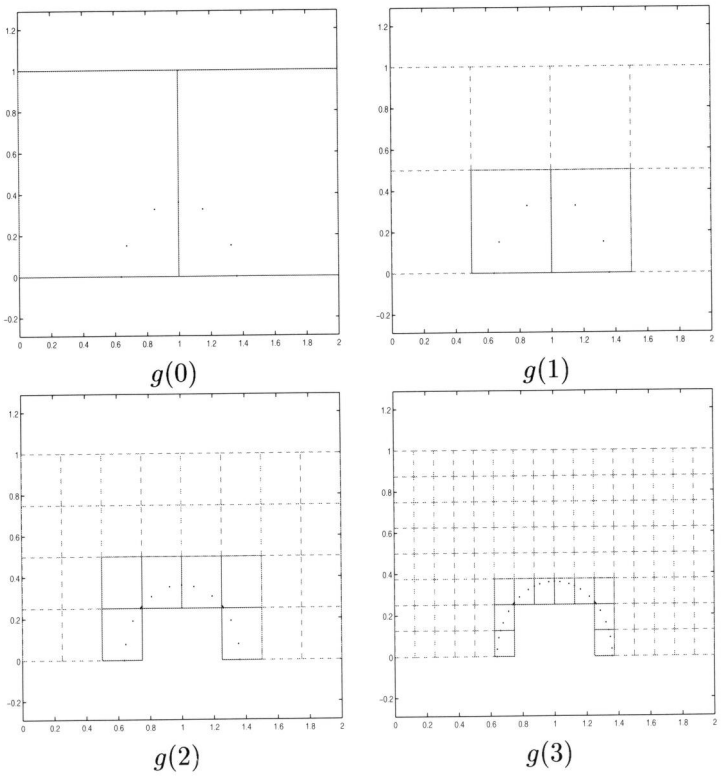

Figure 7.5: The domain $\widehat{\Omega}$, partitioned in $\{g(i),\ i = 0, 1, 2, 3\}$, with a half circle excluded. The embedded boundary is described by $\gamma = \{(x, y) \mid (x-1)^2 + y^2 = R^2 < 1;\ x, y \geq 0\}$ (in this case $R = \sqrt{0.13}$) and is parameterized in each cut cell $\widehat{\Omega}_e$ by means of cubic polynomials. To compute the boundary integrals, four-point Lobatto quadrature is used (black dots) along the parameterized circle segments γ_e.

On the master square $[0,1]^2 \subset \mathbb{R}^2$, we use as a basis the tensor-product polynomials based on (7.11), which is partly hierarchical. A basis for $P^{3\times 3}(\widehat{\Omega}_e)$ is obtained by the usual affine mapping $[0,1]^2 \to \widehat{\Omega}_e$. Hence on the regular grid in Figure 7.5 the approximate solution is:

$$\begin{aligned} u_h(x,y) &= \sum_{1\le e\le N} \sum_{0\le i,j<4} c_{e,i,j}\, \phi_i\Big(\frac{x-x_e}{h_x}\Big)\phi_j\Big(\frac{y-y_e}{h_y}\Big) \\ &\equiv \sum_{1\le e\le N} \sum_{0\le i,j<4} c_{e,i,j}\, \phi_{e,i}(\xi)\phi_{e,j}(\eta). \end{aligned} \tag{7.27}$$

The linear system $L_h u_h = f_h$ arising from (7.26) is obtained from M 'full' cells and $N-M$ cells with an interior boundary segment γ_e. Explicitly, the resulting discrete equations read:

$$\begin{aligned} &\sum_{1\le e\le M} \sum_{0\le i,j<4} c_{e,i,j} \Bigg[\Bigg(\frac{1}{h_x}\int_0^1 \phi'_{e,i}\phi'_{e,\tilde{i}}\,d\xi - \frac{1}{h_x}\langle \nabla\phi_{e,i}\rangle \cdot \Big[\phi_{e,\tilde{i}}\Big]\,|_{\widehat{\Gamma}_{\mathrm{int}}\cup\partial\widehat{\Omega}} + \\ &\qquad \frac{1}{h_x}[\phi_{e,i}]\cdot\Big\langle \nabla\phi_{e,\tilde{i}}\Big\rangle\,|_{\widehat{\Gamma}_{\mathrm{int}}\cup\partial\widehat{\Omega}}\Bigg) h_y\int_0^1 \phi_{e,j}\phi_{e,\tilde{j}}\,d\eta + h_x\int_0^1 \phi_{e,i}\phi_{e,\tilde{i}}\,d\xi \times \\ &\qquad \Bigg(\frac{1}{h_y}\int_0^1 \phi'_{e,j}\phi'_{e,\tilde{j}}\,d\eta - \frac{1}{h_y}\langle\nabla\phi_{e,j}\rangle\cdot\Big[\phi_{e,\tilde{j}}\Big]\,|_{\widehat{\Gamma}_{\mathrm{int}}\cup\partial\widehat{\Omega}} + \frac{1}{h_y}[\phi_{e,j}]\cdot\Big\langle\nabla\phi_{e,\tilde{j}}\Big\rangle\,|_{\widehat{\Gamma}_{\mathrm{int}}\cup\partial\widehat{\Omega}}\Bigg)\Bigg] + \end{aligned} \tag{7.28}$$

$$\begin{aligned} &\sum_{M<e\le N} \sum_{0\le i,j<4} c_{e,i,j} \Bigg[\Bigg(\frac{1}{h_x}\int_0^1 \phi'_{e,i}\phi'_{e,\tilde{i}}\,d\xi - \frac{1}{h_x}\langle\nabla\phi_{e,i}\rangle\cdot\Big[\phi_{e,\tilde{i}}\Big]\,|_{\widehat{\Gamma}_{\mathrm{int}}\cup\partial\widehat{\Omega}}\Bigg) h_y\int_0^1 \phi_{e,j}\phi_{e,\tilde{j}}\,d\eta + \\ &\qquad h_x\int_0^1 \phi_{e,i}\phi_{e,\tilde{i}}\,d\xi\Bigg(\frac{1}{h_y}\int_0^1 \phi'_{e,j}\phi'_{e,\tilde{j}}\,d\eta - \frac{1}{h_y}\langle\nabla\phi_{e,j}\rangle\cdot\Big[\phi_{e,\tilde{j}}\Big]\,|_{\widehat{\Gamma}_{\mathrm{int}}\cup\partial\widehat{\Omega}}\Bigg) + \end{aligned}$$

$$\begin{aligned} &\sum_{\Gamma_{\tilde{e}}\in\partial\Omega_e\cap\Gamma_{\mathrm{int}}} \sum_{0\le k<4} w_k|\Gamma_{\tilde{e}}| \Bigg\langle \nabla\Bigg(\phi_{e,\tilde{i}}\Big(\frac{x(s_k)-x_e}{h_x}\Big)\phi_{e,\tilde{j}}\Big(\frac{y(s_k)-y_e}{h_y}\Big)\Bigg)\Bigg\rangle \cdot \\ &\qquad \Bigg[\phi_{e,i}\Big(\frac{x(s_k)-x_e}{h_x}\Big)\phi_{e,j}\Big(\frac{y[s_k]-y_e}{h_y}\Big)\Bigg] + \\ &\sum_{\Gamma_{\tilde{e}}\in\partial\Omega_e\cap\partial\Omega\setminus\gamma} \sum_{0\le k<4} w_k|\Gamma_{\tilde{e}}| \Bigg(\mathbf{n}_k\cdot\nabla\Bigg(\phi_{e,\tilde{i}}\Big(\frac{x(s_k)-x_e}{h_x}\Big)\phi_{e,\tilde{j}}\Big(\frac{y(s_k)-y_e}{h_y}\Big)\Bigg)\Bigg) \times \\ &\qquad \Bigg(\phi_{e,i}\Big(\frac{x(s_k)-x_e}{h_x}\Big)\phi_{e,j}\Big(\frac{y[s_k]-y_e}{h_y}\Big)\Bigg) + \\ &\nu\sum_{0\le k<4} w_k\widetilde{\gamma}_{\mathrm{D}}\Bigg(\phi_{e,\tilde{i}}\Big(\frac{x(s_k)-x_e}{h_x}\Big)\phi_{e,\tilde{j}}\Big(\frac{y(s_k)-y_e}{h_y}\Big)\Bigg)\Bigg(\phi_{e,i}\Big(\frac{x(s_k)-x_e}{h_x}\Big)\phi_{e,j}\Big(\frac{y[s_k]-y_e}{h_y}\Big)\Bigg)\Bigg] = \end{aligned}$$

$$\sum_{1\le e\le N}\sum_{0\le i,j<4}\left[\int_{\widehat{\Omega}_e} f(x,y)\phi_{\tilde{i}}(\frac{x-x_e}{h_x})\phi_{\tilde{j}}(\frac{y-y_e}{h_y})d\widehat{\Omega}_e\right]+$$
$$\sum_{\Gamma_e\in\partial\Omega\setminus\gamma}\sum_{0\le k<4} w_k|\Gamma_e|\mathbf{n}_k\cdot\nabla\left(\phi_{\tilde{i}}(\frac{x(s_k)-x_e}{h_x})\phi_{\tilde{j}}(\frac{y(s_k)-y_e}{h_y})\right)u_0+$$
$$\nu\sum_{\gamma_e\in\gamma}\sum_{0\le k<4} w_k\tilde{\gamma}_{\mathrm{D}}\left(\phi_{e,\tilde{i}}(\frac{x(s_k)-x_e}{h_x})\phi_{e,\tilde{j}}(\frac{y(s_k)-y_e}{h_y})\right)u_0,\quad 0\le\tilde{i},\tilde{j}<4,\ 1\le e\le N.$$

For some constant $\nu > 0$ on each interior boundary segment, $\mu = \nu/|\gamma_e|$. Notice that in cells $\widehat{\Omega}_e$ with an interior boundary segment, continuity of the approximation u_h is only (weakly) imposed on the edges $\Gamma_{\tilde{e}} \cap \partial\Omega_e$. To compute the integrals over these (partial, rectangular) edges, four-point Lobatto quadrature is used. Also for computing the integrals over the parameterized interior boundary segments γ_e of the curved embedded boundary γ, we apply four-point Lobatto quadrature as shown in Figure 7.5. The unit outward normal $\mathbf{n}_k$ is evaluated at the quadrature point s_k. The other terms in (7.28) are direct extensions of one-dimensional mass and stiffness matrices (as discussed in Chapter 4) and can be straightforwardly computed.

By construction (7.28) is fourth-order consistent, both in the interior of the domain Ω and on the wall $\partial\Omega$, independently of the choice of the constant ν. A first experiment shown in Figure 7.6 confirms this observation.

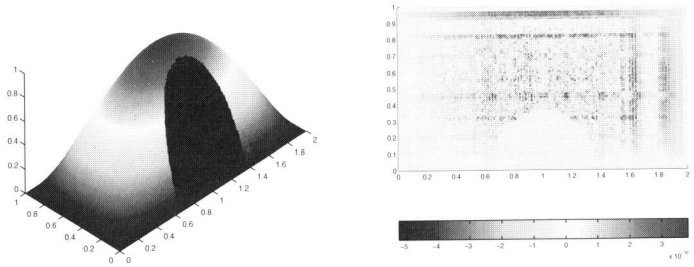

Approx. of $u = 4xy(x-2)(y-1)$ $\qquad$ $||u-u_h||_{L^\infty(\Omega)} = 5.2\times10^{-16}$

Figure 7.6: The solution and the error on the domain Ω of the problem $\Delta u = 8(y(y-1)+x(x-2))$ discretized by the fourth order DG-discretization (7.28) for the embedded boundary condition with $\nu = 0$. The discretization is made on grid $g(1)$ as shown in Figure 7.5. The radius of the circular embedded boundary is $R = \sqrt{0.13}$.

We see the approximation computed by (7.28) for the BVP (7.2) with right-hand side and boundary conditions such that the solution is given by $u = 4xy(x-2)(y-1)$. The error $||u-u_h||_{L^\infty(\Omega)}$ of the approximation is computed, by evaluating the difference between the exact and computed solution on a 50×50 equidistant grid per cell $\widehat{\Omega}_e$. We see that $||u-u_h||_{L^\infty(\Omega)}$ is of the order of machine precision.

Next we investigate the convergence of the discrete system (7.28), where we distinguish two cases: $\nu = 0$ and 10, to see the influence of the regularization term. For this purpose, we choose the right-hand side and boundary conditions in (7.2) such that the solution is $u = \sin(x)\cos(y)$. On the four grids $\{g(0), .., g(3)\}$ as in Figure 7.5 and for radii $R = \sqrt{0.13}$ and $\sqrt{0.50}$ we compute the error $||u-u_h||_{L^\infty(\Omega)}$ of the approximations. Furthermore, to check the regularity of the matrix corresponding with the discretizations on the grids $\{g(0), .., g(3)\}$, we compute the spectral condition number $\kappa = \sigma_{\max}/\sigma_{\min}$ and the minimum real part of the spectrum $\min(\Re(\lambda_i))$. The results are shown in the Tables 7.2 and 7.3.

Table 7.2: The approximation error, the spectral condition number and the minimum real part of the spectrum, of the fourth-order DG-discretization (7.28), with $\nu = 10$, on grids as shown in Figure 7.5. The exact solution is $u = \sin(x)\cos(y)$. For $(*)$ see discussion in the text.

	$R = \sqrt{0.13} \approx 0.361$		
	$\|\|u-u_h\|\|_{L^\infty(\Omega)}$	κ	$\min(\Re(\lambda_i))$
g(0)	2.9294e-003	2.7189e004	1.8183e-004
g(1)	3.3368e-004	2.2476e004	1.5288e-004
g(2)	1.4871e-005	8.0224e004	1.3117e-004
g(3)	3.7363e-006	2.8762e004	4.5802e-005

	$R = \sqrt{0.50} \approx 0.707$		
	$\|\|u-u_h\|\|_{L^\infty(\Omega)}$	κ	$\min(\Re(\lambda_i))$
g(0)	4.2920e-003	1.8397e004	1.6944e-004
g(1)	2.3569e-004	2.9286e004	1.2918e-004
g(2)	4.3262e-005	4.8409e004	9.5886e-005
g(3)	1.7262e-006	5.7696e005 $(*)$	-6.1279e-005 $(*)$

If we first compare in the Tables 7.2 and 7.3 the DG discretization with ($\nu = 10$) and without regularization term ($\nu = 0$) for the circle radius $R = \sqrt{0.13}$ and grids $\{g(0), .., g(3)\}$, we clearly see in this case that, if the regularization term is used, the discrete operator is positive definite and that the spectral

Table 7.3: The approximation error, the condition number and the minimum real part of the spectrum, of the fourth order-order DG-discretization (7.28), with $\nu = 0$, on grids as shown in Figure 7.5. The exact solution is $u = \sin(x)\cos(y)$. For $(*)$ see discussion in the text.

	$R = \sqrt{0.13} \approx 0.361$		
	$\|\|u - u_h\|\|_{L^\infty(\Omega)}$	κ	$\min(\Re(\lambda_i))$
g(0)	4.4432e-003	6.5442e003	-2.4981e-004
g(1)	3.7480e-004	1.4921e004	-0.0195
g(2)	2.9433e-004 $(*)$	5.0569e005 $(*)$	-0.0027
g(3)	2.5061e-006	3.0911e004	-0.0570

	$R = \sqrt{0.50} \approx 0.707$		
	$\|\|u - u_h\|\|_{L^\infty(\Omega)}$	κ	$\min(\Re(\lambda_i))$
g(0)	1.3258e-002	1.7460e004	-0.0162
g(1)	1.0253e-003	2.6406e004	-9.1856e-004
g(2)	3.6020e-005	5.4214e004	-0.0684
g(3)	4.9052e-006	8.0311e005 $(*)$	-0.0770

condition number in all cases is of the same order of magnitude ($O(10^4)$). This in contrast to the unregularized DG method, which suffers from singular embedded boundary conditions (SEBs) on the grid $g(2)$, as can be seen in a small error reduction and a sudden increase of the spectral condition number. Moreover the spectra of the discrete operators are indefinite.

Although the influence of vanishing cut cells is reflected in a suboptimal convergence behavior of the DG discretization, we still observe in case of the regularized DG method an average error reduction of a factor 12 (Table 7.2). Note that, as the grids are refined, the non regular reduction in the error is a consequence of the change in positions of the (embedded) boundary points and hence a change in surface of the fictitious parts in the computational cells $\widehat{\Omega}_e$. See for example the cut cells with relatively small domains of interest Ω_e in the $g(3)$ grid shown in Figure 7.5. As discussed in Section 7.3.1, the convergence can be improved if for vanishing cut cells $\widehat{\Omega}_e$ the surface of fictitious parts $\widetilde{\Omega}_e$ is downsized, while keeping the cells $\widehat{\Omega}_e$ rectangular.

In case of $R = \sqrt{0.50}$, we see that, neither the regularized and nor the unregularized DG method, suffer from SEBs on the grids $\{g(0), .., g(2)\}$: the spectral condition number is in all cases of the same order of magnitude ($O(10^4)$). However, on the $g(3)$ grid we have almost vanishing cut cells, which is reflected in an increase of the spectral condition number and an indefinite spectrum for both discrete operators. Still the solution obtained does not deteriorate. The

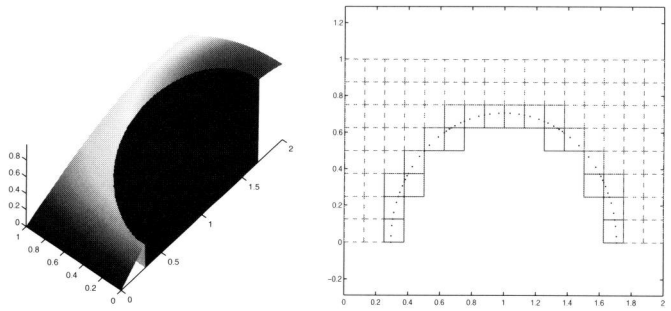

Approx. of $u = \sin(x)\cos(y)$ $g(3)$

Figure 7.7: The solution on the domain Ω of the problem $-\Delta u = 2\sin(x)\cos(y)$ discretized by (7.28), where $\nu = 10$. The discretization is made on grid $g(3)$ as shown. The radius of the circular embedded boundary is $R = \sqrt{0.50}$. Notice the almost vanishing cut cells.

solution of the regularized DG method and the grid for this situation are shown in Figure 7.7.

As an example with a singularity in the neighborhood of the boundary, we solve the BVP $\Delta u = 0$, with Dirichlet boundary conditions such that the solution is $u = \arctan(\frac{x-1}{y})$, on the domain as in Figure 7.5. To avoid the singularity at $x = 1$, we choose $R = \sqrt{0.032} \approx 0.179$ for the circular embedded boundary condition. The solution of (7.28) with $\mu = 10$ on the $g(3)$ grid is shown in Figure 7.8. Table 7.4, shows the error $||u - u_h||_{L^\infty(\Omega)}$, the spectral condition number κ and the minimum real part of the spectrum $\min(\Re(\lambda_i))$, of the DG-discretization on the grids $\{g(0), .., g(3)\}$.

Table 7.4: The error of the approximation, the condition number and the minimum real part of the spectrum, of the fourth-order DG-discretization (7.28), with $\nu = 10$, on grids as shown in Figure 7.5. The exact solution is $u = \arctan(\frac{x-1}{y})$.

	$R = \sqrt{0.032} \approx 0.179$		
	$\|\|u - u_h\|\|_{L^\infty(\Omega)}$	κ	$\min(\Re(\lambda_i))$
g(0)	3.6422e-001	2.6124e+004	2.7731e-004
g(1)	1.2682e-001	3.2321e+004	1.6839e-004
g(2)	5.8684e-002	2.2346e+004	1.5281e-004
g(3)	2.6119e-003	8.3446e+004	1.2924e-004

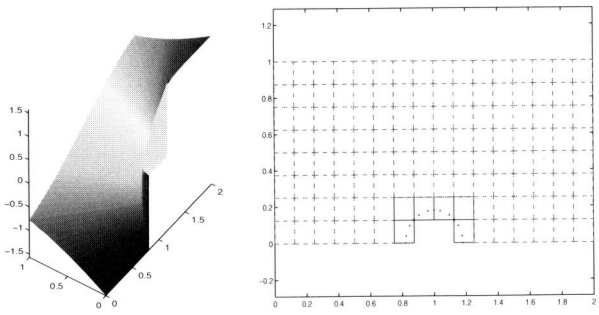

Approx. of $u = \arctan(\frac{x-1}{y})$ $g(3)$

Figure 7.8: The solution on the domain Ω of the problem $\Delta u = 0$ discretized by the fourth-order DG-discretization (7.28), with $\nu = 10$. The discretization is made on grid $g(3)$. The radius of the circular embedded boundary is $R = \sqrt{0.032}$.

7.4 DG formulation for the convection term with embedded boundary condition

Having studied the discretization of the Poisson equation with an embedded boundary condition, and with the aim to solve a convection dominated singular perturbation problem in Section 7.5, we continue with the convection equation with an embedded boundary condition. So we consider on a domain $\widehat{\Omega}$ the BVP

$$\mathbf{b} \cdot \nabla u = f \text{ in } \widehat{\Omega}, \quad u = u_0 \text{ on } \partial\Omega_{\text{in}}, \tag{7.29}$$

where $\mathbf{b}$ is a constant vector denoting the direction of the convection. The boundary of the domain of interest Ω is $\partial\Omega = \partial\Omega_{\text{in}} \cup \partial\Omega_{\text{out}}$, with the inflow boundary defined by $\mathbf{b} \cdot \mathbf{n} < 0$ on $\partial\Omega_{\text{in}}$ and the outflow boundary defined by $\mathbf{b} \cdot \mathbf{n} > 0$ on $\partial\Omega_{\text{out}}$. We also split the boundary $\partial\widehat{\Omega} = \partial\widehat{\Omega}_{\text{in}} \cup \partial\widehat{\Omega}_{\text{out}}$ of the whole domain $\widehat{\Omega}$ in an upwind and a downwind boundary and we consider the following DG formulation (see also Section 6.4.4): find $u \in H^1(\widehat{\Omega})$ such that

$$\begin{aligned} &-\int_{\widehat{\Omega}} \nabla v \cdot \mathbf{b} u \, dx + \oint_{\partial\widehat{\Omega}} \mathbf{n} \cdot \mathbf{b} \, uv \, ds + \int_{\partial\Omega_{\text{in}}} \mathbf{n} \cdot \mathbf{b} \, vu \, ds \\ &= \int_{\widehat{\Omega}} fv \, dx + \int_{\partial\Omega_{\text{in}}} \mathbf{n} \cdot \mathbf{b} \, vu_0 \, ds, \qquad \forall v \in H^1(\widehat{\Omega}). \end{aligned} \tag{7.30}$$

To arrive at the DG-formulation for the convection equation (7.29) on partitionings (7.3), for the embedded boundary parts we have to distinguish inflow boundary parts and outflow boundary parts. For the convection equation, outflow boundary parts can be neglected whereas the inflow parts provide a boundary condition for the solution. Then the DG-formulation for the convection equation on partitionings (7.3) is obtained by extending the upwind technique, as explained in Section 6.5, for multiple cells. So, cells $\widehat{\Omega}_{e,+} \in \widehat{\Omega}_h$, having either the embedded boundary segment γ_e as an outflow wall or do not have an embedded boundary at all, are denoted 'full' DG-cells, while cells $\widehat{\Omega}_{e,-} \in \widehat{\Omega}_h$ with the inflow embedded boundary segment γ_e, are cut cells in which the embedded boundary condition is taken into account. Hence we arrive at the variational form: find $u \in H^1(\widehat{\Omega}_h)$ such that

$$\begin{aligned}
&\sum_{\widehat{\Omega}_{e,+} \in H^1(\widehat{\Omega})} \left[-\int_{\widehat{\Omega}_{e,+}} \nabla v \cdot \mathbf{b} u \, dx + \int_{\partial\widehat{\Omega}_{e,+,\text{in}}} (\mathbf{n} \cdot \mathbf{b} u^-) v \, ds \right. \qquad (7.31)\\
&\left. + \int_{\partial\widehat{\Omega}_{e,+,\text{out}}} (\mathbf{n} \cdot \mathbf{b} u) v \, ds \right] + \sum_{\widehat{\Omega}_{e,-} \in H^1(\widehat{\Omega})} \left[-\int_{\widehat{\Omega}_{e,-}} \nabla v \cdot \mathbf{b} u \, dx \right.\\
&\left. + \oint_{\partial\widehat{\Omega}_{e,-}} \mathbf{n} \cdot \mathbf{b} \, uv \, ds + \int_{\gamma_e} \mathbf{n} \cdot \mathbf{b} \, vu \, ds + \int_{\Gamma_{\text{int}} \cap \partial\widehat{\Omega}_{e,-,\text{in}}} \mathbf{n} \cdot \mathbf{b} \, v(u - u^-) \, ds \right]\\
&= \sum_{\widehat{\Omega}_e \in \widehat{\Omega}_h} fv \, dx + \int_{\gamma_{\text{in}}} \mathbf{n} \cdot \mathbf{b} \, vu_0 \, ds, \quad \forall v \in H^1(\widehat{\Omega}_h),
\end{aligned}$$

where $u^-|_{\partial\widehat{\Omega}_{e,+,\text{in}} \cap \partial\Omega} = u_0$. Here, $\Gamma_{\text{int} \cap \partial\widehat{\Omega}_{e,-,\text{in}}}$ is the set of common interfaces on which the solution of (7.29) is continuous. However, continuity is not required outside the domain Ω and, hence, not on $\widetilde{\Gamma}_{\text{int}} = \widehat{\Gamma}_{\text{int}} \cap \widetilde{\Omega}$.

The discretization of (7.31) together with (7.26) gives a discrete formulation of the convection-diffusion equation

$$-\Delta u + \mathbf{b} \cdot \nabla u = f \quad \text{in } \widehat{\Omega}, \quad u = u_0 \text{ on } \partial\Omega, \qquad (7.32)$$

for domains with embedded Dirichlet boundary condition. Hereby, we expect it to be unlikely, that the discretization of (7.31) in combination with the fourth-order regularized DG-formulation for the diffusion part (7.28) suffers from SEBs.

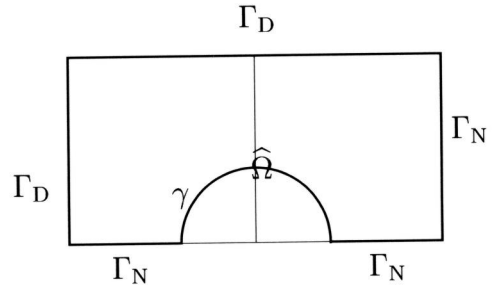

Figure 7.9: The domain for problem (7.33-7.34).

7.5 Application to a convection-diffusion problem with dominating convection on a domain with a curved embedded boundary

In this section we solve the singularly perturbed convection-diffusion problem (see Figure 7.9 and also Figure 7.5):

$$-\varepsilon\Delta u + u_x = f, \quad \text{on } \widehat{\Omega} = \{\,(x,y) \mid -1 < x < 1,\ 0 < y < 1\}\,, \tag{7.33}$$

$$\begin{aligned} u &= 0 \quad \text{on } \partial\Omega = \{\,(x,y) \mid x = -1,\ 0 < y < 1;\ -1 < x < 1, y = 1\}\,, \\ u &= 1 \quad \text{on } \Gamma_D = \{\,(x,y) \mid x^2 + y^2 = R^2, y > 0;\ R < 1\}\,, \\ \mathbf{n}\cdot\varepsilon\nabla u &= 0 \quad \text{on } \Gamma_N = \{\,(x,0) \mid R < |x| < 1\} \cup \{\,(1,y) \mid 0 < y < 1\}\,. \end{aligned} \tag{7.34}$$

The solution of this boundary value problem has a rather complex structure [21]. At the upwind part of the circle a boundary layer of thickness $O(\varepsilon)$ develops, since the solution has to satisfy the Dirichlet boundary condition on the circle. Downwind of the circle, a shear layer of thickness $O(\sqrt{\varepsilon})$ extends over the domain Ω. The transition from the boundary to the shear layer is difficult to analyze. It is interesting to see how well this complex structure is captured by means of a tensor-product fourth order DG-discretization.

The DG-discretization of (7.33) is constructed by a linear combination of (7.26) and (7.31). We take for $S(\widehat{\Omega}_h) \subset H^1(\Omega_h)$, the tensor product of polynomials of degree less than four in each of the coordinate directions. We construct

a basis for $S(\widehat{\Omega})$ from the cubics (7.11), defined on the unit interval and we parameterize the circular embedded boundary by means of cubic polynomials. Then, a discretization of problem (7.33) on meshes as shown in Figure 7.5 is obtained: find $u_h \in S_h(\widehat{\Omega}_h)$ such that

$$
\begin{aligned}
&\sum_{\widehat{\Omega}_e \in \widehat{\Omega}_h} (\varepsilon \nabla u_h, \nabla v_h)_{\widehat{\Omega}_e} - \langle \mathbf{n} \cdot \varepsilon \nabla u_h, v_h \rangle_{\Gamma_{\mathrm{D}}} + \langle \mathbf{n} \cdot \varepsilon \nabla v_h, u_h \rangle_{\Gamma_{\mathrm{D}}} \qquad (7.35)\\
&- \langle \langle \varepsilon \nabla u_h \rangle, [v_h] \rangle_{\widehat{\Gamma}_{\mathrm{int}}} + \langle \langle \varepsilon \nabla v_h \rangle, [u_h] \rangle_{\Gamma_{\mathrm{int}}} + \mu \langle \varepsilon \widetilde{\gamma}_{\mathrm{D}}(v_h), u_h \rangle_{\gamma}\\
&+ \sum_{\widehat{\Omega}_{e,+} \in H^1(\widehat{\Omega})} \left[- \int_{\widehat{\Omega}_{e,+}} \nabla v_h \cdot \mathbf{b} u_h \, dx + \int_{\partial \widehat{\Omega}_{e,+,\mathrm{in}}} (\mathbf{n} \cdot \mathbf{b} u_h^-) v_h \, ds \right.\\
&\left. + \int_{\partial \widehat{\Omega}_{e,+,\mathrm{out}}} (\mathbf{n} \cdot \mathbf{b} u_h) v_h \, ds \right] + \sum_{\widehat{\Omega}_{e,-} \in H^1(\widehat{\Omega})} \left[- \int_{\widehat{\Omega}_{e,-}} \nabla v_h \cdot \mathbf{b} u_h \, dx \right.\\
&\left. + \oint_{\partial \widehat{\Omega}_{e,-}} \mathbf{n} \cdot \mathbf{b} \, u_h v_h \, ds + \int_{\gamma_e} \mathbf{n} \cdot \mathbf{b} \, v_h u_h \, ds + \int_{\Gamma_{\mathrm{int}} \cap \partial \widehat{\Omega}_{e,-,\mathrm{in}}} \mathbf{n} \cdot \mathbf{b} \, v_h (u_h - u_h^-) \, ds \right]\\
&= \mu \langle \varepsilon \widetilde{\gamma}_{\mathrm{D}}(v_h), 1 \rangle_{\gamma} + \int_{\gamma_{\mathrm{in}}} \mathbf{n} \cdot \mathbf{b} \, v_h 1 \, ds, \quad \forall v_h \in S_h(\widehat{\Omega}_h), \ \mathbf{b} = (1,0).
\end{aligned}
$$

Similar as in (7.28) the integrals over the internal and the parameterized embedded boundaries, Γ_{int} and γ_e are computed by a four-point Lobatto quadrature rule.

Figure 7.10 shows the solution of the discretization (7.35) on the $g(3)$ grid as shown in Figure 7.5, for $R = \sqrt{0.13}$ and $\mu = 10/|\gamma_e|$, for the different values of $\varepsilon = 0.5$, 0.25, 0.1 and 0.05.

In all cases, we see clearly a boundary layer at the upwind side of the circle and the shear layer at the downwind side in the domain Ω. The approximations for ε to 0.1 perfectly satisfy the boundary conditions on $\partial\Omega$. For values of $\varepsilon << 1$, the boundary layer is too sharp, to be accurately represented by piecewise cubics on the grid $g(3)$. However, Figure 7.11 shows a side- and top-view of the solution for $\varepsilon = 0.05$ on the finer mesh $g(4)$. The boundary layer is accurately captured and we see clearly the parabolic structure of the boundary layer and the shear layer [21].

7.6 Conclusion

In this chapter we propose a discontinuous Galerkin discretization technique for solving 2-D second order elliptic PDEs on a regular rectangular grid, while the boundary value problem has a curved Dirichlet boundary. This discretization

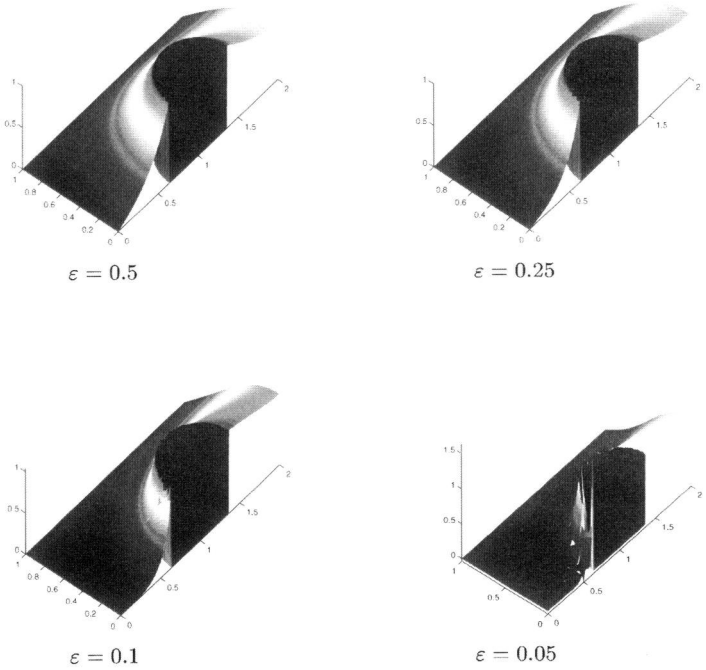

$\varepsilon = 0.5$ $\varepsilon = 0.25$

$\varepsilon = 0.1$ $\varepsilon = 0.05$

Figure 7.10: The approximate solution u_h of $-\varepsilon\Delta u + u_x = 0$, on the domain exterior of the circle, on mesh $g(3)$ as shown in Figure 7.5, for the fourth-order DG discretization with Dirichlet boundary condition $u_0 = 1$ on the circle ($R = \sqrt{0.13}$).

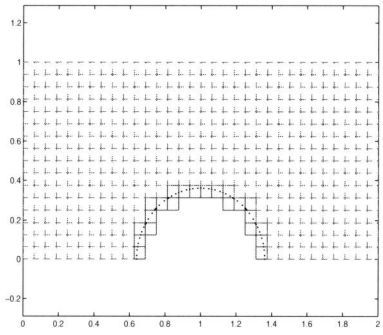

$g(4)$

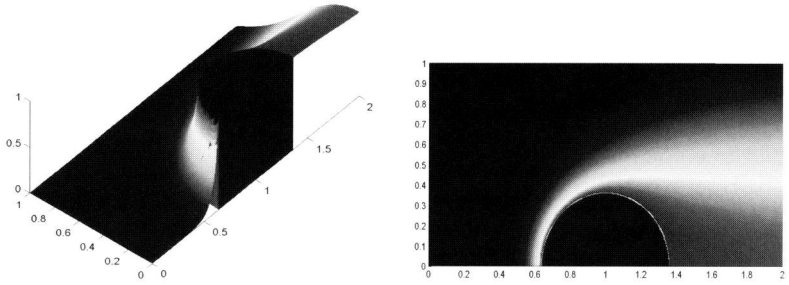

Figure 7.11: Side- and top-view of the approximate solution u_h of $-0.05\Delta u + u_x = 0$, on the domain exterior of the circle, on mesh $g(4)$ as shown, for the fourth-order DG discretization with Dirichlet boundary condition $u_0 = 1$ on the circle ($R = \sqrt{0.13}$).

technique is motivated by our interest in an *hp*-adaptive approach and multigrid solvers, for which we strongly prefer a structured regular rectangular grid. Moreover, in a DG context, the proposed discretization technique results in a significantly simplified numerical discretization and mesh generation in comparison to discretizations using boundary conforming meshes.

For this purpose we extend the domain on which the BVP is defined such that it can partitioned by means of regular rectangular cells. Then we straightforwardly discretize the problem with tensor-product cubics and parameterize the embedded boundary with cubic polynomials. By construction, the resulting DG discretization is fourth-order consistent both in the interior and at the

boundaries.

By a simple 1D-model problem we discuss that the resulting discrete system is not always invertible for arbitrary locations of the embedded boundary. We show for this 1D-model problem that the Singular Embedded Boundary conditions (SEBs) vanish if a regularization term is used, only weighting the embedded boundary with the traces of linear polynomials.

On coarse and finer regular rectangular grids we solve the 2-D Poisson equation with a circular embedded boundary condition, approximated by cubic polynomials. For the Baumann-Oden DG discretization, we show by numerical experiments that on halving the grid size an average error reduction of about a factor 12 can be expected, if a similar regularization term is used, weighting the embedded boundary with the trace of bilinear polynomials. Without introducing more complexity in the discretization, the convergence can be improved if we downsize the fictitious parts of the cells that are only covered for a very small part by the original domain.

As an example we solve the Poisson equation with the singular solution, $u = \arctan(x-1)/y$, with a small embedded Dirichlet boundary condition around the point $(1,0)$, to give an illustration of the discretization technique used for the embedded boundary condition.

To further show the possibilities of the DG-discretization, we solve a convection dominated boundary value problem with a circular embedded boundary condition. The solution of this problem shows sharp boundary and shear layers with a complex structure. The boundary layer and the shear layer, emanating from the curved boundary, are captured accurately by means of piece-wise cubic polynomials. This shows that the proposed DG discretization technique is effective.

Bibliography

[1] M. Abramowitz and I. A. Stegun. *Handbook of Mathematical Functions.* National Bureau of Standards, Dover, New York, 1992.

[2] D.N. Arnold. An interior penalty finite element method with discontinuous elements. *SIAM J.Numer.Anal.*, 19:742–760, 1982.

[3] D.N. Arnold, F. Brezzi, B. Cockburn, and D. Marini. Unified analysis of discontinuous Galerkin methods for elliptic problems. *SIAM J. Numer. Anal.*, pages 1749 – 1779, 2002.

[4] P. Bastian and V. Reichenberger. Multigrid for higher order discontinuous Galerkin finite elements applied to groundwater flow. Technical Report 2000-37, SFB 359, 2000.

[5] C. E. Baumann and J. T. Oden. A discontinuous *hp*-finite element method for convection-diffusion problems. *Comput. Methods Appl. Mech. Engrg.*, 175:311–341, 1999.

[6] C.E. Baumann. *An hp-adaptive discontinuous Finite Element Method for Computational Fluid Dynamics.* PhD thesis, The University of Texas at Austin, 1997.

[7] J. H. Bramble. *Multigrid Methods.* Number 294 in Pitman research notes in mathematics series. Longman Scientific & Technical, Harlow, 1993.

[8] A. Brandt. Multi-level adaptive techniques (MLAT) for singular perturbation-problems. In P. W. Hemker and J. J. H. Miller, editors, *Numerical Analysis of Singular Perturbation Problems*, pages 53–142. Academic Press, New York, 1979.

[9] B. Cockburn. Discontinuous Galerkin methods for convection-dominated problems. In T. J. Barth and H. Deconinck, editors, *High-Order Methods for Computational Physics*, volume 9, pages 69–224. Springer-Verlag, New York, 1999.

[10] R. Cortez and M. Minion. The Blob projection method for immersed boundary problems. *Journal of Computational Physics*, 161:428–453, 2000.

[11] W. Dahmen, S. Müller, and T Schlinkmann. On an adaptive multigrid solver for convection-dominated problems. *SIAM J. Sci. Comput.*, 25:1018–1041, 2003.

[12] P.M. de Zeeuw and E.J. van Asselt. The convergence rate of multi-level algorithms applied to the convection diffusion equation. *SIAM J.S.S.C.*, 6:492–503, 1985.

[13] L. Delves and C. Hall. An implicit matching principle for global element calculations. *J. Inst. Math. Appl.*, 23:223–234, 1979.

[14] D. Goldstein, R. Handler, and L. Sirovich. Modeling a no-slip flow boundary with an external flow field. *J. Comp. Phys.*, 105:354–366, 1993.

[15] J. Gopalakrishnan and G. Kanschat. A multilevel discontinuous Galerkin method. *Numer. Math.*, 95:527–550, 2003.

[16] W. Hackbusch. *Multigrid Methods and Applications.* Springer-Verlag, Berlin, New York, 1985.

[17] W. Hackbusch. *Theorie und Numerik elliptischer Differentialgleichungen.* Teubner Studienbuecher, 1986.

[18] P. W. Hemker. Fourier analysis of gridfunctions, prolongations and restrictions. Technical Report NW 93, Mathematical Centre, Amsterdam, 1980.

[19] P. W. Hemker. On the structure of an adaptive multi-level algorithm. *BIT*, 20:289–301, 1980.

[20] P. W. Hemker. A note on defect correction processes with an approximate inverse of deficient rank. *Appl. Math. Comp.*, 8:137–139, 1982.

[21] P. W. Hemker. A singularly perturbed model problem for numerical computation. *Journal of Comp. and Appl. Math.*, 76:277–285, 1997.

[22] P.W. Hemker, W. Hoffmann, and M.H. van Raalte. Discontinuous Galerkin discretization with embedded boundary conditions. *Computational Methods in Applied Mathematics*, 3:135–158, 2003.

[23] P.W. Hemker, W. Hoffmann, and M.H. van Raalte. Fourier two-level analysis for discontinuous Galerkin discretisation with linear elements. *NLAA*, 11:473–491, 2004.

[24] P.W. Hemker, W. Hoffmann, and M.H. van Raalte. Two-level Fourier analysis of a multigrid approach for discontinuous Galerkin discretisation. *SIAM Journal on Scientific Computing*, 25:1018–1041, 2004.

[25] P.W. Hemker and M.H. van Raalte. Fourier two-level analysis for higher dimensional discontinuous Galerkin discretisation. *Computing and Visualization in Science*, 7:159–172, 2004.

[26] J. Hendry and L. Delves. The global element method applied to a harmonic mixed boundary value problem. *J. Comp. Phys.*, 33:33–44, 1978.

[27] D. W. Hewett. The embedded curved boundary method for orthogonal simulation meshes. *J. Comp. Phys.*, 138:585 – 616, 1997.

[28] D.W. Hewett and C.S. Kueny. The dielectric boundary condition for the embedded curved boundary (ECB) method. Technical Report UCRL-JC-129703, Lawrence Livermore Nat. Lab., 1998. presented at the 16th International Conference on the Numerical Simulation of Plasmas, February 1998, Santa Barbara, CA.

[29] P. Houston, C. Schwab, and E. Süli. Discontinuous *hp*-finite element methods for advection-diffusion problems. Technical Report No. 2000-07, ETHZ, Zürich, Switzerland, 2000.

[30] C. Johnson and J. Pitkäranta. An analysis of the discontinuous Galerkin method for a scalar hyperbolic equation. *Math. Comput.*, 46:1–26, 1986.

[31] Jungwoo Kim, Dongjoo Kim, and Haecheon Choi. An immersed-boundary finite-volume method for simulations of flow in complex geometries. *Journal of Computational Physics*, 171:132–150, 2001.

[32] C.S. Kueny. Embedded curved boundaries and adaptive mesh refinement. Technical Report UCRL-JC-129729, Lawrence Livermore Nat. Lab., 1998.

[33] R.J. LeVeque and Zhilin Li. The immersed interface method for elliptic equations with discontinuous coefficients and singular sources. *SIAM Journal on Numerical Analysis*, 31(4):1019–1044, 1994.

[34] R.J. LeVeque and Zhilin Li. Immersed interface methods for Stokes flow with elastic boundaries or surface tension. *SIAM Journal on Scientific Computing*, 18(3):709–735, 1997.

[35] Z. Li. *The Immersed Interface Method - A Numerical Approach for Partial Differential Equations with Interfaces.* PhD thesis, University of Washington, 1994.

[36] J. Nitsche. Über ein Variationsprinzip zur Lösung von Dirichlet Problemen bei Verwendung von Teilraumen die keinen Randbedingungen unterworfen sind. *Abh. Math. Sem. Univ. Hamburg*, 36:9 15, 1971.

[37] J.T. Oden, I. Babuška, and C.E. Baumann. A discontinuous *hp*-finite element method for diffusion problems. *J. Comp. Phys.*, 146:491–519, 1998.

[38] A. Pardhanani, W. Spotz, and F. Carey. A stable multigrid strategy for convection-diffusion using high order compact discretisation. *Electronic Transaction on Numerical Analysis*, 6:211–223, 1997.

[39] C.S. Peskin. Numerical analysis of blood flow in the heart. *J. Comp. Phys.*, 25:220 – 252, 1977.

[40] S. Prudhomme, F. Pascal, J.T. Oden, and A.Romkes. Review of a priori error estimations for discontinuous galerkin methods. *TICAM report 00-27*, 2000.

[41] W. Reed and T. Hill. Triangular mesh methods for the neutron transport equation. Technical Report LA-UR 73-479, LANL, 1973.

[42] J.F. Remacle, J.E. Flaherty, and M.S. Shephard. An adaptive discontinuous Galerkin technique with an orthogonal basis applied to compressible flow problems. *SIAM Review*, 45:53–72, 2003.

[43] B. Rivière, M. F. Wheeler, and V. Girault. Improved energy estimates for interior penalty, constrained and dicontinuous Galerkin methods for elliptic problems. Part I. *Computational Geosciences*, 3:337–360, 1999.

[44] E. Süli, C. Schwab, and P. Houston. *hp*-DGFEM for partial differential equations with non-negative characteristic form. In B. Cockburn, G. E. Karniadakis, and C.-W. Shu, editors, *Discontinuous Galerkin Methods. Theory, Computation and Applications*, volume 11 of *Lecture Notes in Comput. Sci. Engrg.*, pages 221–230. Springer-Verlag, New York, 2000.

[45] U. Trottenberg, C.W. Oosterlee, and A. Schüller. *Multigrid.* Academic Press, London, 2001.

[46] C. Tu and C. S. Peskin. Stability and instability in the computation of flows with moving immersed boundaries: A comparison of three methods. *SIAM Journal on Scientific and Statistical Computing*, 13:1361–1376, 1992.

[47] M.H. van Raalte. A feasibility study for DG discretisation with embedded dirichlet boundary condition. *APNUM*, 51:361–383, 2004.

[48] P. Wesseling. A robust and efficient multigrid method. In W. Hackbush and U. Trottenberg, editors, *Multigrid Methods*, pages 614–630. Springer-Verlag, New York, 1982.

[49] P. Wesseling. *An Introduction to Multigrid Methods.* John Wiley & Sons, 1992. Corrected Reprint. Philadelpha: R.T. Edwards, Inc., 2004.

[50] M. Wheeler. An elliptic collocation-finite element method with interior penalties. *SIAM J. Numer. Anal.*, 15:152–161, 1978.

Summary

In this thesis we consider numerical aspects for the solution of elliptic boundary value problems that are discretized by discontinuous Galerkin (DG) methods. Recently DG methods show an increasing popularity, because they enjoy a great flexibility in local mesh refinement (h-refinement) and in polynomial order adaptation (p-refinement). In view of these convenient properties and because of our interest in a full hp-self-adaptive approach for the solution of boundary value problems, we study the application of DG methods in a multigrid (MG) algorithm. A MG algorithm may serve as an excellent basis for a full hp-self-adaptive algorithm. Therefore, we present a detailed MG convergence analysis for the discrete equations that arise from the linear second order elliptic partial differential equation discretized by the symmetric DG, the Baumann-Oden DG, the symmetric and non-symmetric interior penalty (IPG and NIPG respectively) methods.

Essential for a properly constructed MG algorithm is the choice of the smoother. This ingredient in the MG algorithm is responsible for smoothing the iteration error during the iterative MG process. In this analysis we study the MG convergence for two different types of block-relaxation methods that may serve as a smoothing procedure in the MG algorithm. We consider the classical *cellwise* block-relaxation methods (block-Jacobi and block-Gauss-Seidel) and the novel *pointwise* block-relaxation methods. In the cellwise iterative process, the block-relaxation is based on a grouping of degrees of freedom according to the cells of the discretization. In a pointwise block relaxation, we associate the grouping of the degrees of freedom with the cell vertices.

Using Fourier smoothing and two-level analysis we study the convergence of MG iteration for the two different types of smoothing procedures. For pure elliptic DG discretizations, we show that, in contrast to the classical cellwise smoothing, MG iteration with pointwise relaxation procedures leads to an efficient MG algorithm. E.g., in our analysis we find that, for DG discretizations of

the two-dimensional Poisson equation, independent of the mesh size, simple MG cycles give an error reduction factor of $0.2 - 0.4$ per iteration sweep. We also demonstrate the MG convergence behavior by numerical experiments. Theory and practice coincide very well.

After the pure diffusion case, we continue to analyze MG convergence for the convection equation and the convection dominated equation. Here, we restrict ourselves to the equations discretized in one space dimension. Also in this analysis we study MG convergence for the cellwise and pointwise smoothers. We find that, in case the diffusion term is discretized by the Baumann-Oden DG method, only a good two-level error reduction factor (0.4) is found if pointwise Jacobi smoothing is used. We further show, that in case the diffusion term is discretized by the non-symmetric DG method, simple MG cycles with cellwise symmetric-Gauss-Seidel smoothing are sufficient to solve the convection and convection-diffusion equation efficiently. Then an error reduction factor of $0.2 - 0.3$ is observed. We present numerical experiments to illustrate the analysis.

For a proper definition of the grid-transition operators in the MG algorithm, it is convenient to discretize the equation on a regular rectangular domain. Then a difficulty arises if the equation is defined on a domain with curved boundaries. The boundary cannot follow the gridlines of the orthogonal mesh. In order to keep the orthogonal basic mesh, we introduce a novel high-order DG discretization technique, in which we embed the curved boundary of the domain in the regular rectangular cells. Starting with the Lagrange multiplier theory we introduce three types of weak forms that can be used for the discretization of the embedded boundary value problem. We consider (i) the Lagrange multiplier form for the embedded boundary, (ii) the hybrid form for the embedded boundary and (iii) the discontinuous Galerkin (DG) form for the embedded boundary.

First we analyze the properties of these forms, considering simple one- and two-dimensional problems on one or a pair of cells. We identify the finite dimensional polynomial spaces, in which we discretize the embedded boundary value problem and we study the consistency and invertibility of the corresponding discrete operators. In our analysis we find that both in case of the Lagrange multiplier form and in case of the DG form for the embedded boundary value problem, the discrete operators are not always invertible for a given location of the embedded boundary. In case of the hybrid discretization of the embedded boundary problem, we do not find such singular locations. However, for a given polynomial space all the three forms are consistent both in the interior of the domain and at the boundary.

Although the hybrid form for the embedded boundary has convenient properties for the regularity of the discrete operator, the use of this form leads to a

rather expensive and complicated discretization algorithm. Therefore, because of the simplicity of the DG discretization, we continue to explore the DG form for discretizations on complete two-dimensional orthogonal meshes. To increase the regularity of the DG form for a fourth-order discretization, we introduce an extra weight on the embedded boundary. The resulting discretization of the embedded boundary value problem is fourth-order consistent both in the interior of the domain and at the boundaries and we find an average discrete convergence factor of about 12. We further discuss that this convergence rate can be improved by a relative simple modification in the DG discretization. By solving a singularly perturbed convection-diffusion problem we give an illustration of the possibilities of this DG discretization technique.

We conclude that this technique leads to a much simpler mesh-generation than in the classical finite element approach. The DG discretization technique for the embedded boundary value problem shows its use for discretizations where orthogonal meshes are preferred, as is the case of our MG algorithm.

Samenvatting

In deze dissertatie bestuderen we technieken voor het numeriek oplossen van elliptische partiële differentiaalvergelijkingen. Het oplossen van deze vergelijkingen, is een belangrijk wiskundig hulpmiddel by het modelleren van allerhande technische en fysische verschijnselen. Over het algemeen zijn deze vergelijkingen echter te gecompliceerd om analytisch op te lossen. Maar numerieke methoden bieden de mogelijkheid de oplossing te benaderen. De computer is daarbij een nuttig hulpmiddel. Hoewel in de laatste tien jaar zowel de rekenkracht als het geheugen van computers sterk is toegenomen, is het numeriek oplossen van partiële differentiaalvergelijkingen over het algemeen erg tijdrovend. Daarom is het van belang dat de numerieke methoden efficiënt omgaan met zowel de opslag van de data als met de rekentijd.

In deze dissertatie richten we ons op een nieuwe klasse van eindige-elementen methoden voor het discretiseren van lineaire tweede-graads elliptische vergelijkingen: de discontinue Galerkin (DG) methoden. We beschouwen de symmetrische DG, de Baumann-Oden DG, de symmetrische en de asymmetrische 'interior penalty' DG methoden. Het bestuderen van deze methoden is van belang omdat een DG methode, in tegenstelling tot de klassieke eindige-elementen methode, zeer goede eigenschappen heeft in het geval van lokale maaswijdte-verfijning en lokale aanpassing van de graad van nauwkeurigheid van de benadering. De toepassing van dergelijke adaptieve technieken kan tot een algoritme leiden dat zowel met de opslag van data als met de rekentijd optimaal efficiënt omgaat.

Het discretiseren van de elliptische partiële differentiaalvergelijking leidt in het algemeen tot een groot stelsel algebraïsche vergelijkingen. Om dit stelsel efficiënt op te lossen gebruiken we een 'multirooster' (MR) algoritme. De keuze van deze methode is gerechtvaardigd, omdat een goed geconstrueerd MR-algoritme een minimale hoeveelheid rekentijd gebruikt. Het is een $O(N)$ oplossingsmethode.

Een essentieel onderdeel van een goed werkend MR-algoritme is de

'smoother', of wel de 'gladmaker'. Dit onderdeel in het MR-proces is verantwoordelijk voor het gladmaken van de iteratiefout gedurend het iteratieve MR-proces. In deze dissertatie bestuderen we de convergentie van het MR-algoritme voor twee verschillende typen block-relaxatie methoden: de klassieke *celsgewijze* (Jacobi en Gauss-Seidel) relaxatie en de nieuwe *puntsgewijze* relaxatie. Het eerste type iteratieve methode relaxeert over de cellen van de DG discretisatie, terwijl de puntsgewijze methode relaxeert over de hoekpunten van de cellen.

Met behulp van Fourieranalyse onderzoeken we het MR convergentiegedrag voor deze twee typen smoothers. Voor puur elliptische DG discretisaties laten we zien dat, in tegenstelling tot de celsgewijze smoother, het gebruik van de puntsgewijze smoother tot een efficiënt MR-algoritme leidt. In onze analyse tonen we o.a. aan, dat voor DG discretisaties van de twee-dimensionale Poisson vergelijking, simpele MR-cycli, een convergentie factor van $0.2 - 0.4$ per iteratiestap hebben, onafhankelijk van de maaswijdte. Met numerieke experimenten illustreren we het convergentiegedrag van de verschillende MR-algoritmen. Theorie en praktijk komen goed overeen.

Nadat we zuivere diffusie geanalyseerd hebben, behandelen we de convergentie van MR-iteratie voor de convectie-diffusie en de convectie-gedomineerde vergelijking. In deze analyse bestuderen we ook de robuustheid van het MR-algoritme. We beperken ons hier tot de één-dimensionale vergelijkingen. Ook hier bestuderen we MR-convergentie met de celsgewijze en puntsgewijze smoothers. We vinden dat, in het geval van de DG-methode waarbij de diffusieterm gediscretiseerd is met de Baumann-Oden DG-methode, alleen een goede twee-niveaux fout-reductie-factor (0.4) wordt voorspeld wanneer de puntsgewijze Jacobi blok-relaxatie als smoother wordt gebruikt. We laten verder zien dat voor de DG methode, waarin de diffusie-term gediscretiseerd is met asymmetrische 'interior penalty' DG methode, eenvoudige MR-iteratie met een celsgewijze, symmetrische Gauss-Seidel smoother voldoende is om de convectie-diffusie en de convectie gedomineerde vergelijking op te lossen, ongeacht de verhouding convectie/diffusie. Met de Fourieranalyse tonen we een reductie in de fout met een factor $0.2 - 0.3$ per MR-cycle aan. Met numerieke experimenten illustreren we deze analyse.

Om goed de informatieoverdracht tussen de verschillende roosters te beschrijven, is het gewenst om de vergelijking te discretiseren op een rechthoekig rooster. Een moeilijkheid treedt dan echter op wanneer het probleem gedefineerd is op een gebied met een gekromde rand. De randen van het domein kunnen dan niet de roosterlijnen van het orthogonale rooster volgen. Om toch een rechthoekig rooster te behouden, introduceren we een nieuwe hogere-orde DG discretisatie-techniek, waarbij de gekromde rand door de vierkante cellen

wordt gelegd. Uitgaande van de Lagrange-multiplier-theorie introduceren we drie formuleringen die gebruikt kunnen worden voor het discretiseren van de inwendige rand. We beschouwen: (i) de Lagrange-multiplier formulering voor een inwendige rand, (ii) de hybride formulering voor een inwendige rand en (iii) de discontinue Galerkin formulering voor de inwendige rand.

Eerst analyseren we de eigenschappen van deze formuleringen aan de hand van eenvoudige één- en twee-dimensionale problemen op één of twee cellen. We identificeren de eindig-dimensionale polynoomruimten waarin een dergelijk inwendig-rand-probleem gediscretiseerd wordt en we bestuderen de consistentie en inverteerbaarheid van de discrete operatoren. Uit onze analyse blijkt dat in het geval van de Lagrange multiplier- en de DG-formulering, de discrete operator niet altijd inverteerbaar is. Dit verschijnsel treedt op voor bepaalde lokaties van de inwendige rand. Echter, voor een hybride discretisatie van het inwendige-rand-probleem vinden we dergelijke singuliere lokaties niet. De drie typen formuleringen zijn alle consistent voor een gegeven graad van de polynoomruimte, zowel in het inwendige als op de rand van het domein.

Hoewel de hybride formulering qua regulariteit van de discrete operator goede eigenschappen heeft, leidt het gebruik van deze methode uiteindelijk tot een dure en ingewikkelde discretisatie-techniek. Gezien de eenvoud van de discretisatie waartoe de DG formulering leidt, besluiten we om deze vorm verder uit te werken voor het inwendige-rand-probleem op een volledig rechthoekig rooster. Maar dan moeten we wel mogelijke singuliere lokaties van de inwendige rand lokaliseren of de discrete operator regulariseren. Voor een vierde-orde DG discretisatie van het inwendige-rand-probleem laten we zien dat de discrete operator kan worden geregulariseerd door een extra gewicht op de inwendige rand te introduceren. De DG-discretisatie van een dergelijk randprobleem is vierde-orde consistent, zowel in het inwendige van het domein als op de rand. De gemiddelde convergentie-factor, wanneer de maaswijdte wordt gehalveerd in de twee coördinaatrichtingen, blijkt ongeveer 12 te zijn, maar deze kan door een relatief eenvoudige ingreep in de discretisatietechniek nog verhoogd worden. Als voorbeeld lossen we een singulier-gestoord inwendig-rand-probleem op, waarmee we laten zien wat de mogelijkheden zijn van onze rand-discretisatie-techniek.

Deze techniek vermijdt het roostergeneratieprobleem dat ontstaat wanneer de klassieke eindige-elementen aanpak (FEM) wordt gebruikt voor de behandeling van kromme randen en de techniek blijkt nuttig te zijn voor het geval dat een DG-discretisatie op een orthogonaal rooster gewenst is, zoals bijvoorbeeld in het MR-algoritme.